THE UNIVERSITY *of* EDINBURGH

Morpholino Oligonucleotides in Responsive Hydrogels for microRNA Sensing

Geraint Johann Langford

Doctor of Philosophy

The University of Edinburgh

2019

Declaration

I declare the research detailed within this thesis has been collected by myself in the duration a PhD studentship under the supervision of Professor Michael Shaver, School of Chemistry, University of Edinburgh.

The work, data, and interpretation presented here is that of myself, except when analysing prior work or where a significant collaborative contribution has been made, in which case it has been clearly specified. Dr Jaclyn Raeburn developed the method for acrydite functionalisation of morpholino oligonucleotides, although the material used herein was modified by me. Dr David Ferrier designed the DNA crosslink (MIR1) and collected the optical data for figures 3.2 (reused in figures 3.20 and 3.26), 3.3 and 4.1 (reused in figures 4.2-4.6) which were reanalysed and presented myself. The measurements for figures 3.20-3.22 (reused in figure 3.29), 4.8 and 4.10-4.12 were conducted by Alex Carroll using my crosslink design (MIR2) and were subsequently reanalysed and presented myself.

This work has not been submitted for any other degrees or professional qualifications.

Signed:

Geraint Johann Langford

30 July 2019

Abstract

In recent years, microRNA (miRNA) has garnered a high level of interest in the field of biosensor development. MiRNA are a class of small, circulating RNA sequences that are essential for healthy control of protein expression. The variation of levels of specific miRNAs has been linked with over 150 diseases since the turn of the millennium, including cancers, cardiovascular diseases, parasitic infections and neurological disorders. The improved prognosis from early detection is stark, but established methods of miRNA detection suffer from poor sensitivity, low throughput, and require specialised laboratory equipment and trained staff to perform the time-consuming techniques. A simple, cheap and sensitive miRNA point of care sensor would be an invaluable tool in healthcare.

This thesis presents the continued optimisation of a miRNA sensing hydrogel with oligonucleotide crosslinks that are selectively cleaved in the presence of the target miRNA sequence. This selective reduction in crosslink density was transduced by a change in the swelling profile of the hydrogel and intelligent crosslink design used to control the swelling response for detecting a miRNA sequence, a short RNA (sRNA) sequence, or a small molecule using an aptamer. Morpholino oligonucleotides (MOs), an uncharged DNA analogue, were functionalised with an acrylamide moiety and used as responsive crosslinks for miRNA sequence detection in a world's first MO crosslinked hydrogel. The MO crosslinks offered significant improvements over DNA crosslinked hydrogels through improved thermal stability, no salt requirement and 1000-fold improved sensitivity, facilitating a wider range of sensing conditions. Analysis was also achieved using a mobile phone camera and laptop, demonstrating portability.

Carbon nanoparticles (CNP) were suspended in the hydrogels to act as a conductive component. As the hydrogel swells the distance between the particles is increased until there is no conductive pathway, resulting in an increase in the hydrogel's resistance. Numerous reproducibility challenges were identified with regards to gel delamination and CNP leaching partly due to inefficient UV photoinitiation of the pigment composite pre-gel solution. SEM imaging identified inconsistent composite homogeneity with areas of higher CNP and gel density in DNA crosslinked

composites, while MO crosslinked composites were homogenous and less conductive.

Inkjet printing of the composite material using an electrostatic dispersion as the conductive component was made possible using MO crosslinks with no salt and ammonium persulfate with TEMED in place of UV initiation. Optimised synthesis resulted in homogenous conductive composites far more robust and reproducible than the UV initiated CNP composite. However, MO solution viscosity resulted in improper aspiration and inaccurate deposition. Potential solutions and improvements are suggested, facilitated by the improvements offered by MO crosslinks.

Lay Summary

Current healthcare infrastructures can be helped by diagnosing disease faster, more accurately and earlier. In all treatable diseases, starting treatment or management earlier is more likely to result in an improved outcome, however, many tests to obtain these diagnoses are invasive, expensive or rely on symptoms that occur at later stages of disease progression. Point of care testing for biomarkers, molecules which indicate a specific disease, can use bodily fluids like blood or urine to diagnose disease faster, more accurately and sooner. MicroRNA, short strands of RNA, are essential cell regulators that can be used as biomarkers. Disease states result in abnormal microRNA levels that can diagnose almost any disease, including identifying between different types and stages of cancer. Current tests for microRNA are expensive, slow and require specialist equipment and trained personnel.

This research aims to develop a new sensor for microRNA using polymers that swell in the presence of the target microRNA strand. This polymer hydrogel is like a sponge that absorbs water and the amount of water it can absorb is controlled by the number of links within the hydrogel. Using DNA links that are broken by the target microRNA strand means that when the target microRNA is in a sample the polymer will absorb more water and swell to a larger size. This can be measured electrically by adding conductive particles. When the polymer is dense, the particles are close and the material is conductive. As the polymer swells, the particles move further apart and the material is less conductive. This enables a simple testing method as results can be easily computerised or handled on a smartphone.

This thesis describes the development of this microRNA sensing polymer. The polymer components and manufacture method were optimised and challenges identified. The use of Morpholino Oligonucleotides, structurally similar to DNA, in a world's first Morpholino Oligonucleotide crosslinked hydrogel offered a 1000-fold improvement in sensitivity over DNA crosslinked hydrogels, with better thermal stability and reduced salt sensitivity. Furthermore, inkjet printing of this material was developed to enable greater throughput and smaller volumes for potential commercialisation. Future work may further develop this material and sensor design into a rapid, simple, low-cost point of care diagnostic device.

Acknowledgements

First and foremost, I have to thank Michael Shaver for accepting me as his student, knowing full well I didn't choose polymers after watching his TEDx talk. Despite my many (many) frustrations throughout this PhD you always did your best to put a positive spin on results and were unnervingly reassuring about your belief in my abilities. Thanks also to my second supervisor Phil Hands and the man who started it all David Ferrier, without you this project and thesis would not exist.

To "Team OCPC": thanks to Dr Jaclyn Raeburn for the help in the earliest days, it's a shame GoT went so downhill! Also, thanks to David Pritchard, Axis-Shield Diagnostics and the EPSRC for their support and financing of this project. To my student Alex; I hope it wasn't too boring! This PhD would not have been possible without the talented staff at the UoE. In particular the SMC technicians (Stewart, Richard, Ewan and occasionally Peter) and Logan Mackay were invaluable. Similarly, thanks to the Bradleys for letting me loose on their printer, and in particular Sesha, without whom chapter 5 would have looked extremely different.

To Michael Serpe and his group in Alberta, thanks for the opportunity to work with you and experience such an amazing country. I can't thank the Edmonton Clansmen RFC enough for being so welcoming and giving me a home away from home, it would have been infinitely worse without you. Dan Norman, for being a quiet flatmate, relatively willing gym partner and a terrible mouse catcher.

To the GML, what an experience! In particular: Dan, for being the best to beat at table tennis (and fantasy football); Cairnsy, for all the drinks, pizza and rugby chat; Fern, for always offering sage advice and founding my favourite pub quiz team. To the Savage King, Meng the Merciless, for being the personification of hard work; Vishal for being the most helpful guy I've ever met; Yas, for all the geeky chats and belatedly Eszter, for smuggling me industrial quantities of paprika, all the trades and help preparing this thesis. To the better half of Ben and Gerry, Dr I hate polymers, for showing me the importance of PPE at home. Thanks to the Garden group for always rooting for me, to the "Fab Nudels" Laura, Yas, Dahlia for some of the funniest coffee breaks

imaginable, and thanks to all my other KB friends and trainers for the much-needed distractions.

Finally, I would like to thank my support network. My family for all their unwavering belief, in particular my uncle Gero for inspiring me to study science and my brothers for getting me into sci-fi. The most thanks undoubtedly goes to Marissa, for helping me through the darkest days, always believing in me, and for having an endless supply of funny videos.

Contents

Abbreviations

∆%	% Volume change	**NIPAm**	N-isopropylacrylamide
A	Adenine	**nt**	Nucleotides
a.c.	Alternating current	**NZD**	Neglected zoonotic disease
AAm	Acrylamide	**OCPCs**	Oligonucleotide crosslinked polymer composites
APS	Ammonium persulfate	**PBS**	Phosphate buffer
ASS	African sleeping sickness	**PCR**	Polymerase chain reaction
BAPO	Bis(2,4,6-trimethylbenzoyl)-phenyl phosphine oxide	**PDA**	Piperazine di-acrylamide
BAW	Bulk acoustic wave	**PDI**	Polydispersity index
C	Cytosine	**PEG**	Poly(ethylene glycol)
c-miRNAs	Circulating miRNAs	**PNAs**	Peptide nucleic acids
cDNA	Complementary DNA	**pNIPAm**	Poly(N-isopropylacrylamide)
CLL	Chronic lymphocytic leukemia	**PoC**	Point-of-care
cLNA	Complementary locked nucleic acids	**POTS**	1H,1H,2H,2H-Perfluorooctyl-trichlorosilane
CNP	Carbon nanopowder	**pre-miRNA**	Precursor-microRNA
CNS	Central nervous system	**pri-miRNA**	Primary-microRNA
CNT	Carbon nanotubes	**RNA**	Ribonucleic acid
d.c.	Direct current	**RPM**	Revolutions per minute
d.nm	Diameter in nm	**RT-qPCR**	Quantitative reverse transcription polymerase chain reaction
DI	Deionised	**SAW**	Surface acoustic wave
DLS	Dynamic light scattering	**SEM**	Scanning electron microscope
DNA	Deoxyribonucleic acid	**SERS**	Surface-enhanced Raman spectroscopy
DOD	Drop-on-demand	**SIC**	SIC black dispersion 1
G	Guanine	**Sol.**	Solution
GEM	General effective medium	**SPR**	Surface plasmon resonance
HPK	1-hydroxyphenylketone	**sRNA**	Small RNA
IDE	Interdigitated electrode	**ssDNA**	Single stranded DNA
LNA	Locked nucleic acids	**T**	Thymine
LoD	Limit of detections	**TEMED**	Tetramethylethylenediamine
MALDI-ToF-MS	Matrix assisted laser desorption/ionisation - time of flight mass spectrometry	**T_m**	Melting temperature
MBA	N,N' -methylene-bisacrylamide	**TMSPM**	3-(trimethoxysilylpropyl methacrylate
MEMS	Microelectromechanical systems	**TTR**	Time to response
miRNA	MicroRNA	**U**	Uracil
MOCHPCs	MOCH polymer composites	**V-70**	2,2'-azobis(4-methoxy-2,4-dimethylvaleronitrile)
MOPS	Morpholinopropane-1-sulfonic acid	**v/v**	Volume/volume
MOs	Morpholino oligonucleotides	**WHO**	World health organisation
NaDDBS	Sodium dodecylbenzenesulfonate	**wrt**	With respect to
NEMS	Nanoelectromechanical systems	**wt%**	Weight percent
NGS	Next generation sequencing		

Chapter 1 Introduction

Detection of biomarkers through use of analytical biosensors is an important aspect of modern biomedical research. Biosensors can be used in a wide variety of applications including clinical diagnostics, drug discovery and biodefense.[1] In particular, sensitive measurement of short nucleic acid sequences remains challenging, yet has huge potential in improving diagnostics and disease monitoring. MicroRNA (miRNA) are a class of short oligonucleotides which can serve as biomarkers for almost all diseases and conditions. Current commercial detection techniques remain too complex, expensive and lengthy for wide-spread use. A simple and cost-effective miRNA detection method could rapidly flourish as a new biomedical technique and revolutionise healthcare. Current pressures on healthcare infrastructures could be reduced with efficient, facile testing, while healthcare in remote areas or developing countries could be greatly improved.

This chapter will introduce miRNA and in particular its potential as a clinically relevant biomarker. The challenges of current detection methods of miRNA will be discussed, as well as invasive techniques that may be replaced by miRNA sensing. This thesis presents an oligonucleotide crosslinked hydrogel and the attempted transduction methods for miRNA detection. In particular, it addresses the limits of optical transduction methods and the challenges of synthesising conductive composites by incorporation conductive particles within the hydrogel. Furthermore, it presents an inkjet printed method of synthesis in a step towards commercialisation. The principles behind each method are introduced herein, as well as the aims and structure of this thesis.

1.1 MicroRNA

MiRNA are non-coding RNAs around 19-25 nucleotides (nt) long.[2,3] The term miRNA was coined in 2001 by Ruvkun *et al.*, having been first described by Lee *et al.* as “small RNAs with antisense complementarity” in 1993.[4–6] Interest in miRNAs as biological

regulators has been increasing since the turn of the millennium, as evidenced by the ever-increasing number of publications per year on this topic (Figure 1.1). Of particular interest is the investigation of miRNA in disease states and the potential use of miRNA as diagnostic biomarkers.

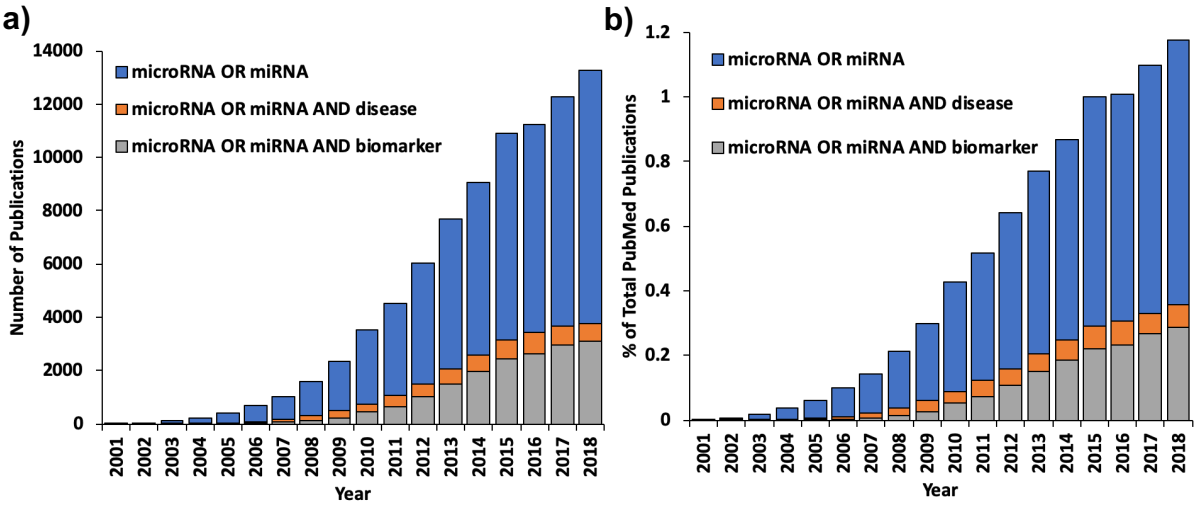

Figure 1.1 Number of publications per year associated with miRNA. Literature search performed on PubMed with search terms "microRNA OR miRNA", "microRNA OR miRNA AND disease" or "microRNA OR miRNA AND biomarker". (a) Number of publications per year (b) Publications per year as the percentage of total publications recorded on PubMed.

1.1.1 Expression, Structure and Activity of microRNA

Mature miRNA sequences are made of a ribose-phosphate backbone with adenine, guanine, cytosine or uracil nucleobases (Figure 1.2). There have been over 2500 miRNA sequences identified in humans, with estimates that 1-3% of the human genome codes for miRNAs which control an estimated 30% of all genes.[7–11] MiRNAs are involved in controlling various essential biological processes including cell proliferation, differentiation, metabolism and apoptosis, with estimates that >60% of human genes have conserved miRNA binding sequences.[8,12–14] As such, miRNA are found in every cell and a variety of bodily fluids, an advantageous feature for potential biosensing applications.[15]

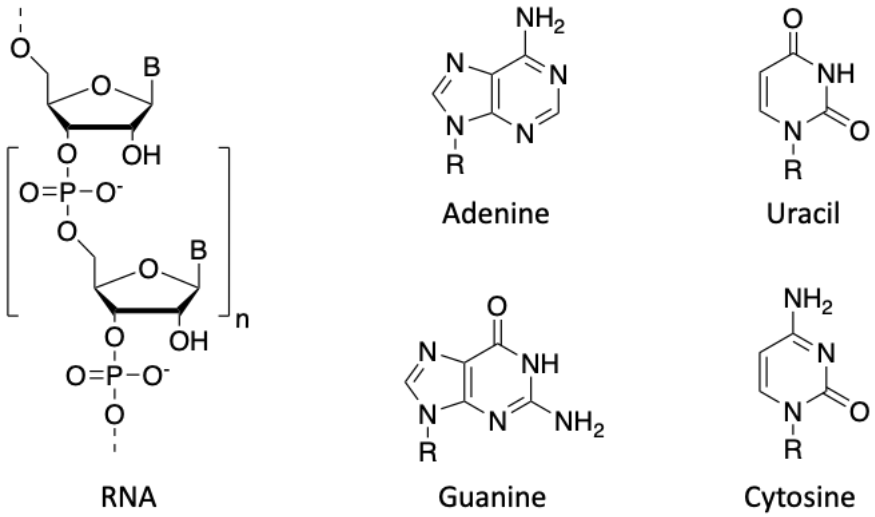

Figure 1.2 Structure of RNA that makes up miRNA, where "B" denotes one of the four RNA nucleobases adenine (A), uracil (U), guanine (G) or cytosine (C). Uracil occurs in place of thymine (T) found in DNA sequences.

Eukaryotic miRNA biogenesis and expression begins in the cell nucleus (Figure 1.3). Much like mRNA, miRNA is transcribed from the DNA template, frequently originating from introns of the pre-mRNA transcript whose exons encode a mRNA.[10,12,16] This co-expression of mRNA and miRNA means that regulatory elements of gene expression can simultaneously control miRNA expression.[10,13,16] Transcription of miRNA genes or introns occurs via RNA polymerase II (Pol II) to form primary-microRNAs (pri-miRNA). These primary transcripts are single stranded RNA molecules and can be >1000 nt long. Pri-miRNA strands typically contain an RNA hairpin 60-120 nt in length, one strand of which contains the mature miRNA sequence.[17] This pri-miRNA hairpin structure is then cleaved from the remaining single-stranded RNA by a microprocessor complex of Drosha, a double-strand-specific ribonuclease, with Pasha (DGCR8), a double-stranded RNA binding protein, forming precursor-microRNA (pre-miRNA).[18]

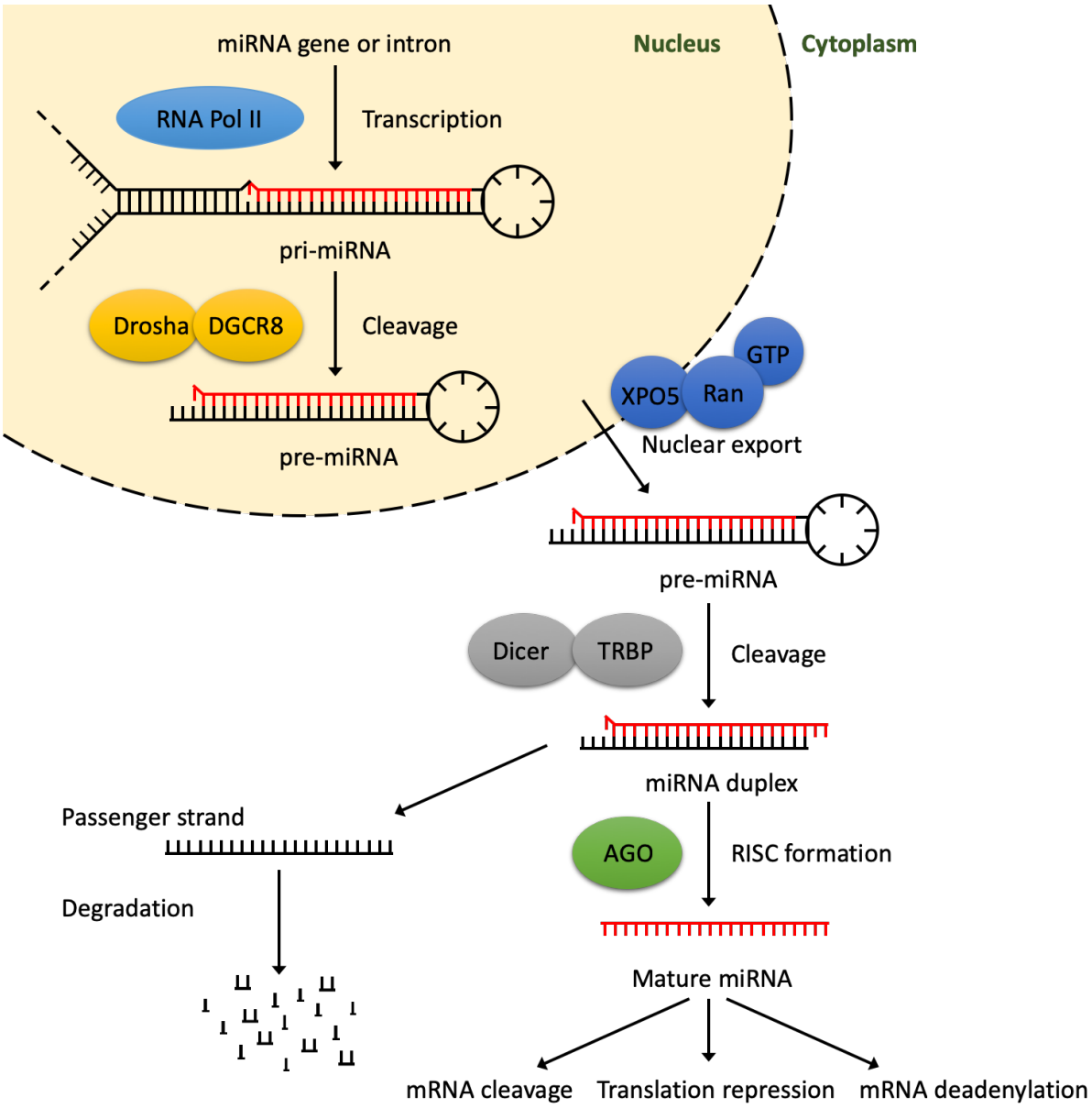

Figure 1.3 Illustration of the canonical linear miRNA biogenesis and processing into mature miRNA (red). The primary miRNA transcript (pri-miRNA) is produced by RNA polymerase II and cleaved by Drosha and Pasha (DGCR8) to form pre-miRNA. The pre-miRNA hairpin is the exported from the nucleus by Exportin-5-Ran-GTP into the cytoplasm where the RNAse Dicer, with a double-stranded RNA-binding protein (TRBP), cleaves the hairpin to a duplex of mature miRNA length. The mature miRNA sequence is then loaded with argonaute 2 (AGO) proteins into the RNA-induced silencing complex (RISC) and guides RISC to the target mRNAs to induce mRNA cleavage, translation repression or deadenylation. The passenger strand is degraded. Figure adapted from Winter *et al.*[16]

The pre-miRNA is then exported from the nucleus into the cytoplasm *via* Exportin-5 (XPO5).[19] The pre-miRNA is then further cleaved by DICER which removes the hairpin structure to leave a partially double-stranded miRNA duplex, with one strand being the mature miRNA sequence.[20] The duplex is loaded onto Argonaute 2 (AGO) proteins,

whereby the mature miRNA strand remains and the passenger strand is discarded and degraded. Mature miRNA is then incorporated into an RNA-induced silencing complex (RISC) and exerts control over mRNA targets through inducing mRNA cleavage, translational repression, or through causing mRNA deadenylation which leads to earlier mRNA decay.[21] Through down-regulation of mRNAs, miRNAs act as post-transcriptional regulators. Each miRNA stand may target multiple mRNA sequences, while each mRNA sequence may be regulated by numerous miRNAs.[22]

1.1.2 MicroRNA in Disease

MiRNAs were first identified as a potential biomarker in 2002, when Calin *et al.* identified that two-thirds (41/60) of chronic lymphocytic leukemia (CLL) cases exhibited miR15 and miR16 deletion or down-regulation.[23] Subsequent research confirmed this finding and further identified an inactivating germline mutation which reduced expression of both miR15 and miR16 which could be implicated in the familial association seen with CLL.[24] It was further discovered that miR15 and miR16 are oncomiRs which act as tumour suppressors through downregulation of B-cell lymphoma 2 (BCL2) expression, an anti-apoptotic oncogene.[25,26]

Since 2002, miRNA have been linked to more than 150 diseases[27] from cancers[11,28–30] and heart disease[31] to viral[11,32,33] or parasitic infections[34] and even neurological disorders like Alzheimers.[35–37] MiRNA can be used to diagnose some of top global causes of death, as well as rarer diseases[38] and physical traumas such as traumatic brain injuries.[39] Further uses include food safety, forensic science and counter-terrorism.[40–43]

The expression of miRNA sequences can be up- or downregulation in response to changes in tissue during healthy cell regulation or in disease states, such as genetic mutations associated with cancer, or be mutated themselves. As such, they are extremely information-rich biomarkers. Furthermore, they can facilitate earlier diagnosis as abnormal miRNA expression can occur during early stages of disease.[44,45]

Table 1.1 Examples of miRNA as biomarkers. Adapted from Maqbool *et al.,* Detassis *et al.* and Salvatore *et al.*[11,30,38]

Disease	miRNA	Expression Status
Alzheimer's disease	miR29a/b, miR107	Down-regulated
B-cell lymphoma	miR155	Up-regulated
	miR17-19b cluster	Overexpression
	miR15a, miR161, miR143, miR145	Down-regulated
Breast cancer	miR21, miR96, miR183, miR182, miR141, miR200a, miR429	Up-regulated
	miR139, miR143, miR145	Down-regulated
Cardiac hypertrophy	miR195	Up-regulated
Cardiac hypertrophy	miR1, miR133	Down-regulated
Colorectal cancer	miR19a, miR21, miR146	Up-regulated
	miR34b/c	Epigenetic silencing
	miR1, miR143, miR145, miR545	Down-regulated
Gastric cancer	miR21, miR152	Down-regulated
Liver cancer	miR885-5p	Up-regulated
	miR424, miR326, miR511, miR125b-2, miR451	Down-regulated
Lung cancer	miR21, miR23, miR187+H15:H29	Up-regulated
	miR30a-3p, miR383, miR448, let7 family	Down-regulated
Lung adenocarcinoma and squamous cell carcinoma	miR21, miR205, miR375	
Lung neuroendocrine cancer histotypes	miR15a, miR22, miR141, miR497, miR129-5p, miR185, miR409-3p, miR409-5p and miR431-5p, miR129	
Muscular dystrophy	miR206	Over-expressed
	miR1, miR133	Down-regulated
Obesity	miR143	Up-regulated
	miR17-92	Over-expressed
Ovarian cancer	miR9	Up-regulated
	miR187	Down-regulated
	miR15a, miR16-1	Frequently deleted or down-regulated
	miR10a, miR622, miR767-5p, miR888, miR1280	Somatic mutations
Pancreatic cancer	miR21	Up-regulated
	miR7, miR137	Down-regulated
Parkinson's disease	miR133	Down-regulated
Prostate cancer	miR21	Up-regulated
	miR15a, miR16-1	Frequently deleted or down-regulated
	miR130b∼301b cluster, miR143, miR145	Down-regulated
Renal cell carcinoma	miR187	Down-regulated
Viral myocarditis	miR1, miR21, miR146b	Over-expressed
	miR155	Up-regulated
Rare Diseases		
Duchenne muscular dystrophy	miR206, miR181, miR1, miR133, miR29	Up- / down-regulated
Amyotrophic lateral sclerosis	miR206	Down-regulated
Sézary syndrome	miR21, miR214, miR486, miR18a, miR342, miR31, let7, miR233, miR199a	Up- / down-regulated
Rett syndrome	miR146a, miR146b, miR130, miR122a, miR342, miR409 miR29b, miR329, miR199b, miR382, miR296, miR221, miR92	Up- / down-regulated
Multiple osteochondromas	miR21, miR140, miR145, miR214, miR195, miR451, miR483	Up- / down-regulated
Hailey-Hailey disease	miR181a, miR125b, miR99, miR106a	Up- / down-regulated
Hepatoblastoma	miR214, miR199a, miR150, miR125a, miR148a, miR492	Up- / down-regulated

As well as facilitating earlier diagnosis, miRNA can be used to predict patient prognosis or monitor disease progression.[30,46] They can give insight into both tumour genotype and phenotype which could be used for more effective personalised

healthcare. Drug resistance, to date mostly investigated with regards to cancer treatments, can be predicted or monitored during treatment.[47,48] For example, in colorectal cancer, miR17 overexpression was linked to innate resistance to chemotherapy through inhibition of tumour suppressor PTEN.[49] Similarly, elevated miR210 levels indicated resistance to trastuzumab treatment (as well as tumour presence and lymph node metastases) in human epidermal growth factor 2 (HER-2) positive breast cancer.[50] Earlier detection of innate or acquired drug resistance would enable more accurate use of the most effective treatments and could drastically improve survival rates.[15] After treatment, abnormal miRNA expression returns to normal, enabling recovery monitoring as well as relapse prediction.[51] MiRNA expression profiles from tumours and metastases were able to identify the tissue of primary origin, which again could be used to improve treatment plans.[52]

Detection of a single miRNA sequence can be used to diagnose disease. Overexpression of miR548c-3p may diagnose castration-resistant prostate cancer (CRPC) as it is currently not linked to other diseases.[53] Similarly, miR92a downregulation can be used to diagnose acute leukaemia,[2] while miR155 has been identified as a risk factor for breast cancer.[54]. Realistically, robust diagnosis would require profiling multiple miRNA sequences to identify a miRNA disease fingerprint, either using a multi-array or by comparing multiple single miRNA sequence detections.[55] For example, a 3-miRNA signature (miR9, miR182 and miR200b) has been identified for muscle-invasive bladder cancer (MIBC),[56] while screening of larger numbers of sequences would enable more reliable diagnosis of other diseases or multiple diseases simultaneously.[15,57]

The use of miRNA profiles consisting of numerous miRNA sequences is a large improvement over other biomarkers such as mRNA or proteins. For example, miRNA profiles were shown to be more accurate in identifying specific cancers than mRNA profiles, especially in cases where the tumour is poorly differentiated from healthy tissue.[58,59] Protein biomarkers are used for diagnosis of a number of cancers such as prostate-specific antigen (PSA) for prostate cancer or carcinoembryonic antigen (CEA) for colon cancer. However, the use of these biomarkers for cancer diagnosis can lead to misdiagnosis as the expression profiles are also altered in many non-cancerous diseases and miRNA may offer improved accuracy and specificity of

diagnosis.[28] For example, PSA results in a relatively high number of false positives in men with benign prostate enlargement.[60]

Many current biomarkers tend to have little use in the clinic, due to a number of issues such as ease of detection and effectiveness of diagnosis, which can be difficult due to genetic variation in patients and populations.[35,61–63] It is believed that the use of miRNA profiling will produce fewer false positives or negatives than protein biomarkers, and give more informative diagnosis with regard to disease resistance.[64] In particular, circulating miRNA could be used in non-invasive testing methods, appropriate for point-of-care (PoC) testing.[15,57,65]

1.1.3 Circulating microRNA as non-Invasive Biomarkers

A number of extracellular miRNAs have been detected in blood, serum, plasma, urine, saliva and other body fluids.[15] These circulating miRNAs (c-miRNAs) are far more stable under harsh conditions such as high temperatures, extreme pH or RNase activity than mRNA. This is believed to be due to association RNA-binding proteins like AGO2 or due to secretion within microvesicles or exosomes, although microvesicles have a relatively short half-life in plasma and can contain RNases.[66,67] The mechanisms for miRNA sorting and secretion are not fully understood, yet appear to be at least partially regulated and are theorised to be implicated in cell-cell communication.[30] Alternatively, miRNA can leach unregulated out of damaged or dead cells after tissue damage.[68]

The first mention of c-miRNAs as cancer biomarkers was by Lawrie *et al.* who identified over-expression of miR155, miR210 and miR21 in serum from patients with diffuse large B-cell lymphoma (DLBCL).[69] Subsequently, c-miRNA expression profiles were identified for prostate cancer, breast cancer, lung cancer, heart failure, pregnancy and many other diseases from serum.[57] Examples of c-miRNA profiles in other body fluids include diagnose lung or ovarian cancer from plasma, bladder cancer diagnosis from urine and oral squamous cell carcinoma identification from saliva.[15]

Although the c-miRNA frequently correlates with tissue miRNA concentrations, this is not always the case. Expression of the miR17-92 cluster and miR17-5p was increased in both the tumour tissue and serum of lung cancer patients,[70] while liver-specific miR122 decreased in liver tissue but increased in serum of patients with hepatocellular carcinoma (HCC).[71] As such, c-miRNA disease profiles should be considered both separately and in combination with tissue miRNA disease fingerprints and may offer further insights into disease progress.

Due to the less invasive and painful methods used for liquid biopsies, patient compliance would be expected to increase. The cost and time required for collection and processing of liquid samples is lower than for non-liquid biopsies, as well as typically being far more simple to collect.[30] Just like intracellular miRNA, c-miRNA can be used to diagnose tumours at pre-operative levels, including prediction of patient prognosis or drug resistance.[44,46,72] Different body fluids contain different miRNA profiles, meaning it is possible to distinguish between body fluids for forensic applications.[40,41,73] It can be expected that c-miRNA based diagnosis will become more reliable with more research into “normal” c-miRNA profiles of healthy individuals. Similarly, as the workflow of sample collection, processing, measurement and analysis becomes more unified or standardised, results will be more reliable and easier to compare.[57,72]

1.1.4 Acute Leukaemia: Circulating microRNA

The target miRNA sequence chosen as a proof-of-concept for miRNA-based diagnostics in this work was for acute lymphoblastic leukaemia (ALL). Leukaemia is a cancer of white blood cells or bone marrow. In 2017 leukaemia accounted for 2.8% (approximately 8500 cases) of new cancer diagnoses in England, of which around 350 cases were ALL.[74] Between 2014-2035 the incidence rates of leukaemia in the UK are expected to rise by 5% to 19 cases per 100,000 people in 2035.[75] Leukaemia accounted for 4600 deaths per year between 2014-2016 in the UK and 24,400 deaths in the US (2016).[76]

Leukaemia is typically divided into 4 subtypes: acute myeloid leukaemia (AML), chronic myeloid leukaemia (CML), ALL and CLL. These types are defined by which bone marrow cells the cancer originates in affecting either myeloid cells, white blood cells that fight bacterial or parasitic infections, or lymphocytes, which fight viral infections. Chronic leukaemia tends to be slower to grow and progress, whereas acute leukaemia grows quickly and can be fatal within weeks to months. Symptoms arising from each subtype are very similar, typically including weakness, fatigue, headaches, unusual bleeding, bruising or purple skin rash, pale skin, repeated infections or fever, weight loss, joint and bone pain and swollen lymph nodes.[77] Many of these symptoms are also similar to viral infections. As such, diagnosis requires complex tests including a blood count and typically a bone marrow biopsy.[78] Further tests can include an x-ray and further scans for swollen lymph nodes and any signs of cancer spreading. A sample of cerebrospinal fluid (CSF) may also be taken to test if leukaemia cells have penetrated the central nervous system (CNS), indicating a poor prognosis. As treatment is conducted relevant tests may be repeated to monitor response to treatment.

Diagnosis and differentiation between leukaemia subtypes takes time, money and experienced clinical staff. As the acute forms of leukaemia progress rapidly and penetration of the CNS makes treatment far more difficult this time reduces the chances of successful treatment.[79] A simple, low-cost and rapid diagnostic method could greatly improve leukaemia treatment and survival rates, especially if able to differentiate between subtypes.

Research conducted by Tanaka *et al.* showed through analysis of 148 different miRNAs in plasma from patients suffering from AML or ALL that miR92a expression was lowered in cases of acute leukaemia. They also found that, compared to healthy controls, the ratio of miR92a : miR638 was decreased in all AML or ALL suffering patients with around a 10-fold difference between the two miRNA sequences. Differentiation between AML and ALL through miRNA fingerprinting was shown to be possible by Mi *et al.* who identified 27 miRNA expression differences between AML and ALL cell lines.[80] In ALL samples, miR128a and miR128b were over-expressed while miR223 and let7b were under-expressed when compared to AML samples. Analysis of these four miRNAs achieved an overall accuracy of 97% from patient

samples. MiR92a was selected as a proof-of-concept sequence to detect, with a view to then expand to detecting other leukaemia relevant sequences.[81]

1.2 MicroRNA Detection Methods

Biosensors are important diagnostic and analytical tools able to detect, and ideally quantify, an analyte. They consist of a biological detecting component which responds to the analyte and a physicochemical detector component that transduces this response into a quantifiable signal (Figure 1.4).[3,82–86] MiRNA biosensors have become an increasingly important field for identifying new miRNA profiles and have great potential for improving disease diagnosis, optimising treatment and monitoring progress both during and after treatment.

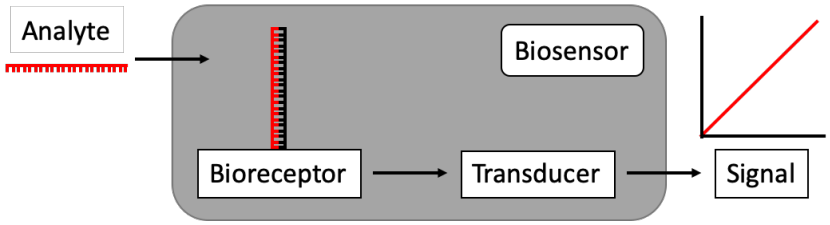

Figure 1.4 General structure of a biosensor. The recognition of the analyte by the bioreceptor is transduced and processed into a readable signal.

A point-of-care device that is cheap, simple and non-invasive could help facilitate widespread miRNA-based diagnostics. It could be used for detecting specific disease-relevant miRNA profiles, potentially in developing countries and remote locations where centralised testing is not possible. A recent example of point-of-care technology is INRstar based engage product, a self-care anticoagulation test which links results to their health care clinic. As well as improving treatment personalisation and reducing risk of stroke,[87] it also reduced data entry errors and saved an estimated 1.5 hrs of nurse time per patient per year.[88] Approximately 1.25 million people in the UK are prescribed oral anticoagulant drugs,[89] meaning up to 11,000 weeks of nurse time could be saved. It can be expected that miRNA-based point-of-care or self-care diagnostics

and disease monitoring would be capable or similar improvements in patient health and reduced pressure on health-care infrastructure.

1.2.1 Ongoing Challenges of microRNA Detection

Accurate determination of miRNA expression levels in specific cell types, tissue or body fluid is essential for translating the potential of miRNA diagnostic into practical applications. Several intrinsic characteristics of miRNA make detection with high sensitivity and specificity challenging.[62] Mature miRNAs lack common sequence features to facilitate selective purification, while the short sequence length makes use of amplification techniques difficult as the primers required for regular polymerase chain reaction (PCR) protocols are unable to bind to the small miRNA template.[90] As a result, PCR methods typically measure pri- or pre-miRNA. The sequence similarity of miRNAs, in particular within the same family or in cases of single-base mutations, requires highly specific sequence detection.

An ideal profiling method would be sensitive for quantitative analysis of miRNA from small amounts of material and able to detect single nucleotide differences. Detection of multiple miRNA sequences simultaneously would enable miRNA disease fingerprinting and simple methodology using cheap materials and equipment to enable widespread testing.[15] Of the available detection methods none are perfect and each has inherent limitations (Table 1.2).[62,91]

Table 1.2 Analytical microRNA detection techniques, advantages, limitations and demonstrated limit of detections (LoD). Adapted from Planell-Saguer *et al.*[62] and Zhang *et al.*[92]

Detection method	Assay type	Advantages	Limitations	Lower LoD
Northern blotting	Solid-phase	Quantitative Specificity Common equipment Established method	Low Sensitivity Low Throughput Large initial sample Labour intensive	nM range
Microarrays	Solid-phase	High throughput Simple analysis Multiplex	Not quantitative Low sensitivity Low specificity	fM range
Electrochemical	Solid-phase	High sensitivity Quantitative Multiplex Electrical output	Uncommon equipment Labelling required for sensitivity Labelling adds complexity	100 aM labelled 50 pM unlabelled
SERS	Solid-phase	High specificity Precise Label-free Multiplex	Uncommon equipment Complex analysis	fM range
SPR	Solid-phase	High Sensitivity High throughput potential Multiplex	Expensive Uncommon equipment Complex	100 fM
High throughput sequencing	Solid-phase	High throughput Direct detection High sensitivity High specificity Investigates known and unknown miRNAs	Expensive Time-consuming Complex analysis	500 aM
Bioluminescence	Solid-phase	High throughput High sensitivity Multiplex	Complex procedure Monitors signal decrease	1 fM
	Solution-phase	High throughput High sensitivity	Monitors signal decrease	pM range
RT-qPCR	Solution-phase	High sensitivity Quantitative High accuracy Established method Multiplex	Expensive Low throughput Complex analysis	fM range
Fluorescence correlation spectroscopy	Solution-phase	High sensitivity Rapid Quantitative High specificity	Specialist equipment	100 fM
***In situ* hybridisation**	Solution-phase	Single cell or subcellular analysis High sensitivity	Slow analysis Semi-quantitative Complex method Low throughput	

Further difficulty arises from the low concentrations of miRNA sequences. The estimated number of copies of a miRNA sequence was estimated to be 500 per cell, although some miRNA sequences have been found with more than 10,000 copies per cell.[68,93,94] This means that despite making up only around 0.01% of total RNA by weight,[95] many miRNAs will exist at higher concentrations than mRNA. Circulating miRNA concentrations will also be dependent on the body fluid being investigated. The total RNA concentration varies considerably depending on the body fluid type

(100-47,000 µg/L or 100-9000[30] up to 23,000[96] copies per µL), with the number of detectable miRNA sequences also varying (200-460 miRNAs with a level of >80% of the global mean).[97] Weber *et al.* also identified a total of 600 different miRNAs from 12 different body fluids, noting that while many miRNAs were present in all body fluids tested, the composition and concentrations differed. Serum concentrations of miRNA typically range between 200 aM – 20 pM depending on the miRNA sequence and this serves as a target for appropriate miRNA detection.[98] Not discussed here are variations arising from sample collection and processing methods or normalisation methods used during data analysis.[15,57]

1.2.2 Solid-phase Techniques

Solid-phase techniques are methods where the probe is captured to a surface for hybridisation to the target miRNA. Solid-phase techniques tend to be more applicable to high-throughput analysis as required for clinical diagnostics using miRNA.

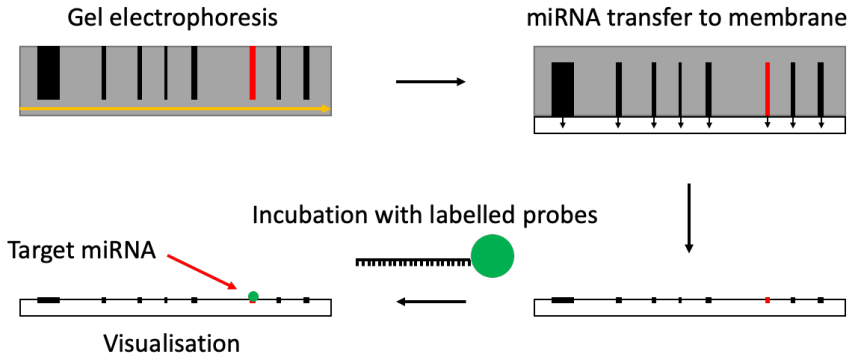

Figure 1.5 Northern blotting procedure. RNA is extracted and separated using gel electrophoresis. The separated RNA is then transferred to a nitrocellulose membrane and incubated with labelled DNA probes to identify the target sequence.

Northern blotting is one of the more prominent methods for detecting miRNAs with a relatively standardised method (Figure 1.5). Gel electrophoresis is used on the sample miRNAs which are then transferred to a nitrocellulose membrane and allowed to hybridise with complementary DNA (cDNA) probes that are complementary to the target miRNAs. The probes are typically labelled with fluorescent or radioactive tags

for detection. Northern blotting was used in identifying some of the earliest miRNAs and remains a gold standard method for miRNA profiling.[5] Despite improvements in speed and sensitivity Northern blotting remains labour intensive and time-consuming making it impractical for large scale studies or diagnostics, as well requiring relatively large sample volumes.[99–103]

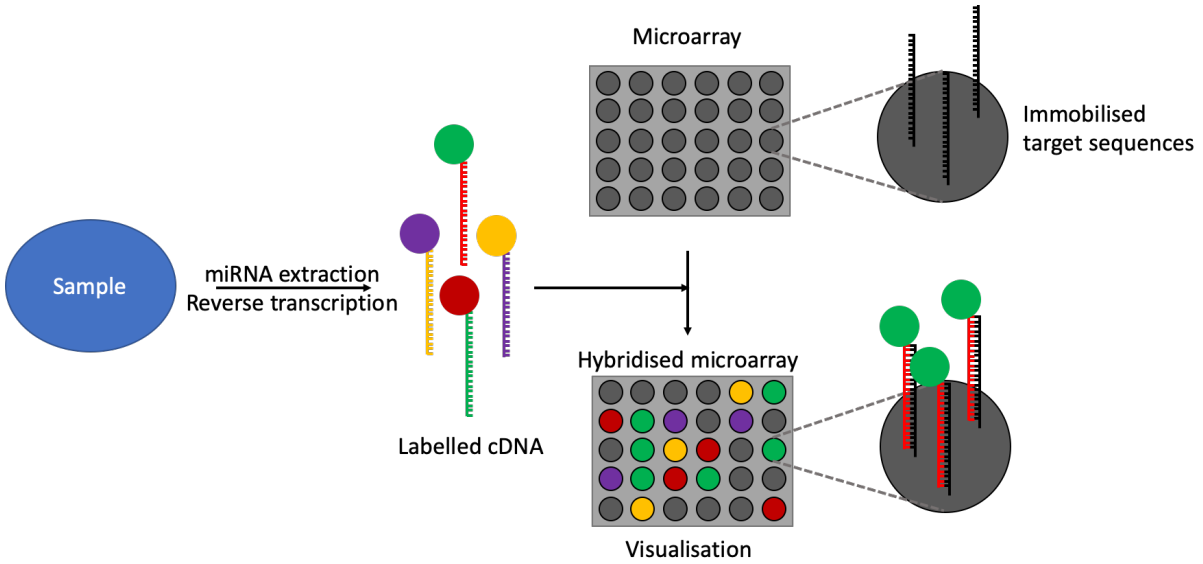

Figure 1.6 Basic microarray procedure. Microarrays are prepared through attachment of individual target sequences to each well. Reverse transcription of the miRNA is then used to generate cDNA probes which are labelled and fluorophores. Incubation of cDNA within the microarray followed by multiple washing steps leaves only cDNA probes bound to the immobilised target sequences. Visualisation and analysis can then be carried out to identify the intensity of each well.

Microarrays facilitate much higher throughput being able to screen large numbers of miRNAs at once (Figure 1.6).[104] After purification, miRNAs can be tagged with fluorophore-labelled oligonucleotides using T4 RNA ligase. The miRNA strands can then hybridise with cDNA probes immobilised in a microarray. The quantity of bound miRNA in each location can then be assessed using a laser to excite the fluorescent tags. A number of variations have been developed using alternative probe design or methods, immobilisation chemistry or signal detection methods.[105–108] Despite being able to carry out genome-wide miRNA investigations, limitations remain regarding hybridisation conditions, such as temperature, and sequence specificity.[109,110] Normalisation of data remains a challenge, microarray chips are fairly expensive and again, a relatively large quantity of miRNA is required.

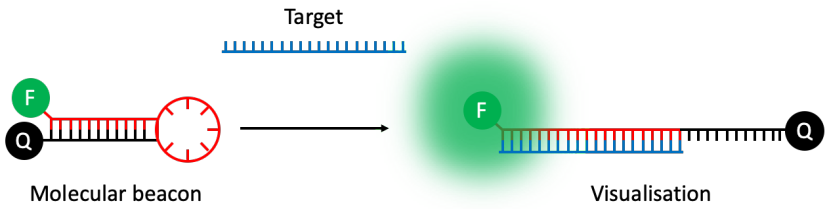

Figure 1.7 Example of hairpin molecular beacon. The cDNA sequence is lengthened with a partially complementary sequence to form a hairpin structure. A fluorophore is attached to one end with an appropriate quencher attached to the other end. Whilst in the hairpin conformation, the fluorophore and quencher are in close proximity, such that the fluorescence is quenched. Introduction of the target sequence displaces the hairpin stem, the distance between fluorophore and quencher is increased and a detectable fluorescence achieved.

Bioluminescence, chemiluminescence or electrochemiluminescence and fluorescence are all similar optical transduction techniques that can be incorporated into microarray technologies. A variety of probe and hybridisation designs have been developed to use cDNA labelling in place of miRNA labels.[111] For example a hairpin cDNA design can be used to bring a fluorophore and appropriate quencher into close proximity, such that fluorescence resonant energy transfer (FRET) results in minimal fluorescence (Figure 1.7). Upon target miRNA hybridisation, the hairpin structure releases resulting in an increased fluorescence. Chemiluminescent labels can be triggered to emit light using a chemical reaction, bioluminescent labels use light-emitting proteins as labels, while electrochemiluminescence emits light based on electrical potential. However, these transduction methods still require numerous labelling and processing steps which increase complexity and cost. Solution-phase bioluminescence methods are simpler and more rapid than the solid-phase techniques. However, widespread use remains unlikely as signal reduction is measured instead of signal increase and is therefore harder to validate.

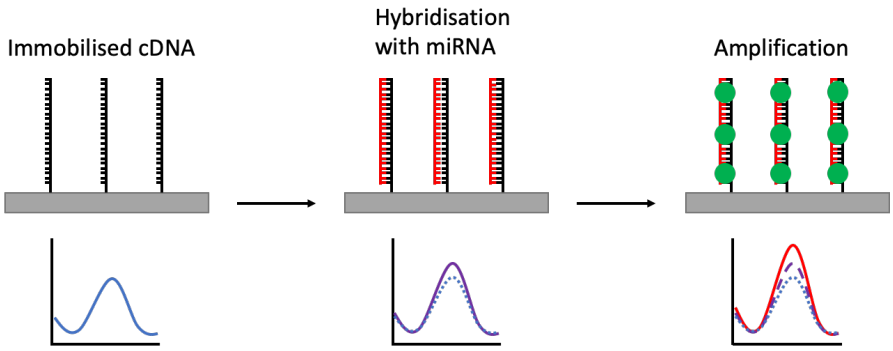

Figure 1.8 Solid-phase electrochemical miRNA detection example. The cDNA probes are immobilised on an electrode, hybridisation of the target miRNA sequence can result in a detectable change in signal, typically amplified using catalysts, enzymes, or reporter molecules such as ferrocene based intercalators.

Electrochemical detection of miRNAs is an emerging method with great potential for simple, quick and low-cost methods for quantitative miRNA detection.[3] They rely upon changes in circuit properties upon hybridisation of the target miRNA with a bound cDNA sequence (Figure 1.8). Signal amplification can be achieved using redox reporters, ferrocene tags or various dsDNA binding probes.[112–115] These techniques have achieved low detection limits relevant to diagnostic applications and typically require small amounts of material. Furthermore, electrode designs can enable multiplexing capabilities and electrical outputs can be easily integrated into user-friendly systems. However, any multi-step process introduces errors at each stage and the labelling steps used for the required signal amplification increase method complexity and cost.

Surface-enhanced Raman spectroscopy (SERS) is capable of detecting Raman signals from single molecules. SERS can achieve rapid, label-free identification of miRNA with single-base specificity by adsorbing silver or gold nanorods onto a glass slide and detecting probe cDNA attachment to the nanorods (Figure 1.9).[116,117] If cDNA hybridises to the target miRNA it will not bind to the nanorod. The resulting Raman spectra can be used to identify the presence of target miRNA. However, each target miRNA spectra must be obtained prior to assay development and any sequences with overlapping peaks are unable to be differentiated.[118] SERS is also a relatively specialist technique with equipment and knowledge not as widespread as more established methods.

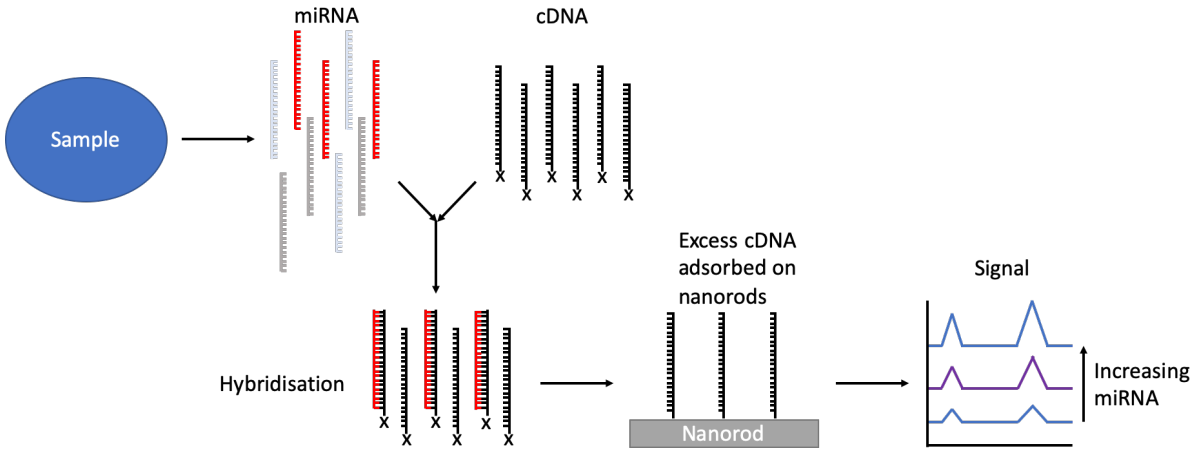

Figure 1.9 Surface-enhanced Raman spectroscopy (SERS) assay for miRNA detection using gold or silver nanorods as SERS substrates. Thiolated cDNA probes able to adsorb to the nanorods are first mixed with the miRNA sample. Hybridisation with target miRNA prevents the cDNA from binding to the nanorods meaning only excess cDNA will be attached, resulting in a quantifiable response dependent on how much cDNA binds to the nanorods.

Surface plasmon resonance (SPR) based methods also offer label-free miRNA detection. One method developed by Corn *et al.* attached complementary locked nucleic acids (cLNA) to the SPR chip surface and then added the target miRNA to hybridise.[119] Subsequently, poly(A) polymerase was allowed to add poly(A) tails to the miRNA and then gold nanoparticles modified with poly(T) tails were added to bind to any poly(A) tails. This method achieved appropriate sensitivity and high-throughput capabilities for miRNA quantification appropriate for miRNA profiling. The cost of equipment and relatively specialist knowledge required makes this technique inaccessible for many researchers.[120,121]

1.2.3 Solution-phase Techniques

Solution-phase techniques are methods where the probe hybridises to the target miRNA in solution. Due to the improved freedom of movement compared to solid-phase techniques, solution-phase methods typically offer a faster response time.

Quantitative reverse transcription polymerase chain reaction (RT-qPCR) is the gold standard for RNA quantification and frequently used to validate other techniques.[108,122]

RNA must first be transcribed into cDNA by reverse transcriptase and the cDNA can then be used as the template for qPCR cycles. RT-qPCR is sensitive, accurate, and relatively easy with fairly common equipment. However, miRNA targets are difficult to detect due to the short sequence lengths. Early detection was based on detecting the longer pri- or pre-miRNA sequences, although these are not always relevant to the concentrations of mature miRNA.[90] Separation of mature miRNA from its precursors adds further labour steps and processing time.[123]

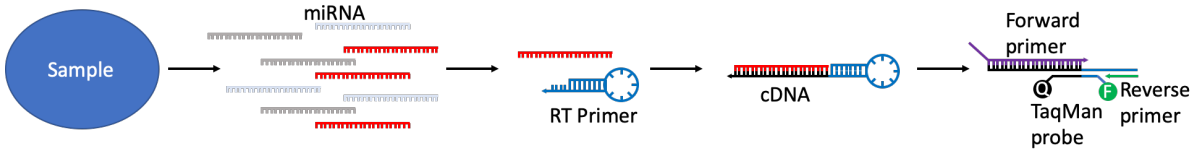

Figure 1.10 Scheme of the TaqMan-based RT-qPCR method. The RT stem-loop primers bind to the target miRNA and are reverse transcribed. The resulting transcript is then quantified using typical TaqMan PCR with an miRNA specific forward primer, reverse primer and TaqMan probes.

RT-qPCR of mature miRNA sequences was achieved using a stem-loop RT-PCR method based on TaqMan assays (Figure 1.10).[124] Raymond *et al.* also developed a method using SYBR Green and cLNA primers,[125] while other techniques typically use primer extension or poly(A) polymerase.[126] In each case the cost is increased by the required reagents. Droplet digital PCR (ddPCR) can improve sensitivity, accuracy and precision when compared to RT-qPCR.[96,127] A number of portable PCR technologies have claimed to be point-of-care devices,[128–130] while examples of devices made of affordable off-the-shelf components reduce equipment costs.[131] Despite reducing test times, the required reverse transcriptase step ensures a relatively complex method and reagent costs remain high.

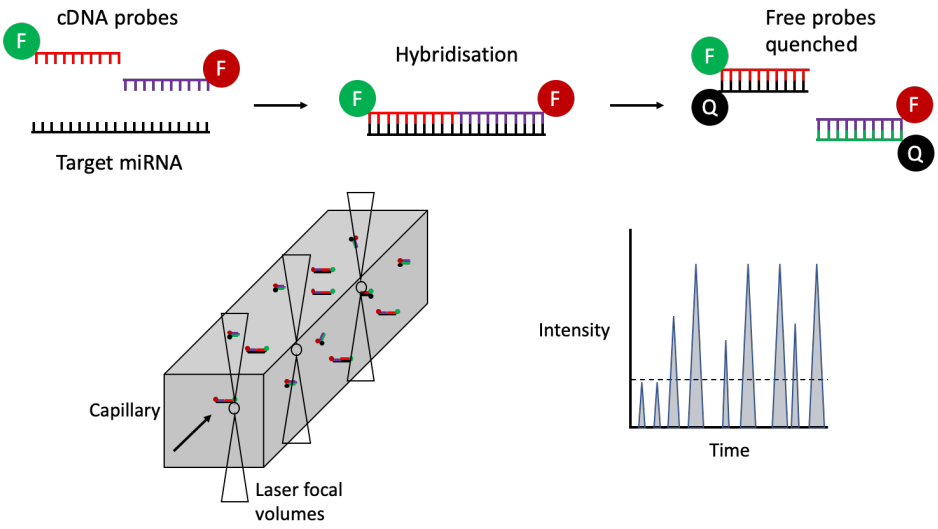

Figure 1.11 Fluorescence correlation spectroscopy scheme for miRNA detection. MiRNAs are mixed with two cDNA probes with differing fluorophores. Excess cDNA are mixed with complementary quencher probes. The miRNA hybridised with the two fluorophore probes are then flowed through a capillary and investigated using a series of laser focal volumes. Data analysis measures the flow velocity between laser spots and emissions are presented as spikes in signal intensity over time.

Fluorescence correlation spectroscopy is capable of miRNA quantification using a microfluidic multi laser system to count individual molecules as they flow through the system (Figure 1.11). The lack of target capture, amplification or reverse transcription are all highly attractive features.[62] Neely *et al.* developed a dual probe labelling system which could count single molecules of mature miRNA using fluorescence correlation spectroscopy.[132] Fluorophore-labelled cDNA hybridise with the target miRNA while unbound cDNA is hybridised to a quencher probe to reduce background fluorescence. The fluorophore count is then used to calculate the number of molecules present. Despite the sensitivity, specificity and rapid response time, the requirement of specialised equipment makes widespread use improbable.

In situ hybridisation can detect miRNA in cell lines or tissues by using labelled cDNA in fixed cells ensuring conserved morphology.[133] Use of cLNAs improved sensitivity and specificity yet the low throughput and lack of quantification make this unlikely to be used in a clinical setting.[134] *In situ* hybridisation remains an important tool in miRNA expression validation and understanding.[92]

High-throughput sequencing of miRNAs using next generation sequencing (NGS) led to the majority of discoveries of miRNA since 2007 due to the ability to process many

sequences in parallel quickly.[135,136] Although findings required validation using alternative methods due to inherent sequencing biases, NGS remains attractive as a first-pass diagnostic method as it is independent of hybridisation or previous knowledge.[62] Although current techniques vary substantially in adapter and primer sequences, cost and accuracy, further development may facilitate the use of NGS for miRNA diagnostics.[137]

1.2.4 Micro- and Nano-electromechanical Techniques

Micro- and nano-electromechanical systems (MEMS and NEMS) are 3D devices manufactured on the micrometer or nanometer respectively, emerging as potential oligonucleotide sensors.[138,139] In general, the microfabrication techniques required would enable mass production and multiplexing, while resolution and sensitivity tend to increase as the sensor size decreases. Similarly, the small size typically requires smaller sample volumes and facilitates faster response times, while electrical outputs facilitate integration with user-friendly systems. A summary of the LoD and limitations of techniques discussed here is shown in Table 1.3.

Table 1.3 Summary of micro- and nano-electromechanical systems (MEMS and NEMS). Adapted from Ferrier *et al.*[138]

MEMS/NEMS-based Techniques	Lower LoD	Limitations
Bulk acoustic wave (BAW)[140]	75 aM	Sensitive to solution viscosity and test conditions
Surface acoustic wave (SAW)[141]	1 pM	Sensitive to solution viscosity and test conditions
Cantilevers[142]	2 aM	Sensitive to solution viscosity and test conditions
Nanowires[143]	1 aM	Complex synthesis and expensive
Nanopores[144]	1 fM	Sensitive to solution ions Low throughput Limited multiplex capabilities

Bulk acoustic wave (BAW) devices are made of a quartz layer with an electrode on either side (Figure 1.12). When an a.c. voltage is applied the resonant frequency is dependent on the dimensions and total mass.[145] Functionalisation using thiolated cDNA can then capture the target miRNA, which increases the total mass resulting in a detectable change in resonant frequency.[140] However, the resonant frequency of BAW devices will also be affected by solution viscosity making clinical samples problematic.[146]

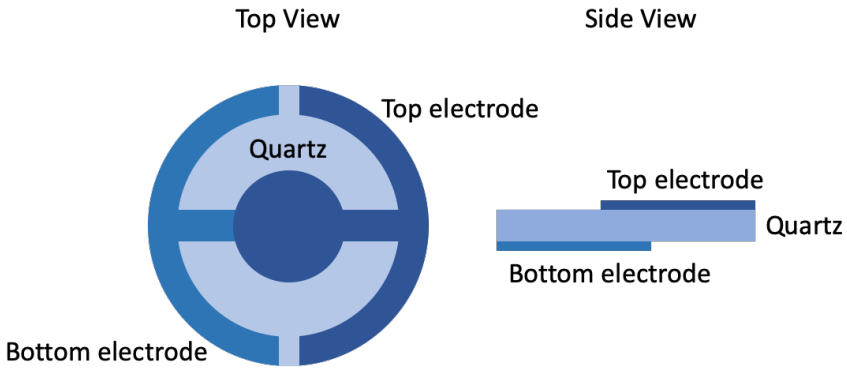

Figure 1.12 Illustration of a typical bulk acoustic wave (BAW) device. Immobilised cDNA on the BAW device enables miRNA capture. The change in mass results in a detectable change in oscillation frequency.

Surface acoustic wave (SAW) devices are similar to BAW devices. Delay-line SAW devices use a piezoelectric substrate between a transmitting interdigitated electrode (IDE) and a receiving IDE.[138] In resonator SAW devices the IDE is in the centre of the device with reflectors at either end of two piezoelectric substrate areas. In both designs the time take to travel and amplitude of the a.c. waves is affected by molecules bound to the sensing area, enabling detection of target miRNA bound to substrate-bound cDNA.[141,145] Although sensitive and easily combined with microfluidics, SAW devices remain affected by solution viscosity, mechanical stress and temperature.

Cantilevers consist of a micro- or nano-scale beam anchored at one end. Attachment of cDNA to the cantilever enables target miRNA binding.[147,148] This binding can be detected by the bend of the cantilever, or by changes in oscillation frequency. Some success has been achieved in human plasma, using gold nanoparticle probes for amplification.[142] Once again, the sensitive and specific micro- and nano-cantilevers

are vulnerable to affects from changes in temperature and changes in fluid viscosity or flow.

The flow of electrons through nanowires can be affected by charged moieties on the surface. Nanowires can be functionalised with cDNA.[143,149,150] The subsequent binding of target miRNA causes a measurable increase in charged molecules on the surface. MiRNA sensing using nanowires is fast, sensitive, specific and label-free. However, current fabrication methods are both lengthy and expensive, while they are also sensitive to any ions present in solution.[138]

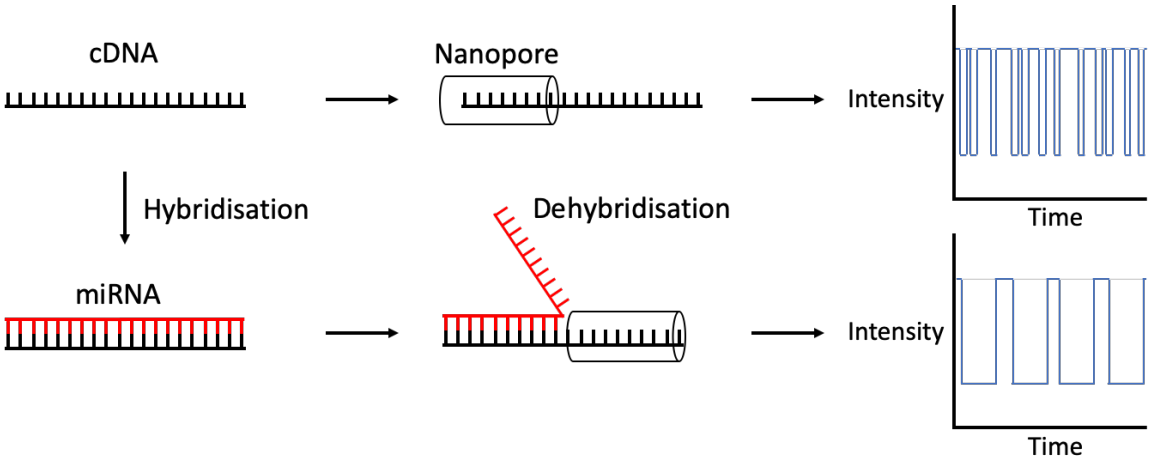

Figure 1.13 Illustration of a nanopore based miRNA sensor. The regular flow of ions through the nanopore is impeded when an oligonucleotide strand passes through. Size exclusion allows only single strands to pass through the pore, such that duplexes must dehybridise before crossing through the nanopore. The dehybridisation step elongates the crossing time, resulting in longer ion flow disruptions.

Nanopore sensors measure the ionic current flow across a membrane with a nanoscale pore enabling the flow of ions across the membrane.[144,151] If an analyte the same size as the pore flows through then the flow of ions is temporarily stopped, changing the measured current. The number and frequency of drops can therefore infer the concentration of analytes. Use of cDNA probes to form duplexes with target miRNA strands leads to longer current drops as the duplex has to dehybridise as it crosses the pore, enabling differentiation of target miRNA from complex solutions (Figure 1.13).[42] Due to their scale, nanopore sensors are suited to small sample volumes and can be sensitive and specific as well as being label-free and reusable. However, they have a low throughput and limited multiplex capabilities.

1.3 ssDNA Crosslink Bioreceptors

1.3.1 ssDNA as Bioreceptors

Although miRNA can be detected through electrostatic interactions,[152] sequence specificity is essential for achieving any practical applications. Most miRNA biosensors use the inherent specificity afforded by designing cDNA probes for base-pairing with the target miRNA sequence. These predominantly rely upon canonical base-pairing discovered by Watson, Crick, Franklin and Wilkins,[153,154] although in some cases Hoogsteen or Wobble base pairs may be relevant.[155,156] RNA detection can be modelled using ssDNA, replacing any uracil nucleotides with thymine.

Hoogsteen and Wobble base pairs are more relevant in examples of DNA and RNA aptamers enabling secondary structures like guanine-quadruplexes.[157,158] Aptamers can be compared to antibodies,[159] using oligonucleotide secondary structures to bind various substrates such as adenosine,[157,160,161] cocaine,[162,163] proteins like thrombin, amyloid β-protein[164] or α-synuclein[165] or metal ions.[166] The flexible secondary structure enables various binding mechanisms reliant on hydrophobicity, molecular shape recognition or intercalation and can be used to design transducible responses in biosensors.[85,167]

The interaction between cDNA and target miRNA can be predicted and is typically reported as the melting temperature (T_m), the point at which 50% of strands are unhybridised.[168] The T_m is sequence specific and will be higher if the sequence contains more GC nucleobases both due to increased hydrogen bonding and base stacking. Similarly, the T_m can predict mismatch interactions whereby the fewer matching basepairs the lower the T_m and the less stable any hybridisation.

Due to the sequence similarities within miRNA families and the potential of single-base mutations in disease, detection with single base pair specificity is essential for real world applications. To illustrate this, Table 1.4 shows the Let miRNA family sequences, and the respective T_m for each sequence if hybridising to the cDNA of let7a.[118] Despite the cDNA being most favourable for binding the target miRNA, a single base pair

mismatched miRNA would still hybridise with the cDNA and complicate measurements through competitively interaction.

Table 1.4 Adapted from Driskell *et al.*[118] Mismatches to cDNA for let7a are in bold. Hybridisation T_m predictions were calculated at 150 mM NaCl, using "Nearest Neighbor" calculations.[168] cDNA T_m predictions were calculated with full complementarity, cDNA7a T_m predictions were calculated with deletions in place of mismatches to cDNA for let7a.

	miRNA	**Sequence**								**T_m (°C)**	**T_m (°C)**
cDNA	7a	ACT	CCA	TCA	TCC	AAC	ATA	TCA	A	cDNA	cDNA7a
let7 miRNAs	let7a	UGA	GGU	AGU	AGG	UUG	UAU	AGU	U	69.7	69.7
	let7b	UGA	GGU	AGU	AGG	UUG	U**G**U	**G**GU	U	74.4	68.6
	let7c	UGA	GGU	AGU	AGG	UUG	UAU	**G**GU	U	72.0	69.0
	let7d	**A**GA	GGU	AGU	AGG	UUG	**C**AU	AGU		71.8	67.2
	let7e	UGA	GGU	AG**G**	AGG	UUG	UAU	AGU		71.9	68.8
	let7f	UGA	GGU	AGU	AG**A**	UUG	UAU	AGU	U	66.4	66.5
	let7g	UGA	GGU	AGU	AG**U**	UUG	UA**C**	AGU		69.2	65.7
	let7i	UGA	GGU	AGU	AG**U**	UUG	U**GC**	**U**GU		71.5	64.5

1.3.2 ssDNA Hybridisation in Biosensors

One simple method to improve ssDNA bioreceptor specificity is to add a competing strand to which partially matches and it prehybridised to the cDNA sequence. Binding of target miRNA then requires competitive displacement of this blocker strand.[169,170] Competitive displacement is dependent on the affinity and concentration of the target miRNA. A number of different designs of hybridised bioreceptors exist (Figure 1.14) and different reporter molecules or molecular beacons can be attached to aid transduction.[171] Alternatively, hybridised ssDNA can be used in materials as crosslinkers able to control swelling or gel-sol transitions.[172,173]

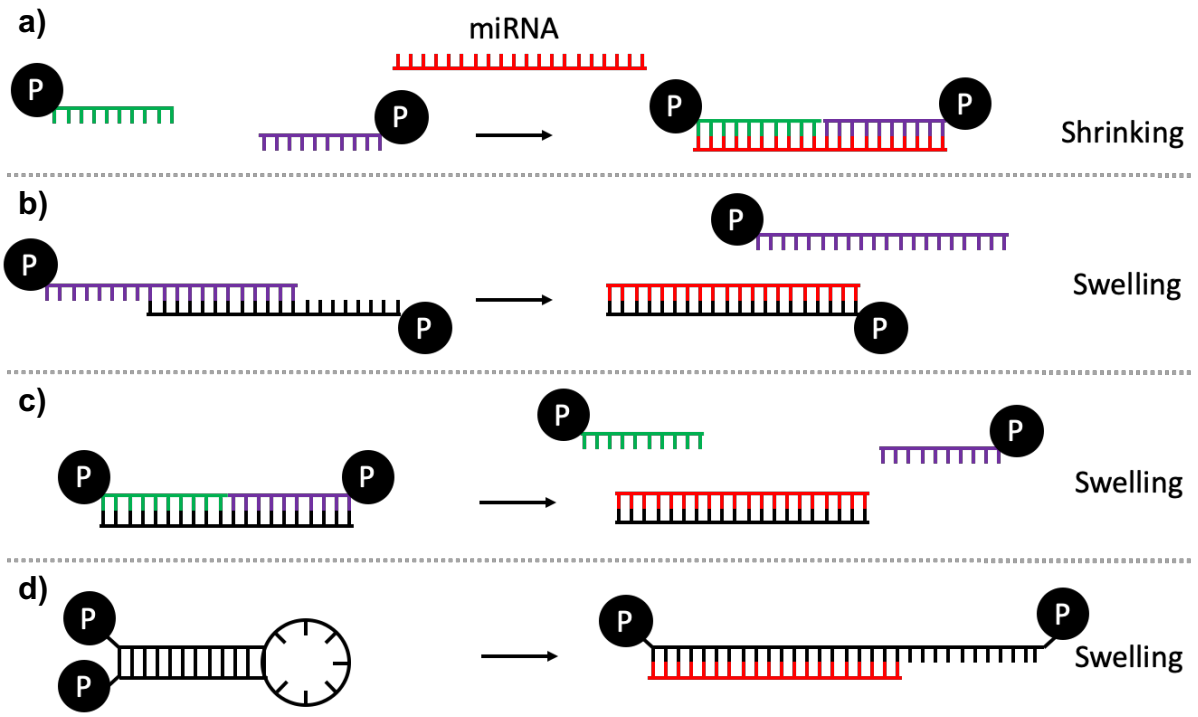

Figure 1.14 Illustration of oligonucleotide crosslinks able to control hydrogel swelling and dissolution. Location of chemical attachments to the polymer backbone (black circles with white "P") and hybridisation design can cause increased swelling (or dissolution) or cause gel shrinking (or gelation) in response to the target analyte sequence. (a) Addition of miRNA results in hybridisation with two cDNA probes, bringing them into closer proximity to form a crosslink. (b) A crosslink formed of single fully complementary cDNA with a blocking strand both attached to the polymer. The blocking strand is displaced by the miRNA sequence, thereby breaking the crosslink and increasing swelling. (c) Two blocking strands act as tethers for the cDNA strand. Binding of the miRNA to the cDNA displaces both blocking strands to break the crosslink. (d) Stem-loop crosslink design where both 5' and 3' ends of the hairpin are attached to the polymer. Hybridisation with the miRNA target displaces the stem sequence and lengthens the crosslink as the hairpin is linearised. Adapted from Peng *et al.*[174]

Hybridisation based on stem-loop structures can be problematic depending on the target miRNA sequence.[175] If there is no self-complementarity in the miRNA sequence then nucleotides must be added, while too much self-complementarity may not have enough unpaired nucleobases to form a loop. Furthermore, the miRNA sequence length limits how long the stem hybridisation can be, meaning the T_m may be inappropriate for a number of synthetic or testing conditions.

Alternatively, displacement of a separate blocker strand which is partially complementary to the sensor cDNA (which is fully complementary to the target miRNA) can be used to trigger a number of signalling mechanisms.[171] A single blocker strand can be designed for any cDNA and target miRNA sequence and can be tailored to the required stability and response time by varying the complementary sequence

length.[176] Various double blocker systems have been used with two separate blocker segments and these may be more applicable when detecting longer sequences.[177] The cDNA strand may itself be anchored to a support structure, or merely hybridised to anchored blocker strands depending on the desired response. Similar hybridised structures have been utilised for aptamer sensor signalling.[178] Various DNA based responsive materials utilise DNA three- or four-way junctions[174,179] and can be used to control programmable materials.[180] However, these tend to be more expensive due to material cost and design complexity.

1.3.3 Ongoing Challenges of ssDNA Bioreceptors

There are a number of concerns when using DNA as bioreceptors. Compared to many responsive materials DNA or RNA are relatively expensive, although costs would be reduced on a commercial scale. This can become a limiting factor in experimental design depending on funding sources. For example, ssDNA is frequently used in place of RNA at early stages of biosensor development as it is both cheaper and more stable.

Other challenges arise from DNA structure. Enzyme degradation may be used in some signalling pathways, for example using duplex-specific nucleases to cut double-stranded DNA from a surface or release reporter molecules.[181,182] However, it can be a concern during testing on biospecimens as many body fluids contain nucleases as uncontrolled or unexpected oligonucleotide degradation can cause false negatives or positives.

Another concern when using DNA for miRNA detection is the relatively low T_m defined by the target miRNA sequence and length.[82] Depending on the sensor design, this can limit the usable temperatures for any processing or testing steps. As T_m is dependent on miRNA sequence this would not be an issue for longer miRNAs with high GC contents, but might be problematic for shorter miRNAs with low GC contents. Furthermore, if using any of the blocker strand designs discussed above, the blocker sequence will also be defined by the target miRNA and the hybridisation length with

the cDNA sensor would need to be shorter than the target miRNA to facilitate displacement.

The solvent choice, pH and salt concentration will also all affect the hybridisation strength and T_m of any DNA based bioreceptor.[183–193] Most physiological conditions are amenable to DNA hybridisation such that the pH and salinity would be appropriate and could be maintained during purification steps with appropriate buffers, indeed low salinity may be used during purification to remove any secondary structures or associated proteins.[194] However, the solvent, pH and salinity conditions dictate available processes for device manufacture and synthesis. For example, if blocker strands are combined with sensor cDNA as a late wash step, far more conditions are usable than attempting to maintain hybridisation during synthesis.

1.4 Morpholino Oligonucleotides

Numerous DNA analogues have been developed in response to some of the challenges of using DNA in sensors. In particular, LNA have been widely explored in almost all miRNA detection methods discussed previously (Figure 1.15).[100,103,106,132,195] Use of cLNA in place of cDNA increases the T_m *via* enhanced base stacking and backbone rigidity.[196–198] The specificity and sensitivity of detection is thereby also increased. Alternative DNA analogues originally developed as antisense oligonucleotides have shown similar increases in T_m and similar potential in diagnostic applications.[196,199] Of these, peptide nucleic acids (PNAs) and morpholino oligonucleotides (MOs) offer an added benefit of uncharged backbone moieties, reducing the effects of salinity on hybridisation.

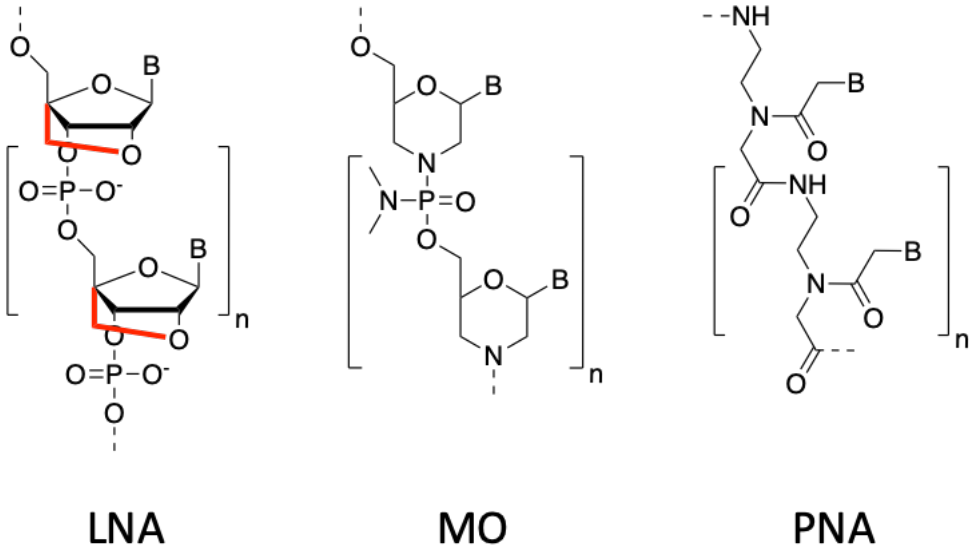

Figure 1.15 Structures of LNA, MO and PNA where nucleobases (A, G, C or T) are represented by "B".

1.4.1 Morpholino Oligonucleotide Synthesis and Structure

MOs are amongst the least explored of all the DNA analogues in diagnostics, in part because they are one of the most recently developed. Devised by Summerton in 1985 and developed by 1997, they consist of a morpholino ring subunit with a nucleobase connected *via* phosphorodiamidate linkers. Subunits are synthesised from ribonucleotides.[200,201] Oxidative opening of the ribose ring results in a dialdehyde in place of the 2' and 3' hydroxyls, which is then closed with ammonia to form a morpholine ring. Reduction of the resulting ring removes the 2' and 3' hydroxyl groups before protection of the amine group by conversion to tritylamine and addition of a chlorophosphoroamidate moiety to the 5' oxygen. Oligomers are then synthesised by linking the morpholino subunits in a 2-step addition cycle on solid resin support. A deprotected amine carries out a nucleophilic addition / elimination reaction to form a phosphorodiamidate linker. Subsequent detritylation is then carried out to prepare the oligomer for the next subunit addition.

MOs exhibit good solubility, nuclease resistance and increased T_m with DNA and RNA.[200–202] As such, like LNAs and PNAs, MOs exhibit improved affinity and specificity for DNA or RNA sequences. The uncharged phosphorodiamidate linker removes the electrostatic repulsion between MO and DNA or RNA that otherwise occurs between

oligonucleotides with charged phosphate or thiophosphates. As such, MOs have been shown to be less affected by solution salinity.[203]

1.4.2 Morpholino Oligonucleotides Uses

From 1999 onwards MOs have been used in numerous antisense applications in gene knockdown studies, including knockdown of miRNA.[204–210] MOs have also been investigated in a number of diagnostic techniques.[211] MOs have been used in microarrays with low salt concentrations for detection of 25 nt long sequences.[212] Gold nanoparticles were functionalised with MOs to create a pH sensitive motif with DNA for *in situ* tests,[213] Similarly, stem-loop structures with molecular beacons was developed for *in situ* sequence detection.[214] Other examples include more fluorescence,[215] SPR[216] and combined with PCR.[217]

The greater benefit of using uncharged oligonucleotides and minimal salt concentration is for signal maximisation in electrochemical transduction methods. Electrochemical studies have been spearheaded by Levicky *et al.* with studies into capacitive transduction DNA-MO binding on electrode surfaces.[218–220] The accumulation of charged DNA strands resulted in increased charge density resulting in the capacitive signals and has been combined with eletrokinetic methods to concentrate DNA samples.[221] Similar work was conducted by Wang and Smirnov using nanochannels, while MOs have also been utilised in nanowire devices.[222,223] Cao *et al.* discovered that MO enzyme resistance was also conferred to any MO hybridised DNA and Burki *et al.* developed a fluorescent assay based on unhybridized DNA digestion.[224,225]

Compared to DNA and other analogues, MO have been relatively unexplored in diagnostic applications. The improvements offered by MOs would be especially relevant when used in clinical samples, where enzyme resistance, improved specificity and salt insensitivity would make MOs more robust bioreceptors. Furthermore, sensor design and use may be simplified when the effects of these factors are reduced and a wider range of processes may be used during manufacture due to the increased

stability of MOs. As such, MOs deserve further exploration within the field of medical diagnostics.

1.5 Oligonucleotide Crosslinked Hydrogels

The previous sections outlined the potential benefits of miRNA detection and the challenges or limitations of the currents methods of doing so. In an attempt to overcome some of these challenges, Prof. Shaver and Dr Hands combined their expertise, in polymers and electronic noses respectively, and established Dr Ferrier's PhD project developing oligonucleotide crosslinked polymer composites (OCPCs).[226,227] The following sections will introduce the concepts that form the principals behind this method for simple, multiplex capable, rapid and affordable miRNA detection.

1.5.1 Polymer Hydrogels

Hydrogels are crosslinked hydrophilic polymer networks that can swell to absorb large volumes of water (up to over 90 wt% water) without dissolving. In biosensing and biotechnology applications hydrogels offer a number of benefits. Firstly, they offer a 3D matrix for bioreceptors and analytes similar to solution-based techniques, which can avoid any surface density concerns regarding 2D solid-phase. Many hydrogels are inherently resistant to bio-fouling and swelling in water are facilitates the diffusion of substances such as analytes from body fluids.[228] Finally, their properties can be easily manipulated in a number of ways such as copolymerisation with mixed monomers, varied monomer, crosslinker or initiator concentration or the incorporation of porogens.[229–232]

Simplistically, gelation occurs when clusters of polymers link to form a single continuous network. The classical theory of gelation was developed by Flory and later Stockmayer with assumptions that all monomer functional groups are equally reactive and no bonds form closed polymer loops, meaning no intramolecular reactions.[233,234]

Subsequently, a variety of percolation theories have been developed to better account for realistic polymerisation conditions.[235]

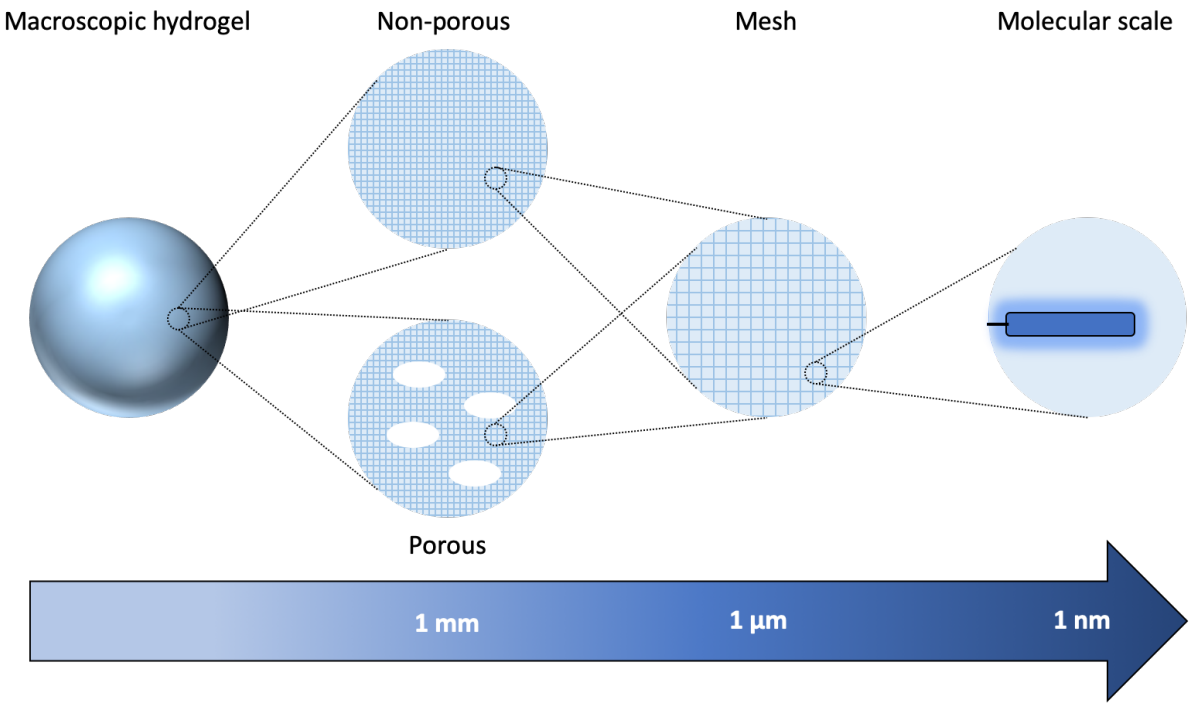

Figure 1.16 Hydrogels at the macroscopic scale include the size, shape and porosity of the structure with pores typically 10-500 µm. The mesh size is the distance between polymer strands, 5-100 nm, while the molecular scale includes interactions such as oligonucleotide hybridisation events. Adapted from Li and Mooney.[236]

Synthetic hydrogels can be prepared and classified in numerous ways depending on the materials and method of synthesis and the resulting structures.[237] The hydrogel properties can be considered at various scales (Figure 1.16).[236] Monomer unit interactions can be considered on the nano-scale, while the micro-structures include the mesh size and crosslink distribution. On the macroscopic scale the porosity of the hydrogel may have a large influence on properties, while the gel shape, size and diffusion coefficients will also affect hydrogel properties and swelling.[238] Simplistically, hydrogel swelling pressure (π_{sw}) can be considered as the interaction of a solvent with the network microstructure (Equation 1.1). The osmotic pressure of the polymer network (π_{osm}) is the driving force of swelling, resulting from the polymer-solvent interactions, while the elastic response of the material results in resistance to the network deformation of swelling (π_{net}).

Equation 1.1 Hydrogel swelling as polymer elasticity and swelling pressure.[239]

$$\pi_{sw} = \pi_{osm} - \pi_{net}$$

Water in hydrogels can be classified into three types: bound water, made up strongly bound, weakly bound and non-bound water, associated water, again strongly or weakly associated, and free water.[240] The water activity is also important as it acts as a solvent affecting nanoclusters or nanodomains as well as microdomains and influencing gel structure, density, electroconductivity and other properties. Solute diffusion, adsorption, release, etc. in hydrogels is important in many biotechnology fields. It is dependent on the hydrogel free volume, hydrodynamic drag on the solute, path length (increased by obstruction) as well as the interaction with the polymer matrix and material. The hydrogel porosity, including porosity within macrostructure walls, can also influence diffusion and adsorption of solutes.[241] Dehydration of gels can alter the hydrogel nano- and microstructures and may cause gel deformations.[231] Rehydration of dried gels typically results in a reduced amount of strongly and weakly bound water. Diffusion of low- and high-molecular weight solutes showed that non-bound water in macropores behaves similarly to free water, yet solute interactions with macropore walls can result in adsorption or penetration which can then influence water behaviour.

1.5.2 Oligonucleotide Crosslinked Hydrogels

A number of different “smart” or “intelligent” hydrogels have been developed that exhibit structural changes in response to pH,[242,243] temperature,[244] ionic concentration,[245] light[246] or electrical[247] or magnetic fields.[248–251] Triggered response to DNA or RNA has been achieved in a number of ways. Serpe *et al.* specialise in responsive poly(*N*-isopropylacrylamide) (pNIPAm) microgels in Fabry-Pérot etalons which, when functionalised with N-(3-aminopropyl) methacrylamide hydrochloride (APMAH), would collapse in response to charged ssDNA (Figure 1.17).[152,252] If combined with magnetic particles functionalised with cDNA, the target miRNA sequence could be extracted and then quantified by the non-sequence specific etalons.

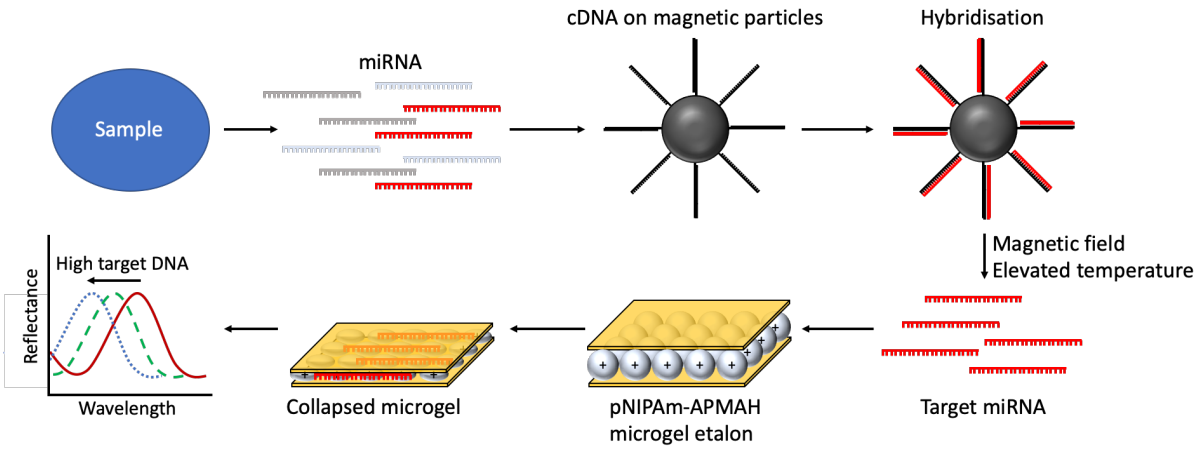

Figure 1.17 Target miRNA is purified using magnetic particles functionalised with cDNA. Once hybridised, magnetic particles can be extracted with a magnetic field and the miRNA removed through elevated temperatures. Swelling of the pNIPAm-APMAH microgel etalons with the resulting solution of target miRNA results in gel shrinking as the negatively charged miRNA interacts with the positively charged microgels. The collapse is then transduced through the altered optical properties of the etalon structure. Adapted from Serpe *et al.*[253]

By grafting ssDNA into hydrogels the bioreceptor capabilities of ssDNA can be conferred to the material to generate responsive smart hydrogels.[174,254,255] Rather than detecting non-specific DNA concentrations, this utilises the specificity of DNA sequences for label-free detection. Various hybridised DNA crosslinks have been incorporated into hydrogels in a number of designs. These can be classified as either gel-sol responsive hydrogels, wherein only oligonucleotide crosslinks are used so that displacement of the blocker strand results in hydrogel dissolution, or gel-swelling responsive hydrogels, using a mixture of covalent crosslinks and oligonucleotide crosslinks so that the swelling is controlled by the number of intact crosslinks without dissolution occurring.

Yang *et al.* developed an aptasensor design using oligonucleotide crosslinks in PAM (Figure 1.18a).[256] Synthesis of two polymers using free radical redox initiation, with each containing grafted DNA, enabled gelation upon mixing. Entrapment of gold nanoparticles during gelation resulted in a measurable signal as the gel-sol transition triggered by the analyte enabled nanoparticle release. However, relatively high concentrations of DNA were required to cause gelation. Similar hydrogels also undergoing gel-sol transitions have been used to release small molecules or quantum dots as reporter molecules.[173,257]

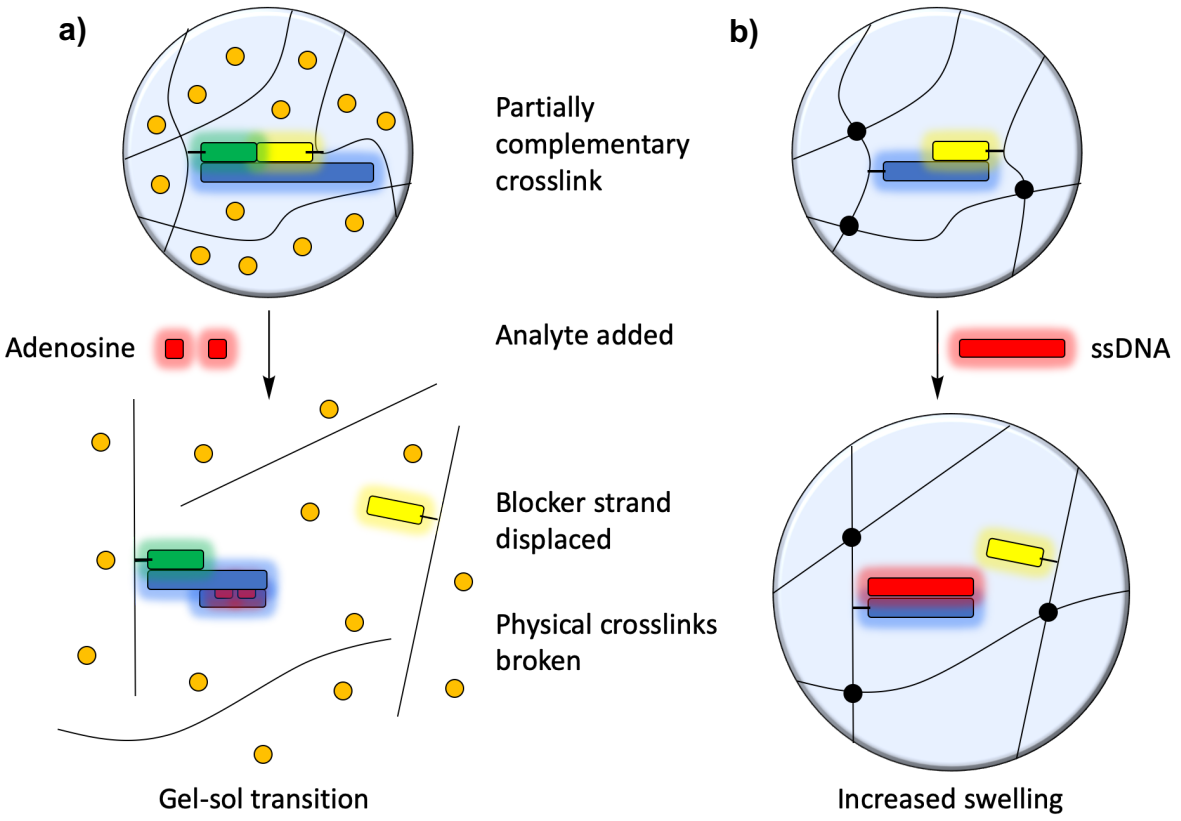

Figure 1.18 Illustrations of oligonucleotide crosslinked hydrogels. (a) Response of the aptamer based oligonucleotide crosslinked hydrogel developed by Yang *et al.*[258] Upon introduction of adenosine, the aptamer sensing strand refolds and displaces one of the blocking strands. Crosslink breakage resulted in a gel-sol transition and gold nanoparticle release. (b) Swelling response of the oligonucleotide crosslinked hydrogel developed by Stokke *et al.*[259] Binding of the analyte sequence to the sensing strand displaces the blocking strand, resulting in a reduced crosslink density and increased swelling capability.

Stokke *et al.* also developed a design for oligonucleotide crosslinked PAM gels (Figure 1.18b).[259] They incorporated MBA chemical crosslinks alongside the oligonucleotide crosslinks and generated a measurable selective response to ssDNA sequences using the increased swelling capabilities resulting from oligonucleotide crosslink displacement whilst avoiding dissolution. This required a far lower concentration of DNA to enable responsivity and their investigations into the effects of crosslink length and hydrogel charge density greatly informed this work.[176,260,261] Furthermore, their characterisation of gel swelling responses to analyte concentration or mismatches was far more thorough than gel-sol transition techniques and the reduced material costs compared to gel-sol methods was beneficial.

1.5.3 Hydrogel Swelling Transduction Methods

Transduction of the swelling of hydrogels can be achieved through a variety of methods, each with benefits and drawbacks. The most basic transduction can be achieved by measurement of the hydrogel mass, whereby a greater swollen volume results in a greater mass. The simplicity of this method is attractive as even the most basic scales can be used; however, small volumes require more specialised equipment for measuring much smaller changes in mass. Acoustic wave devices have been discussed previously and can be used to measure small mass changes in hydrogels,[262] yet the complications arising from sensitivity to liquid viscosity make these unattractive for miRNA biosensing using hydrogels.[146]

Optical transduction of swelling is another commonly used technique to monitor hydrogel swelling. At a most basic level, imaging can be used to calculate the area or volume of a gel. Much like mass transduction, this has limited use at smaller scales. More sensitive approaches have been developed using interferometry. Serpe *et al.* use etalons to monitor microgel layer swelling.[263,264] Etalons may be miniaturised and could be developed to have multiplex capabilities, yet the lack of specific DNA recognition by microgels would add complexity to detection of multiple miRNA sequences.[152] Stokke *et al.* deposited hydrogel droplets on the end of an optical fibre and achieved great sensitivity (Figure 1.19),[265] while Kim *et al.* developed a bioresponsive hydrogel microlens.[266,267] Similar techniques include Bragg diffraction based sensors[268] and refractive index sensors such as SPR.[269] The advantages of optical transduction include high sensitivity and relatively common equipment, yet the optical sources and detectors are relatively bulky and expensive for a PoC technology.[172]

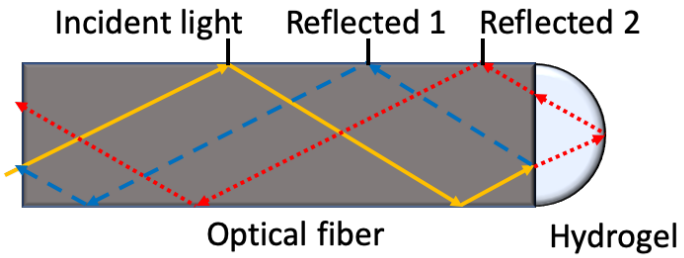

Figure 1.19 The interferometric technique used by Stokke *et al.* to monitor hydrogel swelling. The incident light was sent through the optical fiber and reflected at the fiber-gel interface (Reflected 1) and the gel-solution interface (Reflected 2). The interference wave provides a measurable signal of the hydrogel volume. Adapted from Stokke *et al.*[265]

Alternatively, optical transduction can be achieved using a particle release, whereby hydrogel swelling would result in increased rate and extend of particle release. Yang *et al.* utilised this release mechanism in their adenosine or thrombin detection relying upon a gel-sol transition,[256] while numerous investigations into particle release rely on gel swelling only and the have identified the effect of crosslink density.[236,270] However, particle diffusion may be slower than hydrogel swelling, such that Yang *et al.* relied upon manual agitation to increase release.

MEMS and NEMS discussed previously can be applied to hydrogels. Hydrogels can be polymerised into piezoresistive pressure sensor chambers[271] or attached to microcantilever structures.[272] The small size and cost of MEMS and NEMS remain attractive, however, the difficulties around sensitivity to solution viscosity remain problematic for hydrogel swelling transduction.

Electrical transduction of swelling may be achieved through use of conductive polymer composites. Composite materials combine two or more materials with different properties to achieve materials with a combination of the individual properties of each material.[273] Conductive polymer composites typically combine a conductive material such as a metal powder, conductive polymer or carbon-based material with a non-conductive polymer to achieve a conductive material.[274] They have been applied to sensing through development of electronic noses or tongues.[275,276] In the case of conductive hydrogel composites, the electrical properties change as the hydrogel properties change enabling electrical monitoring of swelling.[274] Sensor designs could

readily be multiplexed with basic electrode designs and electrical transduction could be transduced with common technologies like smart-phones.[277,278]

1.5.4 Oligonucleotide Crosslinked Polymer Composites

The conductivity of a composite material is dependent on the arrangement of conductive sections within the polymer matrix. As such the size, concentration and morphology of conductive particles will define whether conductive pathways can be formed. If sufficient conductive pathways are achieved, the material is in a percolating state, wherein the whole material has become conductive. Percolation theory can best be summarised in Figure 1.20, showing the conductivity regions as the conductive filler concentration is increased.[274,279] Although the exact shape of the three conductance regions will be dependent on the filler and matrix used, the general shape will always exhibit a region of low conductance or insulation dominance, where there is not enough conductive filler to create an electron transfer pathway, a middle region, in which the increased concentration of conductive filler begins to form increasing amounts of conductive pathways and rapidly increases conductance, and a conductive or percolating region where the increasing conductance plateaus having passed the percolation threshold. A similar trend can also be seen for mechanical properties where the strength of a filler may impart increased mechanical strength to the composite.

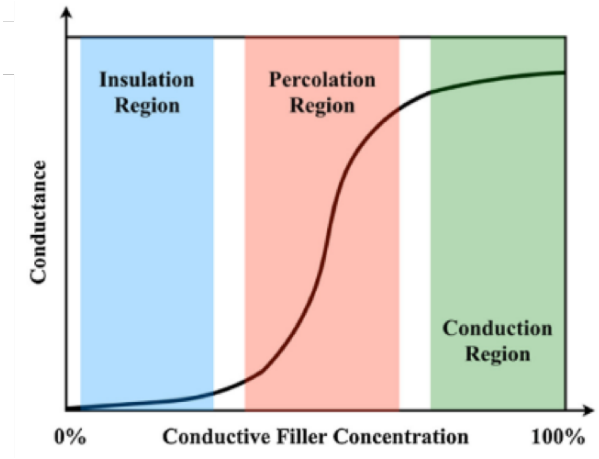

Figure 1.20 Theoretical graph showing change in conductance as conductive filler concentration increases. Figure taken from Zhao *et al.*[274]

The conductive filler morphology will define the method of conductivity achieved and effects like quantum tunnelling can facilitate conduction even when filler particles are not in direct contact. For nanomaterials, the total resistance is a combination of constriction resistance and tunnelling resistance.[280] Constriction resistance involves the intrinsic resistance of the material and the contact spots and pressure between conductive particles. When in contact, particles may undergo reversible plastic deformation or permanent plastic deformation depending on the material and pressure. Tunnelling resistance is the resistance arising from any coating on the conductive material which can be a surfactant, oxide layer, or polymer matrix. The total resistance is therefore a combination of the resistance through a particle and the resistance of particle-particle contact, as well as the contact to the electrodes and geometry of conductive filler packing.

When using conductive composite hydrogels there is a risk of deformation during cooling or drying. When a conductive filler has a lower thermal expansion coefficient than the polymer matrix cooling can exert tensile stress on the polymer, although if above the polymer glass transition temperature (T_g) the relaxation of the polymer can relieve this stress.[281] During drying, capillary action between conductive particles will also cause internal stress and may cause hydrogel deformation.

Percolation theory may be adapted to predict the conductivity of composite systems. One example of this is the general effective medium (GEM) theory which describes the conductivity of a two-component composite (Equation 1.2), where σ_d, σ_h and σ_m are the conductivities of the low conductivity component, high conductivity component and the resulting effective conductivity of the composite.[282] The volume fraction of low conductivity component, f, may be expressed as the volume fraction of the high conductivity component ($\emptyset = 1 - f$) while f_c is the critical volume fraction and t is dependent on the morphology and arrangement of the conductive filler.

Equation 1.2 The general effective medium (GEM) equation and associated definitions.[282]

$$\frac{f(\sum_d - \sum_m)}{\sum_d + [f_c/(1 - f_c)]\sum_m} + \frac{(1-f)(\sum_h - \sum_m)}{\sum_h + [f_c/(1 - f_c)]\sum_m} = 0$$

Where:

$$\sum_d = \sigma_d^{\frac{1}{t}}$$

$$\sum_h = \sigma_h^{\frac{1}{t}}$$

$$\sum_m = \sigma_m^{\frac{1}{t}}$$

Ferrier *et al.* developed an oligonucleotide crosslinked polymer composite consisting of carbon nanopowder in a PAM gel with both MBA and DNA crosslinks on an interdigitated electrode.[81,227] Detection of the miR92a sequence was achieved through optical transduction and using a d.c. two-wire resistance measurement, however, limitations in both sensitivity and reliability indicated extensive optimisation and improved understanding was required for development into a usable technology.

1.6 Commercialisation

This work was conducted within the specifications defined within the associated patent.[226] Furthermore, it was conducted in collaboration with Axis-Shield Diagnostics Ltd. (subsequently Alere Inc. then Abbott Laboratories through purchase and/or merger). As such, aims included taking steps towards commercialisation requirements. One element of this was the potential for automatised dispensing and synthesis, in particular inkjet printing.

1.6.1 Inkjet Printing

Inkjet printing is a computerised dispensing method most commonly used for non-contact deposition of ink onto a material. Inkjet printing can be either continuous or drop-on-demand (DOD).[283,284] Continuous inkjet printing creates a continuous stream of droplets that can be deposited at high velocity from relatively long distances. DOD printing is more commonly used in domestic inkjet printers. Thermal and piezoelectric dispensing are the two most frequently used DOD methods in research (Figure 1.21). Thermal printers use resistors which can be heated to create a vapour bubble. This bubble expands to push out a droplet. As the resistor cools the bubble collapses and draws fresh ink to refill the nozzle. Piezoelectric DOD printing uses capillaries with an electrically deformable material. Upon introduction of a voltage, the deformable material contracts the capillary to expel a droplet. Ink is replenished in the nozzle as the deformable material relaxes.

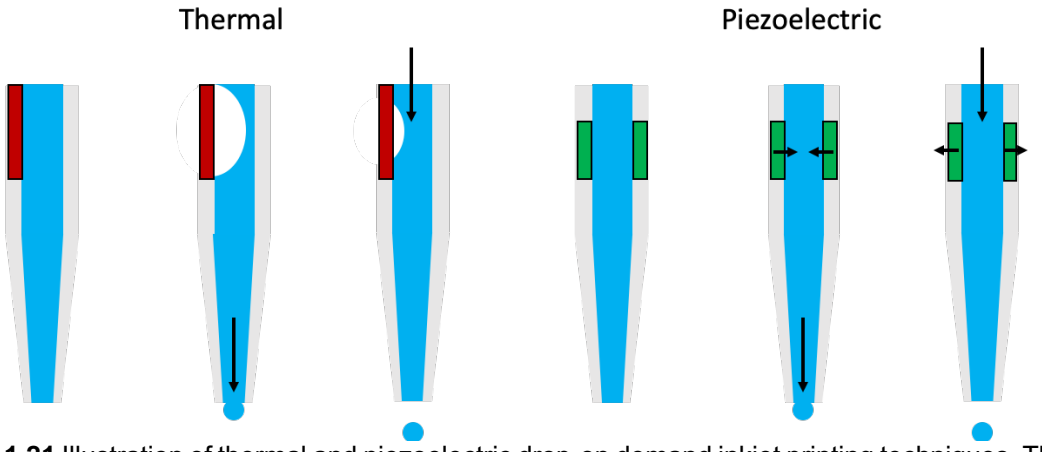

Figure 1.21 Illustration of thermal and piezoelectric drop-on demand inkjet printing techniques. Thermal inkjet printing uses a heated resistor to create vapour bubble to eject a droplet. Piezoelectric printing uses a voltage to deform and contract the material and expel a droplet.

Printable substrates need to be stable for long periods without aggregation or sedimentation which may cause nozzle blockages. Continuous printing can use volatile solvents which dry quickly, whereas DOD techniques tend to rely on water-based inks or materials. In piezoelectric printers, the viscosity and surface tension of the ink define printability.[285,286] Print nozzles with various coatings may improve droplet

formation,[287] although highly viscous materials have limited printability outside of valve-jet printers.[288]

Inkjet printing offers a method for precise deposition of material, both in terms of location and volume. The non-contact nature of printing and high velocity of droplets enables mixing of components and facilitates printing or printing onto soft materials such as hydrogels. Further advantages include the ease of use, small scale and high throughput capabilities which could readily be translated onto the commercial scale. Bradley *et al.* utilised inkjet printing to test polymer microarrays, mixing various combinations of monomers to rapidly assess polymer capabilities.[289–292]

1.7 Summary

This introduction outlined the expression and activity of miRNA as well as its important role in disease. The potential of miRNA as circulating non-invasive biomarkers was discussed with regards to a huge variety of diseases. Existing miRNA detection techniques were presented, including both the strengths and limitations which have prevented miRNA from being utilised in diagnostic applications.

Oligonucleotide based sensor designs and crosslinks were presented in applications for sequence specific identification of miRNA sequences. The limitations of ssDNA crosslinks were presented, in particular with regards to temperature stability and required buffer conditions. Advantages of DNA analogues were discussed, with MOs presented as the most attractive option due to their insensitivity to salt concentration and the novelty of MO crosslinks in hydrogels.

The benefits of hydrogels in biosensing applications, namely their resistance to bio-fouling, aqueous nature and the 3D network combining both solid- and solution-phase benefits were discussed and responsive smart hydrogels presented using grafted DNA crosslinks. DNA crosslink displacement as a bioreceptor element was shown to control gelation or swelling capabilities of DNA functionalised hydrogels. Techniques for transduction of hydrogel swelling showed limitations with regards to appropriate volume size or portability and electrical transduction was presented as the ideal

method for multiplexed analysis of small volumes of hydrogels. Incorporation of conductive carbon nanopowder into hydrogels was shown as a viable way to electrically transduce hydrogel swelling by Ferrier *et al.* albeit with a number of reliability and sensitivity improvement requirements. Inkjet printing was presented as a method to improve system reliability through precise deposition, with added benefits of scalability.

1.8 Aims

This thesis described the development of oligonucleotide crosslinked hydrogels and composites for miRNA sequence detection through optimisation of the DNA crosslinked polymer composites developed by Dr Ferrier. Identification of the optimal materials, composition and synthetic protocol aimed to obtain reproducible, sensitive and specific miRNA detection comparable to established techniques. Furthermore, the use of MO crosslinks aimed to achieve a world's first MO crosslinked hydrogel and explore the potential of these DNA analogues in diagnostic or material applications to expand the knowledge base of these analogues.

Transduction through electrical measurements rather than optical monitoring was desired, with a view to achieve multiplex capabilities. Development of a synthetic protocol using inkjet printing aimed to achieve a facile production method as proof for potential commercialisation and to further the knowledge of printable oligonucleotide composite materials.

Chapter 2 Materials and Methods

2.1 Materials

All materials were purchased from Sigma Aldrich and used as received aside from *N*-isopropylacrylamide (NIPAm) which was recrystallised in hexane (Table 2.1) and the Morpholino Oligonucleotides and ssDNA oligonucleotide sequences (Table 2.2) which were purchased from GeneTools and Integrated DNA Technologies, respectively. Deionised (DI) water was obtained by an ELGA DI water system with a Filtromat activated carbon filter, ELGA Purelab Prima 120 reverse osmosis unit, C260 and C270 deionising cylinders, 0.2 μm membrane filter, UV disinfection and monitored using conductivity meters.

Table 2.1 Purity of hydrogel polymerisation materials as specified by Sigma Aldrich.

Acrylamide (AAm)	≥99%
N-isopropylacrylamide (NIPAm)	97%
N,N' -methylene-bisacrylamide (MBA)	99%
1-hydroxyphenylketone (HPK)	99%
Phosphate buffer (PBS), aqueous, pH 7.4	1.0 M
Ethylene glycol	≥99%

2.2 Hydrogel Preparation

2.2.1 Oligonucleotide Crosslink Sequences

The APT1 crosslink design was replicated from work by Yang *et al.*[256] and APT2 was adapted from APT1. The ASS analyte sequence was provided by Dr Finn Grey and later published.[293] The MIR analyte sequence is taken from miRNA 92a-1[2] and the MIR1 crosslink was designed by Dr Ferrier based on previous work by Stokke *et al*.[227,259] Random sequences were randomly generated. Mismatch sequences A_{MM1}

and A_{MM5} were designed for MIR and MOR crosslinks with 1 and 5 mismatches with regard to the MIR crosslink sensor strand. Polymerisable DNA sequences were ordered from IDT with 5' Acrydite™ functionalisation. MO sequences were ordered from GeneTools with either 3' primary amine (MOR1) or 5' acrylate functionalisation (MOR2).

Table 2.2 Nucleotides matching the sensor strand are coloured red. Sensor strand nucleotides matching blocking strands are underlined (italicised if two blocking strands are used). Polymerisable groups are denoted by "*". Crosslink length was estimated using Equation 3.1. DNA-DNA crosslinks T_m predictions were calculated at 150 mM NaCl, aside from APT1/2 (300 mM NaCl), using "Nearest Neighbor" calculations.[168] MO-RNA interactions calculated and supplied by GeneTools. MO-MO interaction calculated using Equation 3.2.[204,294]

Adenosine Aptamer	Sequence (5'-3')	Sequence Length (nt)	Crosslink Length (nm)	Charge Density (mol%)	T_m (°C)
Analyte	Adenosine (x2)			+0.0	
APT1					
Sensor	*ACT CAT CTG TGA* AGA GAA CCT GGG GGA GTA TTG CGG AGG AAG GT	44			
Blocker	*CCC AGG TTC TCT	12	7		44
Tether	*TCA CAG ATG AGT	12	7	27.2	38
APT2					
Sensor	*AGA GAA CCT GGG GGA GTA TTG CGG AGG AAG GT	32			
Blocker	*CCCAGGTTCTCT	12	7	17.6	44
African Sleeping Sickness					
Analyte	GGG GGC CGG GTC CGC TTA GCG GGG ACT TCT TGG AC	35		+14.0	
Random	GAT TGC AAT TCT CTC AAA GTA TTA TGC AGG CCG GC	35		+14.0	
ASS1					
Sensor	*GTC CAA GAA GTC CCC GCT AAG CGG ACC CGG CCC CC	35			
Blocker 1	*TAT CAC CCC TGG GGG CCG GGT C	22	14	22.8	52
ASS2					
Sensor	*GTC CAA GAA GTC CCC GCT AAG CGG ACC CGG CCC CC	35			
Blocker 2	*GAC TTC TTG GAC	12	7	18.8	35
ASS3					
Sensor	*GTC CAA GAA GTC CCC GCT AAG CG*G ACC CGG CCC CC*	35			
Blocker 2	*GAC TTC TTG GAC	12	7		35
Blocker 3	*GGG GGC CGG GTC	12	11	23.6	52

Leukaemia miR92a					
Analyte	TAT TGA ACT TGT CCC GGC CTG T	22		+8.8	66
Random	ACG TCT AGA CGT AAC GAA GGT C	22		+8.8	18
A_{MM1}	TAT TGC CCT TGT CCC GGC CTG T	22		+8.8	65
A_{MM5}	TAG TGC ACT TGT GCG GCC CTG G	22		+8.8	57
MIR1					
Sensor	*ACA GGC CGG GAC AAG TGC AAT A	22			
Blocker	*TAG TGC GTT TTA TTG CAC TTG T	22	14	17.6	32
MIR2					
Sensor	*ACA GGC CGG GAC AAG TGC AAT A	22			
Blocker	*TAT TGC ACT TGT	12	11	13.4	33
Leukaemia miR92a (MO)					
Analyte	TAT TGA ACT TGT CCC GGC CTG T	22		+8.8	86
Random	ACG TCT AGA CGT AAC GAA GGT C	22		+8.8	
A_{MM1}	TAT TGC CCT TGT CCC GGC CTG T	22		+8.8	
A_{MM5}	TAG TGC ACT TGT GCG GCC CTG G	22		+8.8	
MOR1					
Sensor	ACA GGC CGG GAC AAG TGC AAT A*	22			
Blocker	TAG TGC GTT TTA TTG CAC TTG T*	22	6	0.0	66/38
MOR2					
Sensor	*ACA GGC CGG GAC AAG TGC AAT A	22			
Blocker	*TAT TGC ACT TGT	12	13	0.0	66/38

2.2.2 ssDNA Preparation

Lyophilised DNA from IDT was dissolved in 1 mM PBS at room temperature overnight. Analyte, mismatch and random sequences were aliquoted and stored at -20 °C. Prior to use, aliquots were defrosted, diluted to the appropriate concentration and degassed by sonication for 30 mins. Appropriate volumes of equimolar sensor and blocker strands were combined with 300 mM NaCl (3 M stock solution) and heated to 95 °C for 2 mins. The crosslink solution was then cooled slowly to room temperature before pelletisation using IPA precipitation. An equal volume of IPA (-20 °C) was added, the solution incubated at -20 °C for 30 mins then centrifuged at 13300 rpm for 30 mins. The supernatant was decanted and DNA pellets were washed with 1 volume of 70 % v/v ethanol (-20 °C) 3 times. Pellets were then dried overnight at room temperature and stored at -20 °C. Before use, pellets were defrosted at room temperature prior to dissolution.

2.2.3 Morpholino Oligonucleotide Functionalisation

The MO sensor and blocker strand used in crosslink MOR1 were obtained from GeneTools with a 3' primary amine modification attached *via* an ethyl linker. To replicate the Acryidte™ functionalistion on DNA strands an acrylamide functionalisation was developed by Dr Jaclyn Raeburn (Figure 2.1). Sensor and blocker strands were, separately, dissolved in DI water to 1 mM (750 nmol in 750 µL). 2 molar equivalents (75 µL) of 20 mM N-succinimidyl acrylate (NSA, Sigma-Aldrich, ≥97% purity) in DI water were added and stirred at room temperature for 24 hrs and reaction progress was monitored using MALDI-ToF-MS (Appendix A). Solutions were lyophilised and then washed with excess ethyl acetate (2 mL, 50 °C) to remove succinimide. Conversion and purification were assumed to be 100% efficient without any lost material as the limited material prevented further characterisation. Sensor and blocker strands were then prepared as detailed below (Section 2.2.5).

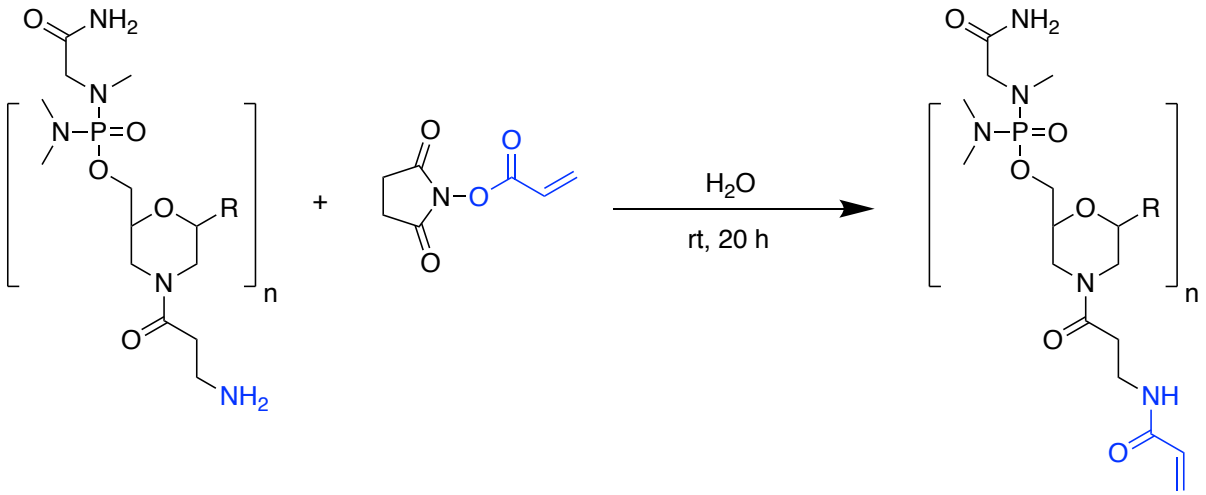

Figure 2.1 Reaction scheme of a MO strand with N-succinimidyl acrylate (NSA) to form acrylamide-functionalised MOs.

2.2.4 MALDI-ToF-MS of Oligonucleotides

Modified MOR1 sensor and blocker strands were assessed using MALDI-ToF-MS using an Ultraflex II ToF/ToF mass spectrometer (Bruker Daltonics) operated in negative mode with a Smartbeam II laser. The raw data was processed using FlexAnalysis software (Bruker Daltonics). Aliquots of reaction mixture were removed and mixed in 1:1 ratio with the MALDI matrix and salt (1:1 mix of 2,4,6-trihydroxyacetphenone monohydrate (THAP) in acetonitrile (62.5 mM) and ammonium citrate dibasic (DAHC) in water (75 mM)). The plate was prespotted with 0.5 µL of THAP (250 mM) and 1 µL of sample mixtures were spotted in triplicate. Spectra are provided in Appendix A.

2.2.5 Morpholino Oligonucleotide Preparation

Equimolar sensor and blocker MOs were dissolved in DI water (at a concentration of 1 mM) and aliquoted in appropriate quantities. Mixtures were then heated to 95 °C for 2 min, cooled to room temperature and subsequently lyophilised as smaller aliquots for use in gel preparation. Once lyophilised, aliquots were stored in sealed containers at room temperature.

2.2.6 Hydrogel Sample Preparation

Pre-gel solutions were prepared from stock monomer solutions of acrylamide (AAm, 40 wt%), *N,N'*-methylene bisacrylamide (MBA, 0.13 M) and NaCl (3 M) in 1 mM, pH 7.4 phosphate buffer solution (PBS). Typical gels included 1-hydroxycyclohexyl phenyl ketone (HPK, 0.1 M) in ethylene glycol as a radical photoinitiator. Mixing appropriate amounts of these stocks gave final concentrations of 10-20 wt% AAm with 0.6-1.5 mol % MBA and 0.13 mol % HPK with regard to AAm and 0-300 mM NaCl. Typical pre-gel

stocks contained carbon nanopowder (<50 nm particle size, 1 wt% for optical transduction, 2 wt% for electrical transduction). The combined stock solution was then pipetted into a 1.5 mL Eppendorf centrifuge tube containing the appropriate oligonucleotide crosslinks to a final concentration of 0.4-0.6 mol % (5.6 mM in the gel assuming 100% conversion) and stored at 4 °C overnight. Mixing was carried out at 500 rpm by vortex mixer, followed by manual agitation.

2.2.7 UV Photoinitiation

Typical hydrogel samples were prepared in 1 or 2 µL quantities by pipetting the manually agitated pre-gel (and oligonucleotide) stock onto a 7.7 x 22.8 mm silicon oxide chip with a silanised layer for polymer attachment to the chip surface described below (Section 2.4.3). Once deposited, the pre-gelator droplet on each chip was irradiated with a Dymax Bluewave 75 UV curing light source (280–450 nm, 19+ W/cm^2) for 60 s to initiate polymerisation and gelation. Gels for optical transduction were washed in 1 mM phosphate buffer solution (pH 7.4) with the same NaCl concentration as the pre-gelator solution (0-300 mM) at 4 °C for 1 hour, the wafer was then patted dry and stored at 4 °C for 16-24 hrs until constant mass and moved into the test environment (20 ±1 °C, 40 % humidity) before swelling. Gels for electrical transduction were stored at 4 °C without washing for 16-24 hrs until constant mass before swelling.

Photoinitiation using alternative initiators was conducted as above, using equimolar HPK in acetonitrile (ACN). Equimolar bis(2,4,6-trimethylbenzoyl)-phenyl phosphine oxide (BAPO, 97%) in ACN was tested in place of HPK, as well as a mixture with HPK (equimolar total with half BAPO and half HPK).

2.2.8 Thermal or Redox Initiation

Thermal initiation was investigated using 2,2'-azobis(4-methoxy-2,4-dimethylvaleronitrile) (V-70, ≥98%) as initiator in place of HPK. V-70 was dissolved in

ACN (0.1-0.25 M) and added in place of HPK. As V-70 is a biradical initiator it was tested both equimolar to HPK (double the number of radicals) and after a 2-fold dilution (equimolar radicals). Initiation was carried out by incubation at 37 °C for 10 mins, after which the droplet was dry. Gels were then cooled to room temperature and stored at 4 °C overnight.

Redox initiation was carried out by mixing ammonium persulfate (APS, ≥98%, 10 wt%) and tetramethylethylenediamine (TEMED, 99%) into pre-gel solutions at various concentrations (0.13-1.3 mol% wrt AAm). Initiation was triggered either by mixing two pre-gel aliquots containing either APS or TEMED, or by adding APS to a pre-gel solution containing TEMED. APS was dried onto electrode chips and pre-gel solution containing TEMED was pipetted on top.

2.2.9 Conductive Particle Dispersion

The conductive particles in pre-gel solution preparation, either CNP or carbon nanotubes (CNT, multiwalled, O.D. x I.D. x L: 10 nm x 4.5 nm x 3-6 μm), were weighed (1-3 wt%) into a microcentrifuge tube (1.5 mL) and the appropriate volume of pre-gel solution added. Initial mixing was manual and followed by vortex mixing (1000 rpm) before pipetting into any oligonucleotide stock. After oligonucleotide dissolution, mixing was carried out at 500 rpm using a vortex mixer, followed by manual agitation prior to pipetting.

Surfactant investigations compared morpholinopropane-1-sulfonic acid (MOPS, ≥99.5%) buffer with PBS, and tested sodium dodecylbenzenesulfonate (NaDDBS) as a surfactant on CNP or CNT. 0.1-2.0 wt% CNP were mixed manually followed by vortex mixing (3000 rpm, 5 mins) in 1 mL of 1 mM PBS or 20 mM MOPS buffer. When surfactants were mixed by weight, surfactant and 2 wt% CNT or CNT were weighed into a glass vial and vortexed with DI water for 1 min before 3 hours sonication using a sonication bath.

2.3 Optical Transduction

2.3.1 Imaging and Analysis

Swelling properties of the hydrogels were characterised by taking images of the gels using a Sony XCD-X710 Firewire Camera with a MEDALight LP-300 lightbox as backlight using IC Capture image acquisition software (Figure 2.2). For swelling kinetics studies gels were imaged in solution (5 mL) every 10 s and gels required CNP incorporation for adequate contrast between gel and solution. For end volume only measurements gels were swollen in solution (5 mL) and dried carefully to remove excess liquid on the outside of the gels before imaging. Samples were measured in triplicate and moved into the test environment (20 ±1 °C, 40 % humidity) before swelling.

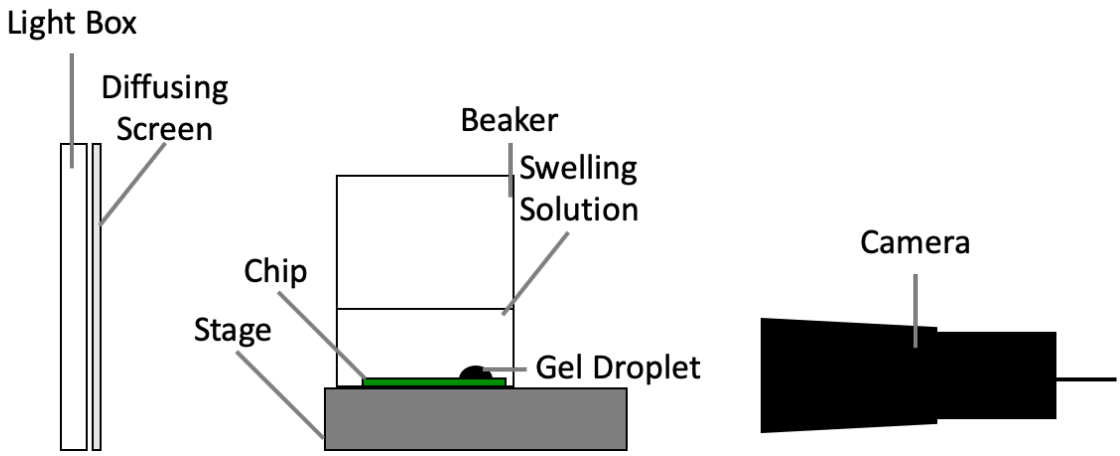

Figure 2.2 Illustration of polymer gel imaging set-up. Gels on electrode chips were positioned in front of a back-light and imaged using a Sony XCD-X710 Firewire camera. Not to scale.

Images were processed and analysed using custom MatLab code written by Dr Ferrier which calculated the gel volume using the contrast between the background and the gel and calibrated using the width of the chip. The distance between the wafer edges were used for scale and the square area to be investigated defined. The contrast

between gel and background is then used to define the gel edges. The area of a circle is then calculated at each pixel height using the distance between gel edges as the diameter and the sum of these circle areas defined in pixels. Subsequently, the volume of pixels is converted to μL using the scale defined by the wafer edges. The full MatLab code is provided in Appendix B.

2.3.2 Salt Study

Sample solutions and gels were prepared as described above (Section 2.2.6) without NaCl and washed in 1 mM phosphate buffer without NaCl. Samples were then placed in a 5 mL solution containing the 'analyte' or 'random' DNA sequence (1 μM) with varying NaCl concentrations (0-300 mM) at 20 ±1 °C. Swelling was monitored in triplicate optically (Section 2.3.1).

2.3.3 Thermal Study

Gels (1 μL) were prepared without NaCl as above (Section 2.2.6). 3 samples were placed in a 5 mL solution of 1 mM phosphate buffer pre-heated to temperatures varying from 20-65 °C ±2 °C and kept at the set temperature for 1 hour. Gels were then removed from solution, patted dry and imaged.

2.3.4 Mobile Measurements

Gels (1 μL) were prepared without NaCl as above (Section 2.2.6). Samples were placed in 5 mL solution of 1 mM phosphate buffer with either A1 or R1 ssDNA (10 pM) in triplicate for 30 minutes. Gels were then removed from solution, the wafer dried, and the gel imaged using a OnePlus 5T camera (20 MP) with a SODIAL(R) 30X Zoom

LED Magnifier Clip-On Cell Phone Mobile Phone Microscope Micro Lens attachment. Images were analysed using Digimizer (MedCalc Software bvba) software to measure gel areas.

2.4 Electrode

2.4.1 Design

The electrodes used in this thesis were designed by Dr Ferrier based on commercial designs. They consisted of an interdigitated electrode (IDE) array on a silicon (Si) substrate with a silicon dioxide (SiO_2) surface layer (Figure 2.3). The array had 30 digits in total, 10 µm wide with 40 µm spacing spanning an area of 1.5 x 1.46 mm which would be covered by a 2 µL gel droplet. The IDE array was connected to two contact pads. The electrode arrays were platinum (Pt) on titanium (Ti).

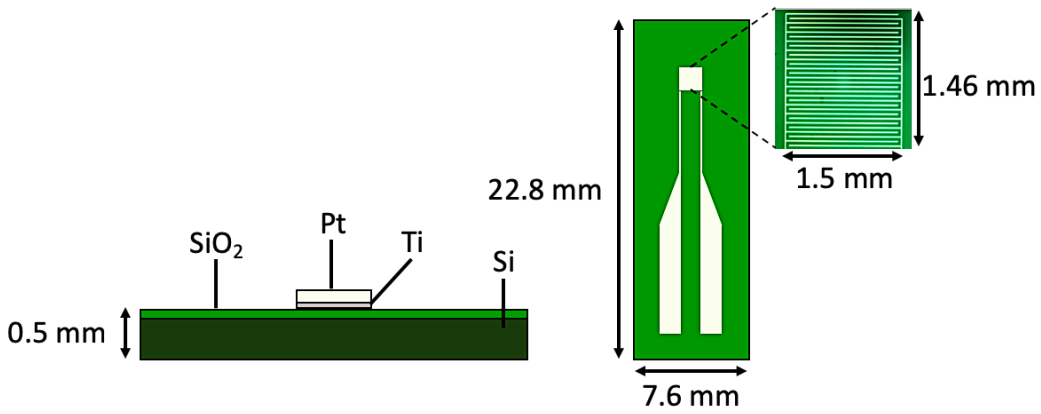

Figure 2.3 Illustration of electrode chip layers and design. Interdigitated digits are 10 µm and 40 µm apart.

2.4.2 Fabrication

Electrodes were fabricated in the Scottish Microelectronics Centre (SMC) clean-room facility with controlled temperature (20 ± 1 °C) and humidity (40%). Si wafers (4”) were oxidised in a wet-oxidation furnace at 1100 °C for 40 mins to generate a 500 nm thick SiO_2 surface layer, followed by 30 mins in a plasma asher to remove any moisture on the surface.

Wafers were subsequently treated with hexamethyldisilazane (HMDS) *via* 10 minutes in a sealed container with HMDS vapour to increase photoresist adhesion. Photoresist (AZ nLOF 2070-3.5) was spin-coated on the surface at 700 rpm for 5 s then 3000 rpm for 45 s (1000 rpm/s acceleration) to a depth of approximately 3.5 µm, then soft-baked on a hotplate at 110 °C for 1 min.

After the photoresist application, wafers were exposed to UV irradiation (350 – 450 nm, 4 mW/cm^2) for 30 s with hard-contact through a photolithography mask designed by Dr Ferrier (chrome on glass). Wafers were then baked on a hotplate at 115 °C for 1 min. Photoresist development was carried out by immersing wafers in developer solution (AZ726) for 2 mins, then rinsed with DI water and dried with N_2. Metal deposition was carried out by Stewart Ramsay. Electron-beam evaporation was used to deposit a 10 nm thick layer of Ti for adhesion, followed by 50 nm of Pt.

Removal of the negative photoresist layer was achieved by soaking wafers in stripper solution (1165) at 50 °C for 1 hr and subsequently sonicated to remove any remaining undesired metal. Wafers were then rinsed in IPA, then DI water and dried with N_2.

After optical electrode assessment, a photoresist (SPR350) layer was spin coated (500 rpm, 5 s, then 3000 rpm, 30 s) and soft-baked (90 °C, 1 min). Wafers were then diced into individual IDE devices. The photoresist layer was then removed with a rinse of acetone, IPA, then DI water, before being dried with N_2. Defective electrodes were discarded and each electrode was inspected again before use to ensure the appropriate electrode structure.

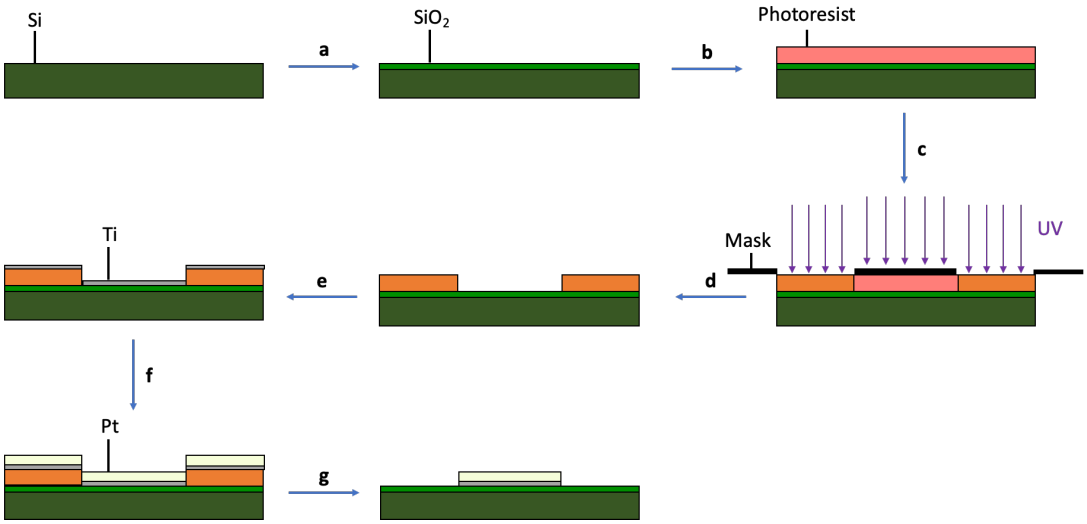

Figure 2.4 Electrode fabrication. (a) Insulating layer of SiO_2 is grown on Si wafer surface. (b) A layer of photoresist is developed. (c) UV irradiation through a photolithography mask to pattern areas of photoresist. (d) Photoresist is developed. (e) Ti layer is evaporated onto the wafer. (f) Pt layer is evaporated onto the wafer. (g) Lift-off removes remaining photoresist leaving only the desired pattern of Ti and Pt.

2.4.3 Wafer Surface Functionalisation

Silicon oxide chips were cleaned using 10 wt% NaOH for 4 hrs then rinsed with DI water. Chips were soaked in 0.01 M HCl for 10 mins, before pipetting 2 µL of 3-(trimethoxysilyl)propyl methacrylate (TMSPM) onto the gelation area (the IDE array). Chips were then rinsed after 16 hours with acetone, then DI water and dried with N_2 before use.

2.5 Electrical Transduction

2.5.1 Set-up and Analysis

Electrical measurements presented herein were all d.c. resistance measurements. The equipment set up is shown in Figure 2.5a. Electrode chips were connected to a Keithley 2000 digital multimeter connected to a computer *via* USB cable and controlled by custom a LabVIEW script developed by Dr Ferrier. Measurements were either taken every 2 s, averaging 5 readings taken 100 ms apart, or every 10 s averaging 10 readings 100 ms apart. The multimeter was set to auto-range, adapting the current to the resistance measured (100 μA if <100 kΩ, 10 μA if >100 kΩ).[295] The length of testing varied up to 1 hr with a baseline measurement taken of dried gels in air for 60 seconds. Resistance during swelling was conducted by immersing the gel and electrode chip into 1.5 mL of test solution in a water bath (23 ± 1 °C). For horizontal well measurements the same set up was used, with a 3D clip on well used in place of water bath and microcentrifuge tube Figure 2.5b. After baseline measurement, 50 μL of solution was pipetted into the well to begin swelling.

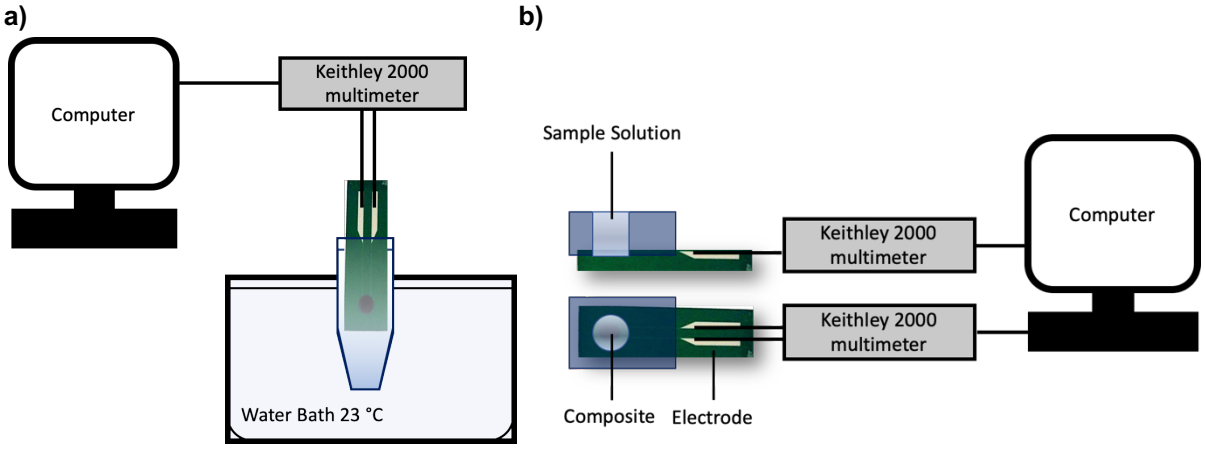

Figure 2.5 Illustration of the electrical measurement set-up. The electrode being tested is connected to the Keithley 2000 multimeter (d.c.) which is connected to a computer *via* USB cable. The computer utilises LabView to control and collect data. (a) The electrode is suspended vertically in a microcentrifuge tube containing the sample solution. (b) The electrode is held horizontally with the clip-on-well attached and the sample solution is pipetted on top of the gel.

2.6 DLS Measurements

Dynamic light scattering (DLS) was used to investigate the particle size and stability in solution. Measurements were carried out on a Malvern Zetasizer Nano ZS using a backscatter angle of 173° after a 3-minute equilibration time. Appropriate amounts of CNP were weighed out and suspended in relevant solutions *via* vortexing and manual agitation. Sedimentation studies were carried out with measurements taken every minute for 30 mins.

2.7 Inkjet Printing

Inkjet printing was conducted on a Scienon S5 SciFLEXARRAYER equipped with piezo dispense capillary (PDC 80) with a 50 µm aperture. HPLC-grade water was degassed for 30 min by sonication before using as printer solvent.

2.7.1 Glass Slide Preparation and Surface Functionalisation

Glass slides (76 mm x 26 mm x 1 mm) were washed with DI water and acetone, then placed in a 40 kHz/100 W Zepto O_2 plasma generator. Vacuum was produced (0.5 mbar) and O_2 flowed at a rate of 50 sccm. Slides were treated for 10 mins with power set between 50-100 W. After venting, slides were again washed with DI water and acetone then dried with N_2.

Sucrose (20 wt%) masks were inkjet printed onto glass slides or electrode chips using drop-on-demand configuration. Once dried, 10 µL (2 µL for electrode chips) of 1H,1H,2H,2H-Perfluorooctyl-trichlorosilane (POTS) was pipetted around each slide and slides were stored in sealed containers for 16 hrs. Slides were washed with DI water and acetone to remove sucrose and POTS, then dried with N_2. TMSPM was

spread over the slides with droplets forming where sucrose had been deposited and stored in sealed containers for 24 hrs. Slides were then washed with DI water and acetone then dried with N_2.

2.7.2 Hydrogel Composite Synthesis

Pre-gel solutions were prepared from stock monomer solutions of AAm (40 wt%), NIPAm (40 wt%), MBA (0.13 M) and piperazine di-acrylamide (PDA, 0.104 M) in HPLC grade water. Solutions were made up by mixing monomer stocks into SIC Black Dispersion 1 (SIC) with constant stirring.

Microarrays were printed in a two-step fabrication process. Firstly, APS (5-20 wt%) was deposited as 10% of the total number of drops (100-2000 drops, 35-700 nL) and dried. Secondly, pre-gel solutions (10/20 wt% AAm, 0.6-2.0 mol% MBA, 2-10 wt% TEMED) were then deposited atop the dried APS. Droplets were allowed to dry before moving and were stored overnight at room temperature before testing.

2.7.3 Imaging and Analysis

Composite microarrays were imaged using a Nikon Ni-U Eclipse fluorescence microscope equipped with Pathfinder^{TM} Wellscan software. Each composite droplet in each microarray was imaged in brightfield mode. These images were then analysed using ImageJ analysis software using built in equations to calculate circularity, aspect ratio and roundness.

2.8 Scanning Electron Microscope (SEM)

Samples were prepared as detailed above (Section 2.2.6) on 3.5 mm^2 Si wafers or electrode chips which were subsequently cut to fit onto the SEM stubs. If swollen, gels were swollen in the appropriate solution for 1 hr and then dried. Before imaging gels, were carbon coated using thermal evaporation. SEM imaging was carried out on a ZEISS Sigma HD microscope operating at 5 kV, which was also equipped with backscattering detectors. Imaging was carried out by Dahlia Eldosoky.

Chapter 3 Oligonucleotide Crosslinked Hydrogels

3.1 DNA Crosslinked Hydrogels

3.1.1 Established Systems and Previous work

The hydrogel synthesis and DNA crosslink design developed by Stokke *et al.* for optical interferometry assessment of DNA crosslinked hydrogels[176,259,265] was used as the basis for Dr David Ferrier's development of DNA crosslinked polymer composites during his PhD studies.[81,227] In this work the miRNA sequence of miR92a (A1) was chosen as a target analyte due to its potential use in acute leukaemia diagnosis when compared to miR638 concentrations.[2] The DNA crosslink (MIR1) was designed similarly to those used by Stokke *et al.* with equal length sensing and blocking strands with an overlap of 12 nt (Figure 3.1). Approximate crosslink lengths were estimated as the total distance between each of the 5' acrydite functionalised groups, assuming that the length of 10 nt is 3.4 nm and that each single bond of acrydite was 0.154 nm (Equation 3.1).[296,297] The actual length will be dependent on the mixture of ssDNA and dsDNA length, ionic strength of solution and the strain the crosslink is under, yet this simplification suffices for comparing crosslinks.[298–300]

$$Crosslink\ Length = (n_{single\ bonds} \times 0.154) + (n_{nucleotides} \div 10 \times 3.4)$$

Equation 3.1 Estimated crosslink length where the length of both acrydite groups is summarised as the number of single bonds and the length of oligonucleotide is summarised as the length of nucleotides if dsDNA.

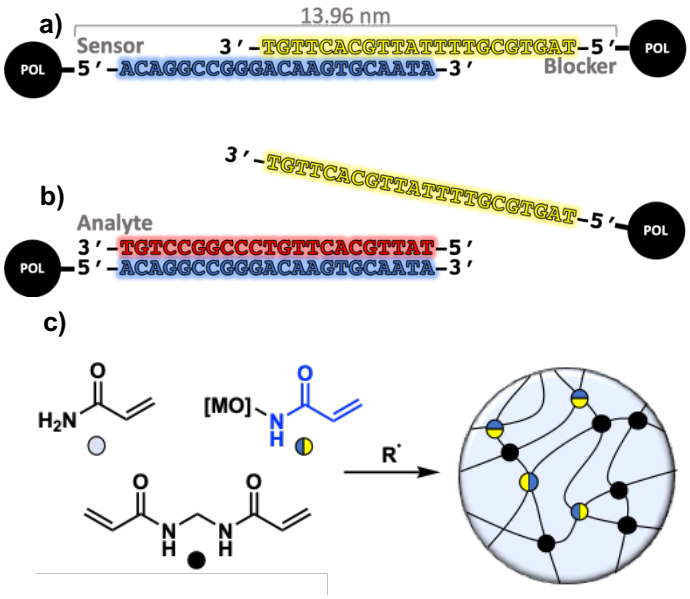

Figure 3.1 (a) The sequences and length of the MIR1 crosslink, tethered in polymer at the 5' ends. (b) Displacement of the MIR1 blocker strand by the analyte strand to break the crosslink. (c) UV-initiated radical polymerization of acrylamide (10 wt%), functionalized MOs (0.4 mol%) and MBA (0.6 mol%) to form a crosslinked polymer hydrogel through radical initiation (0.125 mol%) where mol% is relative to acrylamide.

Hydrogels functionalised with this crosslink performed similarly to those of Stokke *et al.* with a clear difference in swelling rate and end point achieved within 30 minutes when comparing 10 μM solutions of target sequence or the randomly generated sequence (Figure 3.2). This system achieved a limit of detection of 100 nM, below which the response to analyte sequence can no longer be differentiated from the response to the random sequence. Data is shown as the % volume change and unless otherwise stated error bars show the standard error of the mean (Equation 3.2).

a)

$$\Delta\% = \frac{V_m - V_i}{V_i} \times 100$$

b)

$$Standard\ Error\ of\ the\ Mean = \frac{Standard\ Deviation}{\sqrt{n}}$$

Equation 3.2 (a) The % volume change (Δ%), where V_m and V_i represent the measured volume and the initial deposited volume (typically 1 or 2 μL) respectively. (b) Equation used to calculate the standard error of the mean, where n is the number of samples.

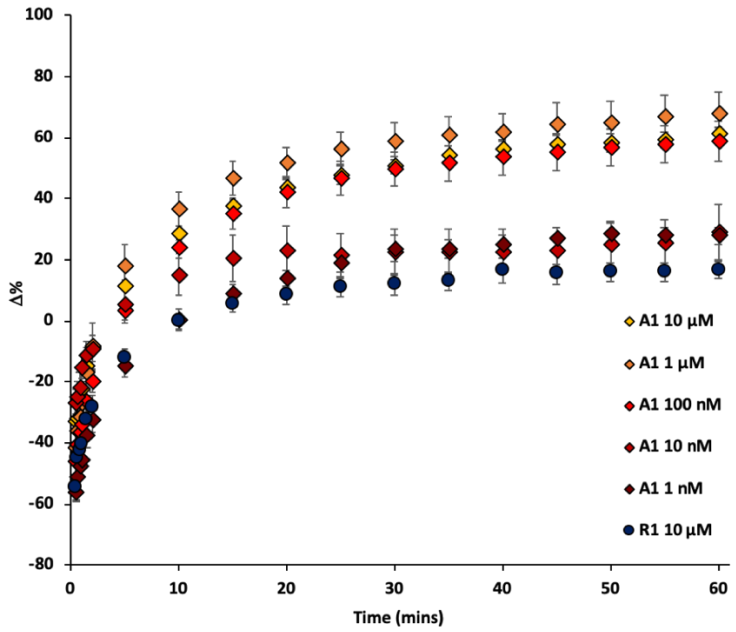

Figure 3.2 Comparison of swelling kinetics showing LoD of MIR1 crosslinked hydrogels with 10 wt% AAm, 0.6 mol% MBA and 0.4 mol% MIR1 DNA crosslinks (wrt AAm) and 1 wt% CNP in A1 or R1 at 10 µM – 10 nM in 150 mM NaCl, 1 mM PBS. Data shown was collected and analysed by Dr Ferrier. Δ% and standard error of the mean calculated using equations 3.2a and b (n = 5).

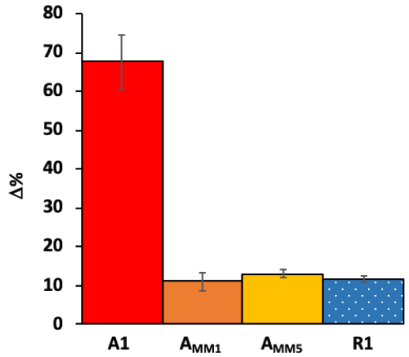

Figure 3.3 Comparison of swollen volume at 60 minutes to test mismatch response of MIR1 crosslinked hydrogels with 10 wt% AAm, 0.6 mol% MBA and 0.4 mol% MIR1 DNA crosslinks (wrt AAm) in A1, A_{MM1}, A_{MM5} or R1 at 1 µM in 150 mM NaCl, 1 mM PBS. Data shown was collected and analysed by Dr Ferrier. Δ% and standard error of the mean calculated using equations 3.2a and b (n = 5).

Similarly, these hydrogels exhibited specificity for the miR92a sequence over even a single base-pair mismatch as shown in Figure 3.3. In this experiment only the end-point swollen volume after 60 minutes was measured and response to both a single mismatch or 5 non-contiguous mismatches was similar to the response to the random sequence, indicating that this material can differentiate single base pair mismatches

which would be highly advantageous for a miRNA detecting biosensor. However, this degree of specificity differs from the results of Stokke *et al.* who reported the response to three probe sequences of equal total length but differing overlap length complementarity to the sensing sequence (10, 14 and 18 matching base pairs) and showed that the longer the match, the greater the rate and extent of swelling.[176] In both cases sequence specificity is shown and the difference in response may be attributed to the differences in transduction method (Further discussed in section 3.4.2).

3.1.2 Adenosine Aptamer Crosslink

Aptamers are oligonucleotide or peptide sequences that bind to a specific target molecule and are frequently compared to antibodies in their binding efficacy. Typically, aptamers are engineered through systematic evolution of ligands by exponential enrichment (SELEX) or variants thereof, with numerous benefits over antibodies in terms of development, synthesis and storage.[301–304] A number of aptasensors using DNA crosslinks have been reported in various technologies including hydrogels.[167,305–307] Transduction of these offers great potential for biosensing and point-of-care applications such as detecting cocaine,[162,163] mercury[166] and proteins for detection of bird flu,[308] Alzheimer's Disease,[164,165] Leukemia[115] and HIV.[309] The adaptability conferred by using aptamers was desired by Axis Shield to expand the scope of applications for sensors developed during this project.

A well-known aptamer sequence for detection of adenosine was utilised as a proof-of-concept.[157,158,160,161] The aptamer sequence recognises and binds two adenosine molecules through formation of a guanine quadruplex.[158] Two crosslinks were investigated (Figure 3.4). The first (APT1) was reported by Yang *et al.* and used an elongated aptamer sequence hybridised to one blocking strand, displaced as the aptamer sequence folds to bind adenosine, and a tethering strand used to attach the aptamer to the polymer through base pair hybridisation.[258] The second crosslink (APT2) removed both the tethering strand and sequence of the sensing strand and instead covalently attached the aptamer strand. This crosslink simplification had been

exhibited by Yang *et al.* when investigating a thrombin-binding aptamer and is more akin to the MIR1 crosslink discussed previously.

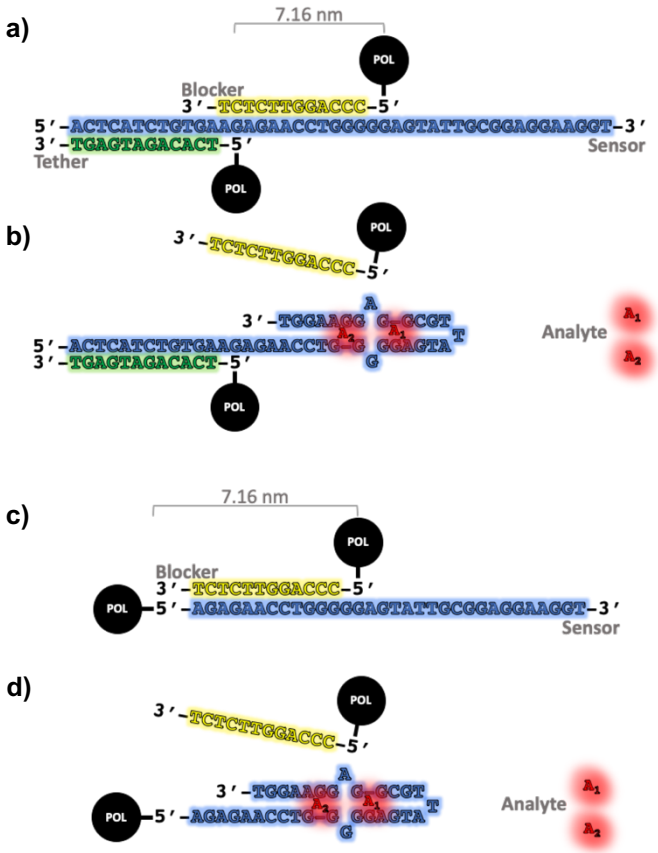

Figure 3.4 (a) The sequences and length of the APT1 crosslink adapted from Yang *et al.* The tether and blocker strand are tethered in polymer at the 5' ends, while the aptamer sensor strand is hybridised to both. (b) Displacement of the blocker strand by the adenosine triggered folding of the aptamer sensor strand to break the crosslink. (c) The sequences and length of the APT2 crosslink, tethered in polyer at the 5' ends. (d) Displacement of the APT2 blocker strand by the adenosine triggered folding of the aptamer sensor strand to break the crosslink.

End-point swollen volumes indicated that both APT1 and APT2 crosslinked gels would show greater swelling capacity when swollen in 2 mM adenosine compared to swelling in buffer alone (Figure 3.5). APT1 gels exhibited greater non-specific swelling in buffer than APT2, most likely due to both longer crosslink length and greater gel charge density, 27.2 mol% and 17.6 mol% wrt AAm respectively.[176,259] As such, the differential between swelling in analyte and random was far greater for APT2 gels, despite APT1 swelling to a larger volume. Furthermore, pregel solutions were viscous and difficult to pipette accurately due to the high DNA concentration (5.6 mM assuming 100%

conversion). Examples of fully detached, damaged, disfigured, partially detached and inaccurately deposited APT1 gels are shown in Figure 3.6. These issues are discussed further in Section 3.2.2. Due to the small volume of the gels, and the need to measure mechanical properties in solution, the hardness or strength of the gels could not be quantified with the available equipment. Although not immune to these occurrences, the APT2 crosslink contained 24 fewer nt units, 35 % less than APT1 so was less viscous and therefore easier to deposit. APT2 gels were also more resilient to deformation. When imaging gels out of solution, any solution outside of the gel is carefully removed with paper tissue. Upon accidental contact, APT1 gels would often partially deform, whereas APT2 gels would remain intact.

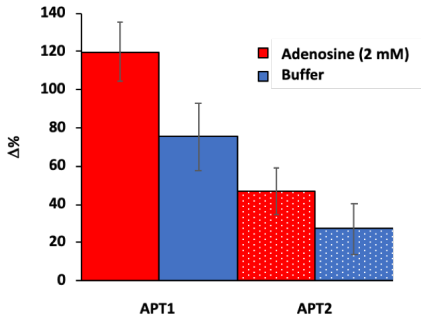

Figure 3.5 Comparison of swollen volume at 60 minutes to test adenosine response of APT1 (solid) or APT2 (dotted) crosslinked hydrogels with 10 wt% AAm, 0.6 mol% MBA and 0.4 mol% DNA crosslinks (wrt AAm) in 2 (red) or 0 (blue) mM adenosine , 300 mM NaCl, 1 mM PBS. Δ% and standard error of the mean calculated using equations 3.2a and b (n = 3).

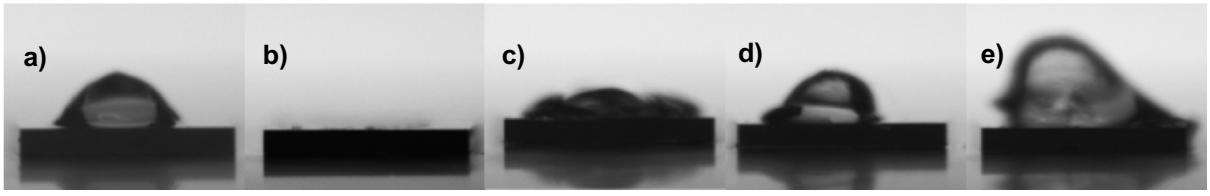

Figure 3.6 Examples of APT1 gel issues (a) the “normal” gel profile (b) fully detached gel (c) damaged gel (d) disfigured gel (e) partially detached and inaccurately pipetted gel.

Swelling kinetics were investigated using 1 wt% CNP as a contrast agent. Due to the difficulties relating to the high viscosity of APT1 crosslinked gels, the number of crosslinks was reduced to 0.2 mol% wrt AAm and the response to 2 mM adenosine is

shown in Figure 3.7. Issues of gel disfigurement remained and as such, testing was only conducted in duplicate. Due to gel irregularities, CNP leaching and some precipitating particles in solution, volume measurements varied greatly during each test (Figure 3.7a). However, as gels were imaged every 10 seconds, these effects can be mitigated by averaging all the measurements over each minute (Figure 3.7b). Despite this, there was no clear increase in swelling capacity in the 2 mM adenosine solution. It is likely that there were too few APT1 crosslinks in the gels to facilitate a measurable difference as similar results were observed in previous work and 0.4 mol% gels were proven to swell to a greater volume in 2 mM adenosine.

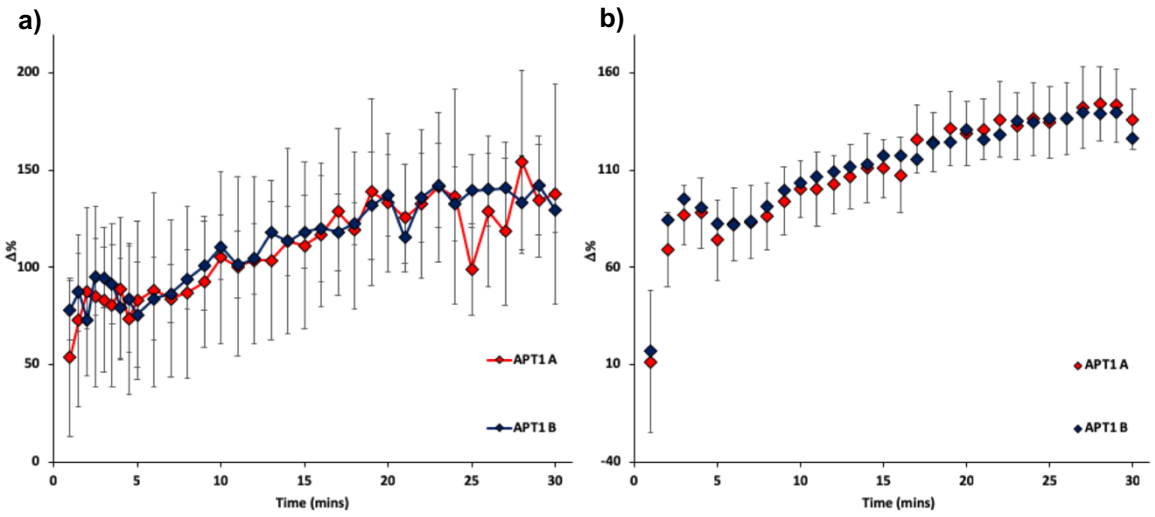

Figure 3.7 Comparison of swelling kinetics of APT1 crosslinked hydrogels with 10 wt% AAm, 0.6 mol% MBA and 0.2 mol% APT1 DNA crosslinks (wrt AAm) and 1 wt% CNP in 2 (red) or 0 (blue) mM adenosine, 300 mM NaCl, 1 mM PBS. (a) shows the average measurement at each time point (b) shows the average of six measurements taken every 10 seconds over each minute. Δ% and standard error of the mean calculated using equations 3.2a and b (n = 3).

As the viscosity issues with APT1 gel preparation were mostly alleviated using the shorter APT2 crosslink, APT2 crosslinked gels were synthesised at the validated 0.4 mol% concentration with 1 wt% CNP for contrast in a similar investigation of swelling kinetics in response to 2 mM adenosine (Figure 3.8). As with the APT1 gels, noisy results were observed due to CNP leaching and some precipitating particles in solution (Figure 3.8a). Again, averaging the measurements over each minute reduced the noise (Figure 3.8b). In either case, the gels swollen in adenosine can be clearly

differentiated after 6 minutes. Were CNP leaching not interfering with volume measurements at the earlier time points, it is expected that the swelling profile would be more akin to the MIR1 measurements and differentiation could be achieved earlier.

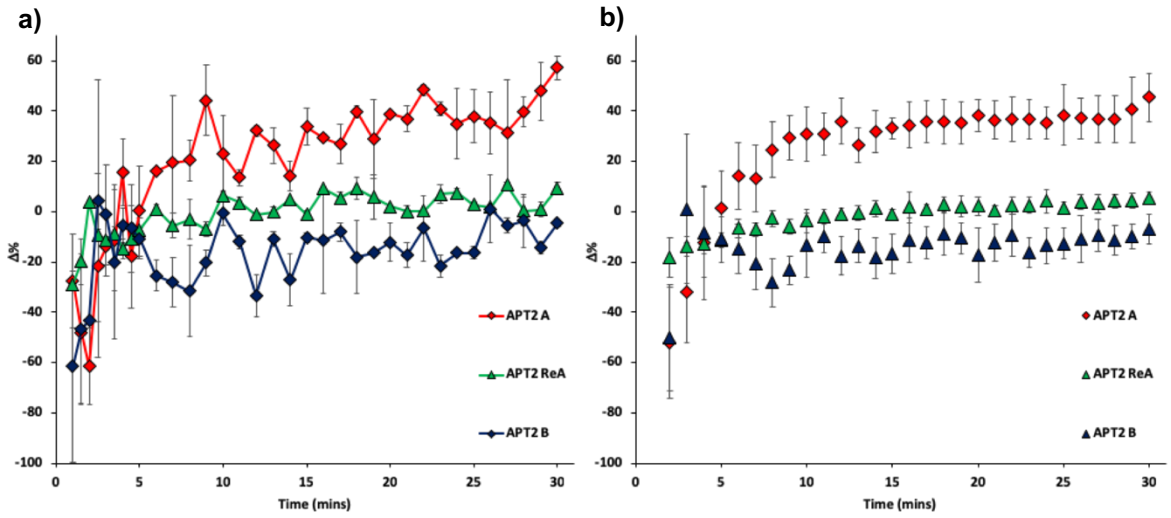

Figure 3.8 Comparison of swelling kinetics of APT2 crosslinked hydrogels with 10 wt% AAm, 0.6 mol% MBA and 0.4 mol% APT2 DNA crosslinks (wrt AAm) and 1 wt% CNP in 2 (red) or 0 (blue) mM adenosine, 300 mM NaCl, 1 mM PBS. (a) shows the average measurement at each time point (b) shows the average of six measurements taken every 10 seconds over each minute. Gels swollen in 0 mM adenosine were then dried and reswollen in 2 mM adenosine (green). Δ% and standard error of the mean calculated using equations 3.2a and b (n = 3).

In an attempt to reduce the influence of CNP leaching during swelling and confirm the differential swelling observed using APT2 crosslinked gels was not a result of inaccurate syntheses, the APT2 B samples swollen in buffer only were dried and then reswollen in 2 mM adenosine (APT2 ReA). These gels showed a far smaller swelling response than those only swollen in adenosine, although still greater than the original swelling in buffer. This may be explained by gel damage caused by the swelling and drying stresses, as well as the lack of CNP leaching. Alternatively, gel damage or non-specific crosslink dehybridisation may equally have increased gel swelling rather than a response to adenosine. Due to lack of material this was not further investigated.

End point swelling showed that both APT1 and APT2 crosslinks could be used to detect 2 mM adenosine in solution. However, difficulties caused by the pregel solution viscosity and high charge density of the gels led to issues of detachment, damage and

disfiguration. In particular, APT1 crosslinks are inappropriate for this hydrogel system as lowered crosslink density removed the sensing capability of the gel. Although aptamer crosslink incorporation and use for sensing have been validated, the limitations of the system adaptability have been highlighted. Shorter aptamer sequences and crosslinks designs could be readily adapted into this system, whereas longer sequences would require further optimisation.

3.1.3 African Sleeping Sickness Crosslink

As discussed previously, there are numerous examples of DNA crosslink structures and it would be expected that this hydrogel synthesis and transduction method could be adapted to detect a large variety of targets through intelligent design of DNA crosslinks. One such target is a small RNA (sRNA) sequence as a potential biomarker of trypanosomes in cattle.[293] Detection of this sequence found by Chiweshe *et al.* was attempted in collaboration with Dr Finn Grey and served as a model for sRNA detection.

Trypanosomes are parasites that cause trypanosomiasis, or African Sleeping Sickness (ASS) and are spread by the Tsetse fly between livestock and humans.[310] ASS occurs predominantly in sub-Saharan Africa in remote rural areas with limited healthcare services and is considered by the World Health Organisation (WHO) to be a Neglected Zoonotic Disease (NZD) with a dual burden on health and agriculture.[311] One of the challenges of ASS is diagnosing and monitoring the disease in both humans and animals as the lack of infrastructure leads to gross under-reporting. Furthermore, traditional diagnosis uses microscopy, which relies upon a minimum threshold of parasitaemia. The ASS biomarker can be used to detect parasitaemia below the detection threshold of microscopy. A simple, portable, point-of-care biosensor would have great potential for addressing and controlling outbreaks of ASS.

To investigate difficulties of charge density and crosslink length, a number of crosslink designs were tested for ASS biomarker detection. The crosslink sensing strand was fully complementary to the ASS biomarker sequence, with different blocking strands to test the effects of crosslink design on hydrogel swelling response (Figure 3.9). The

ASS1 crosslink copied the MIR1 crosslink design, hybridising the sensing strand with a 22 nt long blocking strand (B1) that has 12 nt complementary to the 3' end of the sensing strand. ASS2 instead used a 12 nt blocking strand complementary to the 5' end of the sensing strand (B2), while ASS3 included both the B2 blocker and a blocking strand of 12 nt complementary to the 3' end of the sensing strand (B3) to form a crosslink with 3 attachments to the polymer backbone.

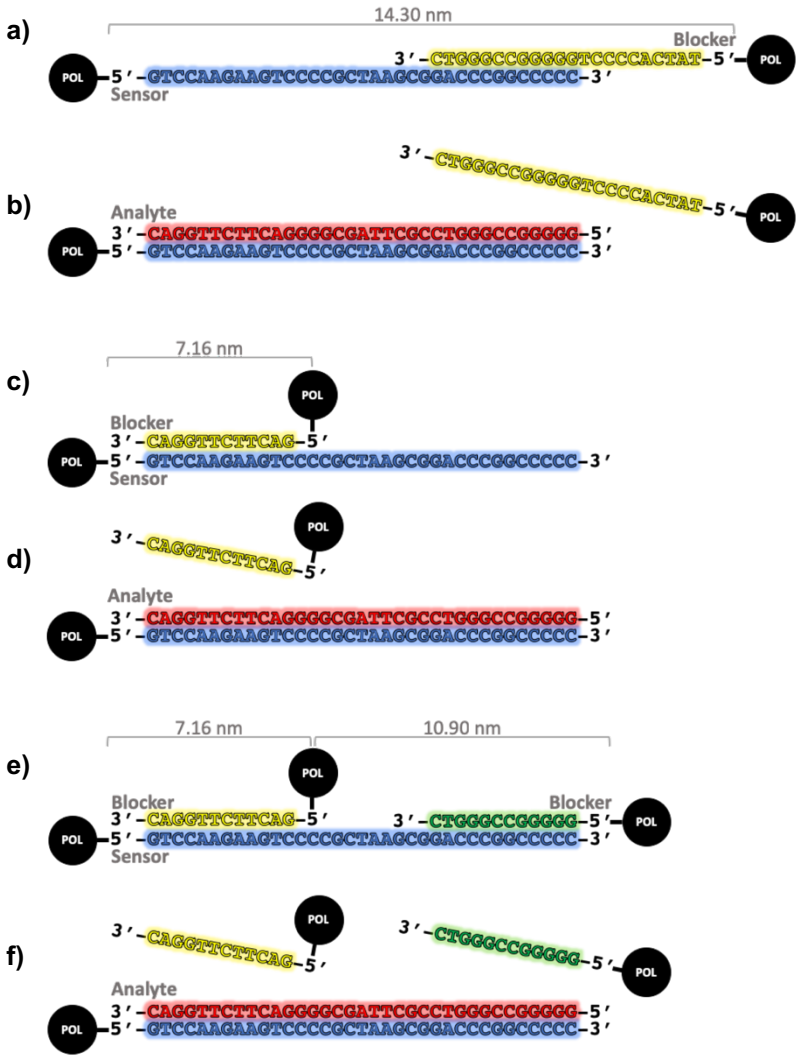

Figure 3.9 (a) The sequences and length of the ASS1 crosslink, tethered in polymer at the 5' ends. (b) Displacement of the ASS1 blocker strand by the analyte strand to break the crosslink. (c) The sequences and length of the ASS2 crosslink, tethered in polymer the 5' ends. (b) Displacement of the ASS2 blocker strand by the analyte strand to break the crosslink. (e) The sequences and length of the ASS3 double crosslink, tethered in polymer the 5' ends. (f) Displacement of the ASS3 blocker strands B2 and B3 by the analyte strand to break the crosslink.

Swelling kinetics of the three crosslink designs reinforced the issues caused by high DNA concentration within the gels and offered potential solutions through intelligent crosslink design (Figure 3.10). In each case gels were swollen in buffer and then dried to wash out loose CNP and oligomers from the gel network. Crosslink ASS1 resulted in relatively frail hydrogels that frequently exhibited deformations or detached from the wafer during swelling, which led to difficulty in obtaining accurate results, much like the difficulties with APT1 crosslinked gels. As such, while the response to the analyte solution was marginally greater than swelling in the random solution, results are too similar to confidently differentiate between the two.

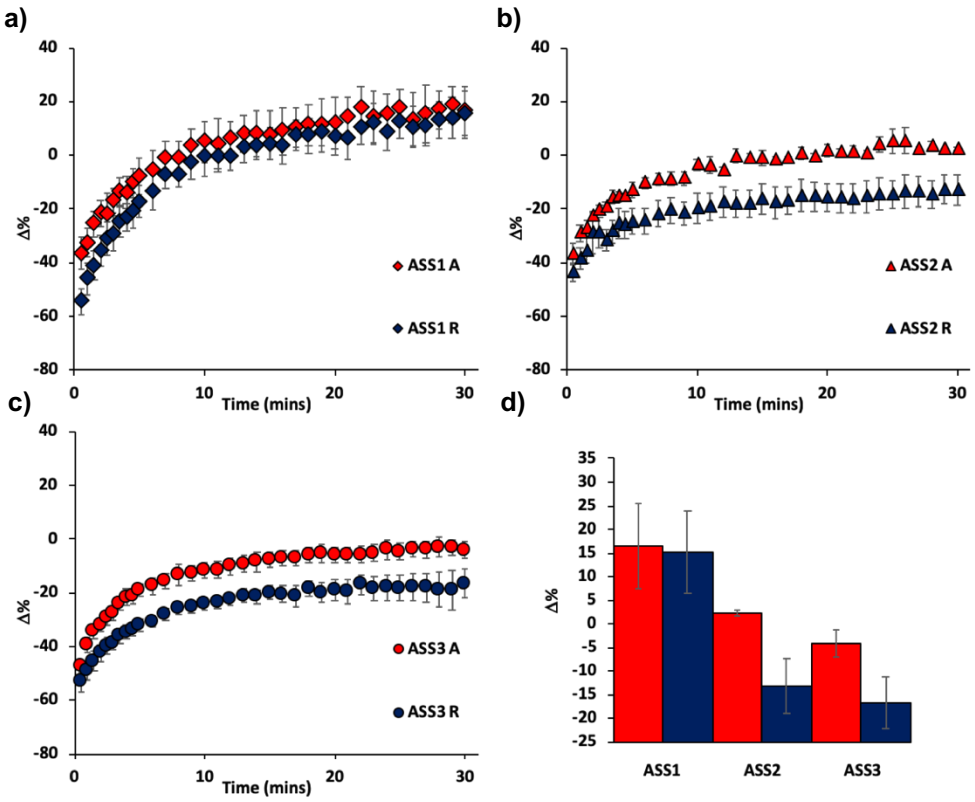

Figure 3.10 Comparison of swelling kinetics of ASS targeted hydrogels with 10 wt% AAm, 0.6 mol% MBA and 0.4 mol% DNA crosslinks (wrt AAm) and 1 wt% CNP in 10 μM analyte (red, A) or 10 μM random (blue, R), 150 mM NaCl, 1 mM PBS. (a) Shows ASS1 crosslinked gels (diamonds) (b) Shows ASS2 crosslinked gels (triangles) (c) ASS3 crosslinked gels (circles) (d) Compares the end point swollen volumes at 30 minutes of ASS1, ASS2 and ASS3 crosslinked hydrogels. Δ% and standard error of the mean calculated using equations 3.2a and b (n = 3).

Despite having similar issues of gel detachment, transduction of ASS2 crosslinked gels swelling response far better identified the analyte solution (Figure 3.10b). The

reduction of crosslink length from 14.3 nm to 7.2 nm and charge density from 22.8 mol% to 18.8 mol% reduced the total swelling in both analyte and random solutions. Addition of the extra blocker strand in ASS3 crosslinked gels, despite increasing the total nucleotide content of the crosslink, further reduced the swelling in both analyte and random, although the difference in response to analyte was slightly less than ASS2 gels. ASS3 gels were the most robust of the ASS sensing gels, though seemingly still less so than MIR1 crosslinked gels. Despite the increased charge density of the hydrogel (23.6 mol%) being more comparable to ASS1, the overall swelling has been reduced as the use of two blocking strands results in a tri-functional crosslink.[312] Differentiation between analyte and random solutions can be made after 1 minute, although lower concentrations may take longer.

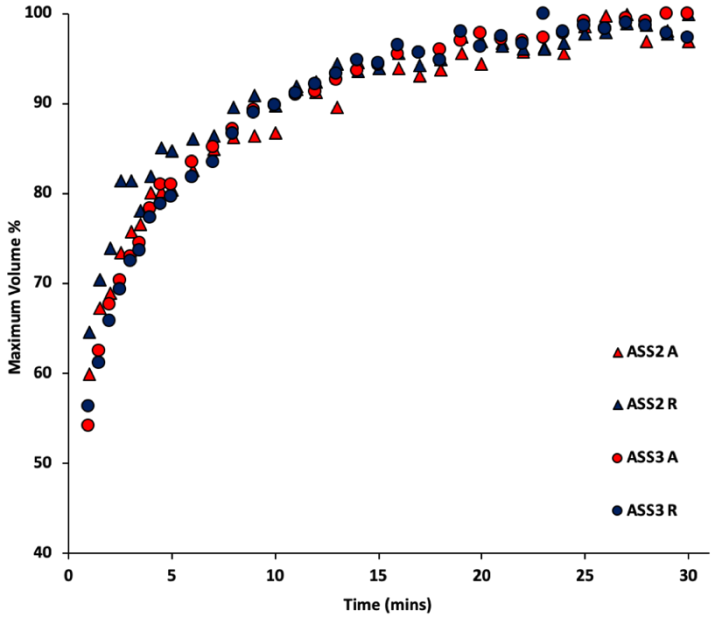

Figure 3.11 Comparison of swelling rates of ASS2 and ASS3 crosslinked hydrogels with 10 wt% AAm, 0.6 mol% MBA and 0.4 mol% DNA crosslinks (wrt AAm) and 1 wt% CNP in 10 μM analyte (red, A) or 10 μM random (blue, R), 150 mM NaCl, 1 mM PBS. The maximum average swollen volume within 30 minutes of swelling was used to calculate the swelling %.

Figure 3.11 shows the swelling data of ASS2 and ASS3 from Figure 3.10b and c as a percentage of their maximum volume. The consistent rate of swelling irrespective of analyte or random solution would suggest that the diffusion of analyte DNA and cleavage of crosslinks occurs faster than the diffusion of water into the gel, although

this may not be the case at lower analyte concentrations. For both crosslink designs, 90 % of swelling is reached after 11 minutes. Clear differentiation was possible earlier yet relying on 90 % swelling values ensures that the maximum differentiation is achieved. This swelling rate has not been affected by the ASS3 extra blocking strand, as the displacement reaction of both crosslinks can occur simultaneously and individually as each blocking strand does not improve the stability of the other. Use of extra blocking strands can therefore facilitate detection of longer sequences like those of sRNA, enabling a wider range of biomarker targets.

3.2 DNA Crosslink Challenges

The synthesis and analysis of the APT and ASS crosslinked hydrogels exemplified the adaptability of DNA crosslinks as bioreceptors yet accentuated a number of challenges caused by using DNA crosslinks in a hydrogel. Although arising from a number of different aspects of gel preparation, these will be summarised as the challenges of DNA crosslink dehybridisation and the detachment of the DNA crosslinked hydrogel from the silicon wafer.

3.2.1 Crosslink Dehybridisation

Typically, crosslink integrity and hybridisation could be measured using fluorophores and quenchers attached to the DNA strands, through introduction of a molecular intercalating dye or via UV absorption measurement.[68,313,314] In hydrogels with 1 or 2 wt% CNP none of these options are viable as the CNP prevents signal detection. As such, the crosslink integrity throughout synthesis and testing can only be modelled and theorised.

The requirements for stable DNA crosslinks greatly limit the usable conditions for sensor synthesis and storage as any dehybridisation of the sensing and blocking strands can result in a false positive signal. DNA melting temperature (T_m) calculators

developed for PCR primer design are particularly useful for predicting properties of DNA crosslinks and the predicted T_m of each crosslink discussed above is shown in Table 3.1. The potential T_m of a crosslink is dependent on both the length and sequence of matching nucleotides, which in turn is dependent on the target analyte sequence as sequences with higher GC content exhibit base-stacking, which strengthen the hybridisation. The driving mechanism of blocking strand displacement is the greater stability of the hybridisation of the analyte sequence to the sensing strand.[169,176] As such, lengthening the blocking strand hybridisation length would strengthen the crosslink, but potentially slow the rate of displacement and potentially lengthen the time to response (TTR). A fast TTR is desirable for point-of-care testing and the effects of blocking strand length investigated elsewhere, therefore longer blocking strands were not used despite the potential benefits.

Table 3.1 Predicted T_m of DNA crosslinks sensor and blocker interactions, predicted using Nearest Neighbour calculations.[168]

Crosslink	Blocker Sequence	GC content (%)	T_m (°C)
MIR1	TGTTCACGTTAT	33	32.79
ASS1	CTGGGCCGGGGG	92	51.88
ASS2	CAGGTTCTTCAG	50	35.36
ASS3	CAGGTTCTTCAG	50	35.36
	CTGGGCCGGGGG	92	51.88
APT1	TCTCTTGGACCC	58	43.94
	TGAGTAGACACT	42	38.11
APT2	TCTCTTGGACCC	58	43.94

Potential sensing applications would be expected to be carried out at either room temperature (23 °C) or body temperature (37 °C). Comparatively, the maximum temperature of the silicon wafer during 60 seconds of UV irradiation used for photoinitiation was 26.5 ±1.5 °C, whereas use in countries of sub-Saharan Africa or the effects of climate change may require storage at temperatures higher than body temperature.[315] To minimise potential of thermal dehybridisation before testing, all gels were stored at 4 °C and all swelling measurements were carried out at 23 ±1 °C. As such, the T_m of all crosslinks used is above the expected conditions encountered during synthesis and testing, yet it remains a limiting feature of DNA crosslinks that prevents a number of alternative initiation methods or conditions.

DNA hybridisation is also dependent on the presence of cationic species able to shield the anionic charges of the sugar phosphate backbone and enable base pairing.[183,184] Without stabilisation of the electrostatic repulsion between two ssDNA backbones the nucleotides cannot get in proximity to base pair. Although biological samples will typically have a relatively high concentration of cations to maintain stable oligonucleotide secondary and tertiary structures, there are a number of benefits to not requiring salt during synthesis discussed further in Section 3.4 and Chapter 5. Similarly, biological samples would be pH 7.4 as high or low pH would denature DNA. Therefore, sampling and processing could maintain an appropriate pH through the use of buffers.

For optical transduction, CNP is used as a pigment to improve the contrast for kinetic swelling measurements as the refractive index of PAM is similar to water and therefore very difficult to accurately image in solution. CNP is hydrophobic and therefore prone to aggregation and precipitation in aqueous solutions if not frequently agitated. A relatively stable pregel mixture with CNP may be achieved with a 50:50 mixture of water:DMSO, however the DMSO would substantially lower the T_m of the crosslink to be unstable at room temperature. The weakening effects of organic solvents and mixtures on DNA hybridisation have been thoroughly explored, limiting the solvent choice to water or mixtures with only a small amount of alternative solvent.[183,185–187,190–193]

3.2.2 Detachment and Deformation

A major concern for accurate transduction using either optical or electrical methods is detachment of the hydrogel from the silicon substrate. During optical measurements detachment can manifest in different ways (Figure 3.12) which result in an over- or under- estimation of volume. A gel can be completely or partially detached from the wafer, identifiable by the gel image profile. A similar issue occurs if there has been any hydrogel damage during synthesis or storage resulting in deformation of the droplet structure. Alternatively, unusual swelling profiles, exhibiting unusual features such as rapid increase or decrease after swelling has plateaued, can be caused when

detachment facilitates horizontal swelling. In each case, delaminated or deformed gels are excluded from results. Analysis is based on the assumption of that the gel droplet is perfectly circular, such that a single diameter measurement at each pixel of height can be used to calculate the droplet volume. The bottom and width of the gel must also be specified to avoid the measurement of gel reflection or of any leached carbon stain. Irregular shapes or gel spreading make accurate width and height selection difficult.

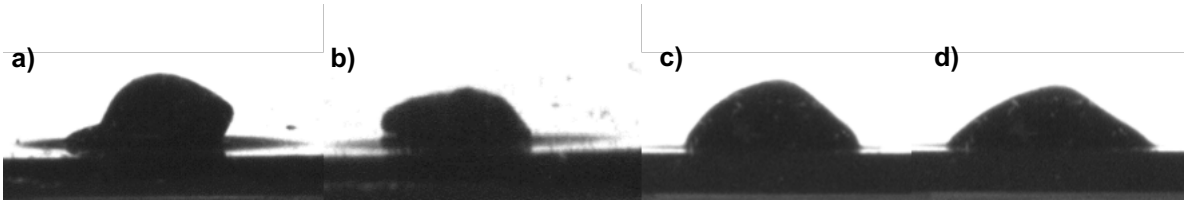

Figure 3.12 Examples of DNA gel issues (a and b) partially detached gels (c and d) same gel before (c) and after (d) edge detachment resulting in excessive horizontal spreading.

The silicon oxide wafer was functionalised using 3-(trimethoxysilyl) propyl methacrylate (TMSPM) Figure 3.13 as described in Section 2.3.3 to form a self-assembled monolayer.[259] The pendant methacrylate groups will polymerise with the monomers of the pregel solution during hydrogel synthesis, thereby providing attachment to the wafer. In spite of this, detachment would still occur.

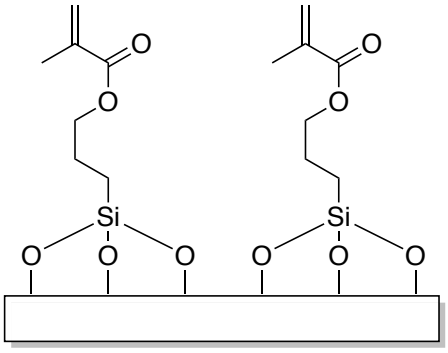

Figure 3.13 Structure of 3-(trimethoxysilyl) propyl methacrylate (TMSPM) monolayer on silicon wafer.

Visible detachment is caused by the stress and strain from hydrogel swelling damaging the attachment to the inflexible silicon wafer, while damage is also caused by the drying stress and strain for sensor storage. The potential damage caused by

hydrogel drying to xerogel are well characterised and can be related to the speed of solvent evaporation.[316–318] Furthermore, the CNP can contribute tensile stress during cooling, due to differences between the thermal expansion coefficients of particle and polymer, and drying, due to capillary action between particles.[280,281] Inspection of dry gels stored under vacuum exhibited fractures throughout, detachment at the gel edges (Figure 3.14). The fractures all appear more conductive than the surrounding area. Whether this is due to CNP concentration, edge effect, or both is unknown. Similarly, drying on a benchtop or in a fume hood greatly increased the rate of detachment compared to drying in the storage fridge. It was found that transferring gels into buffer solution after photo-initiation before drying resulted in less frequent delamination. This step served to facilitate continued gelation before droplet evaporation (~10 mins), while simultaneously washing out any loose CNP and unreacted monomers. It may be expected that this step would increase swelling response if structures removed were large enough to act as porogens.[260] During drying, the salt required for DNA hybridisation crystallises, potentially causing further deformation.[319] Hydrogel drying without washing is required for electrical measurements and will be discussed further in Section 4.3.2.

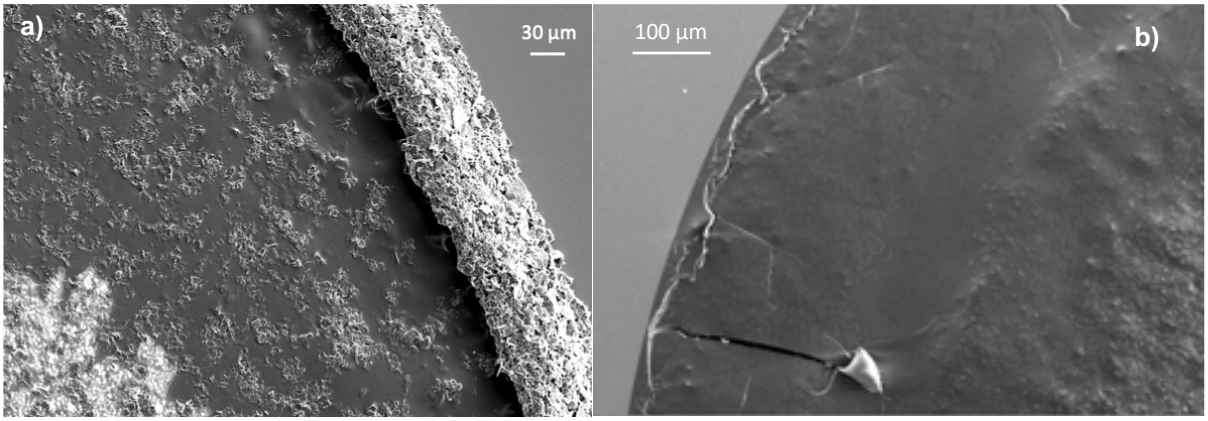

Figure 3.14 (a) SEM image of a dried 10 wt% AAm, 0.6 mol% MBA, 0.4 mol% DNA wrt AAm MIR2 hydrogel, 0 mM NaCl, 1mM PBS. (b) SEM image of a dried 10 wt% AAm, 0.6 mol% MBA, 0.4 mol% MO wrt AAm MOR2 hydrogel, 150 mM NaCl, 1mM PBS, discussed more thoroughly in Section 4.2.2.

As the stress and strain causing detachment is related to the drying and swelling properties of the hydrogel, the effect of DNA is relevant. In particular, the charged backbone conveys a charged moiety to the hydrogel, increasing hydrophilicity and both swelling capacity and rate. The charge density of each crosslink described above

is specified in Table 3.2. No hydrogels crosslinked only with MBA exhibited issues of detachment, whereas ASS1 and APT1 gels most frequently delaminated. These effects can be mitigated by the crosslink length or addition of extra blocking strands as evidenced by the ASS3 crosslink. Though each crosslink example used herein varied both charge density and crosslink length, the effects of each individually have been investigated elsewhere.[176,261,320]

Table 3.2 Total nucleotides per DNA crosslink, charge density at 0.4 mol% wrt AAm and crosslink MW including acrydite functionalisations. Intrinsic viscosity calculated using Equation 3.3.

Crosslink	Total nt	Charge Density (mol%)	Total MW (g/mol)	Concentration (g/L)	[η] (mL/g)
MIR1	44	17.6	14096	79.3	8.0
ASS1	57	22.8	17918	100.8	10.2
ASS2	47	18.8	14826	83.4	8.4
ASS3	59	23.6	18878	106.2	10.8
APT1	68	27.2	21873	123.1	12.6
APT2	44	17.6	14212	80.0	8.0

As well as influencing the swelling properties of the gels, the intrinsic viscosity of DNA may be predicted (Equation 3.3) and increases the viscosity of the pregel solution.[321,322] Although simple solution viscosity may be modelled, the complex pregel mixture has multiple interactions between solutes and would require proper characterisation. Increased viscosity not only retards the rate of propagation but also increases termination by oxygen and will therefore alter the gel network structure.[323–325] Glycerol was investigated to reduce gel shrinkage of polyacrylamide gels, improve DNA hybridisation and stabilise the nanoparticle dispersion.[186,326] However, preliminary tests on gels without DNA and with 1-5 % (v/v) of glycerol appeared to increase CNP leaching and were not investigated further. The rate of polymerisation vs drying is also expected to be important to hydrogel structure and is discussed further in Section 4.3.

$$[\eta] = 3.5 * 10^{-6} \times MW_{DNA}^{1.05}$$

Equation 3.3 Mark-Houwink-type equation for estimation of intrinsic viscosity [η] of DNA crosslinks.

One concern with photoinitiation of a pigmented mixture is the efficiency of UV penetration and the consequential effect on initiation efficiency. Furthermore, hydroxycyclohexylphenylketone (HPK) absorbs relatively poorly in the range emitted by the UV lamp (280-320 nm 1.5 W/cm^2, 230-395 nm 9+ W/cm^2, 400-450 nm 9+ W/cm^2) and is typically used for initiation in clear materials.[327,328] A poor initiation efficiency, or initiation only at the droplet surface, would contribute to poor gel-wafer attachment and delamination as the propagating species may not reach the wafer attached TMSPM groups.[329] Alternative photoinitiators were investigated with Alex Carroll during his master's project. Bis(2,4,6-trimethylbenzoyl)-phenyl phosphine oxide (BAPO), typically used for white or colour pigmented coatings due to its absorption of longer wavelengths, may be used in combination with HPK. A water dispersed version of BAPO is available, however it was unavailable for testing. As such, HPK and BAPO were dissolved in ACN in place of the HPK in ethylene glycol and used to synthesis gels. Figure 3.15 shows a gel synthesised with 0.125 mol% HPK as before, 0.125 mol% BAPO, and a 50:50 mix of HPK and BAPO. Before initiation is was apparent that CNP aggregation and precipitation had increased due to the small amount of ACN in place of ethylene glycol. During swelling the BAPO sample fully washed away, the 50:50 mix mostly washed away, while the HPK gel remained intact. ACN is known to negatively affect free radical polymerisation[330] and UV absorption spectra could not be obtained on pregel solutions, indicating that the CNP absorbs or diffracts to such an extent that only surface penetration can occur.

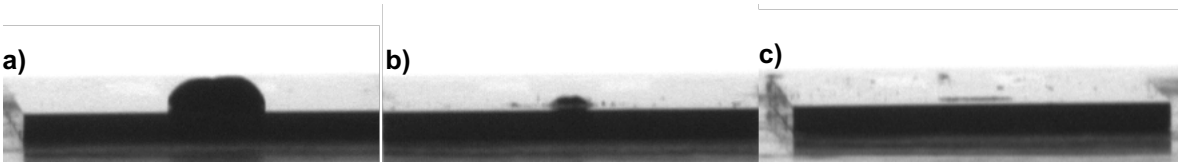

Figure 3.15 Examples of 10 wt% AAm, 0.6 mol% MBA wrt AAm hydrogels in 150 mM NaCl, 1mM PBS. Gels were photoinitiated using 0.125 mol% photoinitiator in ACN (1.76% v/v) (a) HPK (b) 50:50 HPK:BAPO (c) BAPO. Images shown were collected by Alex Carroll.

Increased UV intensity was investigated by shortening the distance between the pregel droplet from the UV lightguide or increased UV photoinitiation duration (Figure 3.16). In both cases no apparent benefit was observed and increased or complete drying of the droplets during photoinitiation due to elevated temperatures (Table 3.1).

Photoinitiation at 2.2” was continued due to concerns of DNA crosslink thermal dehybridisation. Smaller pregel droplets would require less UV penetration for consistent photoinitiation, as well as increasing the surface area to volume ratio which should reduce gel detachment. Computer controlled deposition techniques such as drop-on-demand inkjet printing (Chapter 5) would be required to facilitate smaller volumes as hand pipetted volumes are limited by both pipette size and placement accuracy (Section 3.5.1).

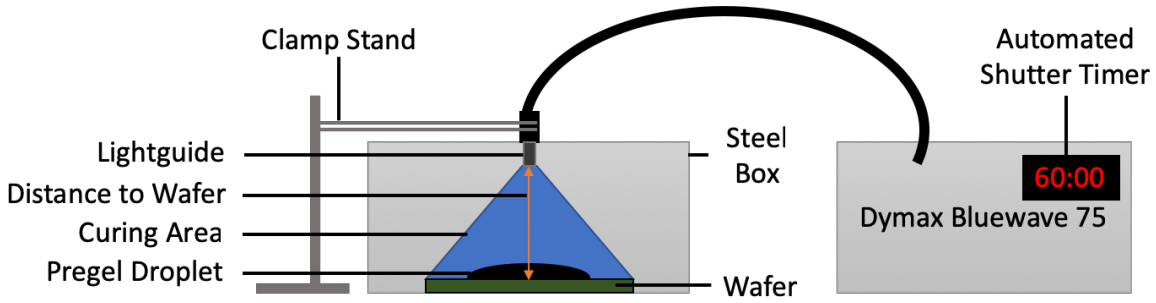

Figure 3.16 Illustration of UV photoinitiation procedure including UV initiation distance. Not to scale.

Table 3.3 Maximum temperature of silicon wafer during 60 seconds of UV exposure.

Distance	2.2"	1.8"	1.5"	1.2"	1"	0.4"	0.3"	0.0”
Temperature (±1.5 °C)	26.5	32.4	34.9	38.7	40.2	45.2	52.9	68.9

Due to issues with photoinitiation, alternative initiation methods were investigated. Ammonium persulfate (APS) is a redox initiator commonly used for polyacrylamide synthesis. Although APS can be thermally initiated, use of an accelerator, tetramethylethylenediamine (TEMED), enables synthesis at room temperature. Due to the DNA crosslink thermal stability only room temperature syntheses were investigated. Attempted synthesis with 0.125 mol% APS and 0.85 mol% TEMED was unsuccessful, most likely due to inhibition by oxygen. Higher concentrations of APS (1.25 mol%) and TEMED (8.5 mol%) did trigger gelation, however inefficient mixing made synthesis impractical for hand pipetting as only partial gelation was achieved in a localised area. Controlled deposition and mixing were achieved using drop-on-demand inkjet printing discussed in Chapter 5.

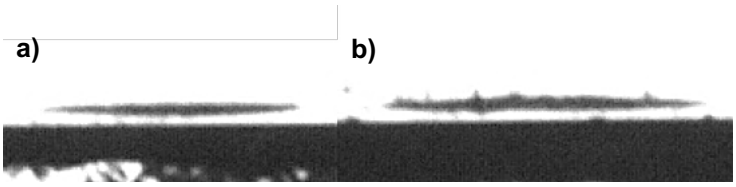

Figure 3.17 Examples of 10 wt% AAm, 0.6 mol% MBA wrt AAm hydrogels in 150 mM NaCl, 1mM PBS after 1 hour of swelling in buffer. Gels were thermally initiated at 37 °C using (a) 0.125 mol% (b) 0.0625 mol% V-70 in ACN (1.76% v/v). Images shown were collected by Alex Carroll.

As mentioned previously, the thermal initiation of APS would dehybridise the DNA crosslinks, however 2,2'-azobis(4-methoxy-2,4-dimethylvaleronitrile) (V-70) is a radical initiator with a self-accelerating decomposition temperature of 30 °C, although the half-life at 30 °C is still 10 hours.[331] V-70 was dissolved in ACN as it is insoluble in water and hydrogels synthesised with 0.0625 or 0.125 mol% in an incubator at 37 °C. As V-70 is a type II initiator, in that it forms 2 radical species, these are therefore 0.125 and 0.25 mol% in terms of radicals formed. The resulting hydrogels were swollen in 1 mM PBS and 150 mM NaCl, shown after 1 hr in Figure 3.17. Upon immersion in buffer, the flakes of hydrogel began to detach leaving only the thin layer visible. SEM images of a V-70 initiated gel exhibited a mosaic of large cracks separating small flakes of gel which appear unattached to each other (Figure 3.18). This cracking is likely caused by the rapidity and extent of droplet dehydration at 37 °C. Humidity control may be used to slow droplet evaporation and synthesise an appropriately robust hydrogel but the required equipment was unavailable.

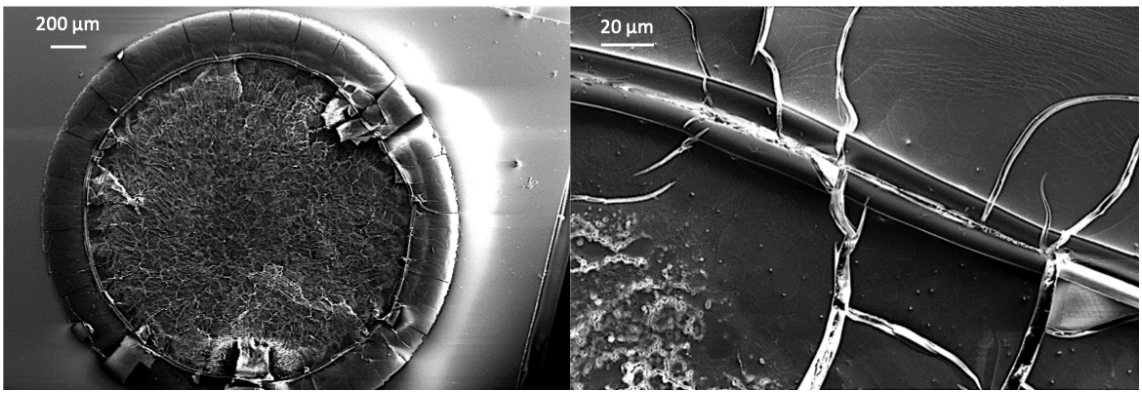

Figure 3.18 SEM images of a dried 10 wt% AAm, 0.6 mol% MBA wrt AAm hydrogels in 150 mM NaCl, 1mM PBS 0.125 mol% V-70 gel thermally initiated at 37 °C.

3.3 Optimised miR92a Sequence Detection

In an attempt to alleviate the effect of nucleotide density on detachment the MIR1 crosslink was redesigned (MIR2). Using learnings from the APT and ASS crosslinks, the 10 nt tail at the 5' end of the blocker strand was removed, whilst maintaining the same 12 nt crosslinking hybridisation with the sensing strand (Figure 3.19). The removal of 10 anionic charges per crosslink resulted in a 23% reduction in charge density and a theoretical crosslink length reduction of 3.4 nm. After preliminary testing confirmed differential swelling in response to analyte, the kinetic tests and analysis reported here were carried out by Alex Carroll as the basis for his master's project.

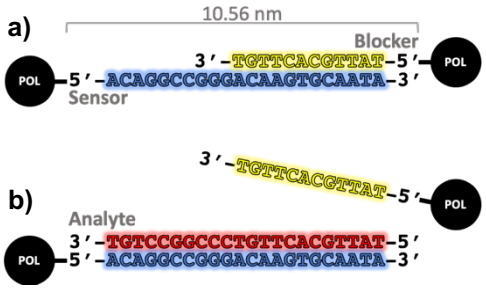

Figure 3.19 (a) The sequences and length of the MIR2 crosslink tethered in polymer at the 5' ends. Blocker sequence is 10 nt shorter than MIR1. (b) Displacement of the MIR2 blocker strand by the analyte strand to break the crosslink.

Figure 3.20 compares the swelling kinetics of MIR2 crosslinked hydrogels to MIR1 crosslinked hydrogels (10 wt% AAm, 0.6 mol% MBA, 0.4 mol% oligonucleotide crosslink wrt AAm) in either analyte or random sequence solutions (10 μM). The MIR2 gels included 2 wt% CNP rather than 1 wt% to be compared to the electrical transduction discussed in Chapter 4. Although this is expected to affect initiation efficiency, polymerisation efficiency and porosity, the comparison remains worthwhile.[235,323,329,332] In both cases swelling in analyte results in a larger volume than in the R solutions, with the rate of swelling and difference in final volume between A and R similar for both MIR1 (42 %) and MIR2 crosslinked gels (43 %). The specificity and LoD of MIR2 crosslinked gels were not tested but can be assumed to be similar to the capabilities of MIR1.

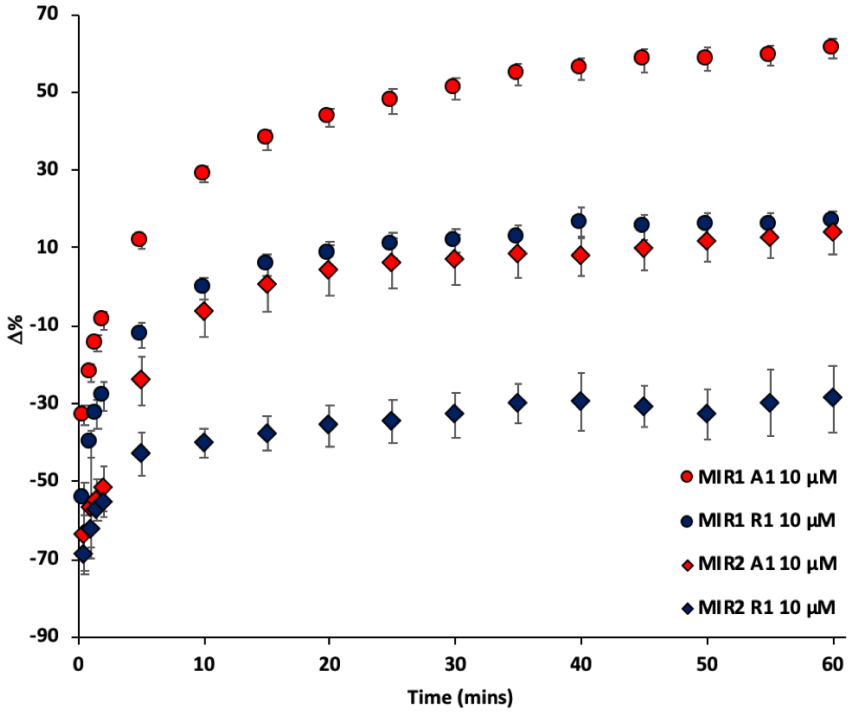

Figure 3.20 Comparison of swelling kinetics of MIR1 (circles, 1 wt% CNP) and MIR2 (diamonds, 2 wt% CNP) crosslinked hydrogels with 10 wt% AAm, 0.6 mol% MBA and 0.4 mol% DNA crosslinks (wrt AAm) in 10 μM analyte (red, A) or 10 μM random (blue, R), 150 mM NaCl, 1 mM PBS. MIR1 data shown was collected and analysed by Dr Ferrier, MIR2 data shown was collected and analysed by Alex Carroll. Δ% and standard error of the mean calculated using equations 3.2a and b (n = 3).

Increased covalent crosslinker density was investigated in order to further reduce the detachment frequency. Although previous optimisation by Dr David Ferrier showed MBA concentrations greater than 1.0 mol% had little to no effect on hydrogel volume, this optimisation was on gels containing no CNP and no DNA.[81] As swelling capacity and hydrogel network microstructure will be affected by the charge density conveyed by the DNA crosslinks,[250] while photoinitiation and propagation rates will also be reduced by particles and pigmentation,[329] optimisation with DNA was required. As such, the swelling response of DNA crosslinked hydrogels were investigated as before in 10 μM solutions of analyte or random with MBA concentrations of 1.0 and 1.5 mol% and 0.4 mol% DNA wrt AAm. The kinetic swelling with each MBA concentration is shown Figure 3.21 while the final swollen volume at 60 minutes, and the rate of detachment are summarised in Figure 3.21d.

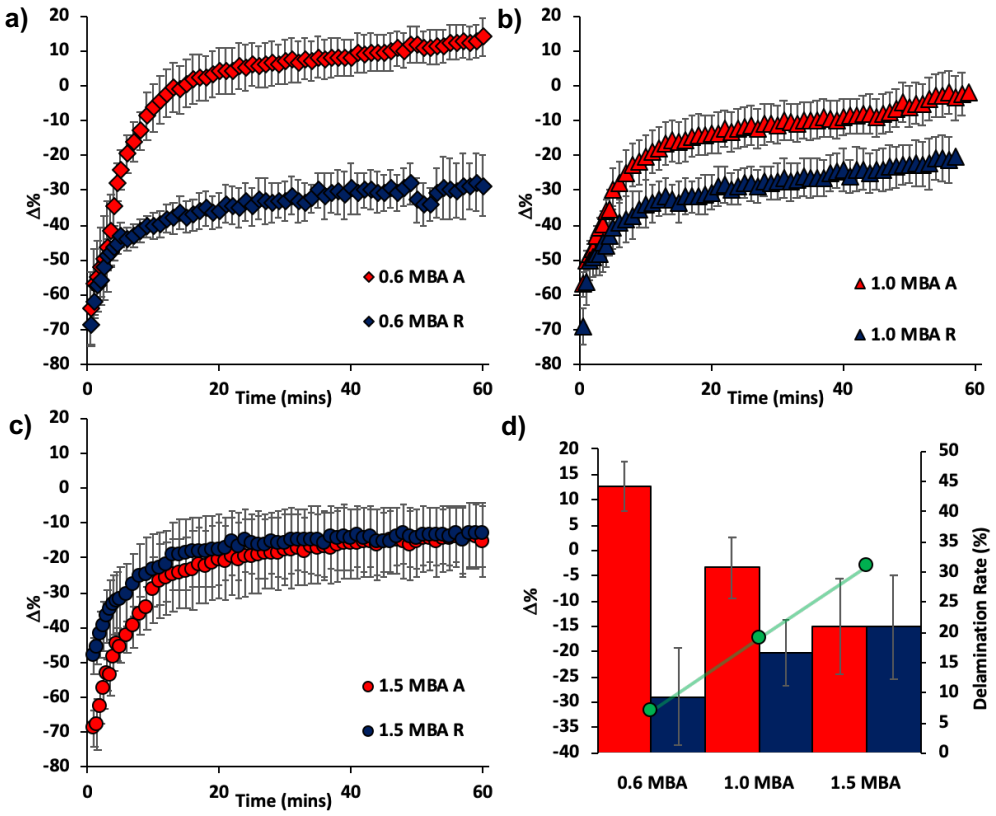

Figure 3.21 Comparison of swelling kinetics of MIR2 crosslinked hydrogels with 10 wt% AAm, 0.6-1.5 mol% MBA and 0.4 mol% DNA crosslinks (wrt AAm) and 2 wt% CNP in 10 μM analyte (red, A) or 10 μM random (blue, R), 150 mM NaCl, 1 mM PBS. (a) 0.6 mol% MBA (diamonds) (b) 1.0 mol% MBA (triangles) (c) 1.5 mol% MBA (circles) (d) Compares the end point swollen volumes at 60 minutes and the gel detachment rate of gels. Data shown was collected and analysed by Alex Carroll. Δ% and standard error of the mean calculated using equations 3.2a and b (n = 3).

The difference in extent of swelling in response to analyte and random sequences and differentiation between the two solutions was reduced as MBA concentration increased, with differentiation is no longer possible at 1.5 mol% MBA. Similarly, the rate of swelling in both analyte and random solutions reduced as MBA increased from 0.6 to 1.0 mol% MBA, taking approximately 18 minutes and 26 minutes respectively to reach 90% of the maximum volumes. The 1.5 mol% MBA gels reached maximum volume faster (17 minutes to 90% in analyte, 12 minutes in random). Generally, increased crosslink density would reduce gel volume and swelling,[333] yet the swollen volume in the random solution instead increased with MBA concentration. This may be an artefact of the UV photo-initiation process, whereby the top layer of the pigmented pregel droplet could polymerise most efficiently forming a polymer of greater density and crosslinking at the surface. At higher crosslink loadings the surface

of the pregel droplet may form a more elastic network better able to reswell to the original deposited size and shape.[334,335] Alternatively, this may be caused by inaccuracies during synthesis (discussed more thoroughly in Section 3.5.2). Figure 3.21d also compared the crosslink concentration to detachment rate and found that, although the DNA crosslink design change resulted in fewer detachments than MIR1 crosslinked gels (~40 %), increasing MBA crosslink concentration led to more gel detachments, likely due to the gel drying causing more fracturing to gels with more rigidity.

Similarly, 20 wt% AAm gels with 0.6 and 1.0 mol% wrt AAm and 0.4 mol% DNA wrt AAm were investigated as an alternative method to reduce detachment and improve gel integrity (Figure 3.22). Although both the 20 wt% AAm compositions reduced detachment issues, there was also no clear differential swelling between analyte or random solutions and the effect of crosslink reduction would be reduced by the increased polymer density. The 20 wt% AAm gels also had a greater swelling capacity than the 10 wt% AAm gels due to the increase in swellable material, which did not reach the maximum swollen volume within 60 minutes as the diffusion of solution and expansion of the gel would both be retarded by increased network density. Although differentiation may increase over longer swelling times point-of-care testing would be far less than 60 minutes. The LoD would also be expected to be worse, although not investigated here. While 0.6 mol% MBA gels had a marginally larger response to the analyte solution than random, smaller measurable change in response is rarely a benefit and the errors from synthesis and measurement are too large to assess reliably using this optical transduction method. These results in the context of electrical transduction are discussed further in Section 4.1.1.

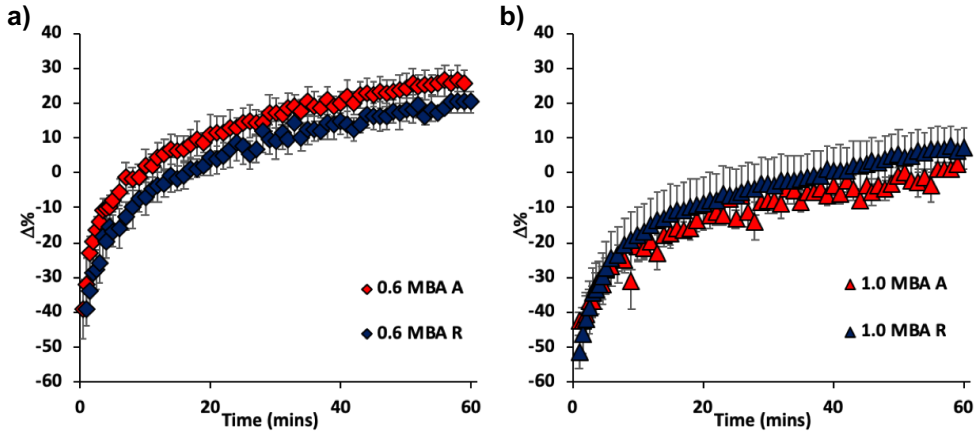

Figure 3.22 Comparison of swelling kinetics of MIR2 crosslinked hydrogels with 20 wt% AAm, 0.6 or 1.0 mol% MBA and 0.4 mol% DNA crosslinks (wrt AAm) and 2 wt% CNP in 10 μM analyte (red, A) or 10 μM random (blue, R), 150 mM NaCl, 1 mM PBS. (a) 0.6 mol% MBA (diamonds) (b) 1.0 mol% MBA (triangles). Data shown was collected and analysed by Alex Carroll. Δ% and standard error of the mean calculated using equations 3.2a and b (n = 3).

In an effort to increase the differential swelling response 10 wt% AAm gels were synthesised with equimolar 0.6 mol% MBA and MIR2 DNA as the greater change in crosslink density when the DNA crosslinks are broken should result in a larger difference in swollen volumes (Figure 3.23). However, as discussed in Section 3.2.2, gel integrity was compromised by the increased DNA concentration, despite the 23% nt reduction compared to MIR1, the total nt content of 0.6 mol% MIR2 would be 16% greater. As Stokke *et al.* reported UV photoinitiated 10 wt% AAm gels with 0.6 mol% MBA and 0.7 mol% DNA wrt AAm gels using a crosslink with a total of 40 nt, it can be surmised that the gel synthesis protocol remains an issue.

Figure 3.23 Example of 10 wt% AAm, 0.6 mol% MBA, 0.6 mol% DNA wrt AAm hydrogel after 60 minutes swelling in 10 μM random solution (150 mM NaCl, 1mM PBS) exhibiting lack of gel integrity and excessive CNP leaching. Image shown was collected by Alex Crroll.

Composition optimisation indicated that for optical transduction the 10 wt% AAm, 0.6 mol% MBA with 0.4 mol% DNA wrt AAm was optimal for the greatest differential response swelling in analyte. The sensitivity of this crosslink was not investigated due

to material shortage but may be assumed to be comparable to that of MIR1 gels. The reduced detachment and investigation of these compositions for electrical transduction is discussed in Chapter 4.

3.4 Morpholino Oligonucleotide Crosslinked Hydrogels

3.4.1 DNA Analogues in Hydrogels

Having identified a number of challenges when using DNA crosslinks for optical transduction, as well as further challenges in using DNA crosslinks in electrical transduction discussed in Chapter 4, it became apparent that DNA crosslinks may not be fit for purpose. In particular, there were concerns of crosslink thermal dehybridisation, while gel detachment resulted in wasted material. For electrical transduction; DNA interaction with CNP, CNP dispersion instability and the requirement of salt preventing the use of electrostatic dispersions were extremely problematic.

One way to overcome the challenges of DNA crosslinks is to use synthesised nucleic acid analogues which maintain the base structure to maintain base-pairing and modify the backbone structure of DNA in an effort to strengthen hybridisation and/or grant immunity to nuclease activity. Examples of these include glycol nucleic acid (GNA), threose nucleic acid (TNA), locked nucleic acids (LNA), bridged nucleic acids (BNA), which utilise phosphodiester linked backbones and require cations for hybridisation to occur, while nuclease resistant phosphorothioate-linked DNA (S-DNA) also requires cations.[196,199] These would not be applicable due to the aforementioned salt crystallisation damage in dried gels and considerations of electrostatic dispersions use for stable pregel solutions (Section 4.3.1). The absence of salt during testing would also disrupt any secondary structures of analyte oligonucleotides. Peptide nucleic acid (PNA) and morpholino oligonucleotides (MOs) (Figure 3.24), utilising phosphorodiamidate and methylene bridged amide backbones respectively, are the only examples of non-ionic DNA analogues that maintain relatively high aqueous solubilities.[194]

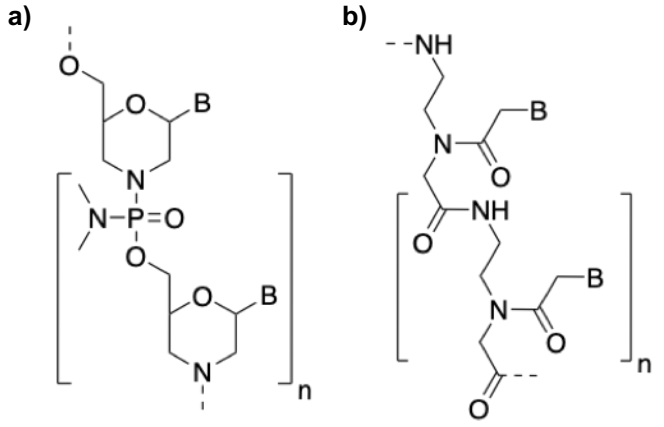

Figure 3.24 Structure of (a) Morpholino oligonucleotides (b) peptide nucleic acid (PNA) where B is any of the nucleobases adenine (A), cytosine (C), guanine (G) or thymine (T).

Many of the benefits of MOs and PNAs over DNA relate to nuclease-resistance, lack of biological macromolecule binding and applications *in vivo* as antisense oligos and are not relevant to *in vitro* diagnostic applications. Nuclease-resistance may prove beneficial in a biosensor application, depending on the test sample nature and preparation, but is not investigated here. As there is no electrostatic repulsion of MO or PNA to DNA or RNA, the uncharged backbone both facilitates hybridisation in non-saline solutions and improves the binding affinity. The lack of electrostatic repulsion does increase the risk of self-hybridisation which would be problematic with some miRNA sequences. As the nucleobase structure is unchanged, it is expected that either MO or PNA crosslinked hydrogels would offer the same adaptability as DNA crosslinks for detection of different miRNA or sRNA sequences. Aptamers can be made using PNA,[336,337] while MO may also be expected to reproduce a number of DNA aptamer structures, although aptamer folding may be hindered and aptamer structures reliant on electrostatic attraction would be unlikely to function if reproduced in PNA or MO. Although PNA exhibits a higher RNA binding strength than MOs, the MO backbone is less flexible as it has fewer rotational bonds and is therefore less liable to suffer from self-hybridisation if the required sensing or blocking strand sequences require some self-complementarity. Furthermore, PNAs have already used in hydrogels, albeit using PNA-DNA “hybrid” crosslinks rather than PNA-PNA and through crosslink formation after synthesis,[338] whereas the properties of MOs as biosensors have only been assessed in electrochemical studies and microarrays.[212,218,339,340]

3.4.2 miR92a Sequence Detection

Preliminary proof-of-concept testing was conducted synthesising MO crosslinked hydrogels (MOCHs) using the MIR1 crosslink sequence. Polymerisable acrylate functionalisation was developed by Dr Jaclyn Raeburn, reacting the purchased primary amine modification on each MO strand with N-succinimidyl acrylate (NSA) to form an amide bond with a vinyl end group. However, this required polymer attachment at the 3' end (MOR1) resulting in a crosslink almost half the length (7.16 nm rather than 13.96 nm) shown in Figure 3.25.

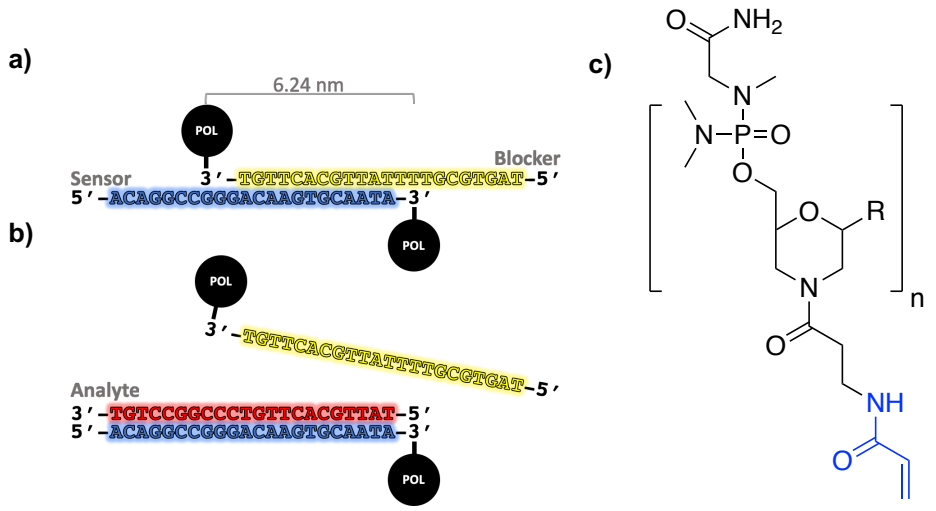

Figure 3.25 (a) The sequences and length of the MOR1 crosslink tethered in polymer at the 3' ends. Sequence is identical to MIR1 which tethered in polymer at 5' ends. (b) Displacement of the MOR1 blocker strand by the analyte strand to break the crosslink. (c) Structure of the 3' acrylate functionalisation used for MOR1.

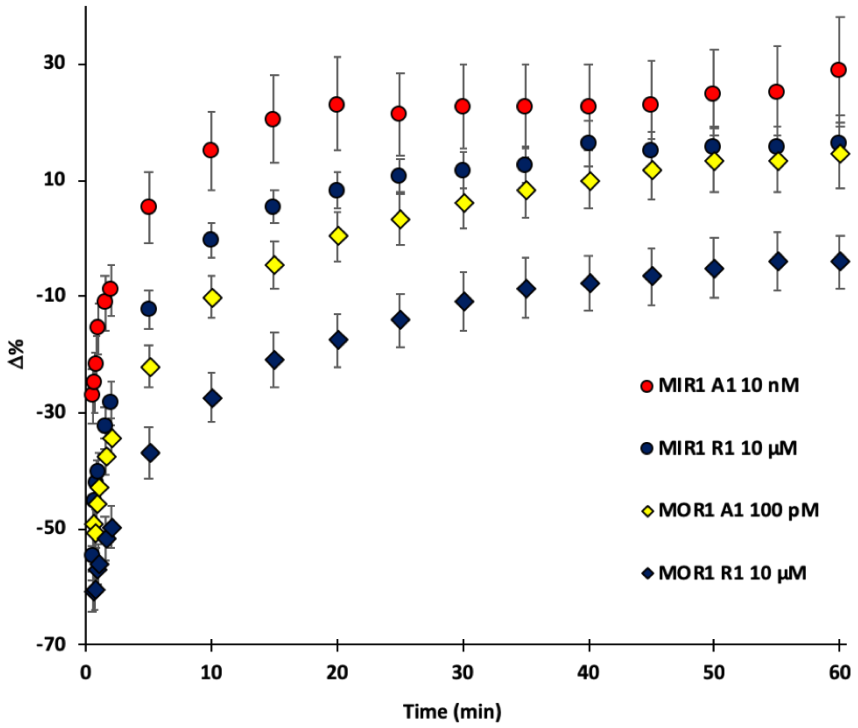

Figure 3.26 Comparison of swelling kinetics of MIR1 (circles) and MOR1 (diamonds) crosslinked hydrogels with 10 wt% AAm, 0.6 mol% MBA and 0.4 mol% DNA/MO crosslinks (wrt AAm) with 1 wt% CNP in 10 nM (red) or 100 pM (yellow) analyte or 10 µM random (blue) in 150 mM NaCl, 1 mM PBS. MIR1 data shown was collected and analysed by Dr Ferrier. Δ% and standard error of the mean calculated using equations 3.2a and b (MOR1 n = 3, MIR1 n = 5).

Comparison of swelling hydrogels crosslinked with MIR1 and MOR1 are shown in Figure 3.26. Much like the MIR2 crosslink, the reduction in crosslink length and the removal of charge density resulted in a lower swelling response to the random solution and although the MOR1 gels continue swelling after 60 minutes, there is clear differentiation between 100 pM analyte solution and 10 µM random solution, a 100-fold increase in sensitivity over the 10 nM LoD for MIR1. It is expected that this is facilitated by the increased affinity for DNA enabled by the lack of electrostatic repulsion from the MO backbone and that the binding of DNA from solution adding tethered charge density to the gels may also facilitate swelling.[261]

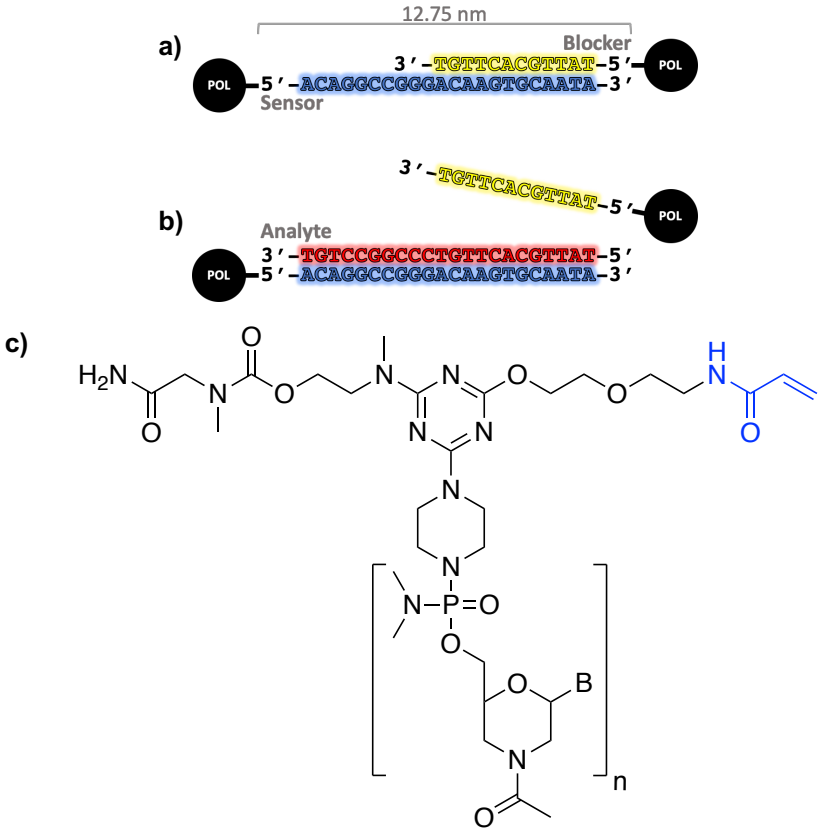

Figure 3.27 (a) The sequences, and length of the MOR2 crosslink tethered in polymer at the 5' ends. Crosslink is identical to MIR2. (b) Displacement of the MOR2 blocker strand by the analyte strand to break the crosslink. (c) Structure of the 5' acrylate functionalisation used for MOR2.

Subsequently, the MIR2 crosslink was synthesised with 5' modified MO strands (MOR2) shown in Figure 3.27. Despite the longer linker between MO and acrylate group, this structure is far more comparable to the 5' functionalised DNA crosslink designs than the 3' functionalised MOR1.

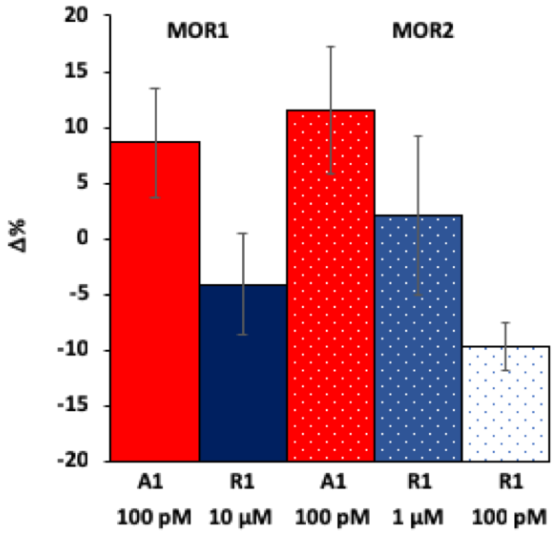

Figure 3.28 Comparison of swollen volume at 60 minutes to test MOR1 (left, solid) or MOR2 (right, dotted) crosslinked hydrogels with 10 wt% AAm, 0.6 mol% MBA and 0.4 mol% MO crosslinks (wrt AAm) in 100 pM A1 (red) or 10 µM – 100 pM R1 (blue), 150 mM NaCl, 1 mM PBS. Δ% and standard error of the mean calculated using equations 3.2a and b (n = 3).

Comparison of swelling response of MOR1 and MOR2 crosslinked resulted in the same LoD (100 pM) and comparable swelling with MOR2 crosslinked gels swelling slightly more than MOR1, possible due to the marginal increase in crosslink length or synthesis errors (Figure 3.28). More thorough testing was achieved on MOR2 crosslinked hydrogels due to material availability. This included swelling in a wider variety of concentrations of R1 solutions (1 µM – 10 pM) which identified that a greater differentiation is achieved when comparing identical concentrations of analyte and random solutions, as well as some concentration dependent responsivity (Figure 3.29).

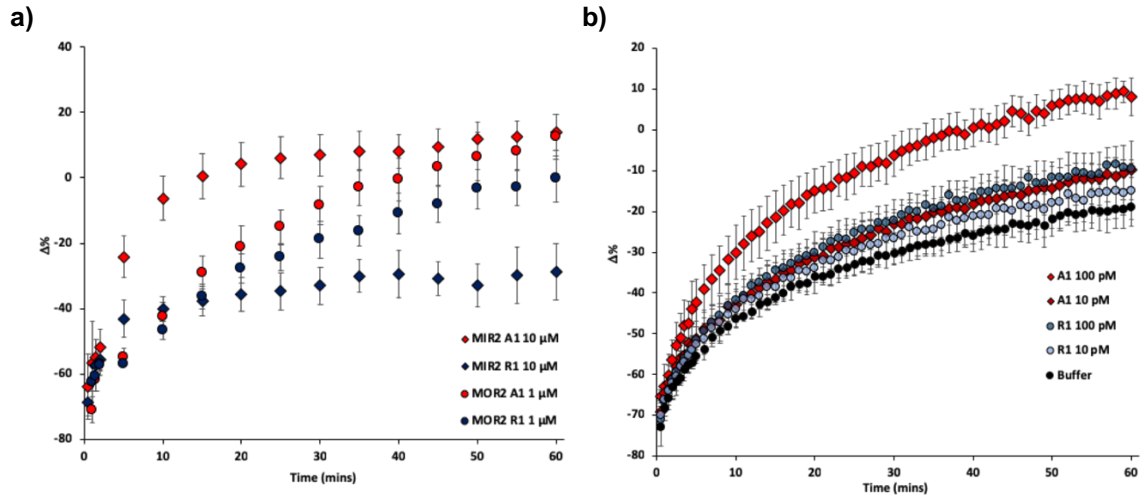

Figure 3.29 Comparison of swelling kinetics of (a) MIR2 (diamonds) or MOR2 (circles) crosslinked hydrogels with 10 wt% AAm, 0.6 mol% MBA and 0.4 mol% DNA/MO crosslinks (wrt AAm) and 1 wt% CNP in 10 – 1 µM analyte (red) or random (blue), 150 mM NaCl, 1 mM PBS. (b) MOR2 crosslinked hydrogels with 10 wt% AAm, 0.6 mol% MBA and 0.4 mol% MO crosslinks (wrt AAm) and 1 wt% CNP in 100 – 10 pM analyte (red, diamonds), 100 – 10 pM random (blue, circles) or buffer only (black, circles), 150 mM NaCl, 1 mM PBS. MIR2 data shown was collected and analysed by Alex Carroll. Δ% and standard error of the mean calculated using equations 3.2a and b (n = 3).

The response rate of MOR2 gels is slower than DNA gels as earliest differentiation is only possible at 10 minutes while swelling also continues beyond 60 minutes. This is most likely due to an increased gel density and decrease in hydrophilicity due to the reduction in charge density as well as the stronger crosslink hybridisation being slower to be displaced. The equivalent crosslinks of MIR2 and MOR2 swell to the same swollen volume after 60 minutes in analyte solution, and the MOR2 gels exhibited greater swelling in a random solution. This may be attributed to improved gel integrity, the effect of solution DNA being tethered by the unhybridized segment of sensor strand, or simply that data was collected and analysed by different users. The MOR2 crosslinked gels remained sensitive and selective at 100 pM and unable to differentiate between 10 pM solutions within 60 minutes, with the MIR2 crosslink not tested for LoD, it is assumed that it would be similar to the 10 nM LoD of MIR1 crosslinked gels.

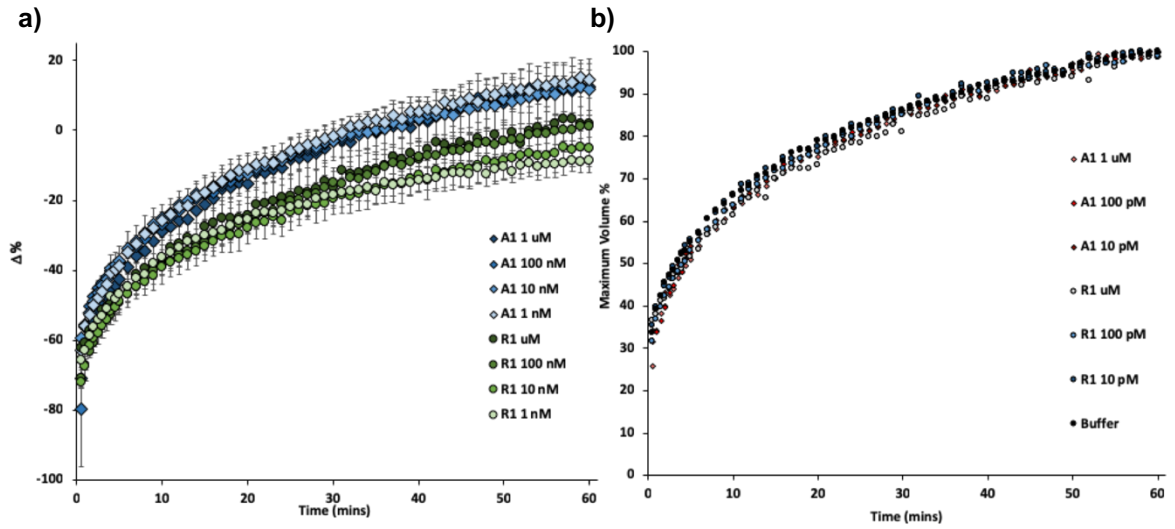

Figure 3.30 Comparison of (a) swelling kinetics of MOR2 (circles) crosslinked hydrogels with 10 wt% AAm, 0.6 mol% MBA and 0.4 mol% MO crosslinks (wrt AAm) and 1 wt% CNP in 1 μM – 1 nM analyte (blue, diamonds) or random (green, diamonds), 150 mM NaCl, 1 mM PBS. (b) swelling rates of MOR2 crosslinked hydrogels with 10 wt% AAm, 0.6 mol% MBA and 0.4 mol% MO crosslinks (wrt AAm) and 1 wt% CNP in 1 μM – 1 nM (red, diamonds), 1 μM – 1 nM random (blue, circles) or buffer only (black, circles), 150 mM NaCl, 1 mM PBS. The maximum average swollen volume within 60 minutes of swelling was used to calculate the swelling %. Δ% and standard error of the mean calculated using equations 3.2a and b (n = 3).

The swelling profile of MOR2 gels remained consistent at each concentration of analyte or random (Figure 3.30a). Although swelling did not reach the maximum swollen volume within 60 minutes, the rate of swelling to the maximum volume within 60 minutes was the same for all concentrations tested, including buffer only (Figure 3.30b). Stokke *et al.* identified three key steps in sensor response of their similar material:

1) Diffusion of DNA from solution into the gel to reach the crosslink.

2) Displacement of the blocking strand by the analyte DNA.

3) Swelling of the gel network.

They showed that in their system the rate determining step is the displacement of the blocking strand by the analyte DNA through fluorescent experiments, compared to changes in ionic strength and calculations of DNA diffusion rates.[259,260] However, in the system used here gels are swollen from their dried state which causes a faster initial swelling due to rehydration.[238,341–343] The swelling of the gel network remains the

rate determining step rather than diffusion of DNA or displacement of the blocking strand, as shown by the identical swelling rate in DNA solutions and buffer solution.

The concentration dependent responsivity, whereby oversaturation with a high R1 solution generates a response indistinguishable from a lower concentration of A1 (Figure 3.31a), may be due to the competitive displacement of the MO crosslinks by a sequence with lower affinity but higher concentration. The swelling response must also in part due to the tethering or localisation of DNA from solution to the MO strands. As the gels are uncharged the hydrophilicity of the hydrogel is lower than in DNA crosslinked hydrogels. Each DNA strand that becomes tethered would add 22 phosphate groups equating to 8.8 mol% charge density. If the blocker strand has been displaced, it is likely that it could also hybridize with a DNA strand from solution which would double the tethered charge density to 44 phosphate groups per MO crosslink, equating to 17.6 mol% charge density. This localized tethering of charge DNA sequences within the MOCHs is believed to cause the concentration dependent increase rate of swelling exhibited at concentrations of 100 pM and above, whereas at concentrations below this the response to the R1 sequence is indistinguishable from swelling in buffer alone. Although this charge density increase would occur in DNA gels also, the effect on swelling will be greater increasing from 0 mol% than from already anionic gels.

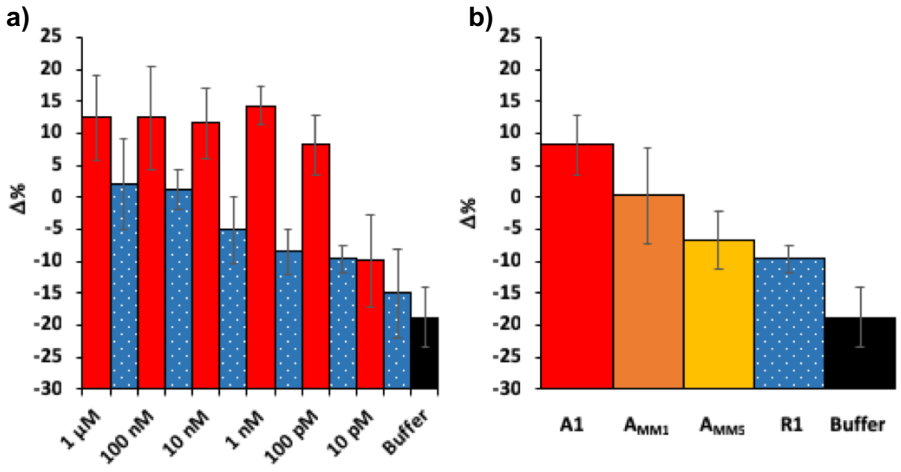

Figure 3.31 Comparison of (a) Swollen volume of MOR2 crosslinked gels with 10 wt% AAm, 0.6 mol% MBA and 0.4 mol% MO crosslinks (wrt AAm) and 1 wt% CNP at 60 minutes in A1 (solid red) or R1 (dotted blue) at 10 pM – 1 μM or buffer (150 mM NaCl, 1 mM PBS). (b) Swollen volume at 60 minutes to test mismatch response, at 100 pM or A1, R1, A_{MM1}, A_{MM5} and buffer (150 mM NaCl, 1 mM PBS). Δ% and standard error of the mean calculated using equations 3.2a and b (n = 3).

As DNA crosslinks had shown high sequence fidelity,[81,259] able to differentiate between a full sequence match and a sequence with one or more mismatches, MOR2 crosslinked gels were swollen with sequences A_{MM1} and A_{MM5} (identical to A1 but with 1 and 5 mismatches respectively). Figure 3.31b details the swelling of MOCHs in 100 pM solutions of A_{MM1} and A_{MM5} compared to swelling in buffer only, A1 or R1. Unlike the MIR1 DNA gel data obtained by Dr David Ferrier, MOR2 gels showed some increased swelling with partial matches, however this is logical and supported by results reported by Stokke *et al*. The greatest response is to A1, with decreasing swelling in A_{MM1}, A_{MM5}, R1 and finally buffer. As before, this is likely due to the thermodynamic favourability of displacement, whereby S1 has the strongest hybridization with so B1 is most rapidly displaced by A1, then A_{MM1}, A_{MM5}, R1 and is not displaced in buffer only. The competitive displacement is quantifiable and could be accounted for during analysis and design to achieve quantitative sensing.[169,176,344]

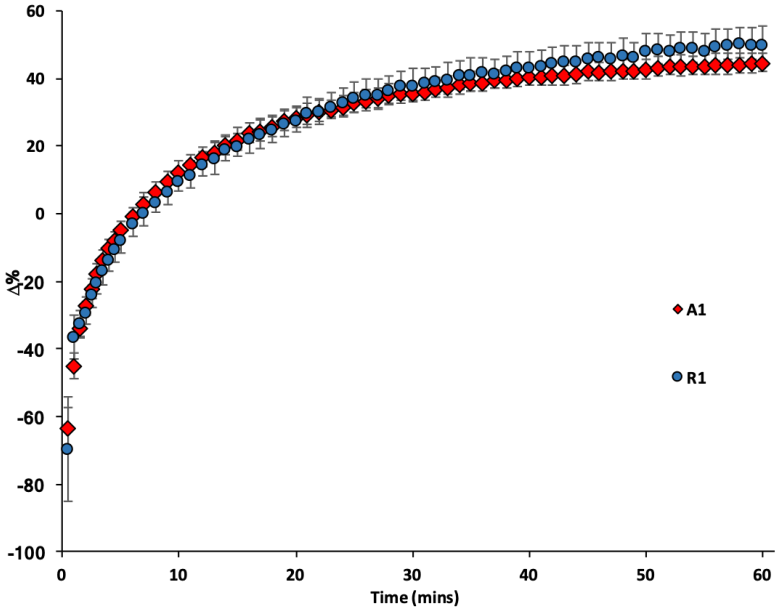

Figure 3.32 Comparison of 1 µL gels synthesised with MOR2 sensor strand only with 10 wt% AAm, 0.6 mol% MBA and 0.4 mol% MO (wrt AAm) and 1 wt% CNP in 0 mM NaCl, 1 mM PBS in 100 pM A1 (diamond, red) or R1 (circle, blue). Δ% and standard error of the mean calculated using equations 3.2a and b (n = 3).

To investigate the effects of DNA tethering, hydrogels were synthesised with only sensing strands (S1) and swollen in 100 pM analyte and random solutions (Figure

3.32). The swelling response in either solution was greater than those with MO crosslinks as the crosslink concentration was lower. There was no clear difference in response to analyte or random solutions, as either would be expected to hybridise with the sensing strand if no blocking strand were present. It would be expected that the hybridisation of analyte sequence to sensing strand would occur more rapidly than that of random sequence to sensing strand, however this is likely too small a difference to be detected in this system and would have to be investigated using UV spectroscopy or fluorescence.

3.4.3 Salt Sensitivity and Thermal Stability of MOCHs

As described previously, salt is required for DNA hybridisation to shield the charges of the phosphate groups in the backbone and prevent backbone repulsion between strands.[183] This salt causes damage during drying as it crystallises and limits the synthetic conditions available for DNA crosslinked systems.[319] MO-DNA hybridization has been shown to be possible with minimal salt present as the phosphate groups are replaced with uncharged phosphorodiamidate groups.[194] MO-MO interactions were therefore expected to be possible without salt. Figure 3.33 shows the effect of altering the NaCl concentration (0-300 mM) in solution on MOCHs (2 µL) synthesized with no salt.

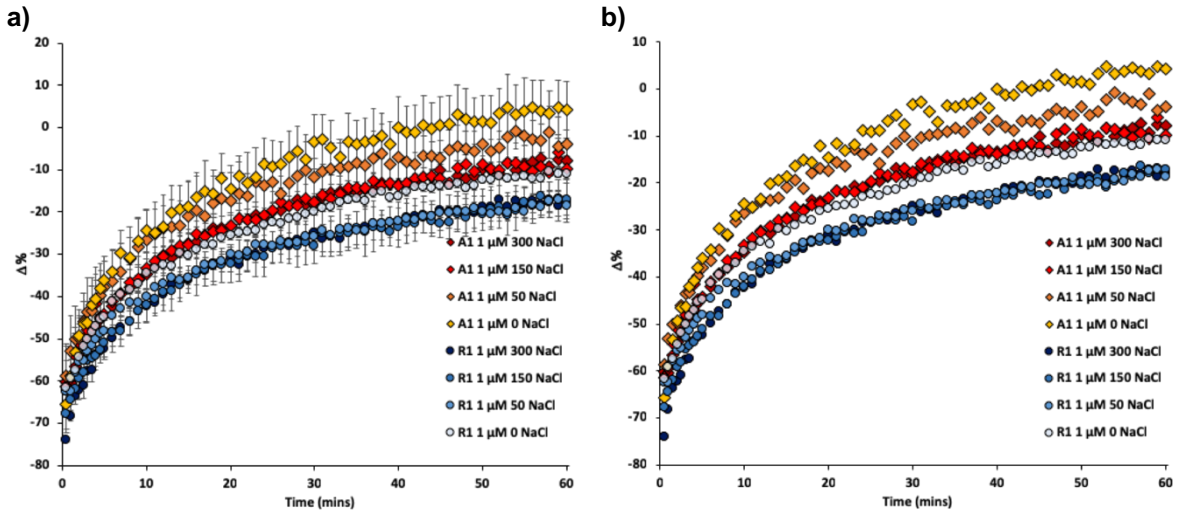

Figure 3.33 Comparison of swelling kinetics of MOR2 crosslinked hydrogels with 10 wt% AAm, 0.6 mol% MBA and 0.4 mol% MO crosslinks (wrt AAm) and 1 wt% CNP synthesised in 0 mM NaCl, 1 mM PBS swollen in 1 μM analyte (diamonds) or random (circles), 0 - 300 mM NaCl, 1 mM PBS. (a) Shows data with error bars showing standard error of the mean. (b) Shows data without error bars for improved clarity. Δ% and standard error of the mean calculated using equations 3.2a and b (n = 3).

As expected, gels synthesized without NaCl retain their sensing capability, indicating that the MO crosslinks remain intact. At each salt concentration, there is a clear differentiation and increase in swelling in A1 over R1. The greatest swelling response to both A1 and R1 occurred without NaCl. This is expected to be both due to the increased hydrophilicity and motility of DNA and that all charges from DNA strands that become tethered through interactions with S1 or B1 being unshielded. Above 50 mM the swelling response to both A1 and R1 are lowered. MOCHs offer a solution to salt sensitivity challenges of the anionic DNA crosslinked gels. Although salt is plentiful in human serum, removal is possible using simple methods, such as magnetic beads that can be used as part of an extraction protocol and would prevent any self-complementarity induced hairpin or self-dimerization that may occur with other miRNA sequences.[345] Removing salt during synthesis also enables the use of electrostatic additives that can otherwise aggregate and precipitate in the presence of counter ions, discussed further in Chapter 5.

Table 3.4 Predicted T_m of DNA or MO crosslinks and of sensor sequence interaction with test sequences used in Table 1. DNA-DNA crosslink calculated at 150 mM NaCl using Nearest Neighbor calculations.[168] MO-RNA interactions calculated and supplied by GeneTools. MO-MO interaction calculated using Equation 3.4. Crosslink displacement estimated by subtracting crosslink strength from sensor strand interaction with a given sequence.

Sensor Strand	Hybridisation Strand	T_m (°C)	ΔT_m (°C)
MIR2	Blocker	33	
MIR2	Analyte	66	33
MIR2	Random	18	-15
MOR2	Blocker (RNA)	66	
MOR2	Blocker (MO)	38	
MOR2	Analyte (RNA)	86	20_{RNA} / 48_{MO}
MIR2	A_{MM1}	65	33
MIR2	A_{MM5}	57	25

The use of DNA analogues with enhanced hybridisation strength is beneficial when targeting short sequences like miRNA. When the analyte sequence is only ~22 nts long, the blocker sequence must be long enough to be stable at room temperature and during synthesis, but not so strong that displacement is excessively slow. The use of more stable, high-GC, crosslinks is not always possible as the crosslink sequence will be dependent on the target sequence. Although blocking strand displacement is not the rate determining step when swelling dried gels here, the rate of displacement is the rate determining step in other systems.[259] Due to the lack of phosphate-backbone repulsion, MO-DNA interactions have a higher T_m than DNA-DNA, and similarly MO-MO interactions are expected to be equivalent or higher again. Table 3.4 shows the predicted thermal stability of the MOR2 crosslink compared to MIR2. The MO T_m was provided by Gene-Tools and is a prediction of MO-RNA hybridisation. Predicted MO-MO hybridisation of the sensing and blocking strand was calculated using Equation 3.4, though this is far less established than DNA predictive calculations.[204,294]

$$\boldsymbol{T_m = 1.9 \times (A + T) + 5.7 \times (G + C)}$$

Equation 3.4 Predicted MO-MO T_m in °C where A, T, G and C are the number of each respective nucleobase in the blocker strand sequence.

Figure 3.34 shows gel stability at or below 45 °C and apparent crosslink dehybridisation at 55 °C and above. This is a great improvement over MIR1 crosslinked gels, which exhibited elevated swelling at 25 °C and above. Although this does not fit either predicted MOR2 crosslink T_m (38 or 66 °C), predictions are never wholly accurate and are for oligonucleotides in solution. The crosslink will be affected by the incorporation into the gel, whereby the kinetic strain of swelling will influence crosslink breaking.[346,347] The importance of this temperature study is significant, as there is the possibility of a false positive result being obtained from a DNA crosslinked hydrogel due thermal dehybridisation at elevated temperatures. Furthermore, thermal stability will be vital to the manufacturing, storage and transportation of a developed sensor and can be used to reduce response time.[259]

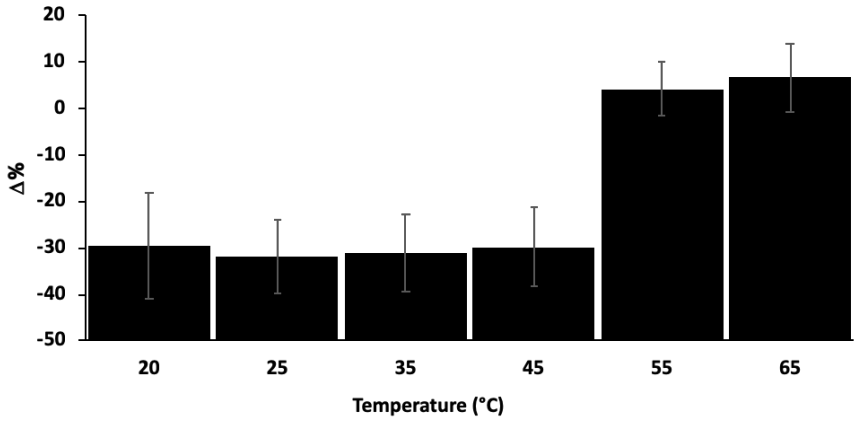

Figure 3.34 Thermal stability of MOR2 crosslinked gels with 10 wt% AAm, 0.6 mol% MBA and 0.4 mol% MO crosslinks (wrt AAm) and 1 wt% CNP prepared and then swollen in 0 NaCl, 1 mM PBS for 60 minutes at 20 – 65 °C. Δ% and standard error of the mean calculated using equations 3.2a and b (*n* = 3).

3.4.4 Optimised miR92a Detection and Portability Exemplification

The optical means of volume measurement used in this work is relatively basic. Were these MO functionalised polymers to be applied to biosensing, using a more sensitive transduction mechanism, may further increase sensitivity and would be the likely basis of a sensor technology built from MOCHs, ideally able to assess an array of gels simultaneously. A simple method to improve sensitivity would be to reduce the volume of material, thereby reducing the number of MO crosslinks required to break to achieve a measurable response. To investigate this, the hydrogel volume was reduced from 2 to 1 µL and the synthesis and swelling conducted with no NaCl as previously shown to maximum the swelling response by theoretically maximizing any charge related swelling from DNA binding (Figure 3.35).

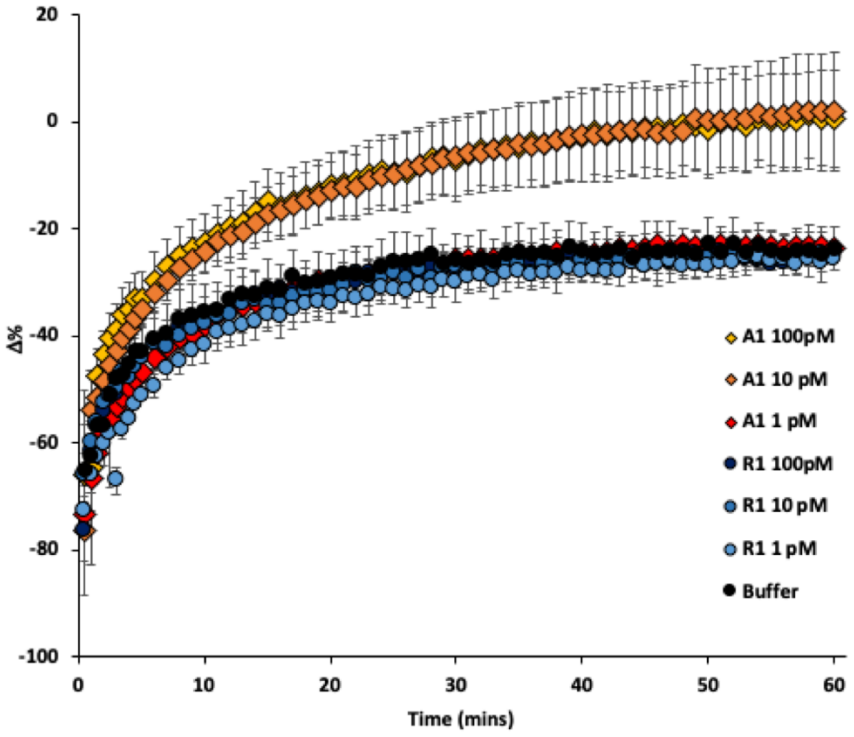

Figure 3.35 Comparison of swelling kinetics of 1 µL MOR2 crosslinked hydrogels with 10 wt% AAm, 0.6 mol% MBA and 0.4 mol% MO crosslinks (wrt AAm) and 1 wt% CNP synthesised in 0 mM NaCl, 1 mM PBS swollen in 1 – 100 pM analyte (diamonds), random (circles) or buffer only (black circles) 0 mM NaCl, 1 mM PBS. ∆% and standard error of the mean calculated using equations 3.2a and b (*n* = 3).

The LoD of the 1 µL no NaCl system was 10 pM, a 10-fold improvement over the 2 µL 150 mM NaCl system and a 1000-fold improvement over the original MIR1 system. As the swelling profile and difference in the % volume change was similar to that of the larger gels (2 µL) without salt swollen in 1 µM analyte and random solutions, a similar signal reduction at higher NaCl concentrations could be expected. Further reduction in volume is expected to further improve sensitivity but requires development of different deposition (i.e. inkjet printing) or more sensitive and precise transduction methods.

It is worth noting that the LoD is obtained using 5 mL solutions as required for accurate optical measurement. Ideally this volume would be reduced for improved practicality. A 1 µL gel prepared as described would have 5.6 nmol of MO crosslinks, assuming 100% conversion, while a 5 mL solution of 10 pM analyte would have 50 fmol of DNA strands. The ratio of solution DNA to crosslinks in shown in Table 3.5.

Table 3.5 The number of analyte or random moles in a 5 mL solution and the ratio compared to the moles of either 1 or 2 µl gels. The ratio of the LoD of MIR1 gels is underlined, while the ratio of the LoD for MOR2 gels is underlined and bold.

Concentration	DNA (mol)	DNA : 1 µL gel	DNA : 2 µL gel
10 µM	5×10^{-8}	8.9×10^{0}	4.4×10^{0}
1 µM	5×10^{-9}	8.9×10^{-1}	4.4×10^{-1}
100 nM	5×10^{-10}	8.9×10^{-2}	4.4×10^{-2}
10 nM	5×10^{-11}	8.9×10^{-3}	$\underline{4.4 \times 10^{-3}}$
1 nM	5×10^{-12}	8.9×10^{-4}	4.4×10^{-4}
100 pM	5×10^{-13}	8.9×10^{-5}	$\underline{\mathbf{4.4 \times 10^{-5}}}$
10 pM	5×10^{-14}	$\underline{\mathbf{8.9 \times 10^{-6}}}$	4.4×10^{-6}
1 pM	5×10^{-15}	8.9×10^{-7}	4.4×10^{-7}

The number of crosslinks based on 100% conversion is realistically an overestimation and crosslinks in more porous locations will not only have a larger influence on gel swelling capabilities but will also be the most readily accessible crosslinks for DNA

strands in solution. As such, not all of the crosslinks are expected to be broken to reach the critical change in swelling that is detectable within 60 minutes.

A simplified gel analysis to exhibit the potential portability and accessibility of MOCHs was developed using basic mobile technology. Single point swelling assessment was conducted using a smartphone with a rudimentary magnifier attachment and free image processing software (Figure 3.36).

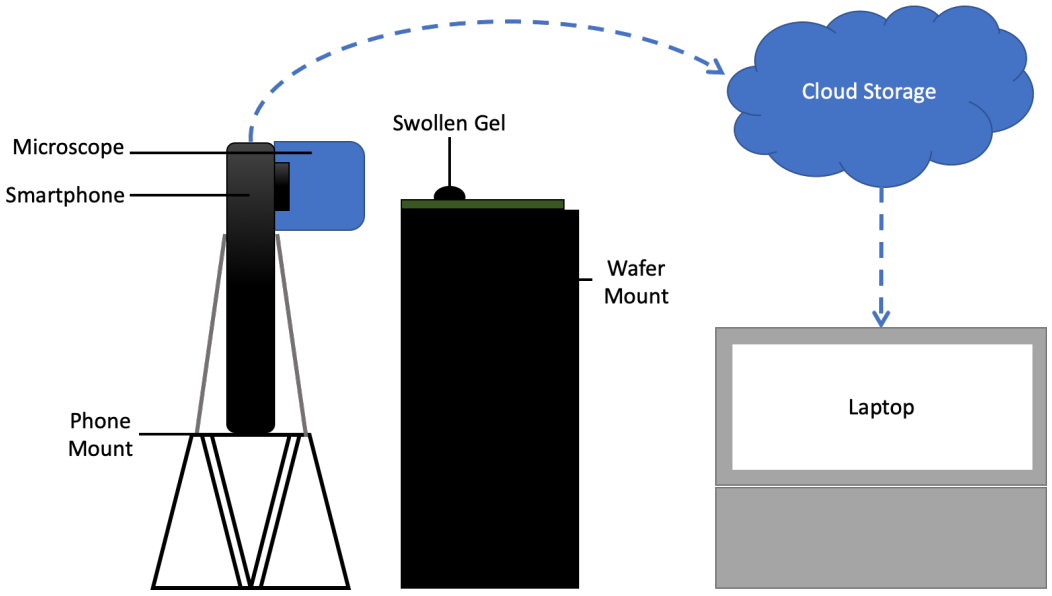

Figure 3.36 Illustration of portable gel analysis using mobile phone camera with a microscope magnifier attachment (x30 zoom) and cloud storage for data transfer to a laptop with appropriate image analysis software, in this case Digimizer[348]. Not to scale.

A typical cropped and analysed image of 1 µL MOCHs swollen in 10 pM A1 or R1 for 30 minutes is shown in Figure 3.37a. Image analysis yields only the gel area (mm^2) rather than a calculation of gel volume, yet suffices for differentiation between A1 and R1 solutions. Consistent vertical and horizontal sample positioning is essential, yet the use of smartphone facilitates rapid data gathering and development of bespoke software may be used to automate and increase the rate of analysis. While further refinement is required to improve the reliability and accuracy of the processing, this portable method suffices for outreach or demonstration of oligonucleotide sequence detection using MOCHs.

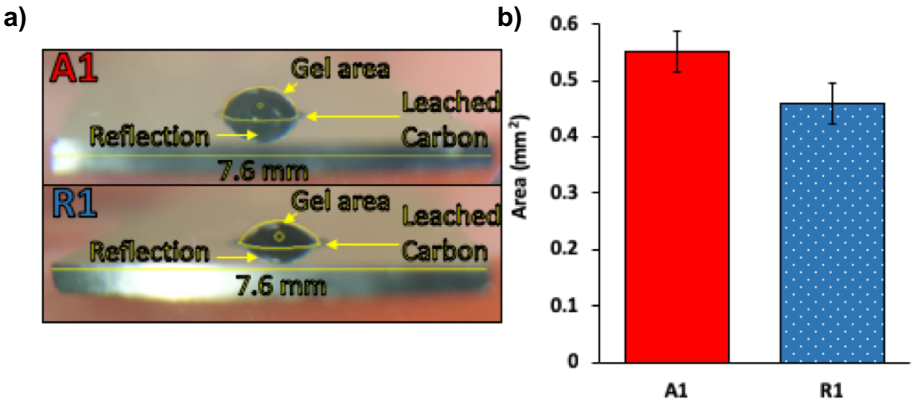

Figure 3.37 (a) Analysed images of 1 µL MOR2 crosslinked hydrogels with 10 wt% AAm, 0.6 mol% MBA and 0.4 mol% MO crosslinks (wrt AAm) and 1 wt% CNP synthesised in 0 mM NaCl, 1 mM PBS swollen in 10 pM analyte (A1, top) or random (R1, bottom) in 0 mM NaCl, 1 mM PBS. Analysis conducted in Digimizer[348] (b) Swollen area at 30 minutes in A1 or R1 (10 pM) from mobile images. Standard error of the mean calculated using equations 3.2b (n = 3).

Simple improvements to the imaging and analysis process may improve reliability. For example, a mount engineered to hold each silicon wafer in position and a corresponding camera mount able to maintain the relative camera position would improve the sampling speed. Use of bespoke software could further improve analysis, calculating volume rather than area. In this case the software was chosen as the mobile phone image compression could not be accessed in the bespoke software used throughout this thesis, with the added benefit of being free software. Automated image transfer and analysis could be developed but would only be useful for demonstrative purposes.

3.4.5 Errors and Accuracy

Throughout the presented optical data error bars have shown the standard error of the mean. With the exception of APT1 and APT2 kinetic swelling, where measurement was disrupted by particulates in the swelling solution, the errors have predominantly been from inaccuracies and gel-to-gel variation introduced during synthesis. The largest SEM in each case is always during the early stages of swelling as this is when the greatest rate of swelling is occurs, so any differences are accentuated. As well as this, early time points were used to ensure gels were appropriately in focus, meaning

some added variation in image quality will affect these measurements (typically at most 1 minute).

The pregel droplet deposition conducted using a P2 micropipette, the systematic error of which is ± 0.03 µL when pipetting 2 µL, equating only ± 1.5 % volume change. The viscosity noted in particular when pipetting crosslinks with higher nt content could result in a thin residual film on the inside wall of the tip, which, despite pre-rinsing or reverse pipetting, would results in lower accuracy and precision. Furthermore, the mixture of CNP within the pregel solution was not a stable dispersion and would begin to aggregate and precipitate as soon as agitation ceased. The depth and speed of pipetting from the pregel solution would therefore to some degree vary the composition, as an aliquot containing more CNP would containing less of the monomers and would subsequently photoinitiate and polymerise differently. The droplet location and spreading were also dependent on pipetting accuracy and would influence the measured volume as the gel distance from the wafer edge used for scale during analysis would affect the calculated volume.

Deposition location is also paramount to accurate analysis. The optical analysis is reliant on using the wafer edge for scale, despite the gel being further from the camera than the edge of the wafer. The distance of the gel from the edge of the wafer therefore contributes to either over- or underestimation of gel volume. Of 24 imaged gels, the average distance was 2.55 mm from the wafer edge, with an imprecision of 9.3 %.

Table 3.6 Measured circularity, aspect ratio and roundness of 17 gels calculated using Equations 3.5 a, b and c respectively. Analysis conducted in ImageJ.

	Circularity	Aspect Ratio	Roundness
Average	0.72	1.07	0.94
Standard Deviation	0.09	0.05	0.04

a) $$Circularity = \frac{4\pi \times Area}{Perimeter^2}$$

b) $$Aspect\ Ratio = \frac{Maximum\ Axis}{Minimum\ Axis}$$

c) $$Roundness = \frac{4\pi \times Area}{\pi \times Maximum\ Axis^2}$$

Equations 3.5 Measurements conducted in ImageJ where an ellipsis applied to gel shapes were used to calculate the area, diameters and perimeter in pixels. (a) Calculation of circularity, where circularity of 1.0 would indicate a perfect circle. (b) Aspect ratio of the length of maximum and minimum ellipsis axes. (c) Calculation of roundness, which compares the gel shape to that of a perfect circle.

Similarly, the volume calculation assumes each gel droplet is perfectly circular, such that the diameter measured from a single angle is consistent throughout. In reality, the circularity, aspect ratio and roundness all indicate the droplets are non-uniform (Table 3.6). As such, the diameter measured by the camera does not reflect that of the whole gel and imaging from multiple different angles, or alternative transduction methods, would be required for more accurate analysis. A hydrophobic parylene mask was available but was not used as it was larger than the droplet diameter and offered minimal, if any, improvements of precision.[349] All of these issues could be improved upon or solved through the use of inkjet printing[283] and use of an appropriately designed hydrophobic mask (Chapter 5).

3.5 Conclusions and Ongoing Challenges

This chapter discussed the use of optical transduction of DNA crosslinked hydrogels to exemplify crosslink designs able to detect the miRNA sequence of miR92a, aptamer crosslinks able to detect adenosine and sRNA sequence detection. Sensing technology developed using this material could therefore be readily adapted to detect a variety of miRNA or sRNA sequences, as well as proteins, heavy metals or small molecules using aptamer-based crosslinks.

The use of DNA resulted in challenges related to the charged backbone and viscosity of pregel solutions manifested as detachment from the wafer substrate or malformed hydrogels and these challenges were exacerbated when using larger DNA crosslinks for aptamer use or sRNA detection. Some control was achieved through intelligent design using minimal blocking strands and tri-functionalised crosslinks.

Concerns of crosslink thermal dehybridisation limited alternative methods of synthesis as elevated temperature or low salt concentrations would non-specifically break the short crosslinks. Attempts at improving photoinitiation, redox initiation and thermal initiation were unsuccessful due to the CNP required for contrast and electrical measurements absorbing UV, inefficient mixing and gel frailty.

The removal of non-essential nucleotides from the MIR1 crosslink for miR92a sequence detection (MIR2) resulted in a reduction of overall swelling and detachment while maintaining the extent of differential swelling. Optimisation of AAm, MBA and DNA concentrations in MIR2 crosslinked hydrogels offered no improvements for optical transduction. Increased MBA concentrations reduced differential swelling and increased detachment, increased DNA concentration reduced gel integrity, while increased AAm reduced detachment but also differential swelling.

A novel MO crosslinked hydrogel system was developed to remove or reduce the issues of thermal stability, salt dependency and anionic charge associated with DNA crosslinks. Selective and specific swelling was observed as with DNA gels in the presence of an analyte DNA sequence with mismatch discrimination, to a 100-fold improved sensitivity of 100 pM. This was further enhanced through halving the hydrogel volume and removing salt from both synthesis and testing to maximise swelling, resulting in a limit of detection of 10 pM. The improved thermal stability coupled with the diminished salt sensitivity suggest significant promise for MOCHs as a more stable and controllable alternative to DNA-based responsive hydrogel systems and facilitate alternative synthesis methods previously unavailable to DNA-crosslinked materials.

Although the advantageous features of DNA crosslinked hydrogels and MOCHs has been explored, the method of optical transduction method employed remains rudimentary. Far more accurate means of optical transduction methods have been

developed, not least by Stokke *et al.* The limitation of many of these remains multiplexing and the use of a multi-array would be required for accurate diagnosis using miRNA fingerprinting. Further optimisation of MOCHs, and their swelling response transduction method, could be used to increase sensitivity to biologically relevant concentrations and be developed into clinically relevant biosensor systems. Simultaneously, the MO crosslink can be easily translated into established DNA crosslinked systems such as nanoparticles, electrochemical sensors or DNA nanotechnology for similar improvements.

Chapter 4 Oligonucleotide Crosslinked Polymer Composites

4.1 DNA Crosslinked Polymer Composites

4.1.1 miR92a Sequence Detection Optimisation

Preliminary efforts to develop oligonucleotide crosslinked polymer composites were again conducted by Dr Ferrier.[81,227] By incorporating appropriate amounts of conductive particles into the DNA crosslinked hydrogel discussed previously, electrical means of transduction were evaluated. Comparison of carbon nanopowder (CNP), micropowder, and graphite identified percolation thresholds for each in polyacrylamide (0.6, 0.2 and 0.1 wt% respectively) when dried while carbon nanotubes (CNT) failed to gel appropriately. Although all conductive fillers had elements of inconsistency in gel resistance changes when swelling, CNP appeared to be the most reliable.

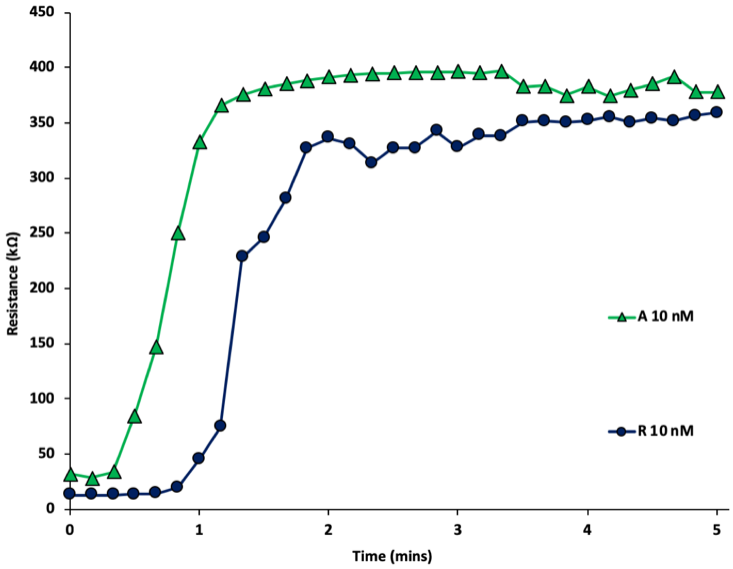

Figure 4.1 The d.c. resistance of MIR1 crosslinked hydrogels with 10 wt% AAm, 0.6 mol% MBA and 0.4 mol% MIR1 DNA crosslinks (wrt AAm) and 2 wt% CNP in A1 or R1 at 10 nM in 150 mM NaCl, 1 mM PBS at 23 °C. Data shown was collected by Dr Ferrier. Standard error of the mean calculated using equation 3.2b (A1 n = 5, R1 n = 4).

Simple d.c. resistance could transduce the swelling of hydrogels from dried states. Within three minutes analyte solutions could be differentiated from random solutions *via* differences in both resistance transition rate and end resistance values. Using this method, a LoD of 10 nM was achieved (Figure 4.1). There were no redox contributions from the composite or the electrodes apparent from cyclic voltammetry measurements, suggesting that the d.c. measurements were not influenced by undesired reactions of the polymer or electrode during testing.

Within the resistance data at 10 nM there is substantial deviation between repetitions (Figure 4.2a). Samples were immersed in solution after one minute of measurement in air (data not shown) and measurements occurred every 10 seconds. Therefore, time points may be at most 10 seconds earlier than reported. All rate differences observed are greater than 10 seconds. Of the data used in analyte response, sample 1 began at more than 2 standard deviations higher resistance than the remaining 4 repeats and if discounted improves the precision of the average (Figure 4.2b).

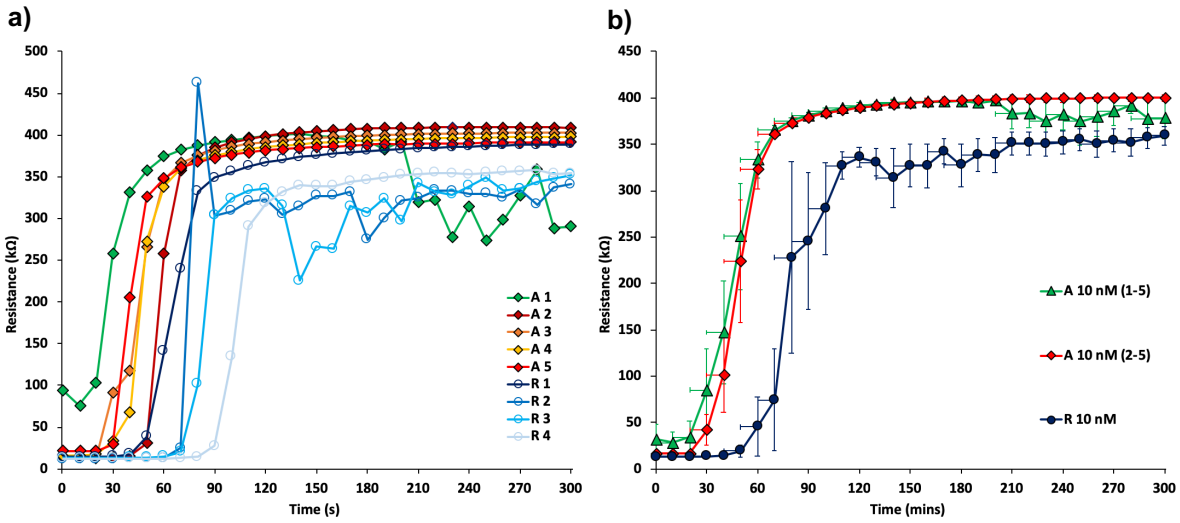

Figure 4.2 The d.c. resistance of MIR1 crosslinked hydrogels with 10 wt% AAm, 0.6 mol% MBA and 0.4 mol% MIR1 DNA crosslinks (wrt AAm) and 2 wt% CNP in A1 or R1 at 10 nM in 150 mM NaCl, 1 mM PBS at 23 °C. (a) Individual resistance profiles of each gel (b) Published (A 10 nM (1-5) and R 10 nM) and updated (A 10 nM (2-5)) averages. Data shown was collected by Dr Ferrier. Standard error of the mean calculated using equation 3.2b (A 10 nM (1-5) n = 5, A 10 nM (2-5) and R1 n = 4).

The random sequence measurements exhibit a number of artefacts observed occasionally during testing. Sample 2 shows an elevated resistance at 80 seconds

which appears as a spike due to the rapid increase followed by rapid decrease in resistance. This only occurs during the rapid resistance increase in within the first two minute of swelling and is believed to be caused by the auto-ranging of the multimeter overestimating the required change in current. The second type of artefact is seen in both samples 2 and 3, whereby the resistance fluctuates by up to 100 kΩ down from the plateaued resistance value. This is theorised to be caused by movement of unentangled CNP, aggregates or polymer composite, either flowing through the hydrogel or affected by rearrangement of the gel network, causing an increase in conductive particle density which reduces resistance. These artefacts can be overcome with a large enough sample size and should be alleviated with appropriate hardware and software.

A wider range of DNA concentrations raised some concentration dependent inconsistencies (Figure 4.3). At 1 μM and 10 nM the analyte solution may be clearly differentiated from the random solution, albeit with the random 1 uM solution exhibiting anomalously low resistance. However, both 10 μM and 1 nM solutions are unable to reliably differentiate between analyte and random by end point resistance. As the optical LoD for MIR1 gels was 10 nM, it can be assumed that in 1 nM the response to analyte strands is not great enough to elicit a response.

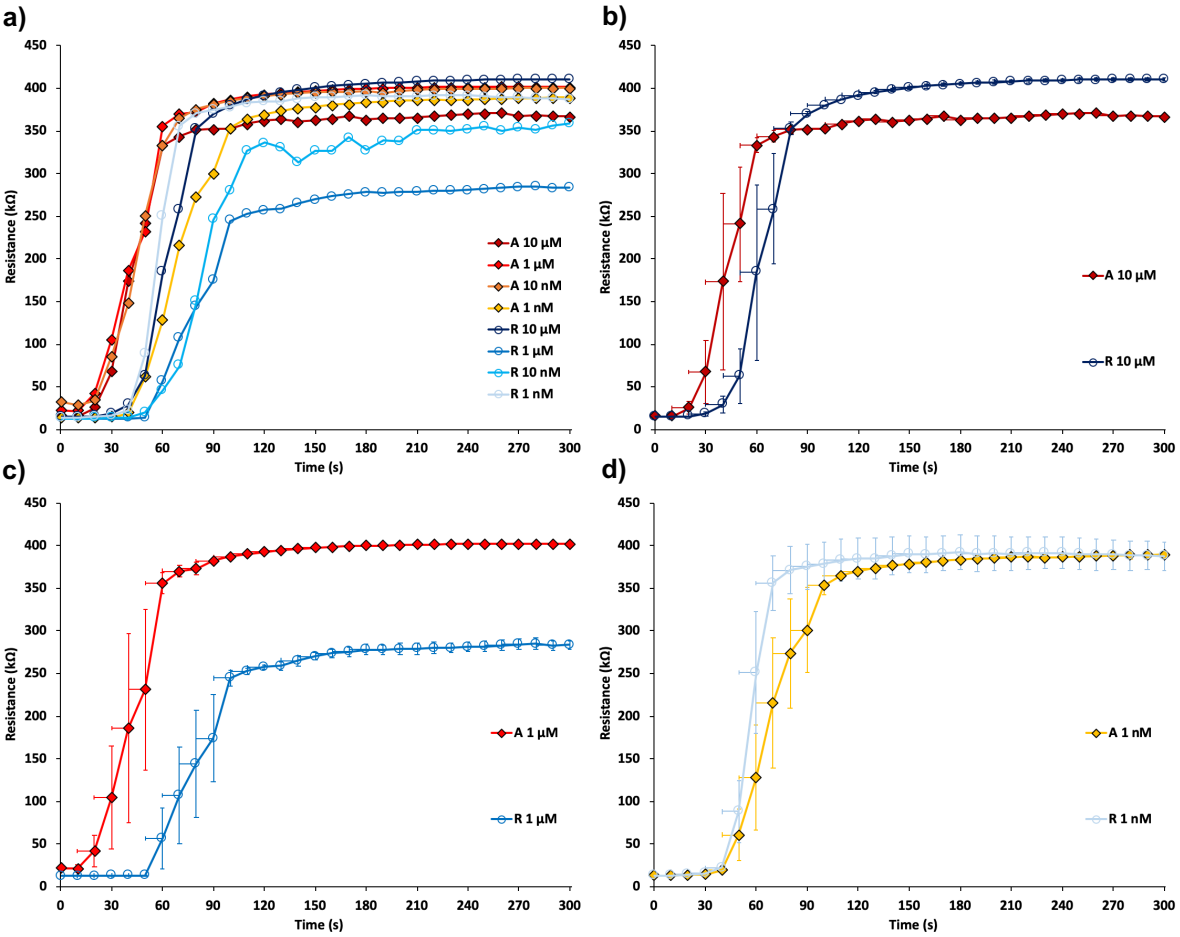

Figure 4.3 The d.c. resistance of MIR1 crosslinked hydrogels with 10 wt% AAm, 0.6 mol% MBA and 0.4 mol% MIR1 DNA crosslinks (wrt AAm) and 2 wt% CNP in A1 or R1 at (a) 10 µM - 1 nM, (b) 10 µM, (c) 1 µM, (d) 1 nM in 150 mM NaCl, 1 mM PBS at 23 °C. Data shown was collected by Dr Ferrier. Standard error of the mean calculated using equation 3.2b (n = 5).

The remaining inconsistencies were attributed to solution DNA effects, suggesting that the localised analyte or random strands in the gel would contribute to conductivity so that higher concentrations of DNA would cause lower resistance values.[350] However, the expected trend if this was correct was not apparent as the 10 µM random solution exhibited the highest resistance of all (Figure 4.4). If solution DNA is affecting the resistance of the system, it cannot be reliably quantified due to the inconsistencies of the measurement method.

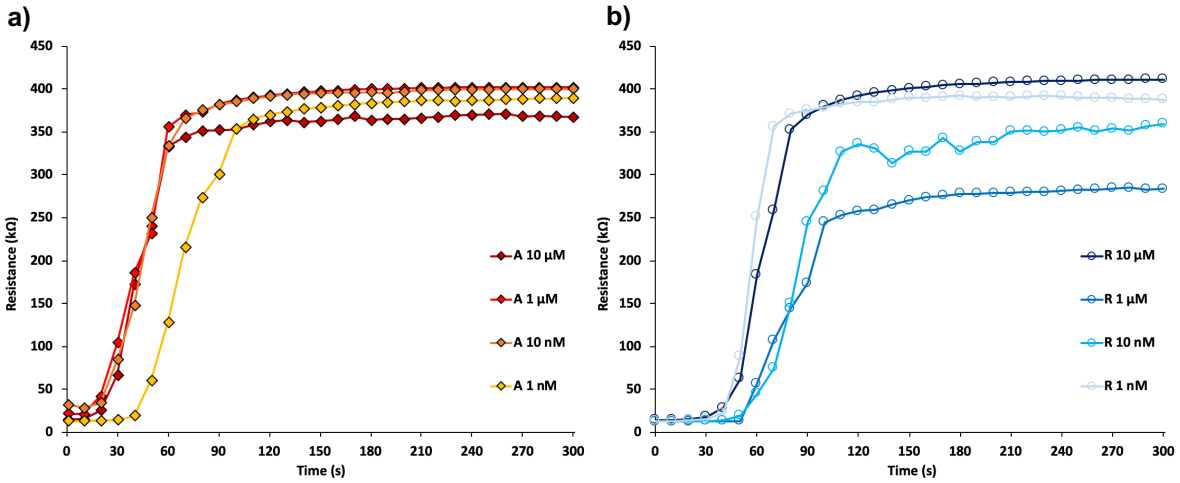

Figure 4.4 The d.c. resistance of MIR1 crosslinked hydrogels with 10 wt% AAm, 0.6 mol% MBA and 0.4 mol% MIR1 DNA crosslinks (wrt AAm) and 2 wt% CNP in (a) A1, (b) R1 at 10 µM - 1 nM in 150 mM NaCl, 1 mM PBS at 23 °C. Data shown was collected by Dr Ferrier.

The standard error of the mean for samples swollen in analyte when maximum resistance is reached is minimal, whereas the random response appears far less precise. As end point resistance may be influenced by DNA concentration and both 10 µM and 1 nM random solutions would give false positives, the rate to maximum resistance may be a more reliable signal and reduce effects from sample variation (Figure 4.5a). All analyte concentration above 10 nM respond earlier than random at any concentration. The fastest random concentration response was 1 nM random solution, which was not as quick as the analyte response. The change from percolating to non-percolating occurs rapidly in less than a minute for all samples, aside from the anomalous 1 nM random solution (Figure 4.5b). As such, rather than the 3-minute time to result suggested previously, the resistance value at 1 minute may better differentiate analyte and random solutions. At 1 minute, for each concentration above 10 nM, the resistance increase in analyte is far greater than that in random solutions.

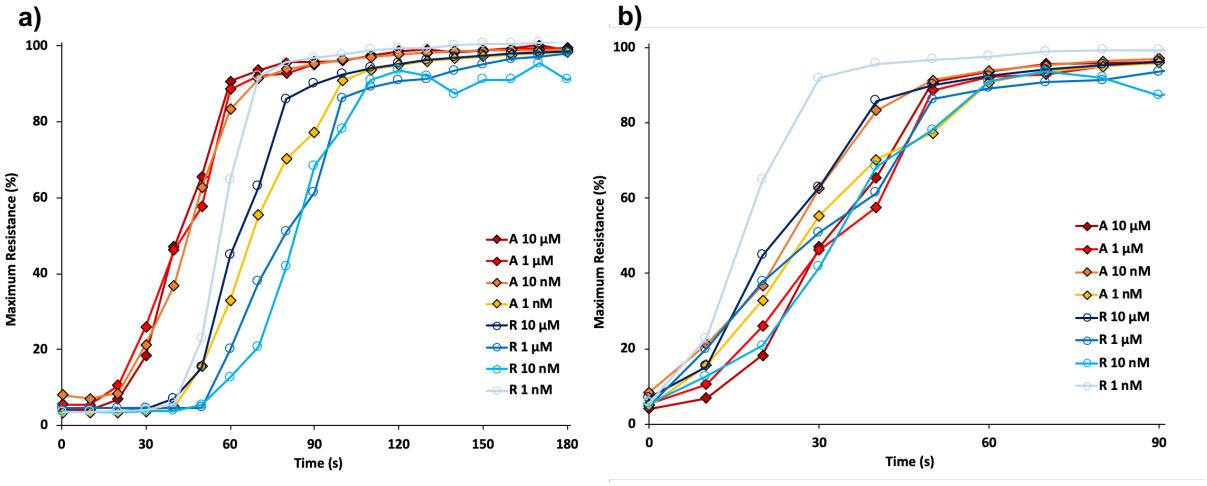

Figure 4.5 The time to maximum d.c. resistance of MIR1 crosslinked hydrogels with 10 wt% AAm, 0.6 mol% MBA and 0.4 mol% MIR1 DNA crosslinks (wrt AAm) and 2 wt% CNP A1 or R1 at 10 µM - 1 nM in 150 mM NaCl, 1 mM PBS at 23 °C. (a) Time to maximum d.c. resistance after immersion in solution (b) Time to maximum d.c. resistance after initial increase in resistance. Data shown was collected by Dr Ferrier.

For all these potentially positive results, reproducibility remains an issue. Despite theorising reasons for the trends seen, outliers remain at both high and low concentrations of DNA and batch to batch variation may account for any or all of the results seen. In particular, it is difficult to investigate what is causing the change in resistance, as the resistance values are not dependent on the gel volume (Figure 4.6). Potential causes of inconsistency are discussed more thoroughly in Section 4.3.

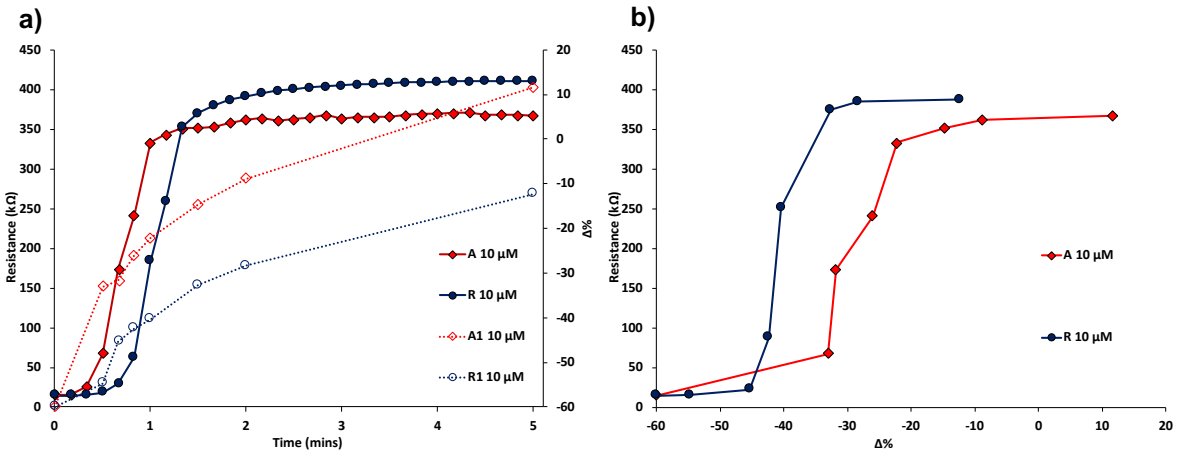

Figure 4.6 (a) The d.c. resistance (solid) compared to the swollen volume (hollow, dotted) (b) the d.c. resistance vs the swollen volume of MIR1 crosslinked hydrogels with 10 wt% AAm, 0.6 mol% MBA and 0.4 mol% MIR1 DNA crosslinks (wrt AAm) and 2 wt% CNP in A1 or R1 at 10 µM in 150 mM NaCl, 1 mM PBS at 23 °C. Data shown was collected by Dr Ferrier. Δ% calculated using equation 3.2a.

Despites the relatively successful results, improvements were required to develop an appropriate and reliable sensor. In particular, delamination of the gel from the electrode surface occurred in approximately 40 % of samples. This was primarily seen in DNA crosslinked gels only, rather than gels only crosslinked with MBA, suggesting that it was related to the hydrophilicity of the gel, the repulsion of the DNA strands from the electrode or a combination of both. For the purposes of this discussion, detachment refers to clear visible detachment of the gel or part of the gel from the wafer, whereas delamination refers to detachment of the gel from the platinum electrode only (Figure 4.7). While detachment will obviously involve some degree of delamination, the difference is used to distinguish when gel resistance values are at 3-4 MΩ or higher, rather than the 300-400 kΩ expected for swollen polyacrylamide–CNP composites. When this occurs, visual inspection does not always indicate detachment. As such, delamination refers to effects observed only through electrical measurements. Any samples reporting MΩ resistance were discarded.

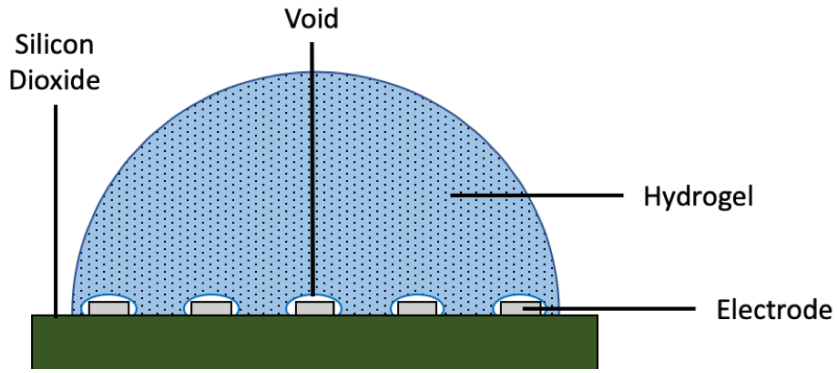

Figure 4.7 Illustration of a potential mechanism of delamination. The hydrogel is attached only to the functionalised silicon dioxide wafer surface. As swelling occurs, the lack of attachment to the platinum electrodes may allow the hydrogel to swell away from the electrode surface, leaving only a void containing solution in contact. Not to scale.

In an effort to address delamination and reproducibility issues, the shorter MIR2 crosslink was investigated. The reduction in crosslink length, and thereby charge density, would be expected to reduce both the gel hydrophilicity and any repulsion effects. As the optical transduction results had indicated that there had been a reduction in detachment in transitioning from MIR1 to MIR2 crosslinks, a reduction in

delamination may be also be expected. The resistance changes when swollen in 10 μM of analyte or random sequence solutions is shown with the swelling profile in Figure 4.8. Two issues are evident from this data. Firstly, the resistance values are still unrelated to the swollen volume, albeit simultaneous monitoring of a gel through both optical and resistance measurements was not possible. Secondly, the selective difference in resistance rate increase and end point seen when using MIR1 crosslinked gels was not observed with MIR2 crosslinks.

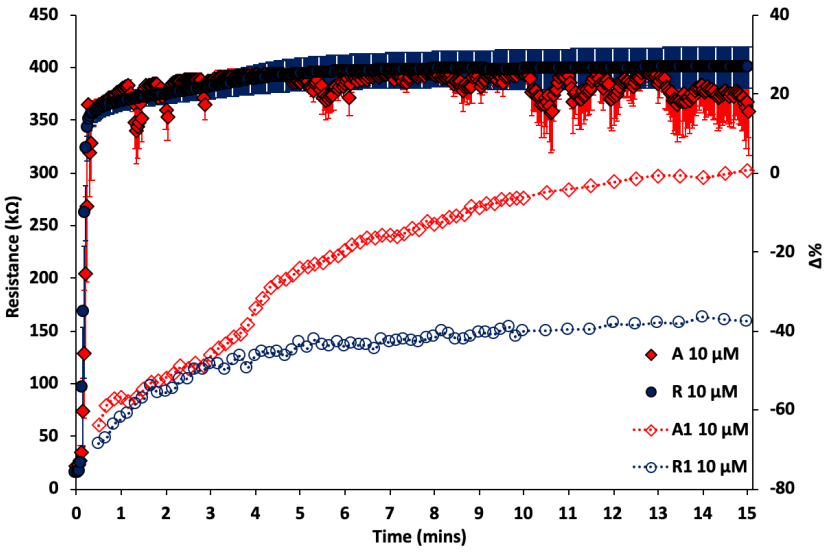

Figure 4.8 The d.c. resistance (solid) compared to the swollen volume (hollow, dotted) of MIR1 crosslinked hydrogels with 10 wt% AAm, 0.6 mol% MBA and 0.4 mol% MIR2 DNA crosslinks (wrt AAm) and 2 wt% CNP in A1 or R1 at 10 μM in 150 mM NaCl, 1 mM PBS at 23 °C. Data shown was collected by Alex Carroll. Δ% and standard error of the mean calculated using equations 3.2a and b (n = 3).

As mentioned previously, the percolating state of these polyacrylamide-CNP composites is only achieved when gels are dried or at the very earliest stages of swelling. Therefore, the transition from percolating to non-percolating state caused by the conductive particle density decreasing as the polymer swells, must occur at the earliest stages of swelling. Swelling beyond this point is then inconsequential to the resistance values measured. Ideally all extents of swelling could be transduced through this electrical measurement to maximise sensitivity and reliability. To achieve this goal using conductive particles as fillers would require a much higher degree of particle encapsulation within the polymer. Polyacrylamide is a porous polymer and the

hydration of these pores is integral to the hydrogel's swelling capabilities. In a composite material with only non-covalent attachment, some of the conductive particles may be entrapped within the polymer chains' entanglement, while some particles are only adsorbed to the polymer or trapped within the pores (Figure 4.9).[273] Although pores may be closed, inaccessible, hydrogels are extremely porous so the majority of pores will be connected to other pores, and thereby connected to the exterior of the material.[351] The resistance profile is then related to not only the polymer swelling, but also the flow of particles through these pores during polymer hydration. The leaching of CNP out of the hydrogel when swelling indicates that particle movement must be occurring. After swelling, the hydrogel remains black, meaning some CNP must remain entrapped in the hydrogel.

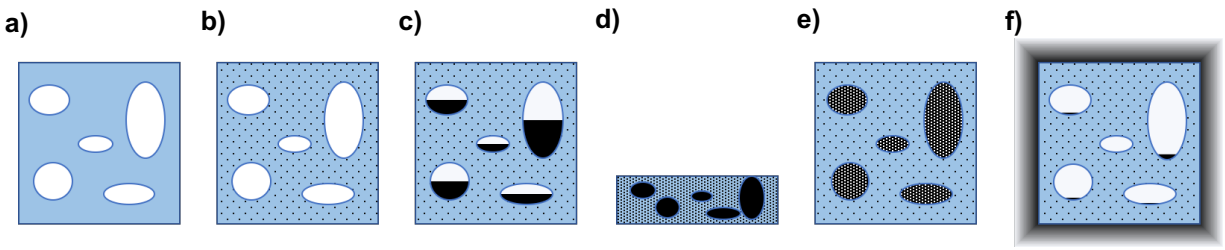

Figure 4.9 Illustration of potential influence of porosity on material homogeneity. (a) Porous hydrogel (b) Conductive particles incorporated into hydrogel through entanglement (c) Higher concentrations of conductive particles where excess particles collect in pores (d) Dried gel exhibiting highest density of conductive particles (e) Reswollen gel creating agitation of non-entangled conductive particles within pores (f) Conductive particles not entangled within hydrogel are able to migrate through the open pores and leach from the material into surrounding solution.

Reducing the particle movement through the network may make the electrical measurement more relatable to the gel swelling. This would be expected to elongate the sensor response time, however, the issues with reliability and delamination must be addressed. Response time may be reduced once a sensor is validated through simple means such as volume reduction. Increased MBA crosslink density was investigated to increase the network density and reduce porosity in an effort to slow CNP movement and potentially increase entrapment, as well as reduce delamination (Figure 4.10).

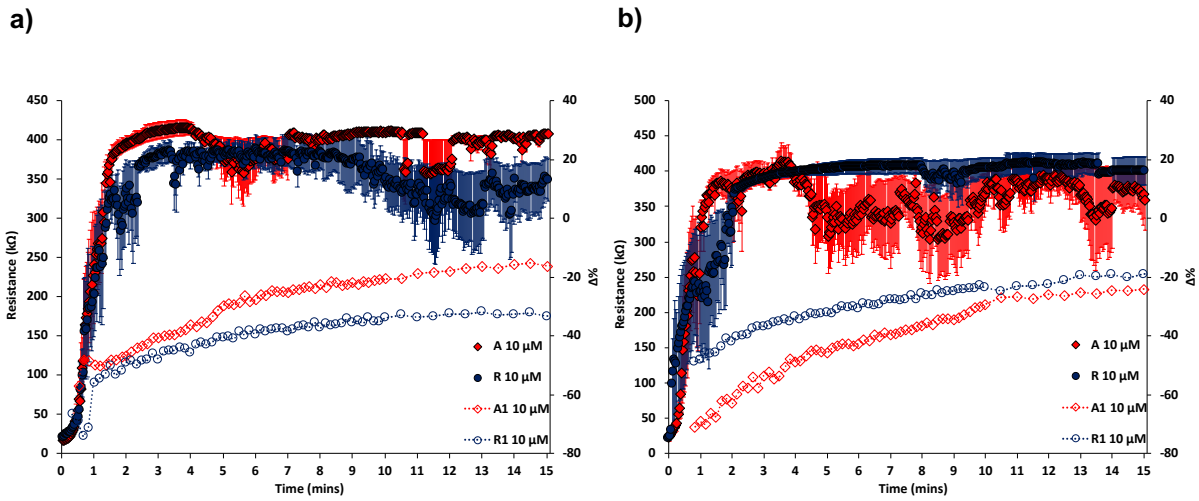

Figure 4.10 The d.c. resistance (solid) compared to the swollen volume (hollow, dotted) of MIR1 crosslinked hydrogels with 10 wt% AAm, 0.4 mol% MIR2 DNA crosslinks and (a) 1.0 mol% (b) 1.5 mol% MBA (wrt AAm) and 2 wt% CNP in A1 or R1 at 10 µM in 150 mM NaCl, 1 mM PBS at 23 °C. Data shown was collected by Alex Carroll. Δ% and standard error of the mean calculated using equations 3.2a and b (n = 3).

Both 1.0 and 1.5 mol% MBA increased the time to reach maximum resistance, from 30 seconds to 90 seconds, when compared to the 0.6 mol% gels. This follows the optical swelling which was also slowed by higher crosslink density. Differentiation between analyte or random solutions was not possible with either higher crosslinked system and resistance remains unrelated to swollen volume. Increased crosslinker also caused more variation between measured resistance. The increased gel density and porosity would be expected to slow CNP particle movement and a decrease in resistance may occur if this movement results in an increased density of conductive particles.

As with the optical transduction, 20 wt% AAm gels were again investigated to increase network density to further investigate the influence of gel density (Figure 4.11). Despite the lack of optical differentiation, there was a clear difference in resistance between analyte and random solutions, both in terms of rate of increase and maximum resistance. The random response at 0.6 mol% MBA is substantially different to the typical resistance profile, taking 5 minutes to plateau after the initial disruption of percolation. The random response at 1.0 mol% MBA exhibited a mixture of the slow resistance increase and the typical rapid increase, both of which plateaued to 350 kΩ which remained less than the analyte response which plateaued at 400 kΩ.

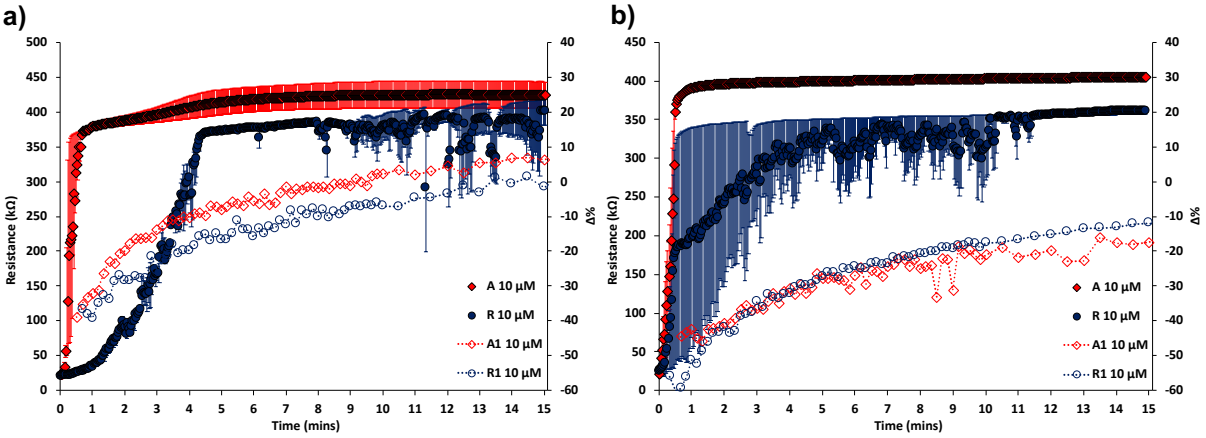

Figure 4.11 The d.c. resistance (solid) compared to the swollen volume (hollow, dotted) of MIR2 crosslinked hydrogels with 20 wt% AAm, 0.4 mol% MIR2 DNA crosslinks and (a) 0.6 mol% (b) 1.0 mol% MBA (wrt AAm) and 2 wt% CNP in A1 or R1 at 10 µM in 150 mM NaCl, 1 mM PBS at 23 °C. Data shown was collected by Alex Carroll. Δ% and standard error of the mean calculated using equations 3.2a and b (n = 3).

The slower resistance change was not exclusive to 20 wt% AAm gels and not exclusive to the response in random solution. Samples prepared by Dr Ferrier using CMP or graphite in place of CNP also resulted in some slower resistance increases, as a larger particle will take longer to move through the hydrogel pores. Samples with higher MBA gels also exhibit occasional slow resistance change, with frequent decreases despite overall increasing resistance (Figure 4.12a). Unfortunately, 20 wt% AAm gels also exhibited slow resistance changes when swollen in analyte solution, albeit with far more variation than the response to the random sequence solution (Figure 4.12b). Inconsistencies are likely due to issues and variation during synthesis. Despite results indicating that 20 wt% AAm gels could improve electrical transduction and differentiation between analyte and random, the increased material density effectively doubled the cost and further testing was not possible to due limited material.

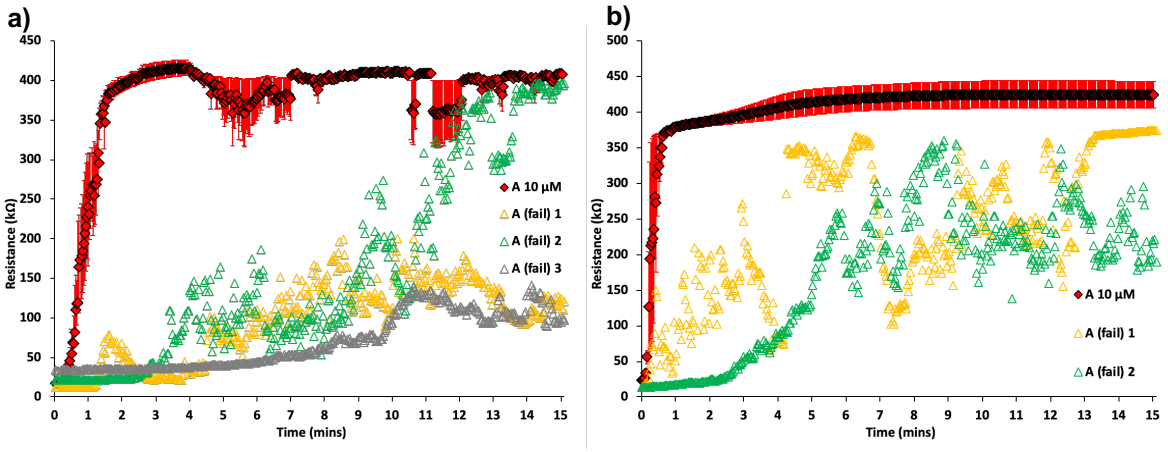

Figure 4.12 Examples of atypical d.c. resistance profiles (hollow, triangles, (fail)) compared to the average of typical profiles (red, diamonds). (a) 10 wt% AAm, 1.0 mol% MBA and 0.4 mol% MIR2 DNA crosslinks (wrt AAm) and 2 wt% CNP (b) 20 wt% AAm, 0.6 mol% MBA and 0.4 mol% MIR2 DNA crosslinks (wrt AAm) and 2 wt% CNP. Swollen in A1 (10 µM) in 150 mM NaCl, 1 mM PBS at 23 °C. Data shown was collected by Alex Carroll. Standard error of the mean calculated using equation 3.2b (n = 3).

The results from increased gel density *via* either MBA or AAm increase would add credence to the theory that CNP movement rather than gel swelling is the major source of resistance change. For electrical transduction the electrodes are placed vertically into a solution of analyte of random DNA (Figure 4.13). After swelling, some amount of CNP is typically visible at the bottom of the 1.5 mL microcentrifuge tube (Figure 4.13c). This CNP leaching reduces the CNP content of the composite and contributes to the inconsistencies in the material resistance. Higher density gels resulted in less visible leaching, although this was not quantified.

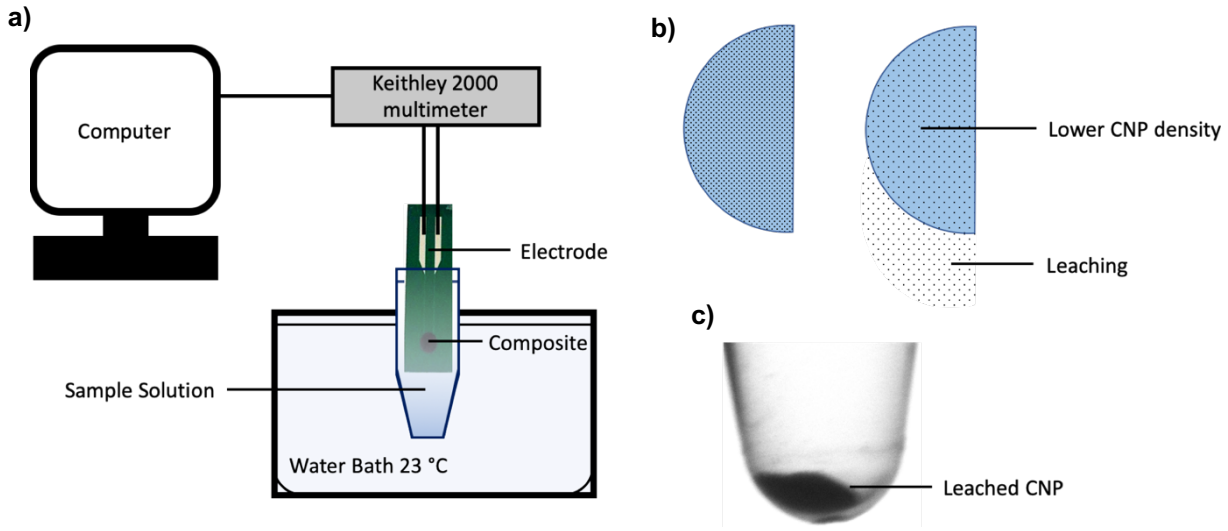

Figure 4.13 (a) Illustration of the electrical measurement set-up. The electrode being tested is connected to the Keithley 2000 multimeter (d.c.) which is connected to a computer *via* USB cable. The electrode is suspended vertically in a microcentrifuge tube containing the sample solution. The computer utilises LabView to control and collect data. (b) Illustration of leaching during vertical swelling of composite. (c) Example of leached material collected at the bottom of the microcentrifuge tube after vertical swelling of APT2 crosslinked hydrogels with 10 wt% AAm, 0.6 mol% MBA and 0.4 mol% APT2 DNA crosslinks (wrt AAm) and 2 wt% CNP in 150 mM NaCl, 1 mM PBS at 23 °C.

CNP leaching also occurs if gels are unwashed before optical transduction (Figure 4.14). In this case gels are swollen horizontally, yet CNP leaching still occurs. In part, this will be due to the flow of water as it is poured into the beaker containing the gels, which may flush loose CNP out of the gel matrix. CNP leaching invalidates the measured volumes of the gels, but illustrates the speed at which CNP movement occurs, far more akin to the rapid response of the resistance measurements.

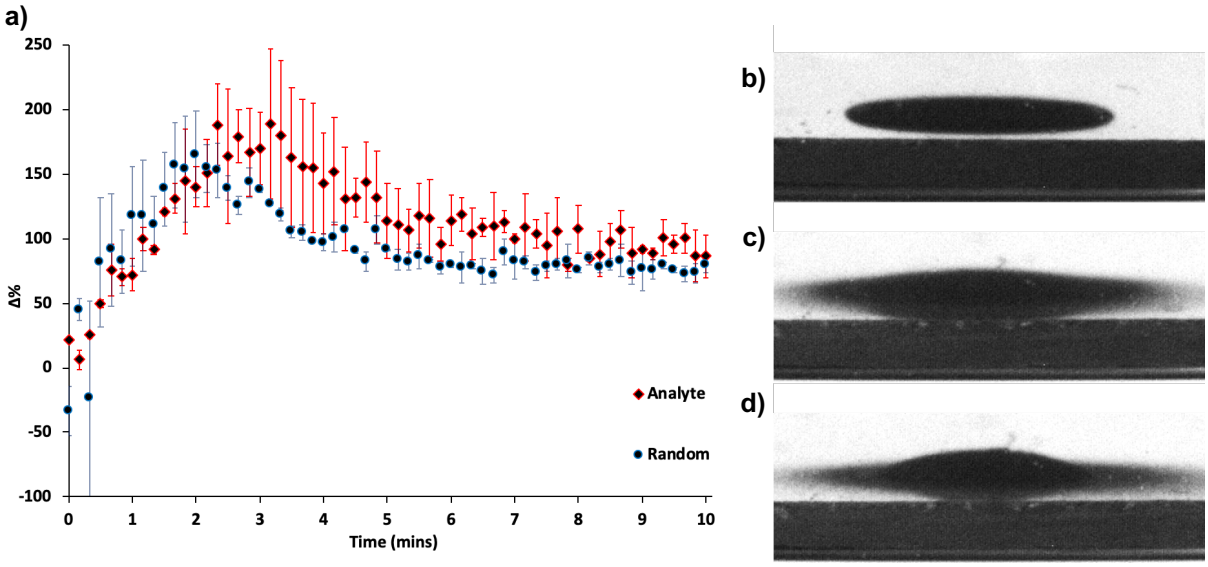

Figure 4.14 (a) Comparison of swelling kinetics of unwashed ASS targeted hydrogels with 10 wt% AAm, 0.6 mol% MBA and 0.4 mol% DNA crosslinks (wrt AAm) and 1 wt% CNP in 10 μM analyte (red, diamonds) or 10 μM random (blue, circles) in 150 mM NaCl, 1 mM PBS. CNP is evident and disrupts optical volume measurements. Δ% and standard error of the mean calculated using equations 3.2a and b (n = 3). (b) Image of early swelling at 30 seconds (c) Image of gel at 3 minutes exhibiting CNP leaching (d) Image of gel at 10 minutes exhibiting leached CNP and sedimentation.

To further investigate the effect of horizontal swelling and reduce the required solution volume, a clip-on mould was 3D printed (Figure 4.15). This mould altered a number of factors during measurement. Firstly, the gels were swollen whilst horizontal. CNP movement would therefore be more likely to move towards the electrode due to the effects of gravity, rather than leaching out of the side of the gels as occurred during vertical swelling. Although some leaching was previously visible during optical measurements on unwashed horizontal gels, the sample volume using the clip-on well was reduced to 50 μL and was pipetted on slowly rather than 5 mL being poured on. The reduction of water agitation may also be expected to slow any flow induced effects of CNP leaching.

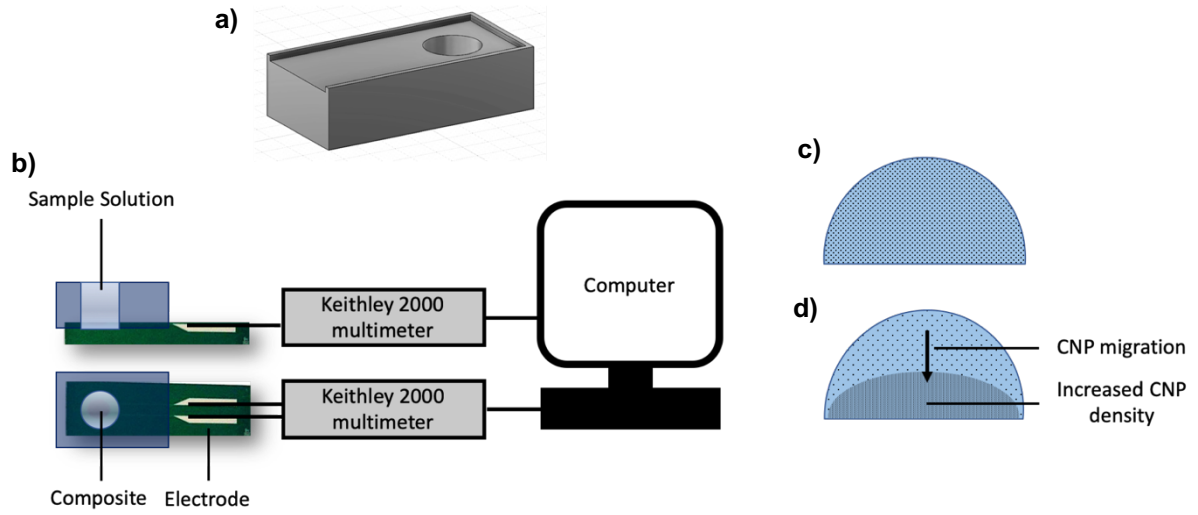

Figure 4.15 (a) 3D printed clip-on-well design (b) Illustration of the horizontal electrical measurement set-up. The electrode being tested is connected to the Keithley 2000 multimeter (d.c.) which is connected to a computer *via* USB cable. The electrode is held horizontally with the clip-on-well attached and the sample solution is pipetted on top of the gel. The computer utilises LabView to control and collect data. (c, d) Illustration of conductive particle movement during horizontal swelling of composite.

The effects of horizontal swelling on resistance are shown in Figure 4.16a, albeit without DNA crosslinks. Although the typical resistance profile was seen, so too was the slower resistance increase. However, rather than slowly increasing to approximately 400 kΩ as with the vertical swelling, the resistance decreases and equilibrates above the initial resistance value of the dried gel. This would be consistent with the premise of CNP migration trending downwards towards the electrode.

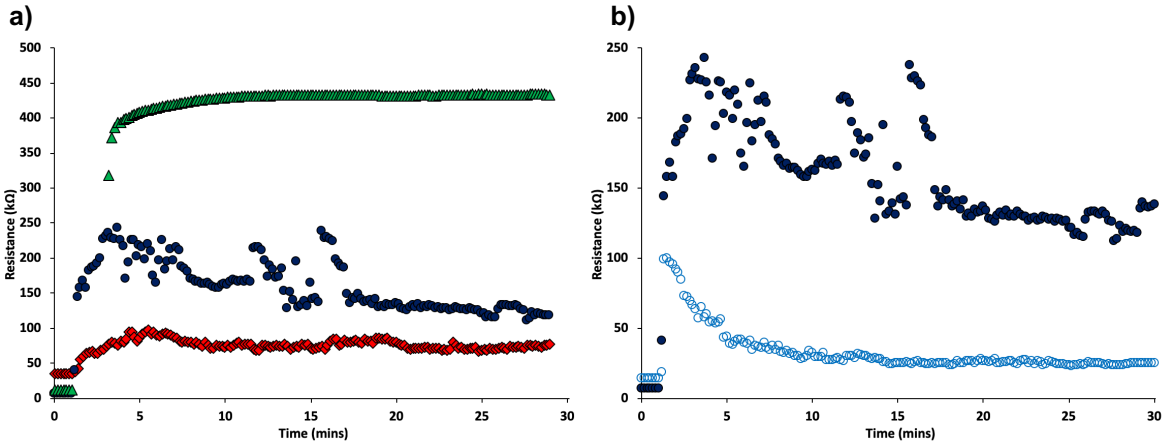

Figure 4.16 The d.c. resistance of hydrogels with 10 wt% AAm, 0.6 mol% (wrt AAm) and 2 wt% CNP in 150 mM NaCl, 1 mM PBS. (a) First swelling resistance (b) First swelling (solid circles) and repeat swelling after drying (hollow circles). Gels were immersed in solution after 1 minute.

Attempts to reswell the gels from Figure 4.16a after loose CNP was washed out were relatively unsuccessful due to delamination resulting in no signal when connecting the electrodes. In these cases, the delamination and gel structure after the stresses of swelling and drying may leave no gel in contact with the electrode, only air.[281] The single successful reswelling is shown in Figure 4.16b, compared to the original swelling. Once again there was an initial increase in resistance, followed by a gradual reduction. This may be explained by the initial swelling causing a reduction in conductive particle density, agitating any remaining loose CNP, before settling towards the electrode. The dried percolating resistance was slightly higher than the first swelling, which would be expected if CNP density had been reduced by washing out loose CNP. The signal is far less noisy than the first swelling and remains at a far lower resistance throughout. The lower resistance may be cause by the rearrangement of gel microstructure during the second drying, or a side effect of the auto-ranging multimeter supplying a lower current during the original swelling measurement.

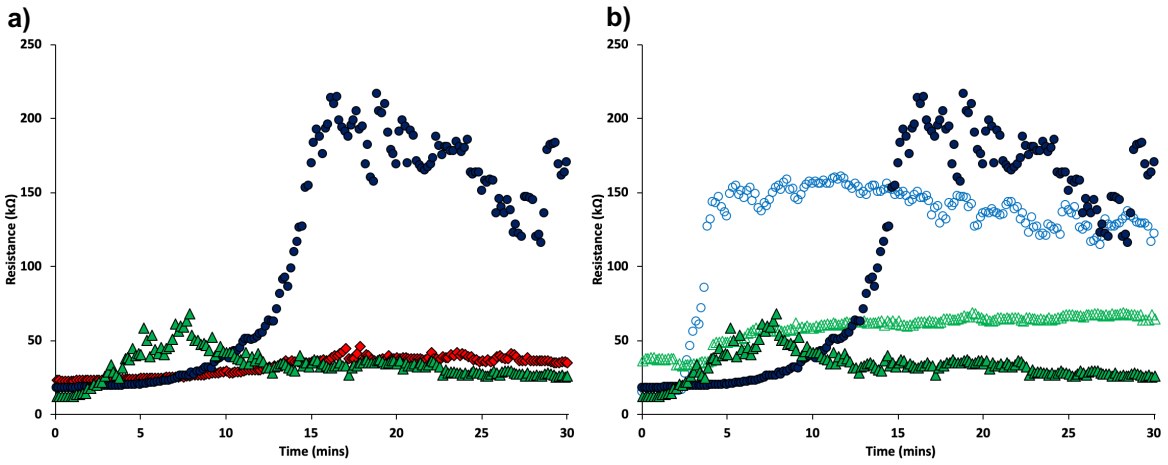

Figure 4.17 The d.c. resistance of hydrogels with 20 wt% AAm, 0.6 mol% (wrt AAm) and 2 wt% CNP in 150 mM NaCl, 1 mM PBS. (a) First swelling resistance (b) First swelling of two samples (solid blue circles and green triangles) and repeat swelling after drying (hollow blue circles and green triangles).

Further investigation of horizontal swelling using 20 wt% AAm gels exhibited only slower resistance changes (Figure 4.17). Due to cost this was not investigated with DNA. In each case the resistance is lower than the typical response, and gradual reduction of resistance is consistently seen. Reswelling was successful on two samples (Figure 4.17b). In one case (blue) the reswelling increased resistance faster

than the first swelling, before trending downwards. The first swelling would have washed out loose CNP, the slower response would therefore be the CNP migration out of the gel, such that the second swelling would be non-percolating far quicker. The other examples (green) had a higher dried resistance and increases to a similar amount at a similar rate yet does not settle to a lower resistance. In this case the settling CNP may have been washed out meaning only entrapped CNP remained. Errors and lack of reproducibility are plentiful with all these measurements and will be discussed further in Section 4.3.

4.1.2 DNA Crosslinked Polymer Composite Challenges

As well as the difficulties using DNA crosslinks for optical measurements discussed in Section 3.2, a substantial number of similar issues are seen when doing resistance measurements. As well as the thermal considerations surrounding DNA crosslinks, the degree of drying would also increase delamination (Figure 4.18). Drying on a bench top, in a fume hood or a desiccator would ensure that the measured resistance would shoot up to MΩs**,** or that no signal would be achieved when the electrode was attached. While this is not dependent on the DNA crosslinks and also occurred with unfunctionalised hydrogels, it indicates that the stress and strain of drying influences delamination as well as detachment.

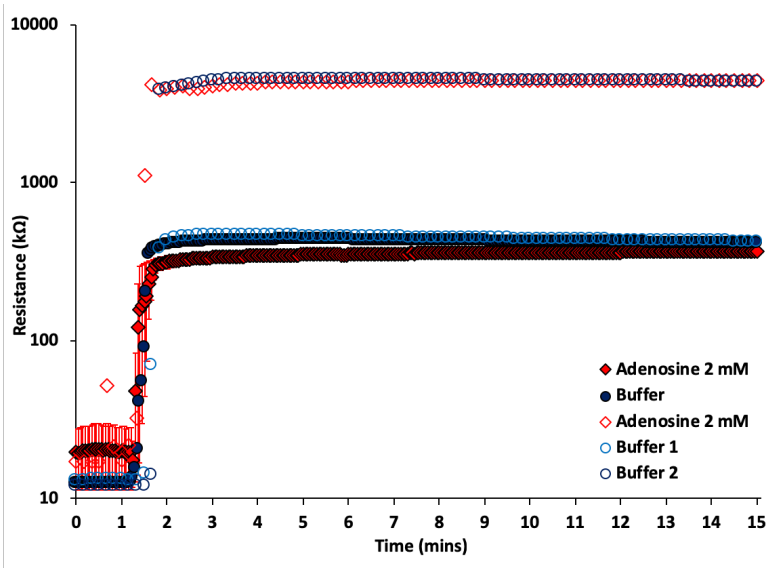

Figure 4.18 The d.c. resistance profiles of APT2 crosslinked hydrogels with 10 wt% AAm, 0.6 mol% MBA, 0.4 mol% APT2 DNA crosslinks and 2 wt% CNP in 300 mM NaCl, 1 mM PBS at 23 °C with either 0 or 2 mM Adenosine. Comparison of gels dried in the fridge after UV irradiation (solid) with typical resistance profiles vs gels dried on the bench top (hollow).

For the APT2 crosslinked gels, typical resistance profiles were achieved, but no reliable differentiation between analyte (adenosine 2 mM) and buffer was achieved. APT1 crosslinked gels at 0.4 mol% would consistently go to MΩs. Only gels with 0.2 mol% APT1 crosslinks would exhibit the typical resistance profile, albeit still with no differentiation between analyte and buffer (Figure 4.19). The trend of increased detachment with higher nucleotide content was identified optically and a similar trend of increased delamination is seen too. As well as the stress and strain of swelling and drying being affected by the hydrophilicity of the hydrogel, therefore being dependant on nucleotide content, the charged DNA may also be affected by the current during measurement (100 μA > 100 kΩ < 10 μA). As in gel electrophoresis, the DNA may be attracted to the cathode and repulsed by the anode, resulting in a further factor influencing delamination. Delamination from the anode only is indistinguishable from delamination from all electrode segments. Any ohmic heating would be expected to be dissipated relatively rapidly into the swelling solution but may influence crosslink stability.

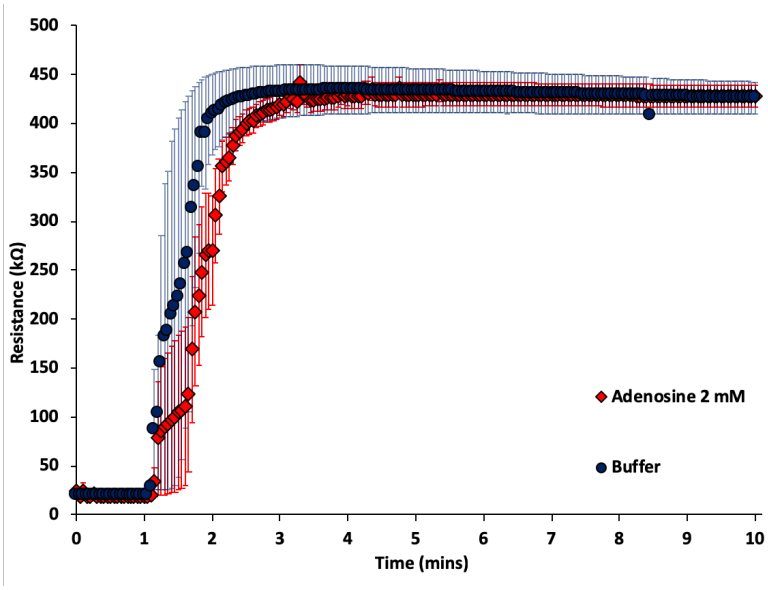

Figure 4.19 The d.c. resistance profiles of APT1 crosslinked hydrogels with 10 wt% AAm, 0.6 mol% MBA, 0.2 mol% APT1 DNA crosslinks and 2 wt% CNP in A1 or R1 at 10 μM in 300 mM NaCl, 1 mM PBS at 23 °C. Standard error of the mean calculated using equation 3.2b (n = 3).

The excessive delamination rate was also apparent with ASS crosslinks. ASS1 crosslinked gels could not achieve a typical resistance response, while the few ASS2 crosslink gels that achieved a typical resistance profile could not differentiate between analyte and random solutions (Figure 4.20). This is likely due to the issues of nucleotide content discussed previously. ASS3 could not be investigated due to a lack of materials.

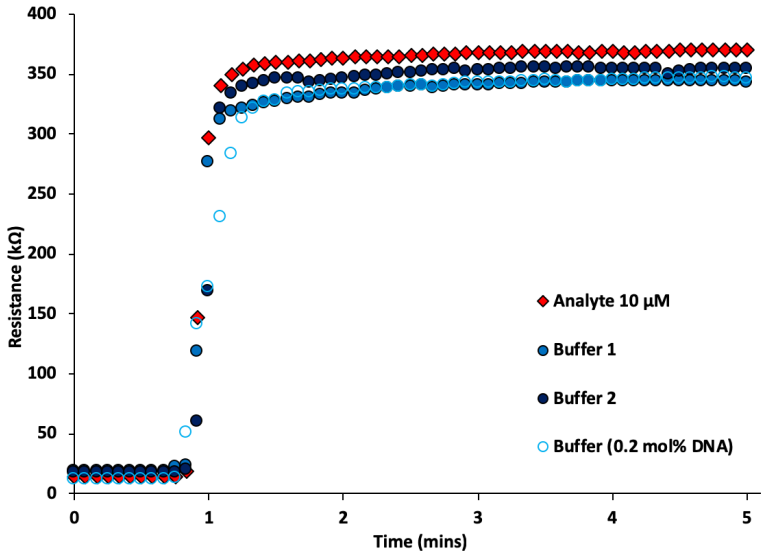

Figure 4.20 The d.c. resistance profiles of ASS2 crosslinked hydrogels with 10 wt% AAm, 0.6 mol% MBA, 0.4 mol% (solid) or 0.2 mol% (hollow) ASS2 DNA crosslinks and 2 wt% CNP in A1 or R1 at 10 µM in 300 mM NaCl, 1 mM PBS at 23 °C.

It is known that CNP and CNT can interact with DNA in solution to form complexes, typically for improved hydrophilicity.[352–355] This can occur both in the pregel solution, and during swelling. In the pregel solution DNA interaction with CNP may be expected to improve CNP dispersion, however, the pregel mixtures required constant agitation to maintain dispersion. Interact with CNP may instead increase aggregation of CNP as a partial coating would create an amphiphilic particle, much like a Janus particle. Basic DLS investigation into the particle size of CNP showed that higher DNA concentrations resulted in a greater variety of particle sizes, averaging to be larger than in buffer alone. It should be noted that the 2-minute equilibration time used for the DLS measurement will have allowed a substantial amount of particles to precipitate before measurement.

Table 4.1 Measured 2 wt% CNP (50 d.nm) diameter using DLS suspended in buffer and 0 – 5 μM of A1, 1 mM PBS.

DNA (μM)	Z Ave (d.nm)	ST DEV	PDI
0.0	2722	36.5	0.5
2.5	5047	932.2	0.9
5.0	3265	875.1	1.0

The influence of solution DNA when testing gels may also be problematic as the rate of particle movement will influence the measured resistance. Furthermore, any DNA which interacts with CNP will be less likely to interact with the DNA crosslinks. Again, these issues will be exacerbated using longer DNA crosslinks and detecting longer or more concentrated DNA. Further investigation into CNP movement, size and the porosity of swollen gels would increase the understanding of the resistance swelling response, although at the relevant concentrations and gel volume was not possible.

The NaCl required for maintaining DNA crosslinks was discussed previously in terms of crystallisation damage. Furthermore, Dr Ferrier found that although a.c. measurements of impedance could detect the transition from dried gel percolating state to swollen non-percolating, the NaCl concentrations required had a significant effect on the complex impedance and masked any changes based on the material itself.

4.2 Morpholino Oligonucleotide Crosslinked Polymer Composites

4.2.1 miR92a Sequence Detection

Morpholino oligonucleotide crosslinks have been shown to improve upon a number of the challenges associated with DNA crosslinked hydrogels in optical transduction. They may also be expected to alleviate some of the challenges in electrical transduction. As uncharged crosslinks, MO crosslinked polymer composites should

not be repelled from the anode, will swell less rapidly as they are less hydrophilic, and the crosslinks will be more thermally stable. Most importantly, MO crosslinks do not require salt to remain hybridised. This will remove any damage from crystallisation during drying and theoretically enable alternative electrical investigation such as a. c. measurements of impedance.

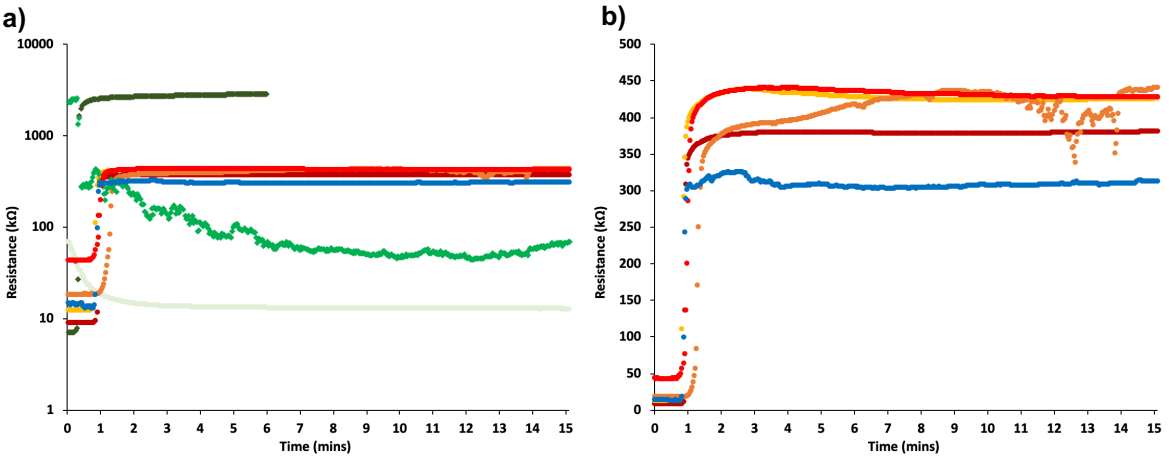

Figure 4.21 The d.c. resistance profiles of MOR2 crosslinked hydrogels with 10 wt% AAm, 0.6 mol% MBA, 0.4 mol% MOR2 DNA crosslinks and 2 wt% CNP in A1 (red-yellow typical end point, green atypical end points) or R1 (blue) at 1 μM in 150 mM NaCl, 1 mM PBS at 23 °C. (a) Log scale showing typical and atypical resistance profiles. (b) Only typical resistance profiles.

MOR2 crosslinked composites synthesised identically to DNA crosslinked hydrogels were frequently not percolating. Occasionally, if transferred to the bench top, they would become percolating suggesting that further drying increased CNP density. This was not a consistent response and as MOCH polymer composites (MOCHPCs) are less hydrophilic than their DNA equivalents, they would be expected to be less hydrated before room temperature drying. Of the gels that did percolate when dried, or were simply <100 kΩs, no reliable or reproducible measurements were possible (Figure 4.21).

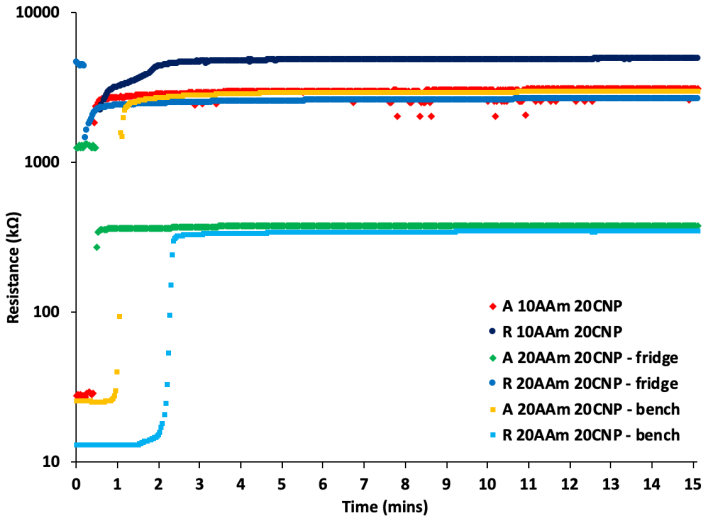

Figure 4.22 Comparison of d.c. resistance profiles of various MOR2 crosslinked hydrogels with 10 or 20 wt% AAm, 0.6 mol% MBA, 0.4 mol% MOR2 DNA crosslinks and 2 wt% CNP in A1 or R1 at 10 nM in 1 mM PBS at 23 °C. Comparison of gel equilibration time at room temperature after storage at 4 °C, either 15 minutes (fridge) or 1 hour (bench).

A wide variety of MOCHPC compositions and conditions were evaluated in an attempt to identify the cause of non-percolation, with no reproducible success (Figure 4.22). Removal of salt from the synthesis, increasing to 20 wt% AAm and longer room temperature equilibration resulted in few typical resistance profiles and still 80-90% of gels were non-percolating.

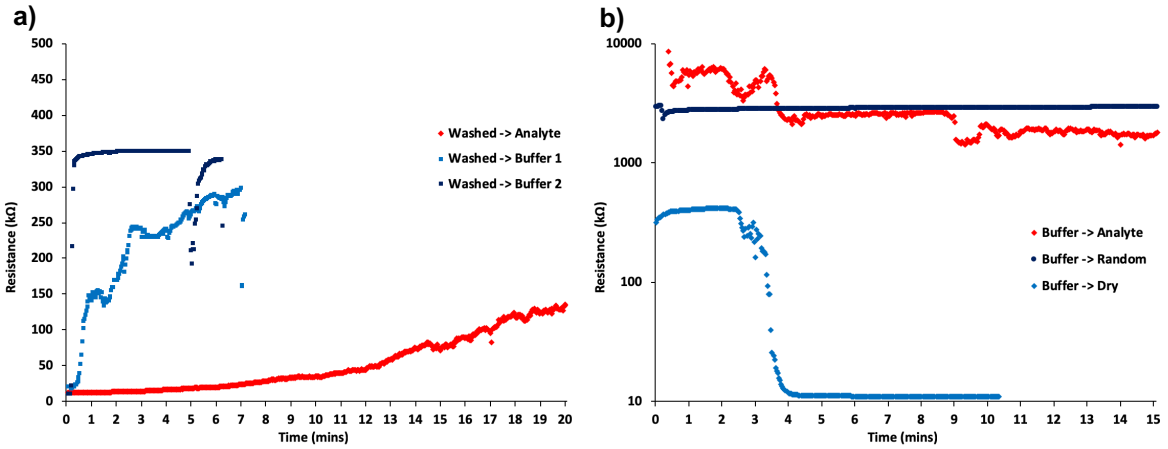

Figure 4.23 Comparison of d.c. resistance profiles of MOR2 crosslinked hydrogels with 10 wt% AAm, 0.6 mol% MBA, 0.4 mol% MOR2 DNA crosslinks and 2 wt% CNP (a) Gels washed in 1 mM PBS for 1 hour immediately after UV irradiation, then dried and stored at 4 °C and swollen in either A1 at 10 nM in 1 mM PBS or in 1 mM PBS only (b) Gels stored in 1 mM PBS (4 °C) immediately after UV irradiation and tested in A1 or R1 at 10 nM in 1 mM PBS at 23 °C from swollen state. Gel after storage in 1 mM PBS (light blue diamonds).

Preparing gels as for optical measurements, washing them in buffer for 1 hour after UV irradiation before drying, achieved percolation in 3 out of 5 samples, yet the resistance profiles were inconsistent (Figure 4.23a). Attempts to store samples in buffer before measurement resulted in 2 out of 3 results at MΩs, and a single sample at 400 kΩs, which was percolating when subsequently dried (Figure 4.23b). These results indicated that, despite the CNP content being consistent, there must be a microstructural difference between DNA and MO crosslinked composites.

4.2.2 Morpholino Oligonucleotide Crosslinked Polymer Composite Challenges

Comparison of SEM images of oligonucleotide crosslinked composites revealed a number of factors potentially influencing the different resistance profiles from the same conditions, while also informing the differences between CNP based DNA and MO crosslinked composites.

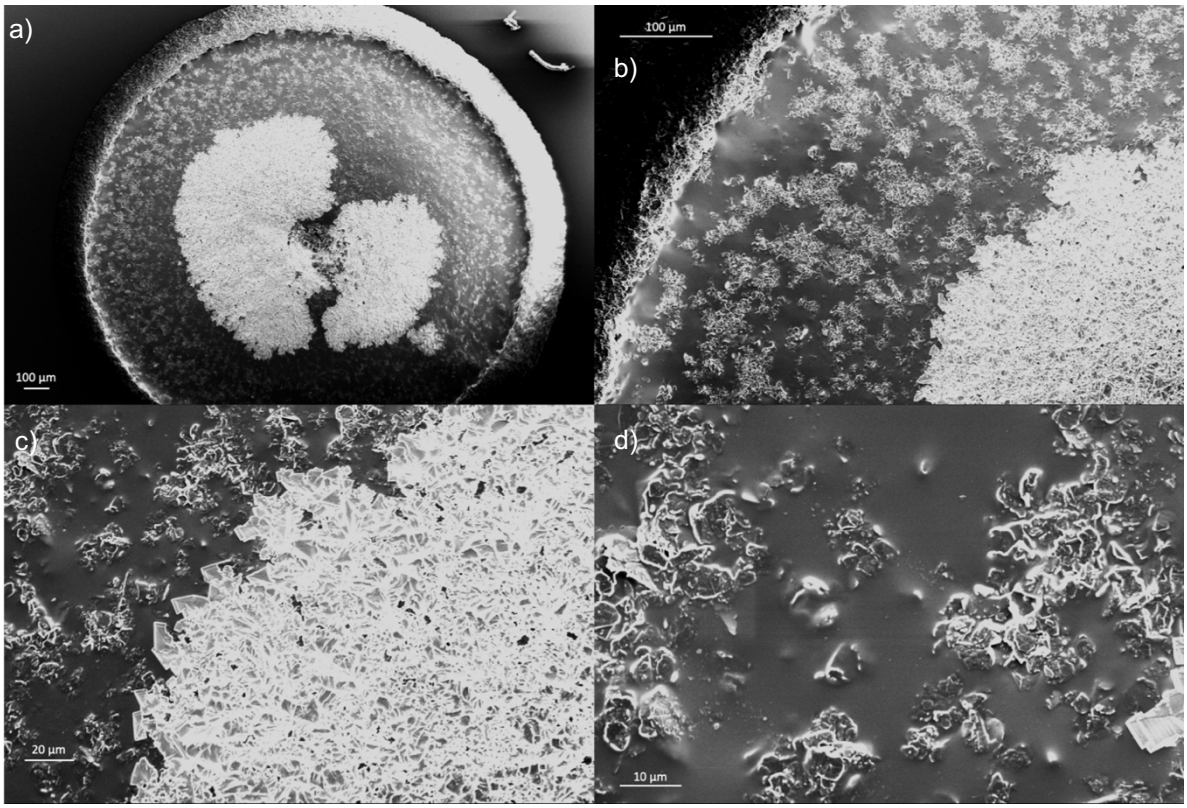

Figure 4.24 SEM images of 10 wt% AAm, 0.6 mol% MBA, 0.4 mol% MIR2 wrt AAm hydrogel with 2 wt% CNP in 150 mM NaCl, 1mM PBS.

The surface of MIR2 crosslinked composites revealed a nonhomogeneous structure (Figure 4.24). The centre of the gel exhibits a large, non-symmetrical formation of NaCl crystals, the gel has numerous cracks and the outer rim appeared to be raised and denser. Sample preparation for SEM including carbon sputtering, involving placing the gel under vacuum. As previously mentioned, drying of the gel tended to increase detachment when swelling so images do not show the gels in the precise state at which they are stored and tested. This drying will likely have exacerbated any fracturing. Due to the SEM induced radiation damage causing gel melting, it was difficult to obtain images at higher magnification.[356] It would appear that the white spots in Figure 4.24d could be CNPs, however it is hard to differentiate due to the edges caused by fractures.[281] The NaCl crystallisation was most apparent mostly in the centre of the gel and was likely an artefact of the hydrogel drying mechanism.

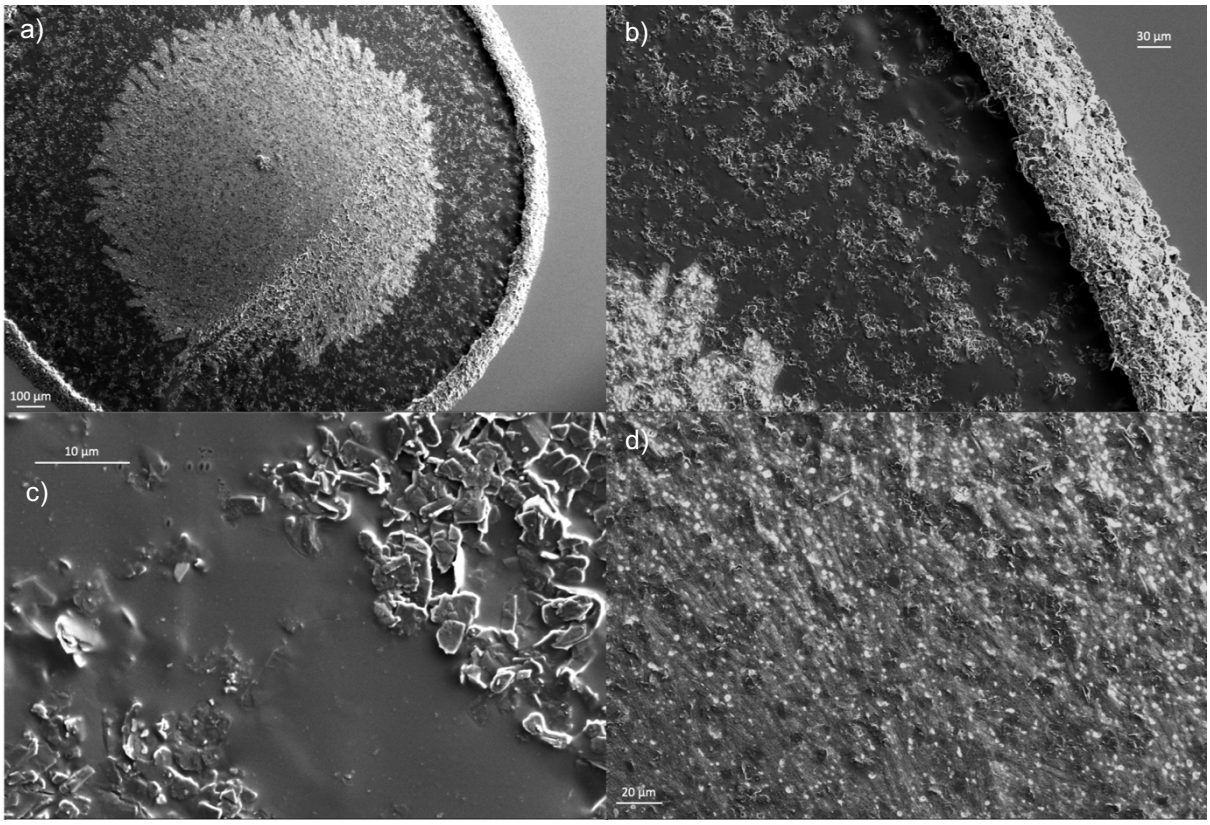

Figure 4.25 SEM images of 10 wt% AAm, 0.6 mol% MBA, 0.4 mol% MIR2 wrt AAm hydrogel with 2 wt% CNP in 1mM PBS.

Although salt was required to maintain DNA crosslinks, MIR2 gels were synthesised without salt to test the influence of salt on gel structure and influence of salt crystallisation on gel damage (Figure 4.25). Again, three predominant morphologies were visible. The centre appeared brighter due to the larger density of CNP (Figure 4.25d), while the edge and midsection appeared relatively similar to the gel with salt. During the UV irradiation of gel synthesis, the centre of the gel would have been the top of the pregel droplet closest to the UV source. This would improve initiation in this area and explain the increased density.[357] The outer edge would be caused by during synthesis too, where a shorter depth would have more consistent UV initiation due to improved penetration. Depending on the rate of polymerisation vs drying, the gel structure may be influence by the coffee ring effect, causing a flow of monomer and CNP to the edges (Figure 4.26).[281]

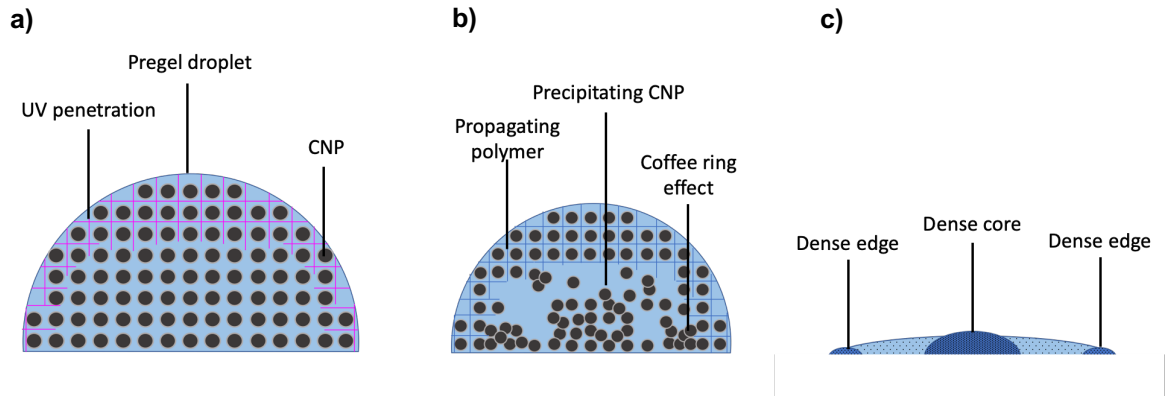

Figure 4.26 Illustration of (a) pregel droplet UV photoinitiation (b) polymerisation and drying (c) dried gel structure.

Given the variability of the incomplete initiation of free radical polymerisation, as well as the poor dispersion and gel attachment issues, the variable resistance responses of these gels may be expected. The resistance issues with MOR2 crosslinked gels were not observed for any DNA or non-oligonucleotide crosslinked gels and therefore would be expected to be more different than these variables would allow.

SEM images of MOR2 crosslinked gels revealed a more homogenous structure, substantially different to the MIR2 crosslinked gels (Figure 4.27). Although the morphology included a denser centre area, it was larger than that of the MIR2 gels.

Similarly, the outer edge was less dense and appeared to be a wider, more consistent material. No surface NaCl crystals were apparent and there was less fracturing. Most importantly for the electrical transduction, small conductive circles were seen, seemingly under the gel surface.

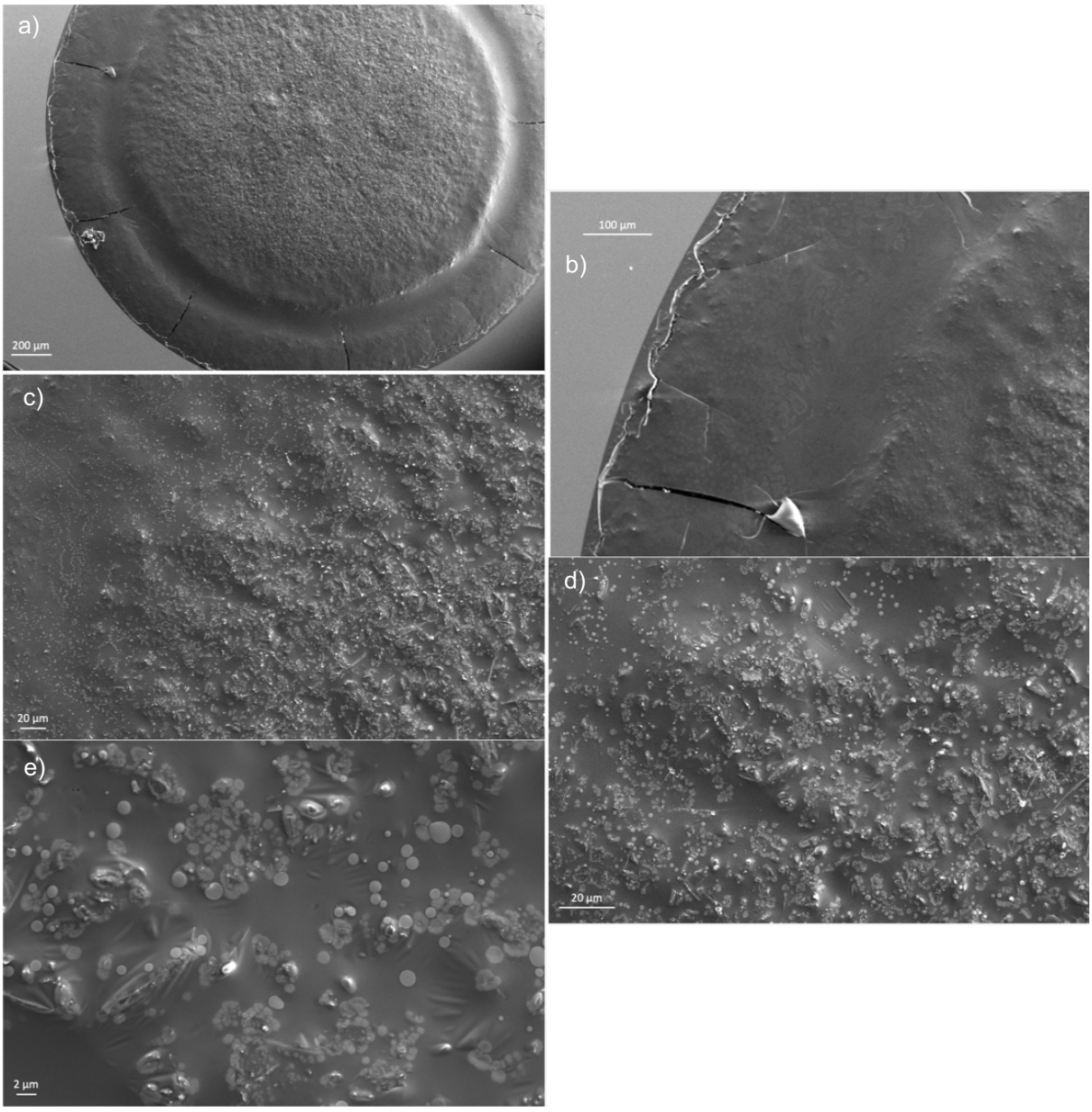

Figure 4.27 SEM images of a dried 10 wt% AAm, 0.6 mol% MBA, 0.4 mol% MOR2 wrt AAm hydrogel with 2 wt% CNP in 150 mM NaCl, 1mM PBS.

Synthesis of MOR2 gels without NaCl exhibited a similar morphology (Figure 4.28). Distinct conductive dots were once again seen, and the gel appeared smoother, potentially due to a lack of salt crystals within the gel pores. The pregel solution

containing MO crosslinks instead of DNA had been observed optically as a more stable dispersion of CNP. If the MO crosslinks interact with the CNP it may prevent aggregation and precipitation, resulting in a more even distribution of CNP.[358,359] While this results in a more consistent material, the density of conductive particles may then not be enough to achieve percolation, whereas with DNA or without oligonucleotides, aggregation and precipitation may increase CNP density closer to the electrode. The altered gel structure may be affected by the droplet contact angle on the silicon dioxide wafer. MO gels exhibited more spreading, indicating a lower contact angle and therefore a thinner droplet. This would enable more thorough photoinitiation and alter the effects of droplet drying, as faster polymerisation would alter the coffee ring effects.[360] The more homogenous material would then be more resistant to fracturing as the stress and strains of drying would be more consistent throughout, as well as being reduced by a less hydrophilic crosslink.

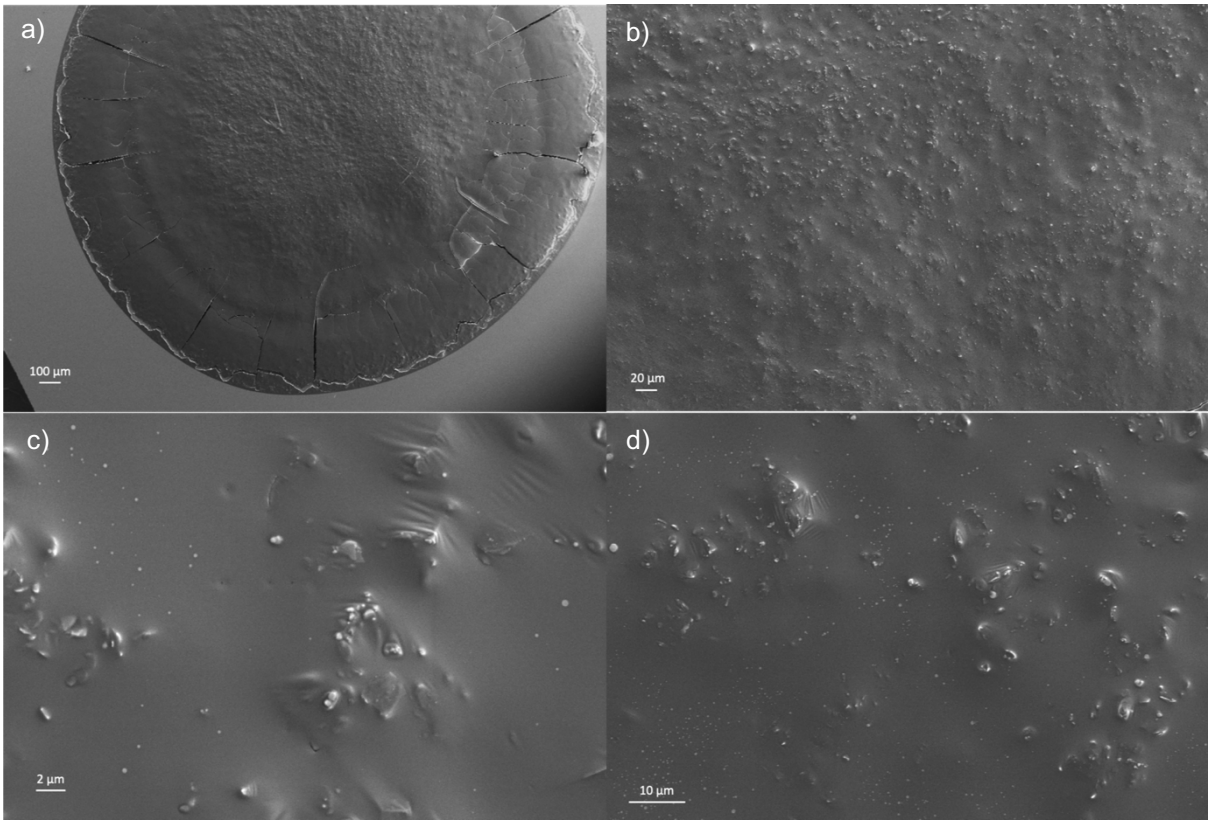

Figure 4.28 SEM images of a dried 10 wt% AAm, 0.6 mol% MBA, 0.4 mol% MOR2 wrt AAm hydrogel with 2 wt% CNP in 1mM PBS.

It was previously theorised that DNA crosslinked composites did not fit standard percolation or general effective medium (GEM) theories due to the porosity of hydrogels as the percolation threshold (0.6 wt% CNP) was lower than theorised (>2.5 wt% CNP).[81,282] Typical models utilise two-phase mixtures, in this case CNP and polymer. The hydrogel pores can be considered as areas or particles of low conductivity, which effectively displace material, thereby increasing the effective concentration of conductive particles in an area. Standard two-phase models therefore cannot be used to accurately predict the characteristics of these composites.[361–363] These features were used to explain the unexpectantly low CNP loading required for percolation. The heterogeneity of DNA gels and lack of adequate porosity characterisation further complicates any attempted modelling, although it can be assumed that there are areas of higher CNP density that may be percolating and areas of lower CNP density that may be non-percolating.[364] The improved homogeneity of MO composites appear to have a more consistent CNP loading throughout, without the percolating areas of high density.[365,366]

Were improved CNP dispersion the cause of poor conductivity of MOR2 crosslinked gels, increasing the CNP content may achieve percolation. Previous work by Dr Ferrier had indicated that CNP loading >2 wt% reduced gel integrity of 10-15 wt% gels, so 20 wt% gels were investigated to increase propagation rate and improve CNP entrapment and gel strength (Figure 4.29).[81] Of both 2.5 and 3 wt% CNP 1 of 3 delaminated. The 2.5 wt% gels exhibited the atypical slower resistance increase, while reswelling of one then resulted in a slower but more typical response reaching 400 kΩs. Conversely, the 3 wt% gels remained <50 kΩs throughout testing and reswelling and resulted in a new resistance profile whereby gels appeared to remain at relatively high levels of percolation throughout. Unfortunately, incorporation of MOR2 crosslinks resulted in only partial gelation whereby gels would wash or flake apart when swelling. This may be expected if the MO crosslinks are improving CNP dispersion and thereby reducing UV penetration during photoinitiation.

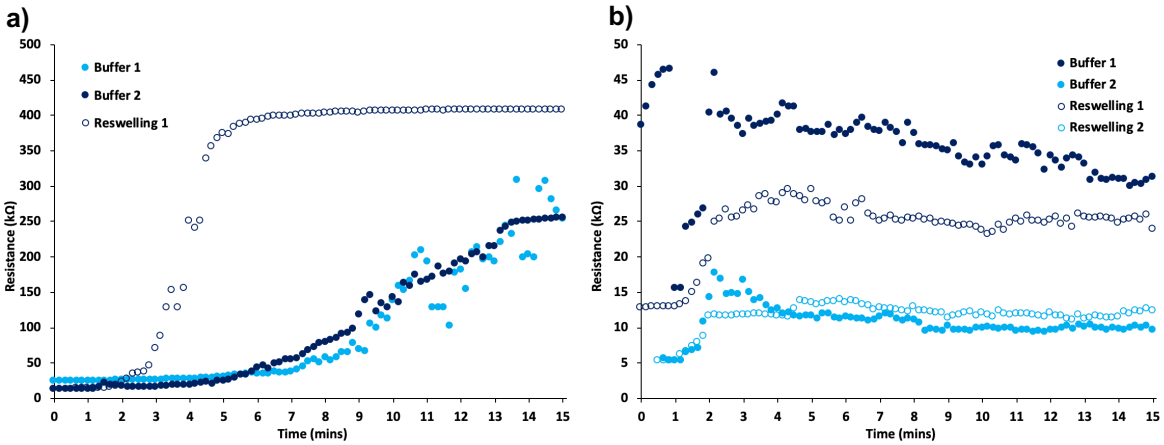

Figure 4.29 Comparison of d.c. resistance profiles of hydrogels with 20 wt% AAm, 0.6 mol% MBA and (a) 2.5 wt% or (b) 3 wt% CNP in 1 mM PBS at 23 °C. Comparison of first swelling resistance profile (solid) and 2nd swelling resistance profile (hollow).

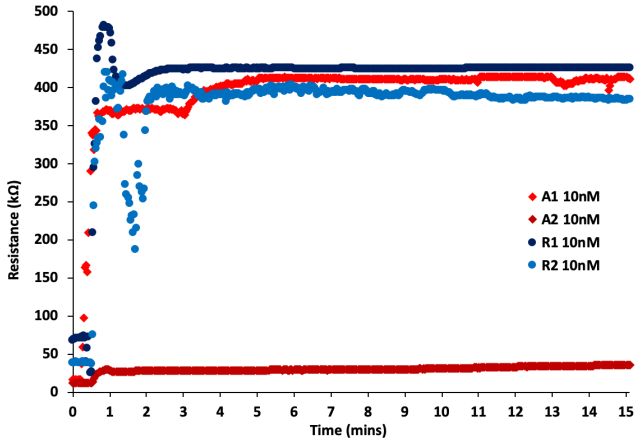

Figure 4.30 The d.c. resistance profiles of MOR2 crosslinked hydrogels with 10 wt% AAm, 0.6 mol% MBA, 0.4 mol% MOR2 DNA crosslinks and 2 wt% CNT in A1 or R1 at 1 μM in 1 mM PBS at 23 °C.

A similar attempt to achieve consistently percolating MO crosslinked gels was using CNT in place of CNP, whereby the larger aspect ratio would be expected to increase conductive particle interaction and thereby increase conductivity (Figure 4.30).[367–369] Half of these achieved typical percolation values when dried (<30 kΩs) and while the other two did not, they were more reliable than the majority of CNP gels tested. Although three gels exhibited almost typical resistance profiles, there was substantial noise and variation, most likely due to a reduction in leaching resulting in movement of conductive particles within the gels. A single sample remained at low resistance,

suggesting that a high density of conductive material remained at the electrode surface. The inconsistencies of CNT composites were investigated using SEM.

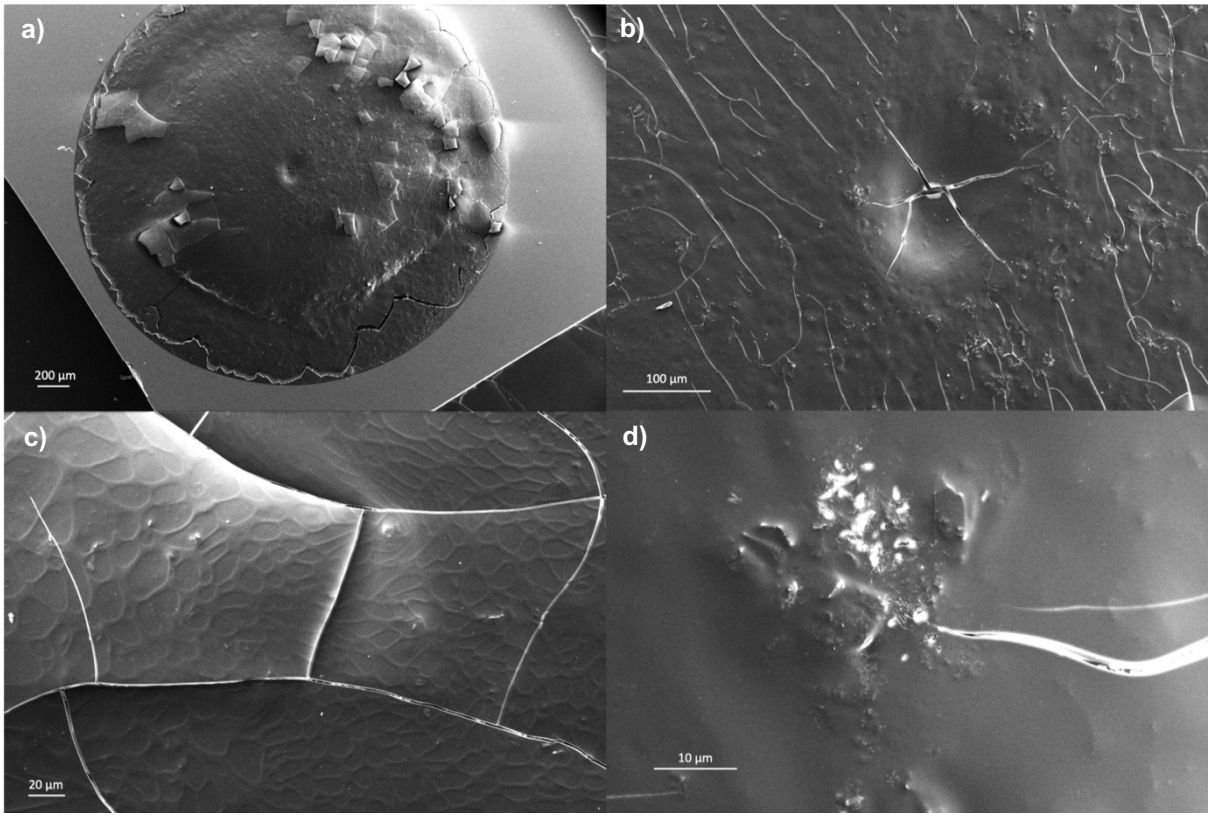

Figure 4.31 SEM images of a dried 20 wt% AAm, 0.6 mol% MBA wrt AAm hydrogel with 2 wt% CNT, 1mM PBS stored on bench top after UV irradiation.

Without oligonucleotide crosslinks, CNT based gels appeared relatively homogenous (Figure 4.31). Both small and large fractures were visible on the surface and very few conductive areas were seen. This may indicate that the CNTs precipitated to the wafer surface or were pressed by size dependent exclusion from the density of the hydrogel network during propagation (Figure 4.32).

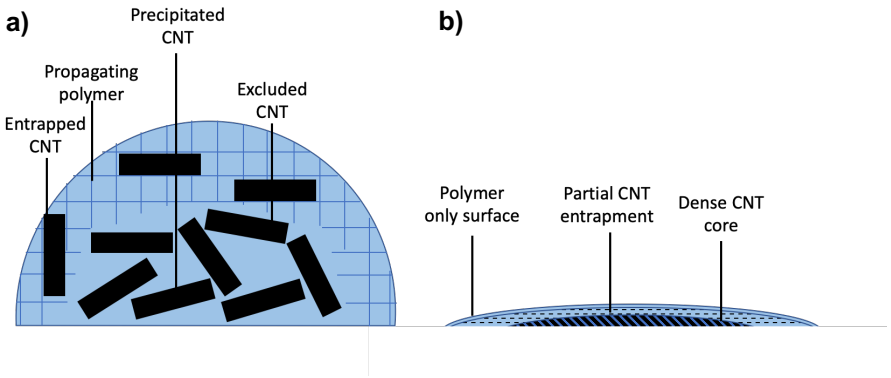

Figure 4.32 Illustration of CNT (a) movement during propagation whereby dense polymer network will push CNT out (b) dried gel potential structure.

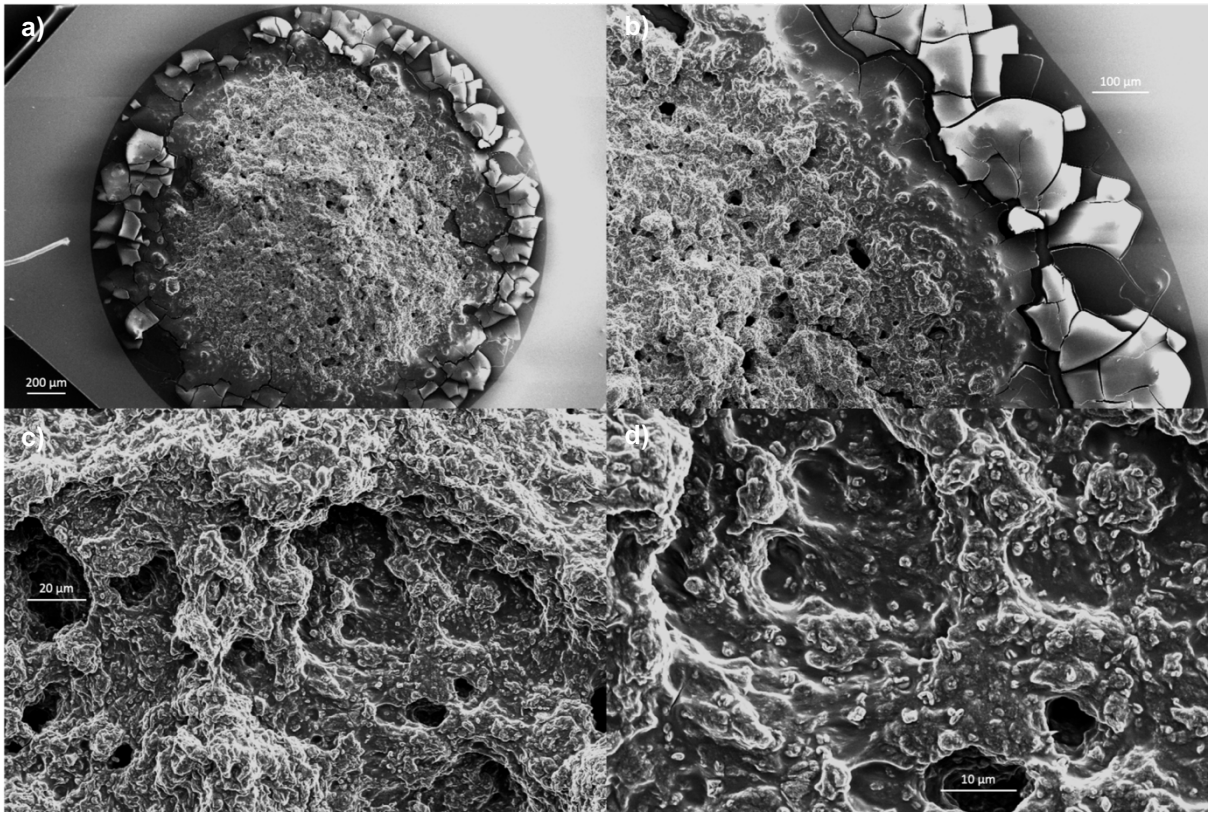

Figure 4.33 SEM images of a dried 10 wt% AAm, 0.6 mol% MBA, 0.4 mol% MOR2 wrt AAm hydrogel with 2 wt% CNT, 1mM PBS stored on bench top after UV irradiation.

Addition of MO crosslinks to the CNT composite resulted in a drastically different gel structure (Figure 4.33). Large cavernous holes are visible over the whole surface of the gel rather than the smooth polymer layer seen before. If the CNT dispersion is improved by interactions with the MOs the CNT may be more likely to be entrapped in

the gel close to the surface. The inconsistencies would suggest that CNT, although improving dried percolation, would not improve the reliability of resistance investigation.

4.3 Carbon Nanopowder Based Composite Limitations

The inconsistencies and poor reproducibility of the composites discussed above prevented reliable electrical measurements. To understand which factors could be improved to achieve appropriate transduction the issues were separated into pregel solution variation relating to the dispersion stability and the factors affecting homogeneity and structural variety of the dried gels.

4.3.1 Dispersion Stability

Composite pregel solutions were observed to maintain a consistent colour for longer when MOs were used, compared to DNA or oligonucleotide free solutions where CNP sedimentation would create a clear layer at the top of the aliquot. Although CNP precipitation did still occur over time, improved dispersion stability would be expected to improve the consistency of carbon loading between samples. Due to the high cost of MOs they could not be used to investigate their effects on dispersion. Instead 3-morpholinopropane-1-sulfonic acid (MOPS) buffer was used to attempt to replicate the effects of MOs on CNP.[358]

A sedimentation study on CNP dispersion in either PBS or MOPS buffer showed little to no benefits (Figure 4.34). A variety of CNP loadings were investigated (0.1 – 2.0 wt%) but at all concentrations and in both buffers, CNP was aggregated and much larger than the specified 50 nm diameter. Furthermore, the PDI was consistently high, indicating a variety of aggregate particle sizes. Despite the obvious sedimentation after the measurement was finished, the count rate did not reduce as would be expected. This is due to both rapid sedimentation occurring during the sample equilibration time

and because particles were seemingly maintained by the surface tension at the top of the sample volume (Figure 4.34g-h). Particles were never observed at the sample surface using pregel solutions, likely due to shape of the microcentrifuge tube.

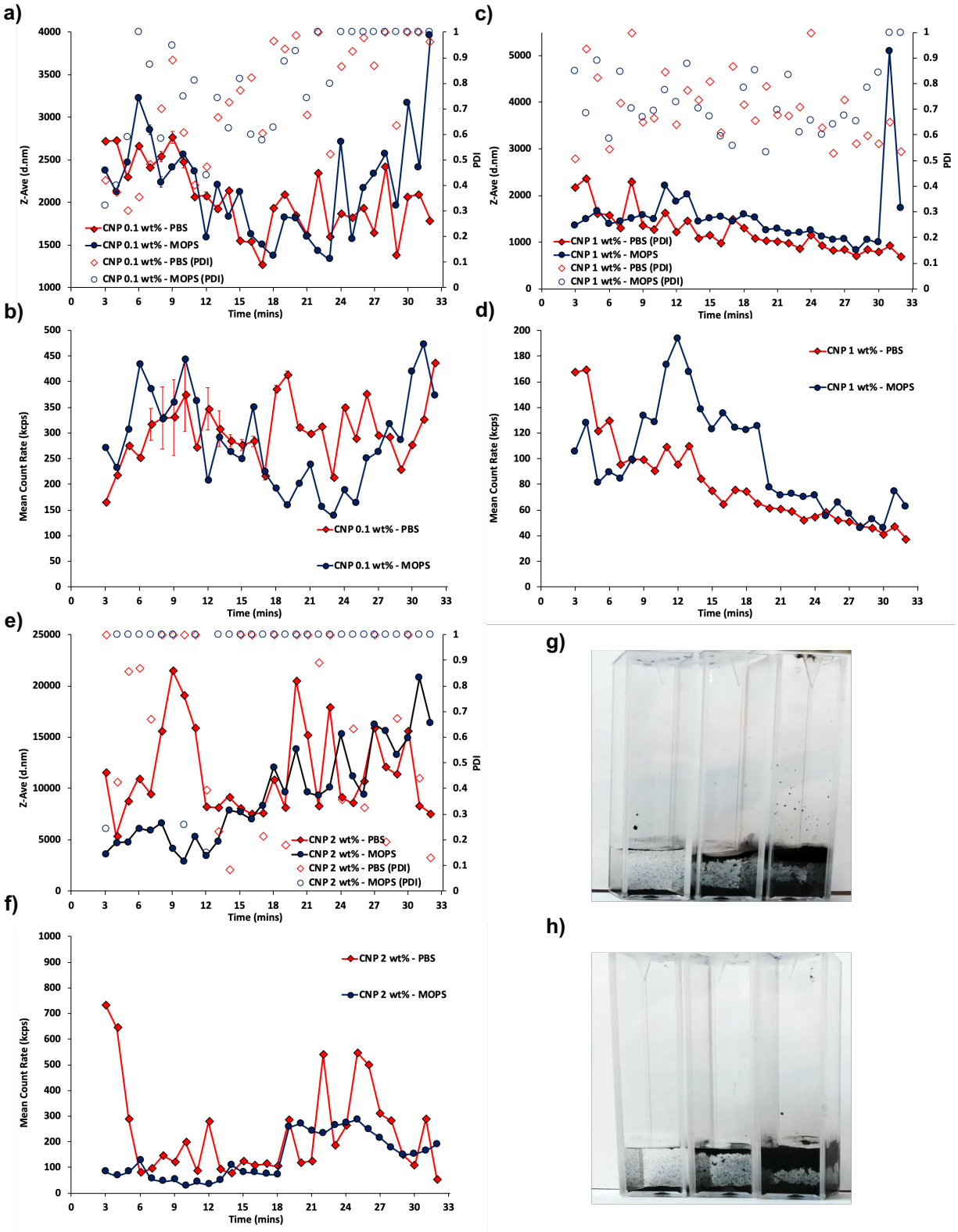

Figure 4.34 Comparison of CNP (50 d.nm) stability at (a, b) 0.1 wt% (c, d) 1.0 wt% (e, f) 2.0 wt% in 1 mM PBS (red, diamonds) or 20 mM MOPS (blue, circles). (a, c, e) DLS determined Z-Average (solid) and PDI (hollow) over time. (b, d, f) DLS measured count rate over time. (g) Image of 1 mM PBS samples after measurement (L-R 0.1, 1.0, 2.0 wt% CNP) (h) Image of 20 mM MOPS samples after measurement (L-R 0.1, 1.0, 2.0 wt% CNP).

Due to difficulties quantifying dispersion stability using DLS, basic optical observations were used instead. Further investigation included an alternative surfactant, sodium dodecylbenzenesulfonate (NaDDBS), and attempted to disperse CNT as well as CNP (Table 4.2).[370–372] All CNT mixtures resulted in a paste which could not be pipetted due to aggregates blocking pipette tips. Of the successfully mixed CNP samples, only the 5:1 ratio of either SDBS or MOPS offered any benefit to dispersion stability with the remaining conditions exhibiting substantial sedimentation within 5 minutes (Figure 4.35).

Table 4.2 Surfactant conditions tested to suspend 2 wt% CNP or CNT. Mixtures were initially vortexed for 60 seconds and then sonicated for 3 hours. Each CNT mixture was unable to be pipetted.

Condition	CNP/CNT (2 wt%)	Surfactant	Wt ratio	NaCl	
A	CNP	NaDDBS	10:1		
	CNT	NaDDBS	10:1		Paste
B	CNP	NaDDBS	10:1	150 mM	
	CNT	NaDDBS	10:1	150 mM	Paste
C	CNP	NaDDBS	5:1		
	CNT	NaDDBS	5:1		Paste
D	CNP	MOPS	1 M		
	CNT	MOPS	1 M		Paste
E	CNP	MOPS	10:1		
	CNT	MOPS	10:1		Paste
F	CNP	MOPS	5:1		
	CNT	MOPS	5:1		Paste

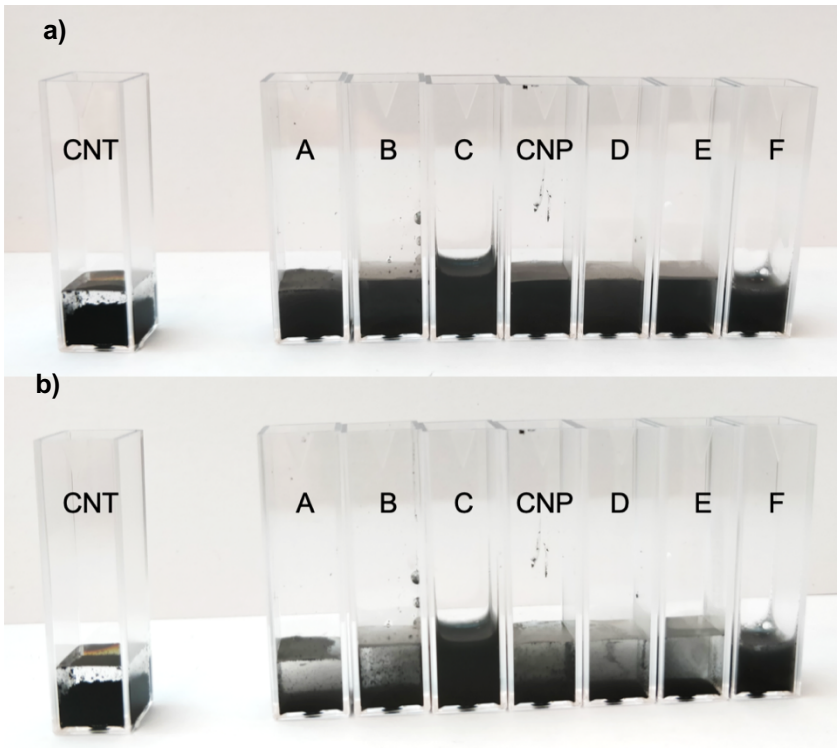

Figure 4.35 Image of CNP (2 wt%) in each condition (A-F) specified in Table 4.2. L-R 2 wt% CNT in DI water, 2 wt% CNP in A, B, C, DI water, D, E, F. (a) Agitated solutions, CNT unagitated. (b) Solutions after 5 minutes.

Comparison of the gel structures of gels made using PBS or MOPS without oligonucleotide crosslinks attempted to identify the effect of MOs on gel structure. The PBS gel was malformed, potentially due to a pipetting error during synthesis (Figure 4.36). The imaged gel was relatively consistently cracked and didn't exhibit the 3 heterogenous features of the DNA crosslinked gels identified previously.

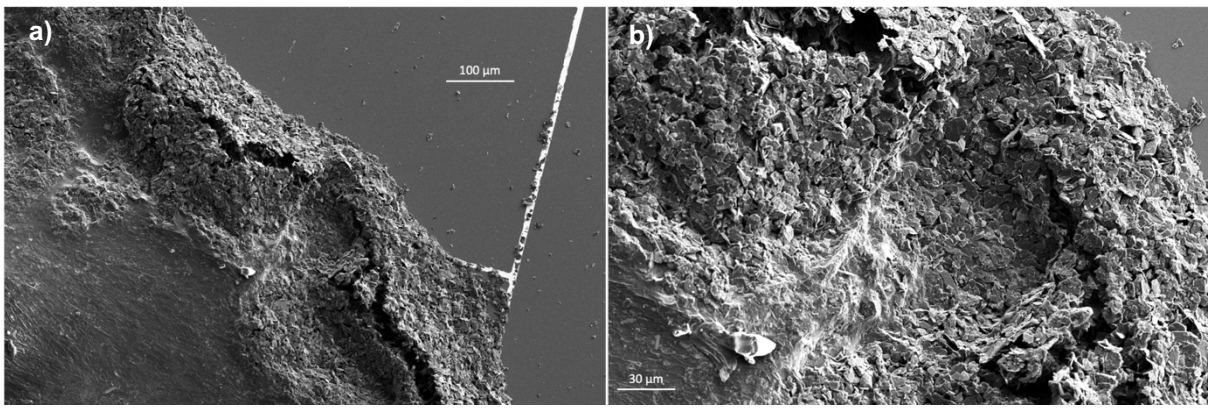

Figure 4.36 SEM images of 10 wt% AAm, 0.6 mol% MBA wrt AAm hydrogel with 2 wt% CNP in 1mM PBS.

The MOPS gel with CNP exhibited a consistent surface structure (Figure 4.37). Small fractures featured homogenously throughout, unlike the smoother MO crosslinked gels. MOPS gels with CNT was similar to the MO crosslinked CNT composite.

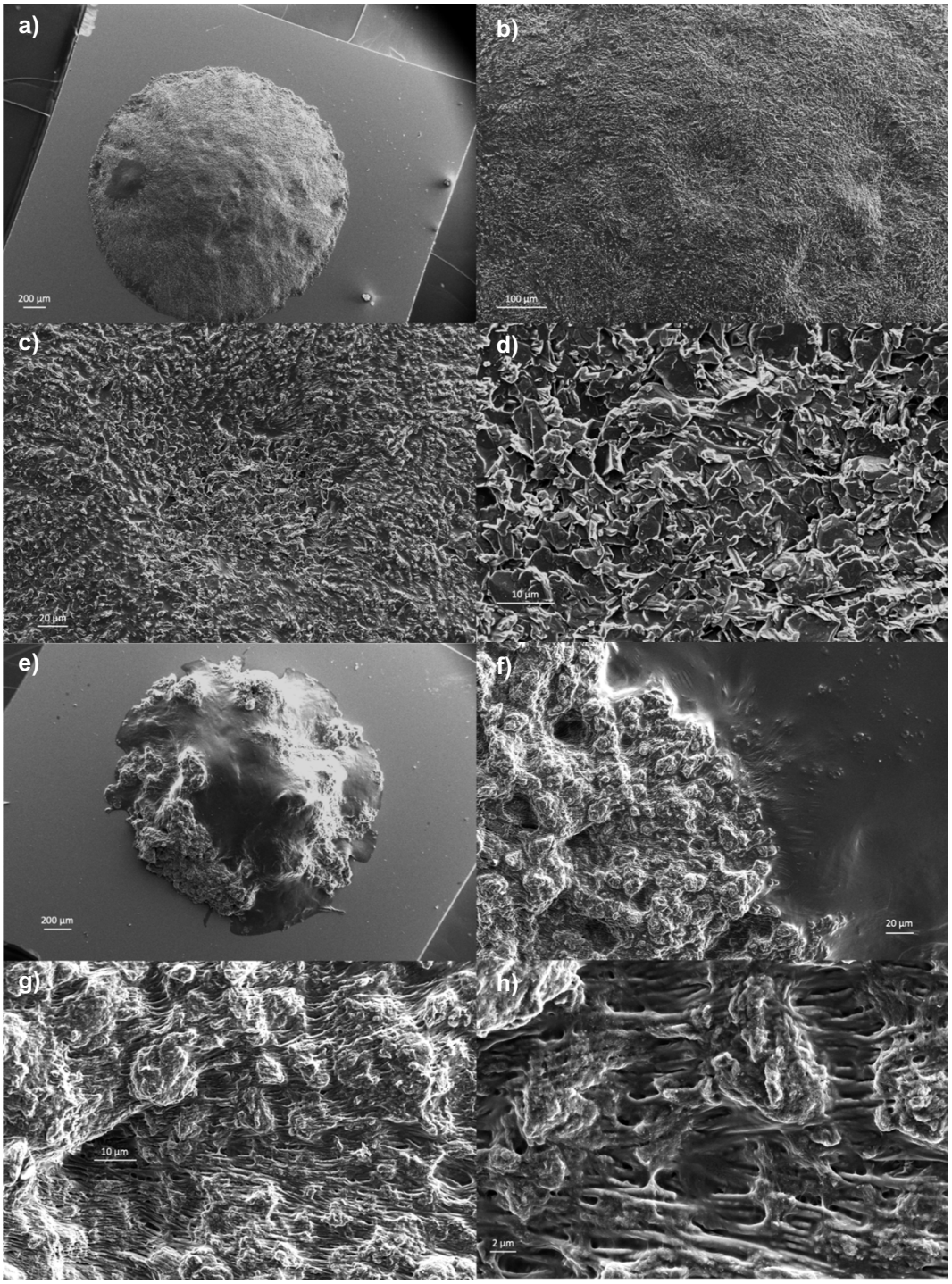

Figure 4.37 SEM images of a dried 10 wt% AAm, 0.6 mol% MBA wrt AAm hydrogel with 2 wt% (a-d) CNP (e-h) CNT, 20 mM MOPS stored on bench top after UV irradiation.

Neither NaDDBS nor MOPS sufficiently improved dispersion stability with sedimentation still evident within 10 minutes. Any sedimentation will decrease the accuracy of synthesis as each pipetted aliquot, while appearing identical, will include a different ratio of CNP and monomers. DNA is known to interact with carbon nanoparticles and MO is expected to interact also. This interaction is undesirable for sensing purposes, as the adaptability of the crosslink design will also have to take into account sequence length effects on composite particles.

A wide variety of water stable surface functionalised nanoparticles are available.[373,374] One frequent method is to attach poly(ethylene glycol) (PEG) or other hydrophilic polymers to the nanoparticle surface, which despite increasing insulation of the conductive filler can result in increased conductivity,[375] but typically would disrupt the electronic structure of the carbon nanomaterial and reduce conductivity.[376] Coatings or surface functionalisation can increase the size of the nanoparticle, which reduces likelihood of entrapment, may increase porosity and may thereby cause increased leaching.[260,377,378] Furthermore, improved dispersion can reduce photoinitiation efficiency. Inkjet printing is extremely beneficial for redox initiation of this system, in terms of precision and mixing of small volumes. Although many particles are appropriate for printing, only an electrostatic dispersion, achieved by surface functionalisation using a charged moiety, was investigated, discussed further in Chapter 5.

4.3.2 Polymer Homogeneity

The lack of polymer homogeneity is sure to influence the lack of reproducible resistance results. The polymerisation does not reach complete conversion, as evidenced by leaching of CNP and small oligomers (Figure 4.38 and Figure 4.39). The degree of conversion will be determined by a wide variety of factors which also influence the homogeneity. These include: temperature, droplet contact angle and thickness, UV penetration, speed of droplet drying, as well as errors from pipetting and UV initiation precision.

Figure 4.38 shows a gel before and after swelling, where the wafer surface goes from being clear to having a ring of leached material. Figure 4.39 also compares an unwashed gel with a clean wafer to one that has been swollen. Similar leached material (Figure 4.39f), to differing degrees, was also observed for DNA crosslinked gels as well as gels without oligonucleotides. The incomplete photoinitiation due to CNP absorption is likely the largest cause of poor conversion.

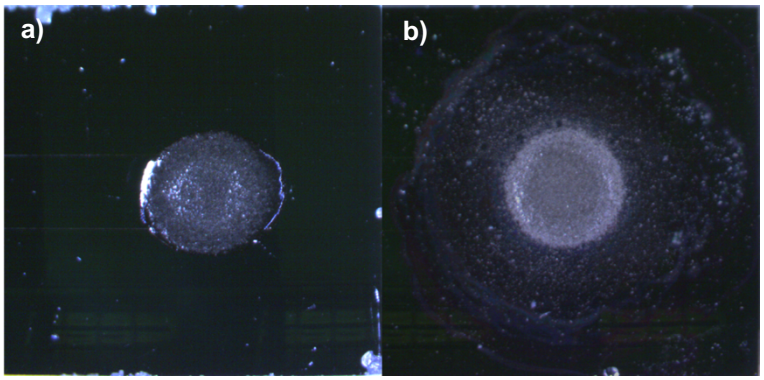

Figure 4.38 Images of a dried 10 wt% AAm, 0.6 mol% MBA, 0.4 mol% MOR2 wrt AAm hydrogel with 2 wt% CNT, 1mM PBS. (a) Unswollen (b) dried after swelling in 1 mM PBS for 1 hour.

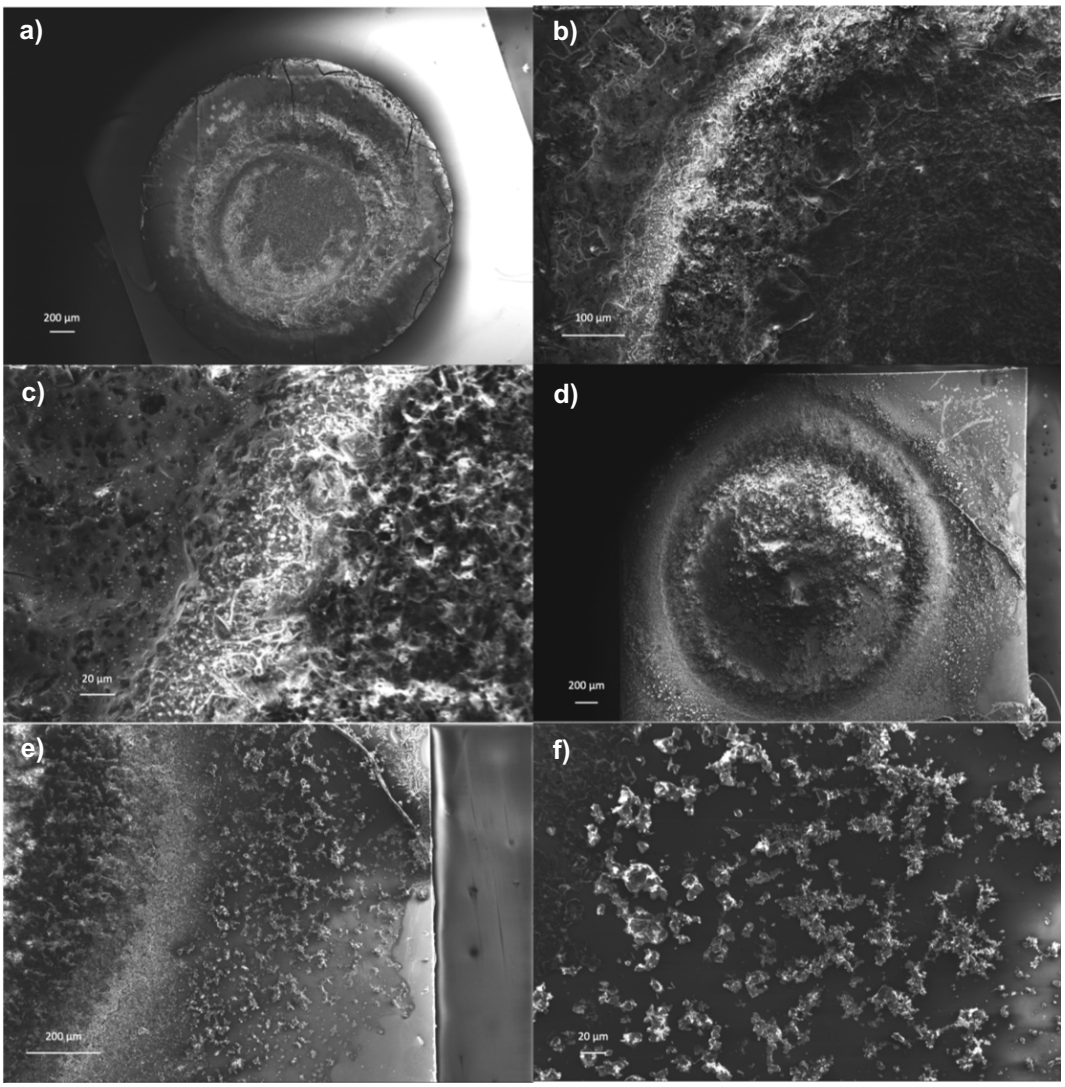

Figure 4.39 SEM images of 10 wt% AAm, 0.6 mol% MBA, 0.4 mol% MOR2 wrt AAm hydrogel with 2 wt% CNP in 150 mM NaCl, 1mM PBS. (a-c) Unswollen (d-f) dried after swelling in 1 mM PBS for 1 hour. Gels were not carbon coated.

MOR2 crosslinked gels appeared to be more homogenous than MIR2 crosslinked gels. This was attributed to both improved dispersion of CNP and a smaller contact angle and depth of droplet resulting in improved photoinitiation. The 20 wt% AAm gels, which gave a variety of resistance profiles, were theorised to be a denser gel. A further effect of increased monomer concentration would be faster propagation, which would affect the balance between polymerisation and the coffee ring effect from droplet drying. SEM images of 20 wt% AAm MIR2 crosslinked gels showed less pronounced morphological differences, while still having a dense middle and edge (Figure 4.40). Despite containing salt, no large crystals were observed, although consistent

fracturing was seen. A hole in the very centre of the gel was observable by eye and was not a typical feature of gels. This hole serves as an example of structural differences caused by errors in pipetting.

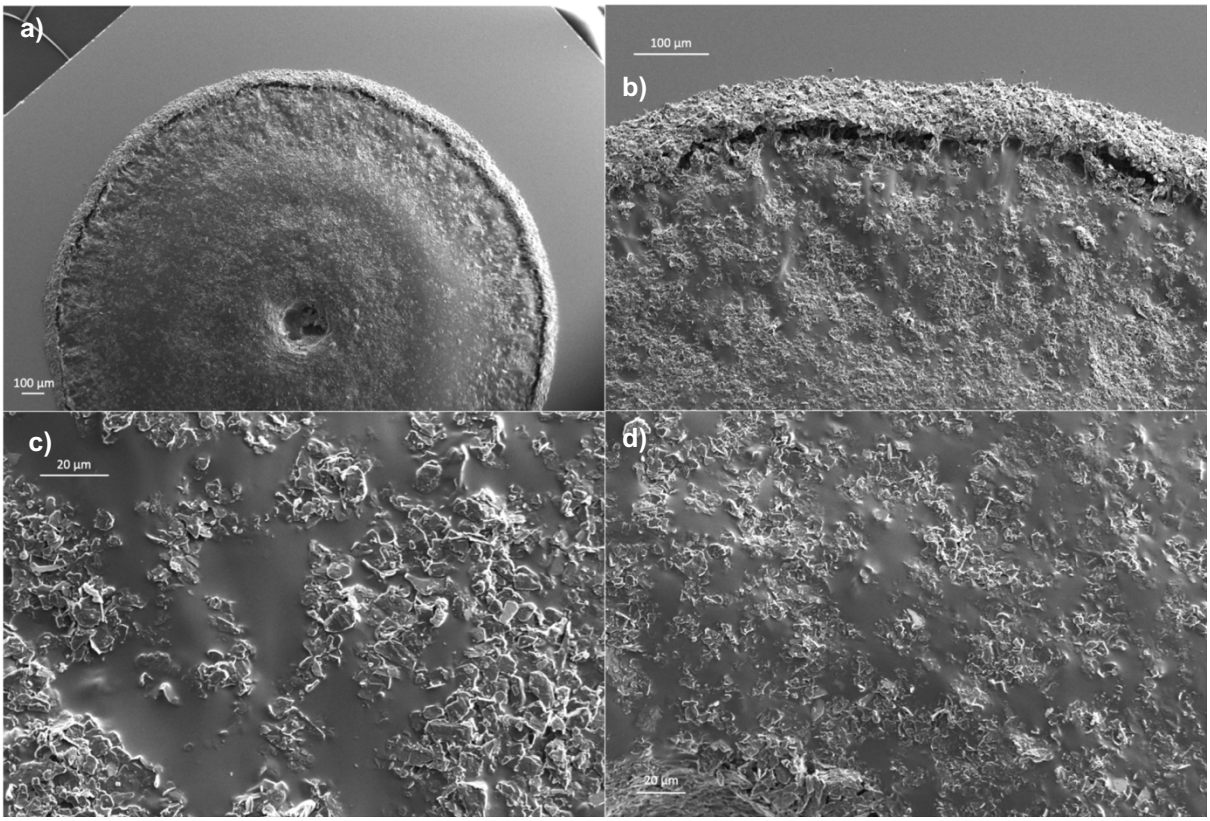

Figure 4.40 SEM images of 20 wt% AAm, 0.6 mol% MBA, 0.4 mol% MIR2 wrt AAm hydrogel with 2 wt% CNP in 150 mM NaCl, 1mM PBS.

Typical synthesis involved moving each gel to 4 °C immediately after UV irradiation. This was due to concerns of thermal dehybridisation of DNA crosslinks and of increased delamination from drying gels. Another source of variation may be the time between UV irradiation and cooling.

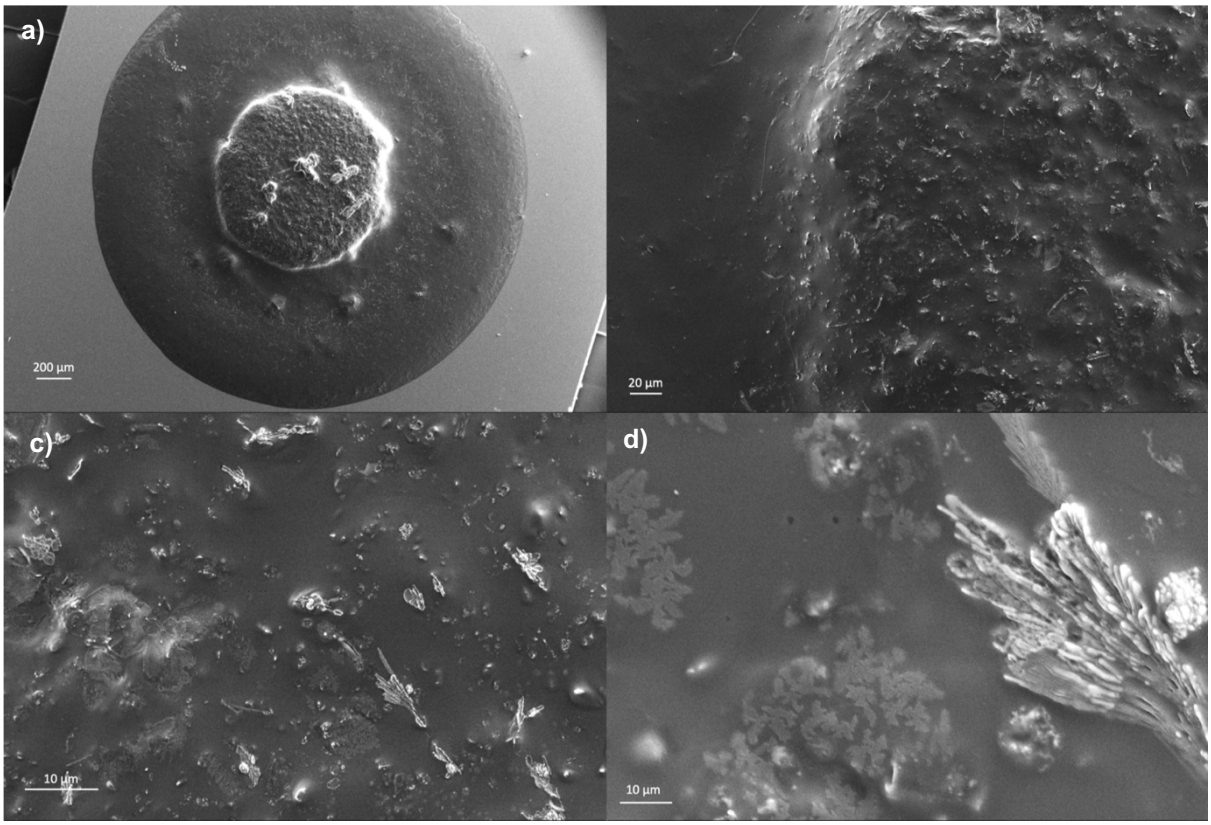

Figure 4.41 SEM images of a dried 10 wt% AAm, 0.6 mol% MBA, 0.4 mol% MOR2 wrt AAm hydrogel with 2 wt% CNP in 150 mM NaCl, 1mM PBS stored on bench top after UV irradiation.

MOR2 gels stored at room temperature after UV irradiation exhibited markedly different morphology (Figure 4.41). Instead of the relatively homologous gels shown previously, there is a higher mound in the centre of the gel which appears to be denser. At room temperature both polymerisation and drying will occur more rapidly. Presumably the more rapid polymerisation has accentuated the increased UV photoinitiation at the top of the pregel droplet. Previously gels with NaCl seemed to increase fracturing, however, in this case the gel without salt is had a large crack around the denser gel middle (Figure 4.42). Although the temperature is not a concern when using the MO crosslinks and the SEM samples may have been damaged by during the carbon sputtering, the potential for inconsistency from drying is a concern. Ideally controlled humidity may be used to store gels before testing and may be easily introduced but appropriate equipment was not available to control the humidity.

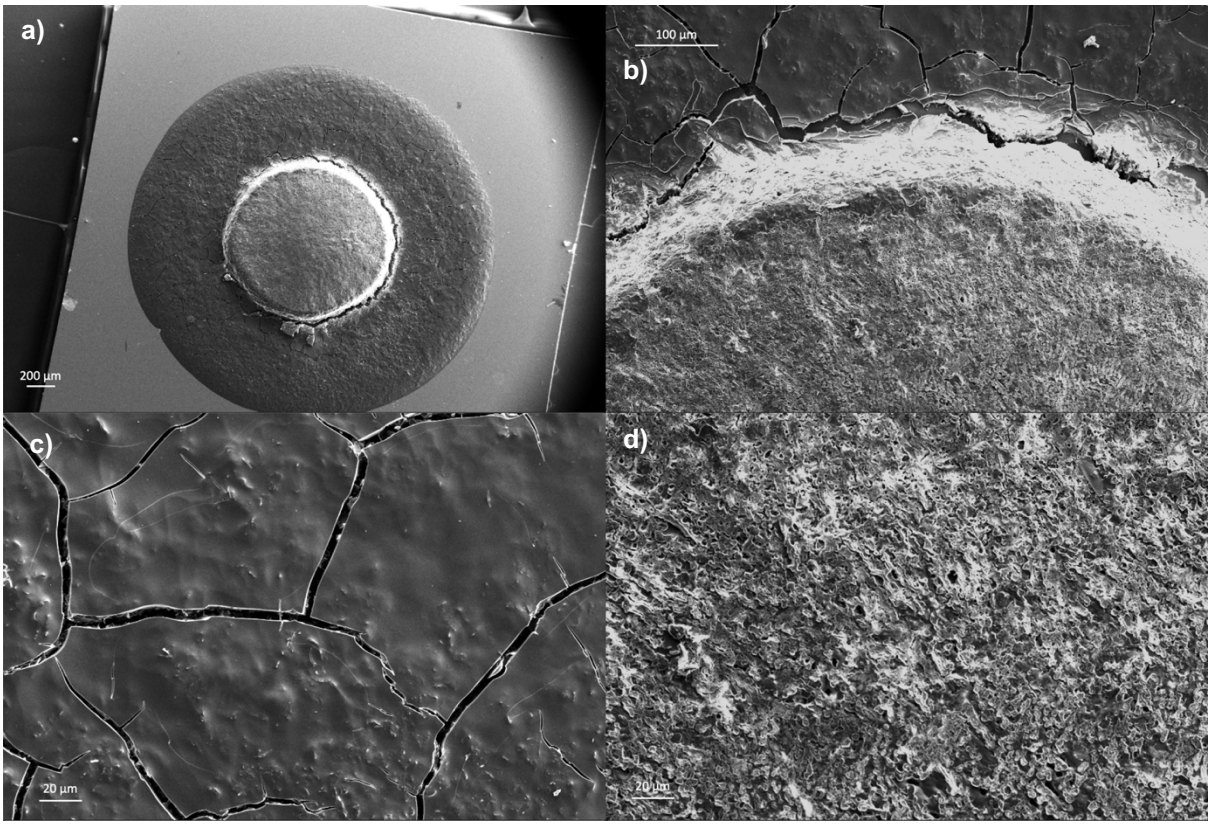

Figure 4.42 SEM images of a dried 10 wt% AAm, 0.6 mol% MBA, 0.4 mol% MOR2 wrt AAm hydrogel with 2 wt% CNP in 1mM PBS stored on bench top after UV irradiation.

Similar morphology was seen for 20 wt% AAm MOR2 crosslinked gels synthesised and stored at room temperature (Figure 4.43). In particular, excessive cracking at the edge of the dense centre in many of these samples indicates that the difference in elasticity caused by the different gel densities can give rise to extremely variable fractures, which will subsequently influence rehydration, leaching, diffusion of analyte and potentially swollen volume. Furthermore, excessive fracturing, such as those seen in the V-70 initiated gels, can cause flaking during gel rehydration. Gel storage in buffer would avoid this risk, but gels were not percolating when swollen.

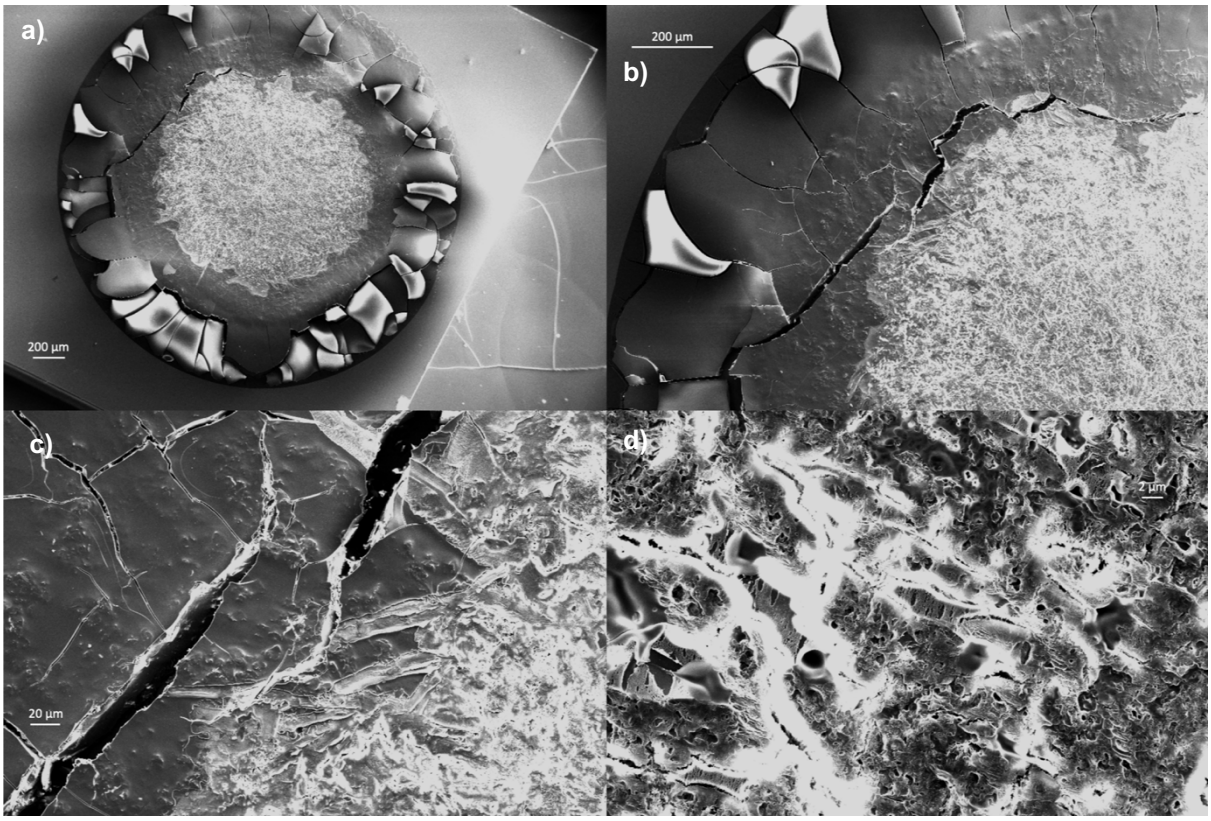

Figure 4.43 SEM images of a dried 20 wt% AAm, 0.6 mol% MBA, 0.4 mol% MOR2 wrt AAm hydrogel with 2 wt% CNP in 1mM PBS stored on bench top after UV irradiation.

The SEM images presented so far have only shown the gel surface and may differ substantially from the internal gel porosity.[379] The gel structure close to the electrode is far more relevant for investigating the gel structure influencing the percolation and resistance with the interdigitated electrode design used.[380] During preparation a single MIR2 crosslinked gel detached while swelling giving an insight into the gel layer close to the electrode (Figure 4.44). This cross-section break was very unusual when compared to typical detachment where the silicon oxide layer would be visible. As well as the material leaching mentioned previously, the wafer surface shows strong attachment of the dense gel edge and a remaining polymer layer. This would indicate that this gel was an aberration from the norm, whereby typically the gel attachment to the wafer surface would break. As such, this may not be indicative of a typical gel's internal structure. Also, the gel was not synthesised on an electrode, so the influence of the platinum surface was not observed. All gel sections exhibited the fracturing seen elsewhere. The underside of the detached layer appeared dotted, potentially indicating a large density of CNPs. Conversely the attached surface did not appear to have such

a high density. Were these features the case for all gels it may indicate that percolation is lost at early swelling stages simply because the movement of this high CNP density layer is the largest factor rather than being controlled by leaching. However, the method of detachment was unusual, and loose CNP will have been washed out by the solution.

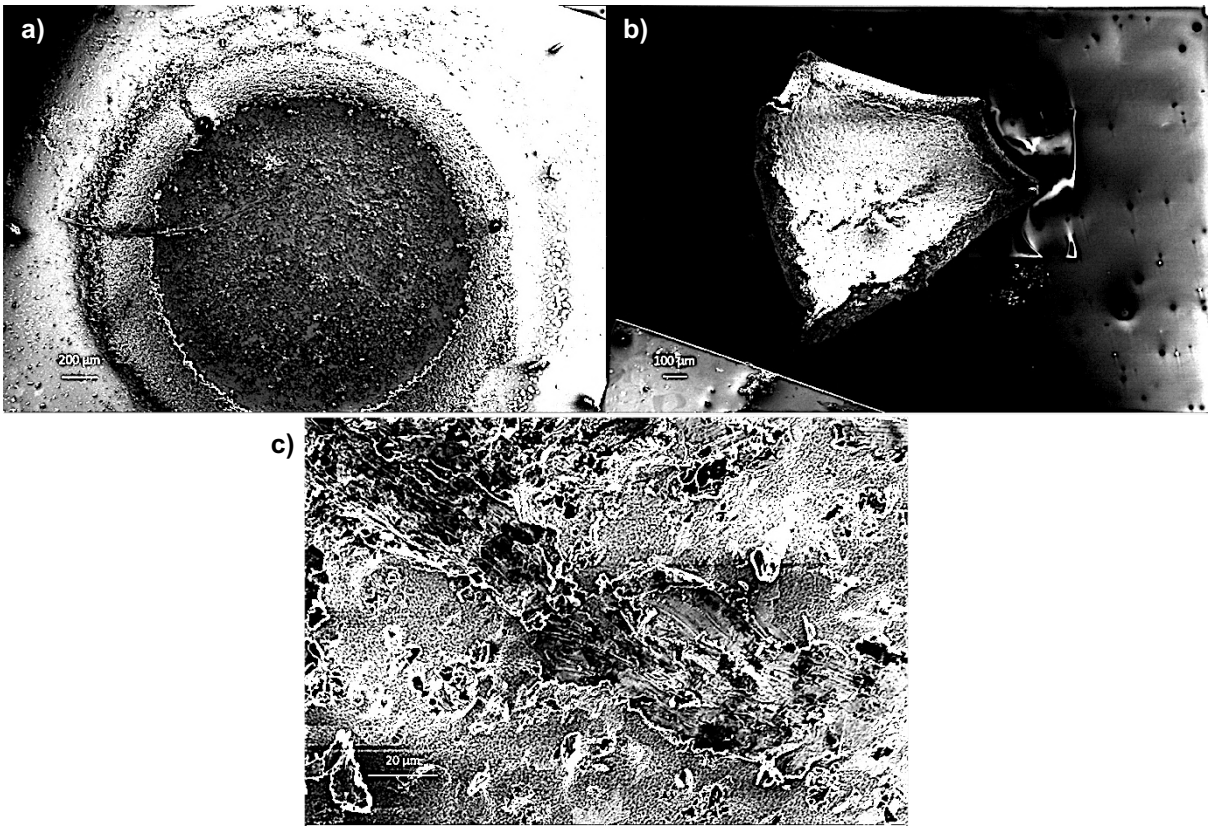

Figure 4.44 SEM images of 10 wt% AAm, 0.6 mol% MBA, 0.4 mol% MIR2 wrt AAm hydrogel with 2 wt% CNP in 150 mM NaCl, 1mM PBS. Dried after swelling in 150 mM NaCl, 1 mM PBS for 1 hour. Partial detachment occurred, (a) remaining attached gel (b, c) underside of detached gel. Gels were not carbon coated.

Modified cryo-fracture was attempted to maintain the wafer integrity whilst investigating polymer closer to the surface (Figure 4.45). In this case an unwashed MOR2 crosslinked gel was fractured. The surface layer of composite once again didn't appear to have a particularly high density of CNP, yet individual particles can be seen. This may confirm that the frequent lack of percolation of MO crosslinked gels was due

to a lack of CNP density, in particular at the electrodes. Further cryo-fracture and cross-section investigation was limited by materials.

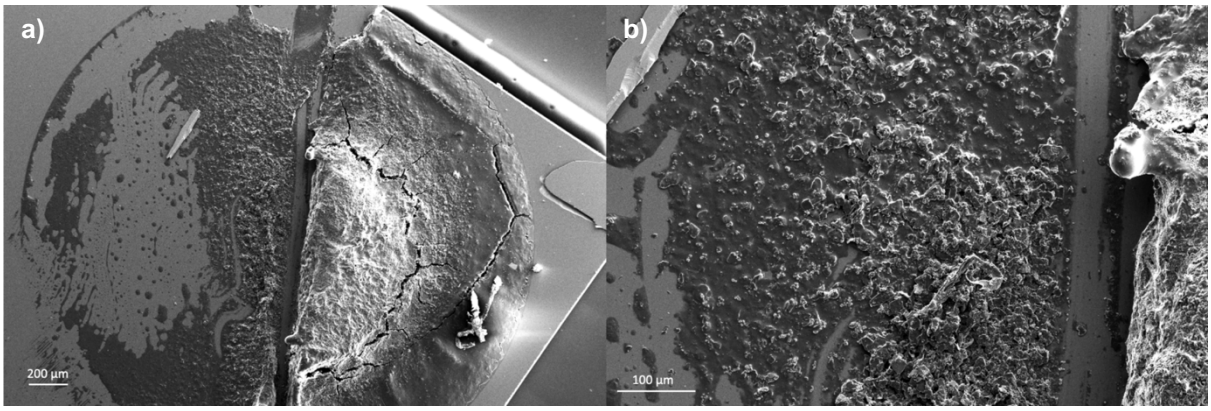

Figure 4.45 SEM images of a dried and cryo-fractured 10 wt% AAm, 0.6 mol% MBA, 0.4 mol% MOR2 wrt AAm hydrogel with 2 wt% CNP in 150 mM NaCl, 1mM PBS stored on bench top after UV irradiation. Attempted cryo-fracture of gel.

Partial cryo-fracture of a MO composite with CNT exhibited slightly different surface morphology (Figure 4.46). Substantially more conductive particles, as short lines rather than dots, were observed. A variety of CNT sizes, due to aggregation, can be seen in clusters or areas of high density. As only single samples were fractured in this manner no definitive conclusions can be made, however, the non-percolating CNP surface had a much lower population of conductive particles than the percolating CNT gel. Furthermore, CNT would precipitate faster and be more likely to be squeezed out of the gel network than CNP so would be expected to have a higher density at the wafer surface. The resistance measurement of the material is to some extent averaged due to the interdigitated electrode design. As such, the inconsistent arrangement of CNT is not of particular concern but may be better controlled with improved polymerisation of a stable dispersion.

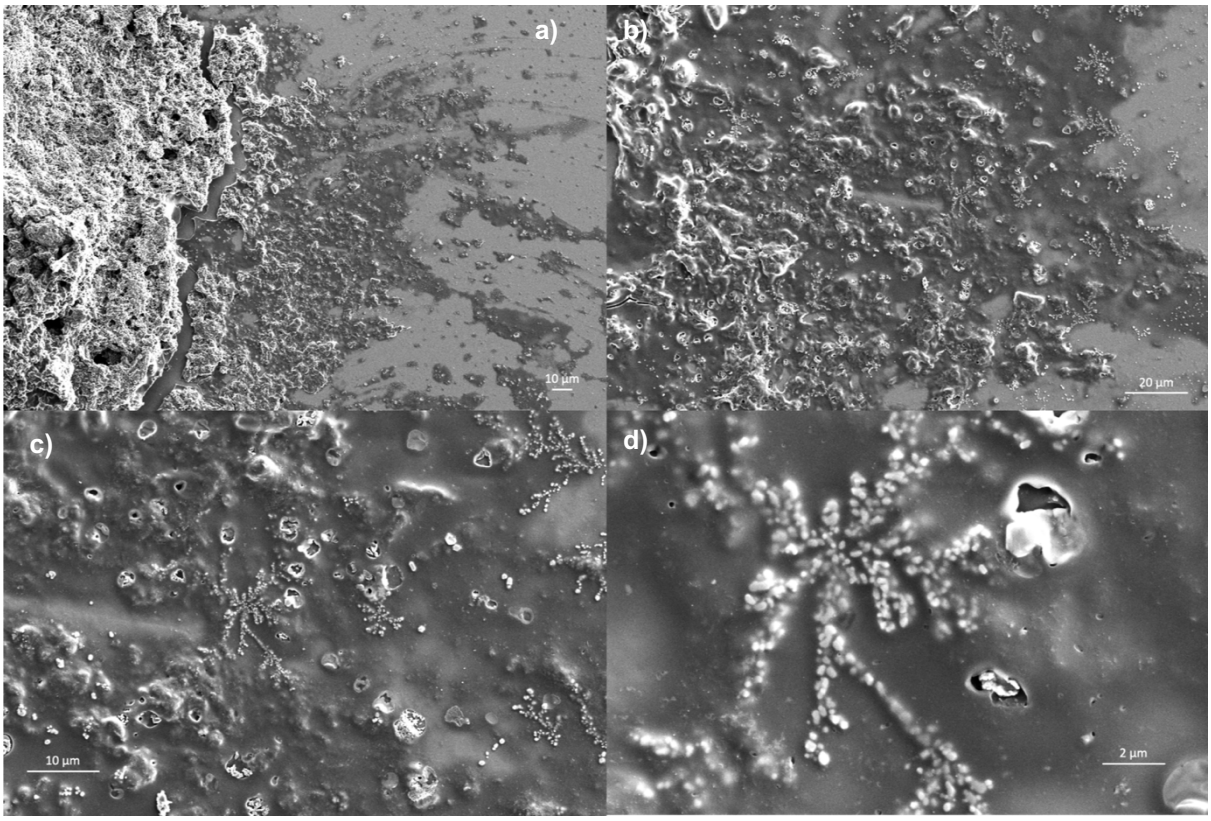

Figure 4.46 SEM images of a dried and cryo-fractured 10 wt% AAm, 0.6 mol% MBA, 0.4 mol% MOR2 wrt AAm hydrogel with 2 wt% CNT, 1mM PBS stored on bench top after UV irradiation.

The combination of factors involved in this composite synthesis is summarised in Figure 4.47. In each case each of these factors is influenced by the composition of the pregel solution. Photoinitiation efficiency is influenced by the intensity of the emitted light and the distance from the light source and will alter the polymerisation and porosity of the gels.[381] The droplet depth, defined by the contact angle and sample volume, defines the distance from the light source. The contact angle is affected by the wafer surface functionalisation and the hydrophilicity of the pregel solutions, such that DNA nucleotide content or use of MO crosslinks defines the contact angle. The reduction of the gel depth will also increase the diameter which enables better attachment to the wafer surface and may reduce the delamination rate. The oligonucleotide used alters the behaviour of the conductive filler, varying the amount of aggregation and precipitation which also changes the rate of propagation, which will define the gel porosity and may cause particle exclusion if the network density is small than the particle size. The different viscosities of each DNA crosslink will also alter the polymerisation rate and CNP movement. A more stable dispersion will however reduce

the UV penetration at the droplet surface. The UV penetration and absorption not only affects the polymerisation rate, but also causes heating which changes the water evaporation rate, which may induce particle flow within the droplet.[382] Similarly, the ambient temperature and will change the rate of evaporation and propagation, as well as stress and strain induced fracturing during drying.[230] Due to the complexity of the system, the cost of materials and the volume dependency of these factors, isolation of each variable was beyond the scope of this thesis.

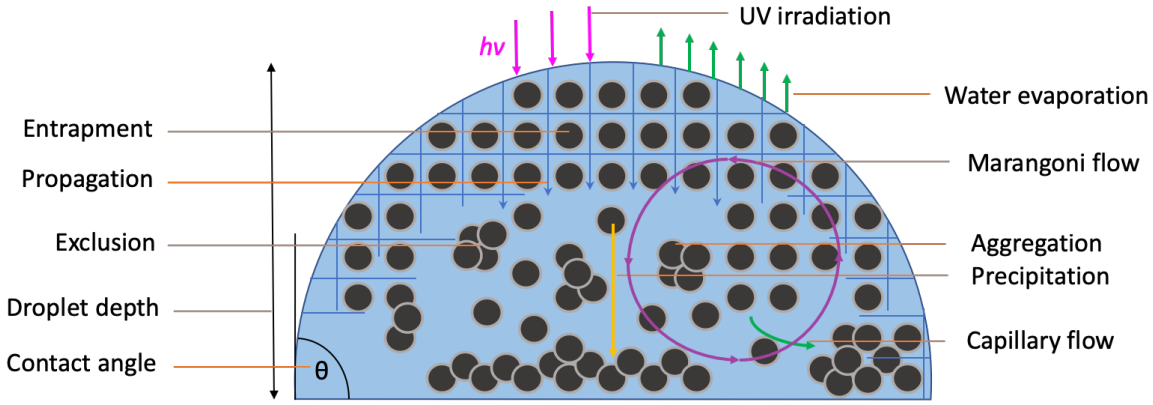

Figure 4.47 Illustration of competing variables defining the end gel structure. Not to scale.

This litany of uncontrolled variables does not include potentially more influential factors relating to hand pipetting. As well as the potential volume inaccuracy discussed previously, the lack of stable dispersion means that even visibly identical aliquots will likely contain varying amount of conductive particles. An aliquot containing more particles will then have a larger ratio of particles:monomer which will alter the gel structure. These issues may be improved using a stable dispersion, which then reduces the efficiency of UV photoinitiation. Hand pipetting droplet placement is another variable whereby the measurement will be affected by the area of material in contact with the electrode. Inkjet printing was investigated to address these issues (Chapter 5).

Issues of delamination and detachment remain, meaning that not only are substantial amounts of material wasted, repeated swellings are rarely successful and washing out of loose particles was not possible without risk of gel damage. While this may be

improved with an alternate sensor design, this was not investigated due to cost and time constraints. Gel attachment is primarily maintained through the silicon dioxide functionalisation with TMSPM.[383] This functionalisation does not occur on the platinum electrode. Platinum functionalisation may be achieved using molecules with a thiol group.[384] Bis(2-methacryloyl)oxyethyl disulphide was used to try and functionalise the platinum such that both electrode and wafer would be bonded to the gel. Preliminary results did not indicate any improvement and x-ray photoelectron spectroscopy (XPS) suggested the platinum remained unfunctionalised. Due to costs and time constraints this was not investigated further.

Given all the uncontrolled variables involved, it may be expected that the resistance measurements would be inconsistent. Whether previous work with the MIR1 crosslinked hydrogels was through chance close to the Goldilocks conditions required is unconfirmed. Even if so, the amount of excluded data required would suggest the system is doomed to fail and the unstable dispersion is unattractive for any potential commercialisation.

4.4 Conclusions and Ongoing Challenges

Despite the previous work by Dr Ferrier detecting a miRNA sequence using DNA crosslinked, questions remain over the reliability of the material and sensor design. Selectivity of data was required for successful differentiation between analyte and random sequences due to inconsistencies and delamination. Use of the longest crosslinks (APT1 and ASS1) resulted in constant delamination and although the reduced swelling of APT2 and ASS2 crosslinks reduced delamination rate, no differentiation of each analyte could be achieved. Attempts to address these issues through removal of non-essential nucleotides from the MIR1 crosslink used for miR92a detection (MIR2), despite optical transduction success, resulted in no differentiation between analyte and random. Increased MBA crosslink concentrations also resulted in no resistance-based analyte detection. Gels with increased AAm resulted in an atypical resistance response to the random sequence with a much slower resistance

increase, however the wide variability of resistance profiles in response to analyte and the increased cost of each sensor meant further evaluation could not be conducted.

Each composition tested exhibited resistance values unrelated to the swollen volume, and investigation using horizontal rather than vertical swelling, with different AAm concentrations, indicated that conductive particle movement and leaching was far more influential than the hydrogel volume. In this way the composite resistance was more akin to a particle release or ion permeability system than originally thought and optical transduction offered little insight. Indeed, the resistance-based differentiation using 20 wt% AAm gels had not been achieved using optical transduction.

Resistance measurements using the MOR2 crosslinks were frequently non-percolating when dried, and inconsistent even if percolating, making resistance-based transduction impossible. SEM imaging comparing MIR2 and MOR2 crosslinked gels indicated that MOR2 gels were relatively homogenous, with good dispersion of CNP within the polymer. MIR2 gels had a dense core and outer edge, each with a higher density of CNP, while the area in between was relatively bereft of CNP. This led to the theory that the areas of high-density polymer and CNP were enabling percolation at lower CNP loadings for DNA gels and that the homogeneity of MOR2 gels was lacking these dense conductive clusters. Investigation of the interaction between DNA or MO and CNP was limited yet indicated that the MO increased the dispersion stability. Attempts to increase conductive particle concentration resulted in poor photoinitiation efficiency and gelation. Further optimisation towards a reliable synthesis procedure required a stable dispersion which could not be photoinitiated due to poor UV penetration. As discussed in Chapter 3, thermal initiation was unreliable due to the risk of thermal dehybridisation and redox initiation was unreliable when hand pipetting. Electrochemical initiation could be used for polyacrylamide synthesis, however electric fields can cause aggregation of conductive species.[385] Similarly, blending with conductive polymers or electrochemical initiation within the hydrogel matrix in place of CNP may improve gel reliability, but preliminary attempts were unsuccessful.[386,387] As such, mechanised liquid dispensing, such as inkjet printing, was investigated for redox initiation in Chapter 5.

Chapter 5 Inkjet Printable Morpholino Oligonucleotide Crosslinked Polymer Composites

5.1 Electrostatic Composite Composition

5.1.1 Solution Stability

For any potential commercial applications, the oligonucleotide crosslinked composites discussed in Chapter 4 require a number of improvements. A consistent pregel mixture is essential if using conductive particles. Rather than rely on constant agitation, a water stable dispersion would be preferred. This can be achieved through a variety of chemical modifications on the particle surface.[388,389] In doing so the particle structure is altered, which can increase size and may reduce conductivity of the particle itself or prevent conductive networks from forming in a composite. Similarly, appropriate concentrations for percolation may be difficult to maintain if systems require low particle concentrations to reduce aggregation. It was theorised that an electrostatic dispersion could be most successful in achieving a stable dispersion as the functionalisation is typically less bulky and frequently relatively conductive.

To this end, Dr Seshasailam Venkateswaran kindly obtained an electrostatic carbon black ink from his contacts within the ink industry. The precise composition and functionalisation of this dispersion remained confidential. The supplied label read “SIC Black Dispersion 1” (SIC) and it was reported as 20 wt% in water. From this information it may be assumed that the dispersion is an electrostatic functionalised silicon carbide and all solutions were made assuming the 20 wt% concentration was accurate. When diluted in water the measured particle diameter was approximately 162 nm (Table 5.1). The neat dispersion was measured as 315 nm with a relatively high polydispersity index (PDI) of 0.71. Best practise for accurate DLS measurements is to use dilute samples that appear hazy. In testing relevant concentrations for pregel composite solutions the samples were opaque. This likely resulted in multiple scattering and may have altered the viscosity of solution. In either case, the particle size cannot be

expected to be accurate, but can be used to detect aggregation. These experimental inaccuracies will likely explain why the measured particle size of the neat solution is larger than those that were diluted. Equally, stirring during dilution may have disrupted any aggregation, as the neat solution was taken from the stock solution without any mixing. Despite the inaccuracies of DLS, the dispersion remained stable far longer than any CNP based solution tested previously and even the measured polydispersity was much improved.

Table 5.1 Measured SIC diameter at different concentrations using DLS, either neat or diluted in DI water.

SIC (wt%)	Solution	Z Ave (d.nm)	ST DEV	PDI
20	Neat	315.0	7.42	0.71
10	DI Water	166.0	2.12	0.43
5	DI Water	170.9	1.60	0.41
2	DI Water	149.0	2.25	0.35

The SIC dispersion appeared to remain stable when diluted at the same loadings as CNP gels used previously for optical or electrical transduction (1 and 2 wt% respectively). However, when mixed with the pregel solutions, aggregation and sedimentation began to occur, albeit not to the same extent as the CNP based pregel solutions (Table 5.2).

Table 5.2 Measured SIC diameter at different concentrations using DLS, diluted in either DI water or a typical pregel solution.

SIC (wt%)	Solution	Aam (wt%)	Bis (mol% wrt 10 wt% AAm)	NaCl (mM)	Z Ave (d.nm)	ST DEV	PDI
2	DI Water	0	0	0	170.3	0.78	0.30
1	DI Water	0	0	0	143.4	0.76	0.27
2	PBS	10	0.6	150	3624.0	355.53	1.00
1	PBS	10	0.6	150	1779.0	402.13	1.00

It was clear that the SIC surface functionalisation interacted with the one or more of the components of the pregel solution. The most obvious would be that the salt disrupted the electrostatic dispersion. DLS measurements comparing SIC in PBS with

and without NaCl showed a large increase in the average particle size in the presence of salt, indicating significant aggregation (Table 5.3). It appeared that the PBS solution may have also increased aggregation, albeit to a much lesser extent and may have simply been due to errors in sample preparation.

Table 5.3 Measured SIC diameter using DLS, diluted in PBS either with or without salt.

SIC (wt%)	Solution	NaCl (mM)	Z Ave (d.nm)	ST DEV	PDI
2	PBS	0	201.0	5.78	0.35
2	PBS	150	1998.3	203.21	1.00

In order to avoid any potential PBS induced aggregation HPLC grade water was used instead. Each component of the pregel solution, aside from the oligos, was mixed with 2 wt% SIC to identify whether any of the essential pregel ingredients caused SIC aggregation (Table 5.4). Only the addition of NaCl caused any aggregation and even then, to a much lesser degree that in PBS. Clearly the SIC electrostatic functionalisation can interact with ions in solution, whereby shielding of the surface charge can lead to aggregation.

Table 5.4 *Measured SIC diameter using DLS, diluted in HPLC grade water, comparing the effects of each pregel component in isolation.*

SIC (wt%)	Solution	Aam (wt%)	Bis (mol% wrt 10 wt% AAm)	NaCl (mM)	Z Ave (d.nm)	ST DEV	PDI
2	HPLC Water	0	0	0	184.1	0.66	0.37
2	PBS	0	0	0	176.1	2.15	0.37
2	HPLC Water	10	0	0	198.7	1.72	0.37
2	HPLC Water	0	0.6	0	181.6	1.79	0.37
2	HPLC Water	0	0	150	314.1	90.22	0.40

As DNA crosslinks require NaCl to hybridise they could not be utilised with the SIC dispersion. Whether DNA itself would interact with the SIC particles was not investigated but would be expected. Although MOs may also interact with SIC particles, this too was not investigated due to limited quantities of material.

5.1.2 Inkjet Polymerisation Composition Optimisation

Early optimisation of SIC based composites was attempted using hand dispensing techniques as before. However, it rapidly became apparent that achieving gelation was extremely problematic. Using the established photoinitiation method led to initial dried resistance of 2 MΩs. Immersion in buffer solution caused the centre of the deposited aliquot to wash away, leaving only the outer edge attached to the silicon dioxide surface (Figure 5.1). The issues of UV penetration of the droplet for photoinitiation of these pigmented materials has been discussed previously. In this case the improved dispersion may have reduced UV penetration, allowing only the droplet edges, the thinnest areas of droplet, to be adequately photoinitiated to achieve attachment to the wafer. There was no visible gelation within the area of loose material that was washed away, suggestion that little to no network formation was able to occur at the droplet surface or centre.

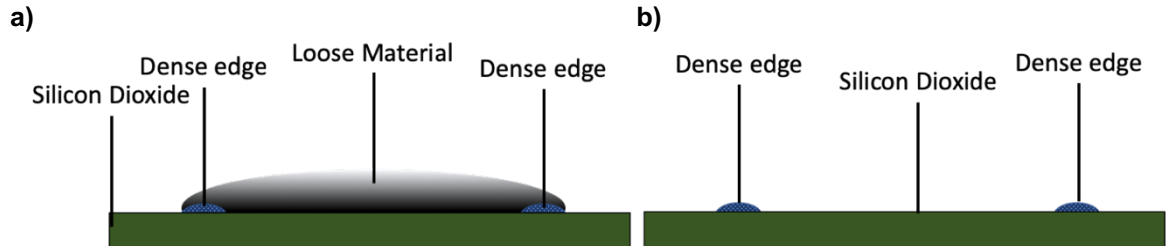

Figure 5.1 Illustration of the poor gelation caused by poor UV photoinitiation efficiency when using SIC in place of CNP. (a) Dried material (b) Washed material.

Higher UV intensity was used in an attempt to improve the photoinitiation efficiency.[357] To increase the UV intensity the droplet was moved closer to the lightguide, from 2.2" to 1.5" away. This theoretically increased the relative UV intensity from 2% to 3% of the total emitted, or rather a 50% increase of the intensity used previously. As this only increased the wafer surface temperature from 26.5 to 34.9 °C it was considered within the appropriate conditions for the MO crosslinks. Despite achieving gelation, the dried resistance was still measured around 2 MΩs. When swollen, the whole gel detached, suggesting that although polymerisation was successful, attachment to the wafer

either did not occur, or that the stress and strains of drying and swelling the gels resulted any attachment being broken.

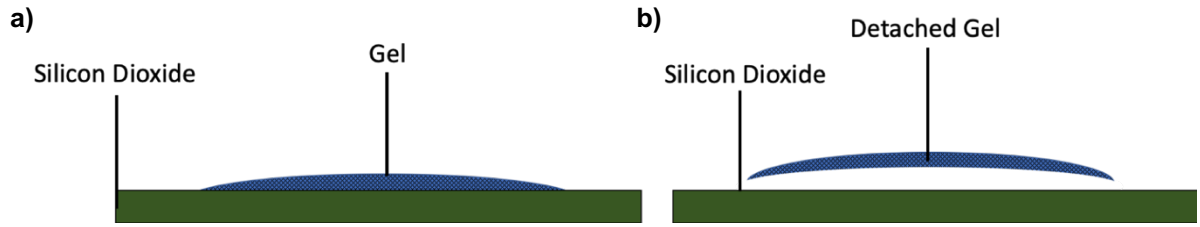

Figure 5.2 Illustration of poor gel attachment caused by increased UV intensity during photoinitiation. Gelation occurs, however, either the propagating species did not polymerise with the surface functionalisation or the excessive drying caused stress which facilitated delamination. (a) Dried material (b) Washed material.

Given the lack of success using photoinitiation, redox initiation was again investigated. It was quickly noted that two main factors inhibited polymerisation. Firstly, inhibition of radical by oxygen in air meant that microliter droplets were unable to polymerise when the photoinitiator was replaced with an equimolar amount of APS. TEMED was premixed with the pregel solution and APS added to initiate polymerisation. Polymerisation using this amount of APS was only achieved on a mL scale after nitrogen flushing and even then, the 1 mL polymerisation efficiency was clearly inferior to larger volumes with loose material apparent upon inversion at each volume (Figure 5.3). The second concern was a lack of mixing resulting in incomplete polymerisation. The rate of polymerisation was obviously much slower than even inefficient photoinitiation. Although not a primary concern given the switch to SIC, it was noted that attempts to use CNP in this redox initiation resulted separate areas of high CNP loading at the top and bottom of the gels as polymerisation must have been slower than CNP precipitation.

Figure 5.3 Images of 15 wt% AAm, 0.6 mol% MBA wrt AAm with 0.125 mol% APS and 0.25 mol% TEMED (a) 2 wt% CNP (b) 2 wt% SIC. L-R 1, 2, 3, 4, 5 mL total volume. Vials flipped and imaged after 8 hrs.

Oxygen inhibition was overcome through a 10-fold increase in concentration of APS and TEMED without the requirement for nitrogen flushing. However, the lack of mixing capabilities when hand pipetting resulted in only localised polymerisation. Consistent mixing was unachievable given the rapid rate of polymerisation, whereby the pipette tip would become blocked by polymer if repeated pipetting was used to mix and stirring would be inconsistent. Similarly, rapid polymerisation precluded mixing the APS with the pregel solution containing TEMED before depositing on the wafer as the pipette tip would rapidly become blocked with polymer.

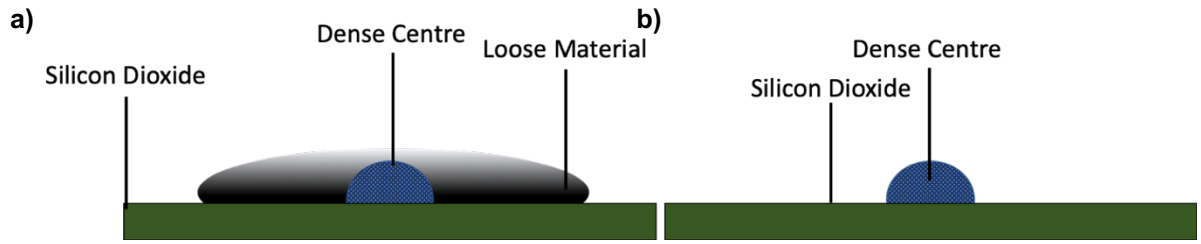

Figure 5.4 Illustration of the localised polymerisation resulting from inefficient mixing during redox initiation. (a) Dried material (b) Washed material.

Drop-on-demand inkjet printing offered a solution to the issues of redox initiation as the deposition of multiple droplets offered a method for mixing small volumes on the wafer surface.[390] Piezoelectric printers use a deformable material that contracts and reduces the volume of a capillary nozzle upon application of a voltage. Upon relaxation, a droplet (approximately 350 pL)[391] is produced as the capillary is replenished by negative pressure.[392] A reliable synthesis would be easily adaptable to different crosslinks, rapidly enabling sensor microarray fabrication for multiple sequence detection.[393–396]

Arrays of various concentrations of monomer, APS and TEMED were investigated to rapidly screen for an appropriate composition. A sucrose solution was used to block functionalisaton of the glass slides with hydrophobic 1H,1H,2H,2H-perfluorooctyl-trichlorosilane (POTS), followed by TMSPM functionalisation of the unfunctionalised well (Figure 5.5a-e). The volume of sucrose used for this mask was also optimised. APS was deposited on the slide and the droplet allowed to dry. The mixture containing monomer, dispersion and TEMED was then deposited, thereby dissolving and mixing the APS to initiate polymerisation (Figure 5.5f-j).

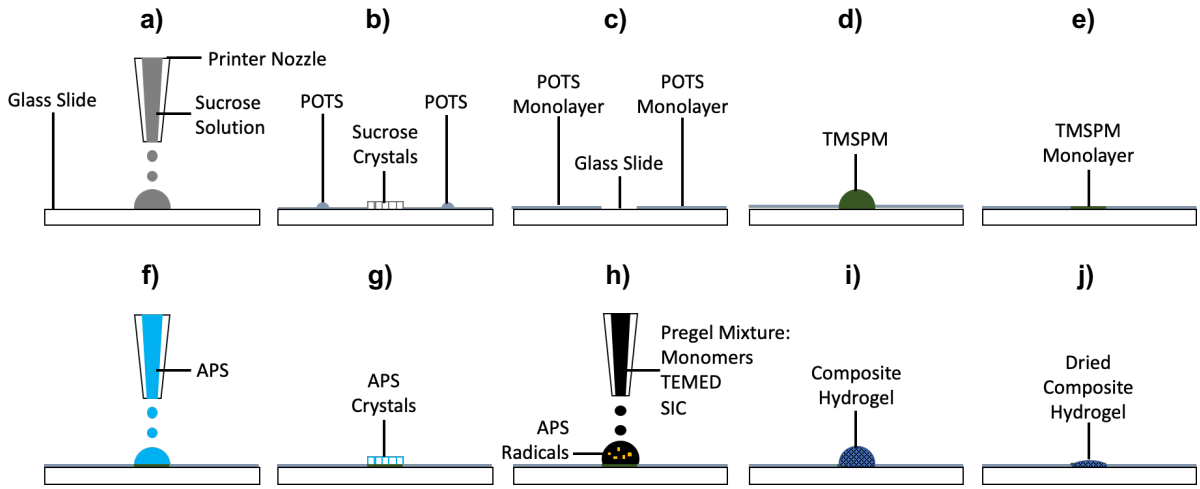

Figure 5.5 Illustration of the optimised inkjet printed hydrogel synthesis. (a) Sucrose solution pattern printed (b) Sucrose solution dried and vapour deposition of hand deposited POTS hydrophobic layer which cannot modify the surface under the sucrose crystals (c) Acetone and water washes to remove excess POTS and sucrose (d) Hand deposition of TMSPM on unmodified areas of glass slide (e) Prepared glass slide with TMSPM monolayer in the deposited sucrose pattern surrounded by hydrophobic POTS. (f) APS solution printed (g) APS solution dried (h) Pregel mixture printed including TEMED which accelerates APS radical formation as it dissolves into solution for polymerisation initiation. Mixing is achieved via the energy of printed droplet movement (i) Pregel solution polymerises to form composite hydrogel (j) Composite hydrogel is dried before testing.

The requirement to use a mask can be seen in Figure 5.6, where printing onto a glass slide functionalised with TMSPM but without the POTS hydrophobic layer from the sucrose mask method resulted in misshapen gels with poor homogeneity. As discussed before, this poor homogeneity and shape would result in batch to batch varying unbefitting for a point-of-care device. Figure 5.6f shows much improved gel containment due to the hydrophobic mask helping to contain the printed solutions in defined areas.[392,397] It is possible that a fully optimised solution, nozzle distance and droplet speed or alternative methods such as printing in oil could reduce or remove the need for a mask.[289] The sucrose mask method is reliant upon the accuracy and precision of sucrose deposition as any imperfections will carry forward to the gel synthesis. A simple photolithography method would be more reliable, potentially using an alternative material such a parylene for hydrophobic modification.[349] These options were not attempted due to time and cost.

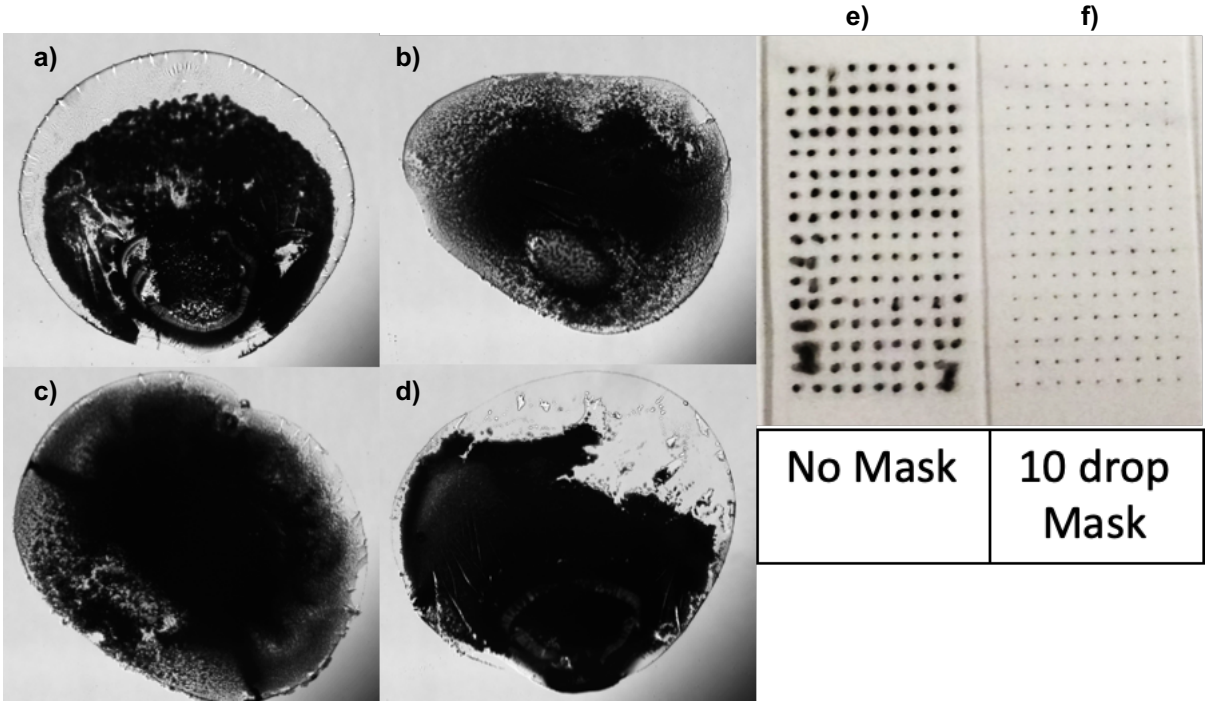

Figure 5.6 Images of printed gels with no mask made with 1 wt% APS (3.5 nL) then (a, b) 10 wt% SIC (14 nL) (c, d) 20 wt% SIC (14 nL) and 20 wt% AAm, 0.6 mol% MBA wrt AAm, 2 wt% TEMED (17.5 nL). (e, f) Images of microarrays made with no mask or a sucrose mask (3.5 nL). Gels were 1 wt% APS (3.5 nL) and 20 wt% AAm, 0.6 mol% MBA wrt AAm, 2 wt% TEMED and either 2 (e) or 4 (f) wt% SIC (31.5 nL).

Printing components separately can circumvent the inability to use salt with the SIC dispersion. However, preliminary attempts printing APS, then dispersion, then monomers with TEMED and NaCl resulted in poor gel homogeneity (Figure 5.7). In part, this was due to incomplete drying of the APS droplet and the SIC droplet, resulting in different mixing efficiency and therefore different morphology. A further concern was that, once dried, SIC nanoparticle resuspension may be inefficient and would likely result in aggregation.

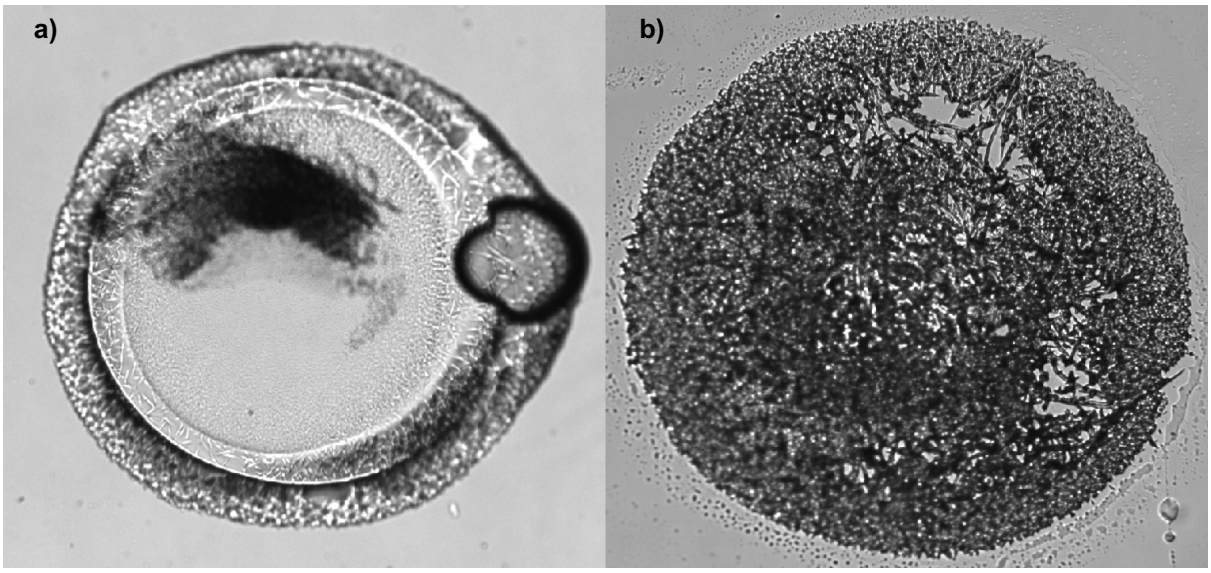

Figure 5.7 Images of gels printed with no mask with 1 wt% APS (3.5 nL) then 0.8 wt% SIC (14 nL) 10 wt% AAm, 0.6 mol% MBA wrt AAm, 2 wt% TEMED (17.5 nL).

Premixing of the pregel solution of monomers, SIC and TEMED and inkjet printing this onto dried APS resulted in far more homogeneous gels (Figure 5.8). Realistically, all that can be concluded from top-down imaging is whether there are any large defects. With these images it can be difficult to differentiate between a poor mask formation, excessive material for the well size, or excessive initiator and accelerator concentrations. For example, Figure 5.8a is somewhat ovular, which is most likely an artefact from the mask. Both Figure 5.8a and b appear to have an undulating edge. This may again be from the mask itself or may be caused by an excess of gel material in the well area. In the case of Figure 5.8c, the irregular polymer at the top and left of the image may be partially due to a poorly deposited sucrose mask. However, the

small branches at the bottom and right would imply that there was some splashing occurring during deposition. For these preliminary tests the APS was not purposefully dried and these irregularities were therefore attributed to splashing when then the pregel mixture was deposited.

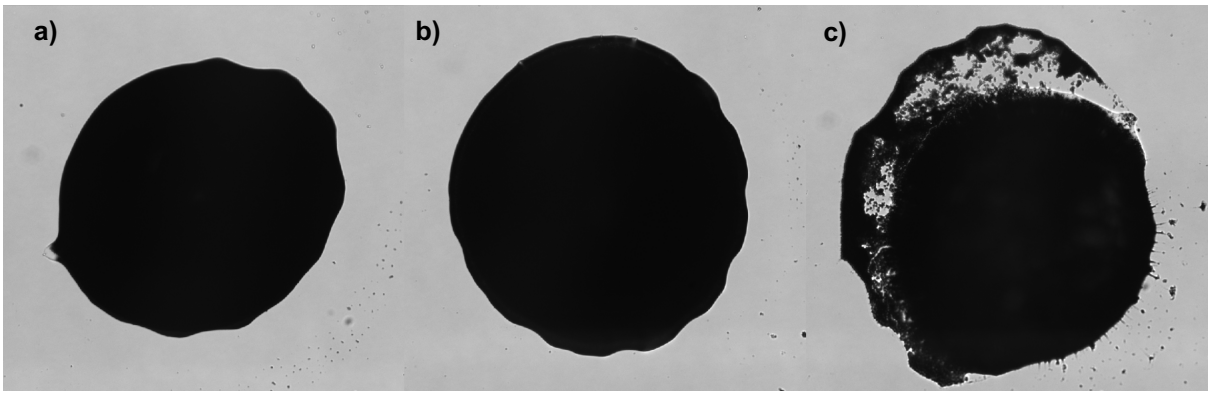

Figure 5.8 Images of gels from microarray printed with sucrose mask (3.5 nL) with 1 wt% APS (3.5 nL), 20 wt% AAm, 0.6 mol% MBA wrt AAm, 2 wt% TEMED and 2 wt% SIC (31.5).

This method of polymerisation by mixing droplets impacting and coalescing on a solid surface required thorough optimisation to maximise reproducibility. The SIC dispersion water stability should minimise the issues of aggregation and precipitation previously discussed. However, a number of other factors will influence the gel structure (Figure 5.9). Deposition and drying of APS will result in an uneven layer due to the capillary flow and Marangoni flow induced by droplet drying. Dissolution and activation of the radical initiator will then also be uneven. The mixing will be influenced by the droplet size and shape, dependent on both the size of hydrophobic mask used and volume of the droplet. Polymerisation will occur close to the solid surface due to the dried APS, unlike the UV initiation occurring at the droplet surface. As the droplet size increases the addition of droplets will impact the droplet and mix in vortex rings.[398] All the while the droplet will be drying as the water evaporates. Again, it is difficult to investigate each individual factor, so microarrays were employed to investigate different synthesis conditions and the resulting gels compared to identify the most reliable synthesis.

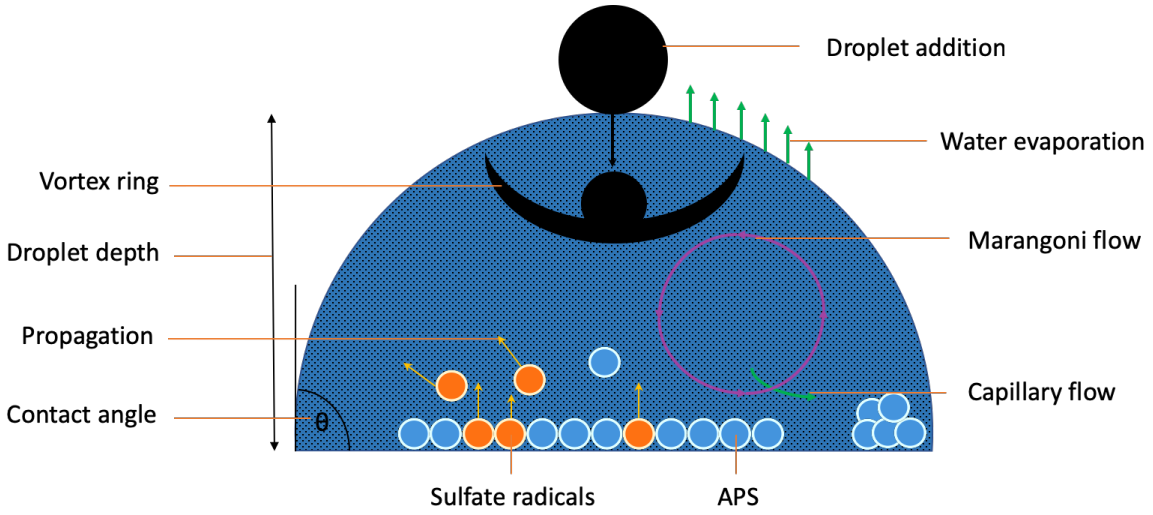

Figure 5.9 Illustration of competing variables defining the end gel structures of inkjet printed gels. Not to scale.

It should be noted that photoinitiation may have been viable for small droplet volumes, however, the minimum volume was limited by the necessity to investigate swelling optically and electrical using the same equipment as before. Optimisation of photoinitiation using smaller droplets may then not have been transferrable to the required volumes and obtaining alternative equipment or appropriate electrodes was not an option. Inkjet printing into an oil layer may also have been beneficial, in both synthesis and storage, but was not investigated due to time and material constraints. Finally, polymers films or alternative shapes may have been developed instead of droplets to enable array-based volume measurements from above or below the glass slides.[399] However, this was outside the scope of this project.

Having established a preliminary method, the mask size, APS, TEMED, SIC and monomer concentrations were all varied to optimise synthesis conditions Figure 5.10. Gel size remained 100 drops, 35 nL, with sucrose masks of 10 or 20 drops, 3.5 or 7 nL. Compositions were tested in triplicate with 5-20 wt% APS, 2-10 wt% TEMED and 0.6 or 1.0 mol% MBA wrt AAm. Each slide tested either 10 or 20 wt% AAm, 2 or 4 wt% SIC. After swelling there were clear swathes of gel detachment or incomplete gelation on a number of slides (2, 4, 5, 7 and 8). These may have been caused by poor slide preparation, for example it may be expected that the larger sucrose mask would exhibit better attachment due to the larger area to attach to. However, slide 3 (3.5 nL mask)

appeared better than slide 7 (7 nL mask) so it is more likely that the mixing within this area is more important that surface area alone. Furthermore, subsequent testing with more optimised compositions had much improved gelation and attachment.

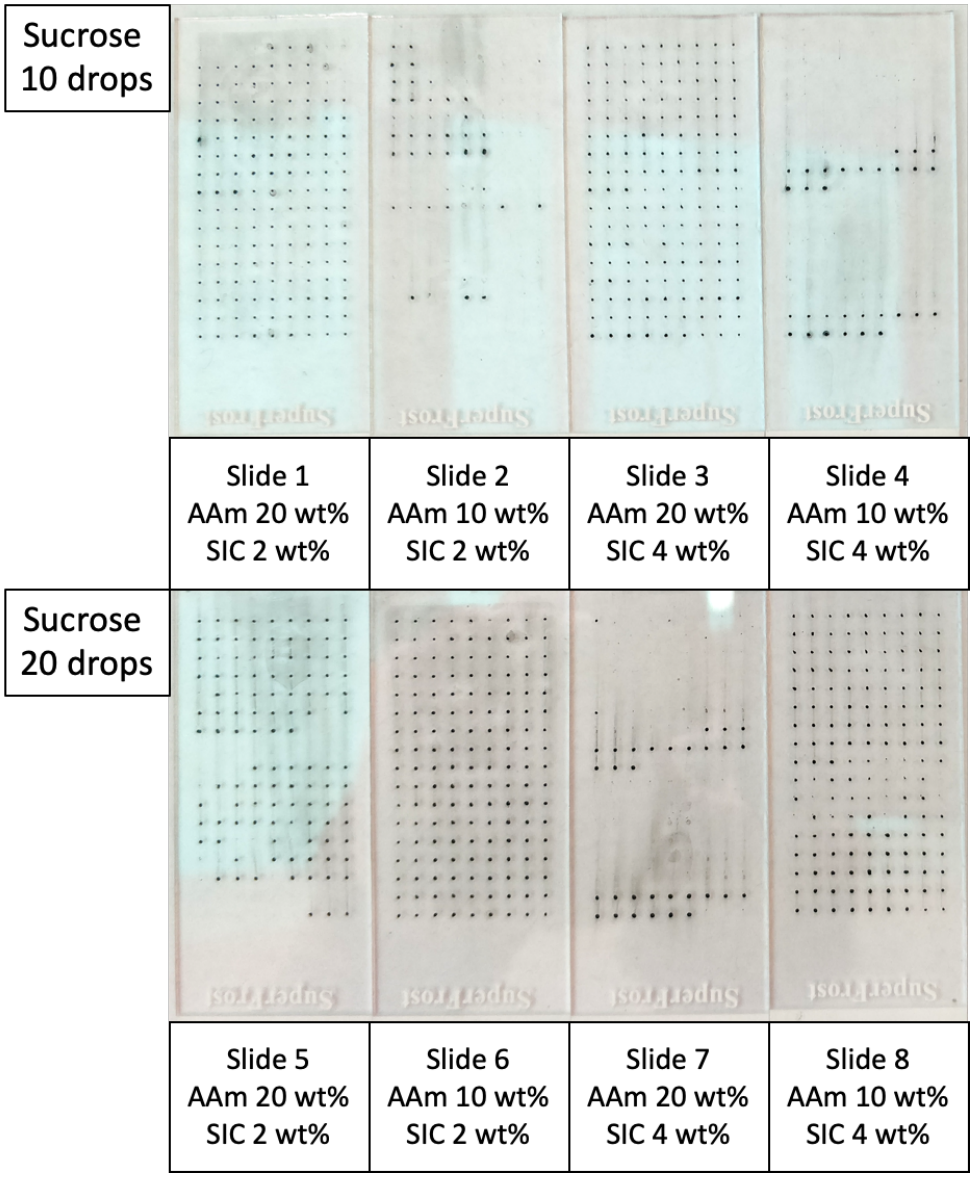

Figure 5.10 Printed microarrays. Sucrose mask was either 10 drops, 3.5 nL (slides 1-4) or 20 drops, 7 nL (slides 5-8). Either 20 wt% (odd-numbered slides) or 10 wt% (even-numbered slides) AAm and either 0.6 or 1.0 mol% MBA wrt AAm, with either 2 wt% (slides 1, 2, 5, 6) or 4 wt% (3, 4, 7, 8) SIC. Each slide varied APS (5-20 wt%), TEMED (2-10 wt%) and tested each combination in triplicate. APS and TEMED concentrations illustrated in Figure 5.11.

Of the better slides for gel attachment, slides 1 and 3 were both 10 drop, 3.5 nL, masks with 20 wt% AAm and are identical aside from 2 and 4 wt% SIC respectively (Figure 5.11). Conversely, slide 6 used a 20 drop, 7 nL, sucrose mask with 10 wt% AAm and 2 wt% SIC. It is clear that the larger mask size used for slide 6 either caused or accentuated any unusual gel shapes as the majority of the gels in the microarray are not circular (Figure 5.11c). As such the 10 drop, 3.5 nL, sucrose mask was considered better and the compositions of slides 1 and 3 therefore more appropriate. As the only difference between slides 1 and 3 is the amount of SIC incorporated, this narrowed the composition to 10 drop mask, 3.5 nL, (for 100 drop, 35 nL, gels) with 20 wt% AAm and either 2 or 4 wt% SIC. Both slides had a number of deformations and detachments even within each triplicate and could not be decided between on these factors alone. During washing, significant leaching was seen from each microarray. Given the concerns over leaching discussed at length in Chapter 4, reduced leaching was considered an important aim. Although not quantified, the lesser SIC content would be expected to leach less as there is a maximum particle incorporation at any gel density and as far as could be observed by eye this appeared to be the case.

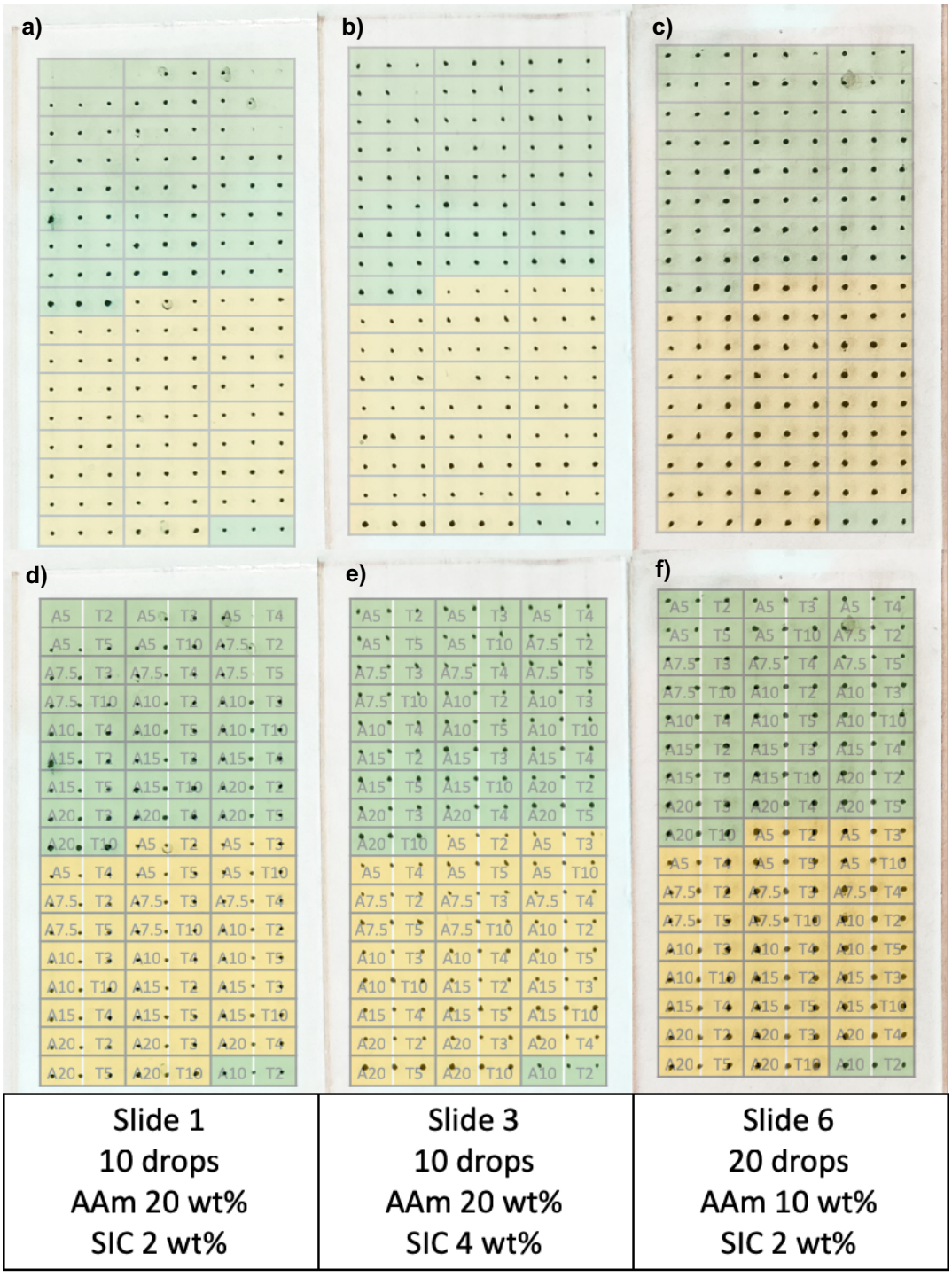

Figure 5.11 Illustrated printed microarrays from Figure 5.10. Slides 1, 3 and 6 exhibited the most attached gels after swelling. (a-c) Microarray pattern depicted with 0.6 mol% (green) or 1.0 mol% (yellow) MBA wrt AAm. (d-f) Each triplicate of the microarray is labelled with the APS (A) and TEMED (T) wt%.

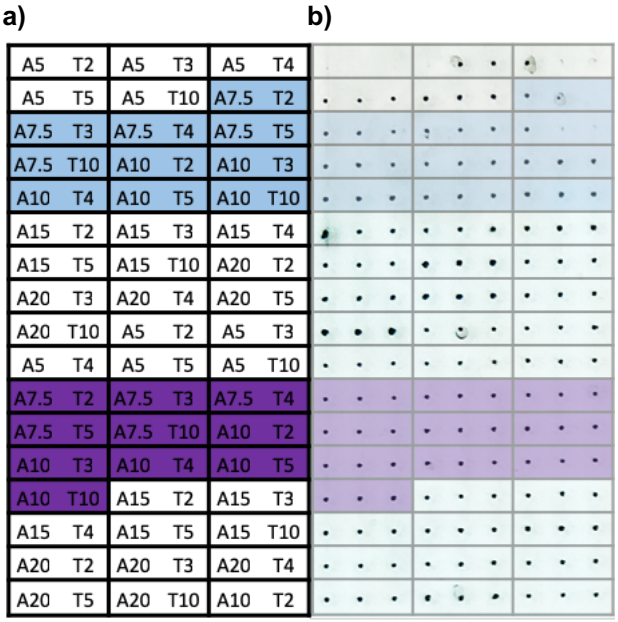

Figure 5.12 Slide 1 (10 drop, 3.5 nL sucrose mask, 20 wt% AAm, 2 wt% SIC) further illustrated to highlight the areas of interest exhibiting relatively good attachment. (a) Microarray pattern showing MBA mol% wrt AAm (0.6 blue, 1.0 purple). (b) Microarray image overlaid with the areas of interest in blue and purple.

Having selected slide 1 as the more reliable slide to avoid gel detachment and particle leaching, closer inspection of each triplicate was used to further optimise the appropriate composition (Figure 5.12). It was apparent that within each composition triplicate there remained significant deviation. Whether this was due to inaccuracies of the sucrose mask, dispersion or a combination of both was not known. As such, both slides 1 and 3 were compared to narrow the APS concentrations for each 0.6 and 1.0 mol% MBA, with apparent homogeneity the primary goal. Having narrowed the APS concentration to 7.5 or 10 wt%, the TEMED concentrations were compared in terms of measurements of gel uniformity (Table 5.5). There was little difference in terms of circularity, aspect ratio and roundness, in part due to the small sample size and the measurement method. In general, the circularity was an improvement on hand-pipetted gels (0.72), while the aspect ratio and roundness were similar. Further optimisation was required to justify selection between 7.5 and 10 wt% APS and 2 to 10 wt% TEMED concentrations.

Table 5.5 Measured circularity, aspect ratio and roundness of each triplicate in the areas of interest from slide 1 (10 drop, 3.5 nL sucrose mask, 20 wt% AAm, 2 wt% SIC) identified in Figure 5.12. Analysis conducted in ImageJ.

MBA (mol% wrt AAm)	APS (wt%)	TEMED (wt%)	Circularity	Aspect Ratio	Roundness
0.6	7.5	2	0.86	1.10	0.91
0.6	7.5	3	0.88	1.09	0.92
0.6	7.5	4	0.86	1.09	0.92
0.6	7.5	5	0.82	1.09	0.92
0.6	7.5	10	0.88	1.10	0.91
0.6	10	2	0.87	1.09	0.92
0.6	10	3	0.86	1.10	0.91
0.6	10	4	0.86	1.10	0.91
0.6	10	5	0.61	1.05	0.95
0.6	10	10	0.83	1.20	0.84
1.0	7.5	2	0.88	1.14	0.88
1.0	7.5	3	0.88	1.07	0.94
1.0	7.5	4	0.87	1.10	0.91
1.0	7.5	5	0.87	1.11	0.90
1.0	7.5	10	0.86	1.08	0.93
1.0	10	2	0.88	1.11	0.90
1.0	10	3	0.89	1.09	0.92
1.0	10	4	0.89	1.09	0.92
1.0	10	5	0.86	1.12	0.90
1.0	10	10	0.87	1.10	0.91

Although it required further optimisation, 10 wt% APS with 5 wt% TEMED was selected for a preliminary test of printing on electrodes for electrical transduction of swelling. Due to the unoptimised scale-up for this test the higher initiator concentration was selected in case elongated mixing and polymerisation time led to oxygen inhibition. Similarly, 5 wt% TEMED was selected to try and avoid the risk of localised gelation while maintaining rapid homogeneous gelation. A sucrose mask was prepared using hand pipetting (0.2 µL of 20 wt% sucrose) but otherwise identical to the printed method. Once functionalised, electrode wafers were placed and held in place with tape. Wafers were 0.5 mm thick, unlike the 1 mm glass slides, so the inkjet nozzle was 0.5 mm further away from the surface. As previously optimised, 20 wt% AAm with 0.6 or 1.0 mol% MBA wrt AAm was mixed with either 1 or 2 wt% SIC. Gels were upscaled to 1000 drops, 350 nL (100 drops, 35 nL APS, 900 drops, 315 nL pregel mixture) and allowed to dry before moving.

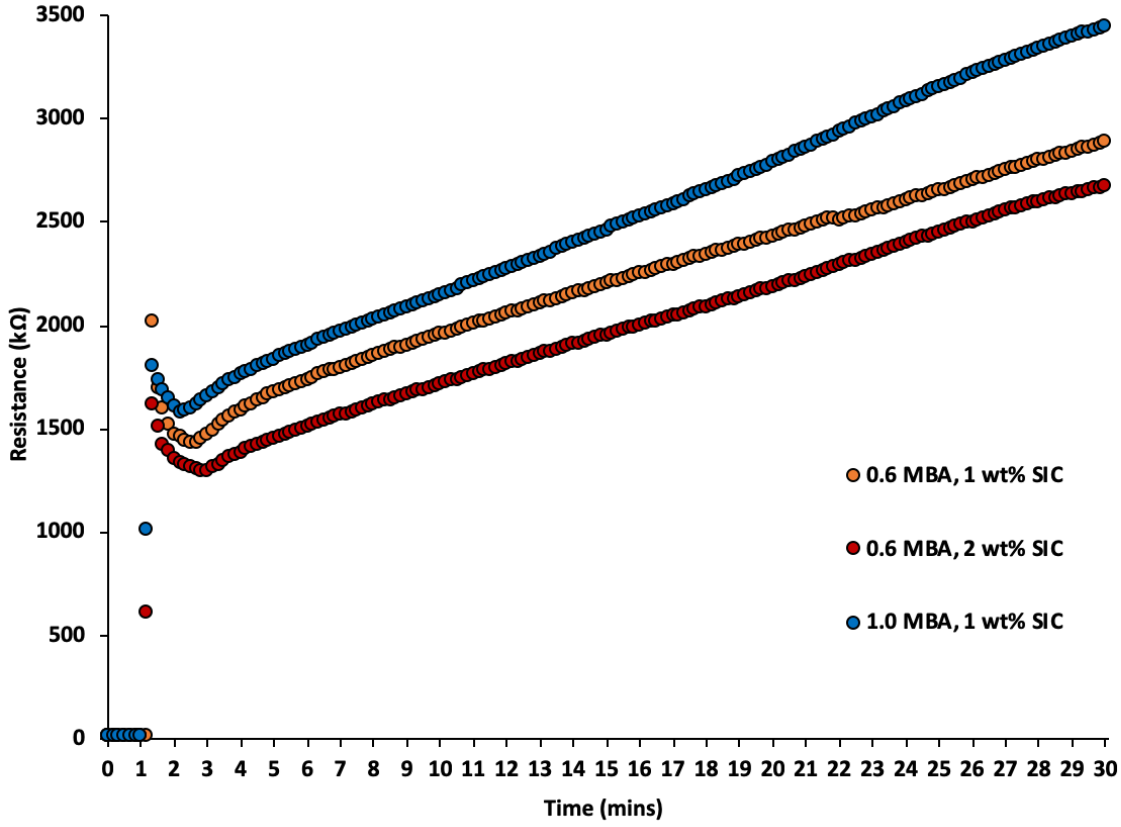

Figure 5.13 The d.c. resistance profiles of 3 gels printed on electrodes. Electrodes were functionalised as glass slides, with 0.2 µL hand-pipetted sucrose mask, POTS and TMSPM functionalisation. Polymerisation was carried out with 10 wt% APS (100 drops, 35 nL) and 5 wt% TEMED, 900 drops (315 nL) with 20 wt% AAm, 0.6 or 1.0 mol% MBA wrt AAm and 1 or 2 wt% SIC. Gels were swollen in 1 mM PBS after 1 minute of measurement.

Initial dried resistance of each gel were similar to CNP based composites and remained stable before swelling. Upon submersion in buffer solution, significant leaching was observed and the d.c. resistance rapidly increased to MΩs. Resistance then decreased significantly (200-500 kΩs), similar to the auto-ranging issue discussed previously, before gradually increasing to higher MΩ values. Leaching appeared to contain some flakes of gel which may explain the continuous increase in resistance if gradually less material is in contact with the electrode. No attempts to reswell gels after the removal of loose material were made, however these results confirmed that further optimisation was required to reduce leaching and fragmentation.

Further microarrays were designed within the previously established optimised conditions (10 drop, 3.5 nL sucrose mask, 20 wt% AAm, 2 wt% SIC) with 7.5 or 10 wt% APS and 4 or 5 wt% TEMED (Figure 5.14). Much like the hand-pipetted CNP gels

discussed previously, the MBA concentration range was increased in an attempt to reduce leaching (Figure 5.14b). Similarly, co-polymerisation with 10 wt% AAm and 10 wt% NIPAm was investigated to reduce hydrophilicity and swelling (Figure 5.14e). Finally, PDA was tested in place of MBA to improve gel integrity (Figure 5.14h).

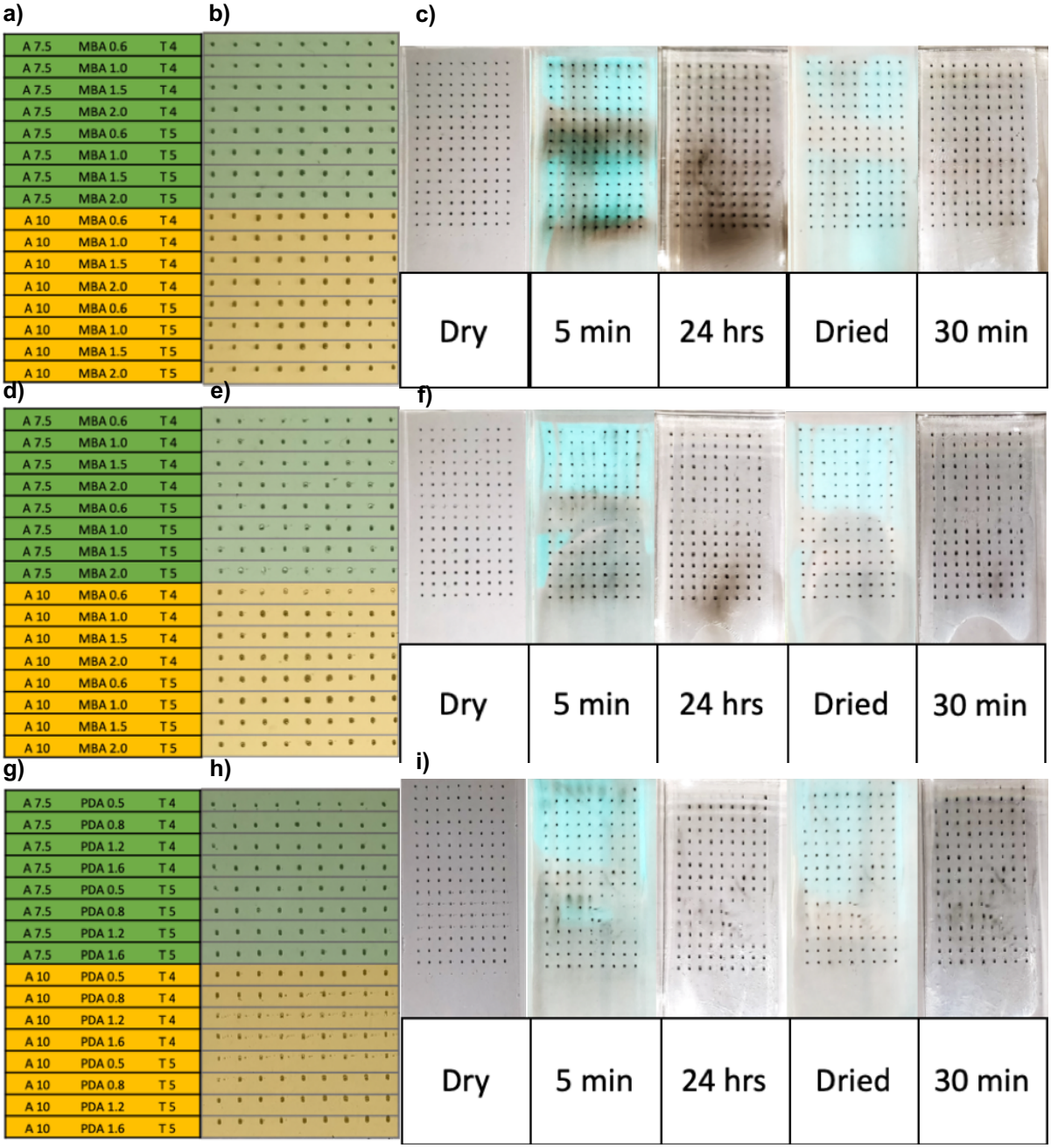

Figure 5.14 Printed microarrays using 10 drop, 3.5 nL sucrose mask, 7.5 (green) or 10 (orange) wt% APS (A), 4 or 5 wt% TEMED (T) and 2 wt% SIC. (a, d, g) Illustration of APS, TEMED and crosslinker concentrations (mol% wrt AAm). (b) 20 wt% AAm with 0.6-2.0 mol% MBA wrt AAm. (c) Swelling slide b in 1 mM PBS, drying and reswelling. (e) 10 wt% AAm and 10 wt% NIPAm with 0.6-2.0 mol% MBA wrt monomer. (f) Swelling slide e in 1 mM PBS, drying and reswelling. (h) 20 wt% AAm with 0.5-1.6 mol% PDA wrt AAm. (i) Swelling slide g in 1 mM PBS, drying and reswelling. Each composition was tested in nonuplicate.

Upon optical inspection of each slide after printing, the AAm based microarray was clearly the most homogeneous as both the copolymer array and the PDA array had

sections of non-homogeneous gels with a mixture of clear and black areas. When swollen in buffer, each microarray exhibited leaching from some of the compositions. For copolymer and PDA microarrays some of the gels also washed away. Subsequent rinsing, drying and reswelling showed little-to-no leaching during the second swelling. Closer inspection of the copolymer array and PDA array showed multiple deformities, whereby few, if any, were as homogeneous as the AAm array (Figure 5.15). Each composition appeared relatively consistent throughout within its nonuplet, indicating that the sucrose mask was unlikely to have caused the deformities. It is likely that both copolymer and PDA materials could be optimised. For example, in each case AAm and MBA were replaced by weight, while an equimolar swap may have been more consistent. However, relatively positive results from the AAm microarray and its similarity to the CNP based work discussed previously meant that further optimisation with NIPAm or PDA was not investigated.

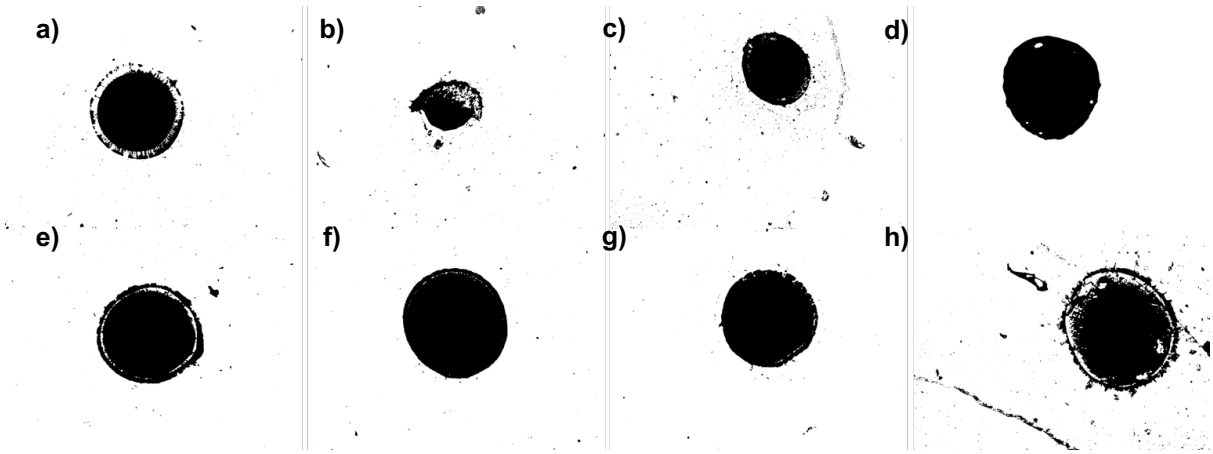

Figure 5.15 Images of microarray gels from Figure 5.14 (a-d) Slide d, 10 wt% AAm, 10 wt% NIPAm gels, 0.6-2.0 mol% MBA wrt AAm (e-h) Slide h, 20 wt% AAm, 0.5-1.6 mol% PDA wrt AAm. Examples shown reflect the typical structures seen throughout each microarray.

As before, the uniformity of the AAm microarray was assessed to further optimise synthesis (Table 5.6). Compositions observed to have leached SIC during the first swelling were considered inappropriate, while the 1.0 mol% MBA with 10 wt% APS and 5 wt% TEMED previously scaled up exhibited splashed polymer droplets (Figure 5.16).

Table 5.6 Measured circularity, aspect ratio and roundness of each nonuplicate in the areas of interest from slide b (10 drop sucrose mask, 20 wt% AAm, 2 wt% SIC) identified in Figure 5.14. Results highlighted grey indicated leaching was observed within 5 minutes of swelling. Results in bold indicate the MBA, APS and TEMED conditions chosen to progress with. Analysis conducted in ImageJ.

	MBA (mol% wrt AAm)	APS (wt%)	TEMED (wt%)	Circularity	Aspect Ratio	Roundness
Swollen	0.6	7.5	4	0.74	1.13	0.89
	1.0	7.5	4	0.74	1.13	0.89
	1.5	7.5	4	0.77	1.13	0.89
	2.0	7.5	4	0.72	1.10	0.91
	0.6	**7.5**	**5**	**0.79**	**1.12**	**0.89**
	1.0	**7.5**	**5**	**0.79**	**1.11**	**0.91**
	1.5	7.5	5	0.57	1.21	0.83
	2.0	7.5	5	0.78	1.10	0.91
	0.6	10	4	0.69	1.13	0.89
	1.0	10	4	0.65	1.16	0.87
	1.5	10	4	0.69	1.10	0.91
	2.0	10	4	0.72	1.12	0.90
	0.6	10	5	0.81	1.16	0.87
	1.0	10	5	0.81	1.11	0.91
	1.5	10	5	0.67	1.07	0.94
	2.0	10	5	0.73	1.22	0.91
Dried	0.6	7.5	4	0.72	1.12	0.90
	1.0	7.5	4	0.58	1.13	0.89
	1.5	7.5	4	0.60	1.13	0.89
	2.0	7.5	4	0.65	1.11	0.90
	0.6	**7.5**	**5**	**0.72**	**1.12**	**0.89**
	1.0	**7.5**	**5**	**0.67**	**1.11**	**0.90**
	1.5	7.5	5	0.74	1.11	0.90
	2.0	7.5	5	0.54	1.19	0.85
	0.6	10	4	0.61	1.09	0.92
	1.0	10	4	0.49	1.11	0.90
	1.5	10	4	0.47	1.15	0.88
	2.0	10	4	0.53	1.11	0.91
	0.6	10	5	0.46	1.11	0.91
	1.0	10	5	0.59	1.11	0.91
	1.5	10	5	0.71	1.13	0.89
	2.0	10	5	0.52	1.06	0.94

Compared to the previous printed microarray the circularity was slightly worse while the aspect ratio and roundness values were similar. This is likely to be from swelling damage or gel rearrangement during swelling. Further evidence for this theory is that the circularity decreases for each composition when dried, indicated further deformation occurred.

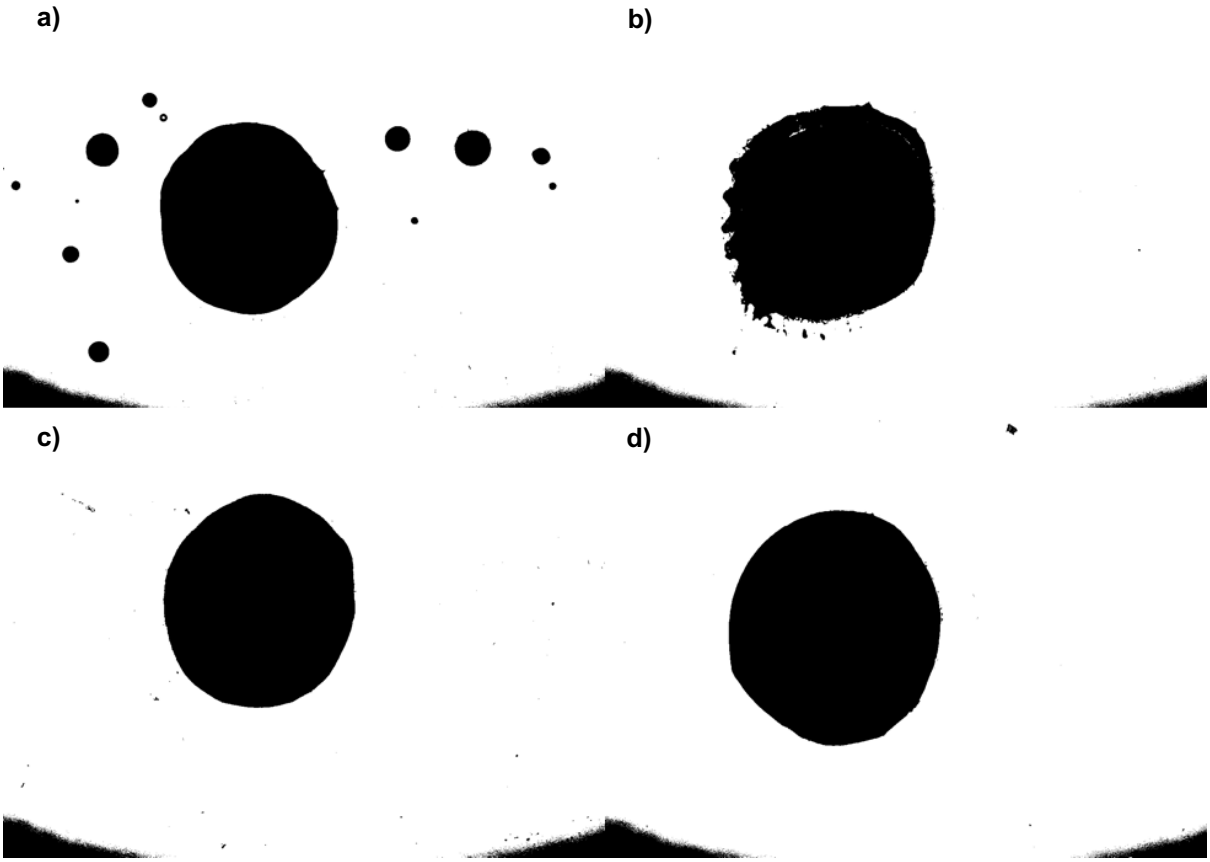

Figure 5.16 Light microscopy images from slide b (Figure 5.14) after 1 hr swelling in 1 mM PBS after previous washing of (a) 10 wt% APS, 5 wt% TEMED, 1.0 mol% MBA wrt AAm, exhibiting droplet splashes. (b) 10 wt% APS, 4 wt% TEMED, 1.0 mol% MBA, exhibiting inconsistent, potentially undulating, edges. (c, d) 7.5 wt% APS, 4 wt% TEMED, 0.6 (c) or 1.0 (d) mol% MBA.

The compositions that exhibited minimal difference between swollen and dried samples was 7.5 wt% APS with 5 wt% TEMED with either 0.6 or 1.0 mol% MBA wrt AAm. Furthermore, the gels using this composition appeared homogeneous, whereas many others had splashed droplets, undulating edges or gaps in the gel material (Figure 5.16).

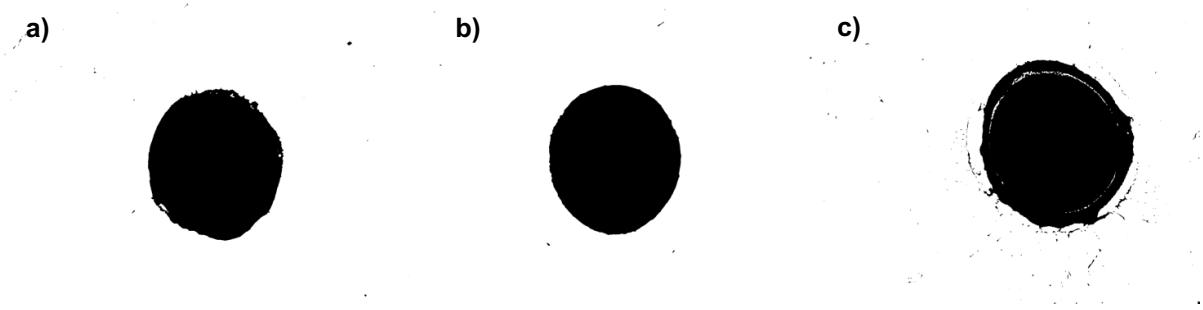

Figure 5.17 Light microscopy images from slide b (Figure 5.14) dried after two washes in 1 mM PBS of (a, b) 7.5 wt% APS, 4 wt% TEMED, 0.6 (a) or 1.0 (b) mol% MBA (c) 0 wt% APS, 4 wt% TEMED, 1.0 mol% MBA.

Images of the dried gels in many cases showed leached material, clear gaps at the gel edges or larger deformations (Figure 5.17). Only gels made with 7.5 wt% APS with 5 wt% TEMED with either 0.6 or 1.0 mol% MBA wrt AAm appeared homogeneous both when swollen and dried. As these MBA concentrations match those used in the optical and electrical system discussed previously, these conditions were utilised for scaling up onto electrodes.

5.1.3 Inkjet Polymerisation Scale Optimisation

Analysis of the previously discussed microarrays was limited by the use of a droplet shape in a microarray, meaning imaging could only be carried out from above or below. Alternative electrode designs or swelling transduction methods could assess smaller volumes, or gels could be printed as films rather than droplets, however the available electrodes were also designed for 2 µL droplets due to the previous requirements of hand pipetting.[389,393] To accurately dispense material onto electrodes an electrode holder was required. After optimising measurements with 3D printing, holders were made by cutting a 1 mm thick aluminium sheet (Figure 5.18). As holes were cut through the aluminium, the wafers were 0.5 mm further away from the inkjet nozzle than gels synthesised on glass slides. The use of holsters enabled the use of printed sucrose masks, as each electrode could be returned to the same position for polymerisation steps.

Figure 5.18 Image of the electrode wafer holders used to align electrodes for printing. Holders were made from 1 mm aluminium and wafer slots were cut through completely. Wafer thickness was 0.5 mm.

Scale up optimisation compared swollen volumes of 175, 350, 525 and 700 nL (500, 1000, 1500 and 2000 drop) gels with either 0.6 or 1.0 mol% MBA wrt AAm (Figure 5.19a). In each case the sucrose mask was 10% of the deposited gel drops. Swollen volumes were compared to identify the minimum gel size that could differentiate between crosslink densities. Only 700 nL gels could reliably differentiate between 0.6 and 1.0 mol% MBA, however, each run could only print 4 gels at a time due to the aspirated volume. As such, 525 nL gels were chosen as twice as many gels could be printed in a single run. All volumes appeared to be homogeneous droplet shapes when swollen (Figure 5.19b). The 525 nL gels offered measurable reduced swelling at 1.0 mol% MBA, albeit within error of the 0.6 mol% MBA gels. Greater sample numbers may improve this as variation of gel shape and location would influence the calculated swollen volume.

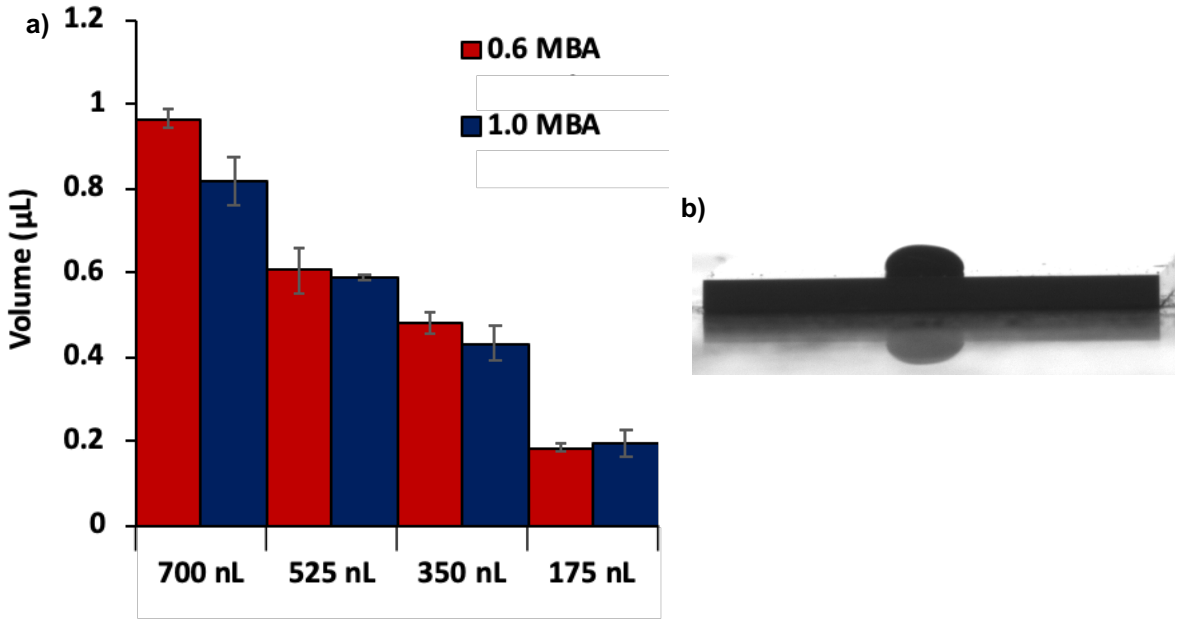

Figure 5.19 (a) Comparison of the swollen volumes of printed gels made with 175-700 nL. The sucrose mask and deposited APS (7.5 wt%) volumes used 10% of the total volume while the pregel solution used 90% or the total volume. Pregel solution was 20 wt% AAm, 2 wt% SIC, 5 wt% TEMED, with either 0.6 (red) or 1.0 (blue) mol% MBA wrt AAm. (b) Image of a 175 nL printed gel. 17.5 nL sucrose mask. 17.5 nL APS (7.5 wt%). 122.5 nL 20 wt% AAm, 2 wt% SIC, 5 wt% TEMED, 0.6 mol% MBA wrt AAm. Standard error of the mean calculated using equation 3.2b (n = 3).

As explained in Chapter 3, the distance of the gel from the front of the wafer will influence the accuracy of the swollen volume as the front edge of the wafer is used for the scale in each image. Similarly the circularity of the gel will affect the accuracy of the calculated volume which is based on the droplet being a perfect circle. For electrical measurements, the contact area with the electrodes will also influence measured results. Table 5.7 shows the gel placement and uniformity of the 175 nL gels. Circularity, aspect ratio and roundness were all comparable to the best of the microarray results, which is more impressive considering the gels were hand-traced rather than automated for improved accuracy.

Table 5.7 Measured gel placement precision (as distance left and distance down explained in Figure 5.20) and circularity, aspect ratio and roundness of 8 printed gels (175 nL) calculated using Equations 3.4a, b and c respectively. Analysis conducted in ImageJ.

	Distance Left (mm)	Distance Down (mm)	Circularity	Aspect Ratio	Roundness
Average	0.42	0.59	0.92	1.14	0.88
Standard Deviation	0.08	0.06	0.03	0.11	0.08
Imprecision	19.3	10.5			

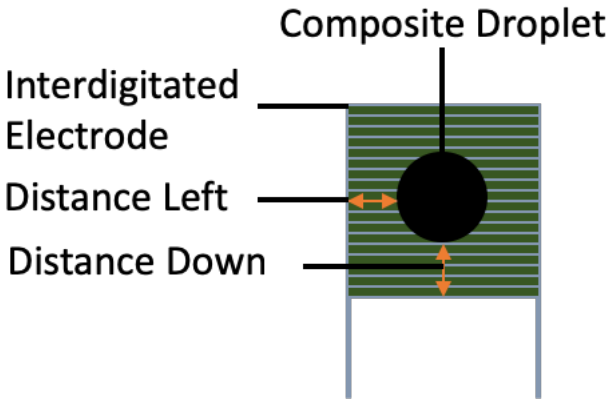

Figure 5.20 Illustration of measurements reported in Table 5.7 used to assess droplet placement whereby "Distance Left" is the distance between the leftmost edge of the interdigitated electrode area and the leftmost edge of the composite droplet and "Distance Down" is the distance between the bottommost edge of the interdigitated electrode area and the bottommost edge of the composite droplet. Not to scale.

For each deposited volume, the gels were towards the front right corner of the interdigitated electrode. This was an artefact of printing using the glass slide map locations. For the larger gels this meant that some of the gel was outside of the interdigitated electrode area. Appropriate mapping or a more accurate holder could alleviate this concern, however it was not conducted as it was already an improvement over the previous hand pipetting accuracy. Each set of 4 electrodes in a holder had slightly different locations and shapes (Figure 5.21). When compared to gels printed on electrodes in the same holder the gels were found to overlap fairly accurately, suggesting that a more precise electrode placement or mapping could alleviate this issue.

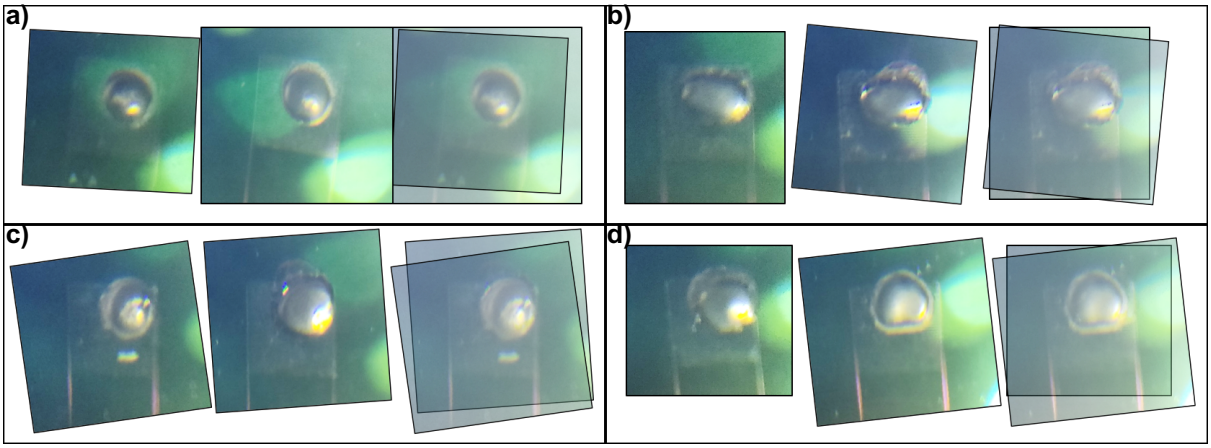

Figure 5.21 Images of printed gel placement precision whereby each electrode holder position (a-d) was used to print on 2 electrodes (i, ii) which when overlaid show minimal deviation.

Having decided to use 350 nL gels, further synthesis on glass slides was conducted to ensure the reliability of the method and further assess the gel structure. 40 of both 0.6 and 1.0 mol% MBA wrt AAm gels were synthesised on glass slides with 35 nL sucrose masks. Due to the gel size, it was not possible to obtain an image of whole gels using the microarray imaging method. Despite this, the gel homogeneity and edges were visible and rather than stitching multiple images together, these edges were assessed (Figure 5.22). It was apparent that numerous gels had clear areas suggesting at least no SIC in those areas and probably with no polymer. After washing, partial gel detachment was apparent at the edges (Figure 5.22d and j). Furthermore, numerous gels showed signs of leaching with dark material surrounding the main gel area (Figure 5.22e, h and i). Although some gels appeared to be homogeneous with minimal-to-no leaching (Figure 5.22c and f), the majority had defects or leaching. Inconsistent gel shape and structure will reduce the accuracy of electrical transduction as the contact area with the electrodes affects the measured resistance.

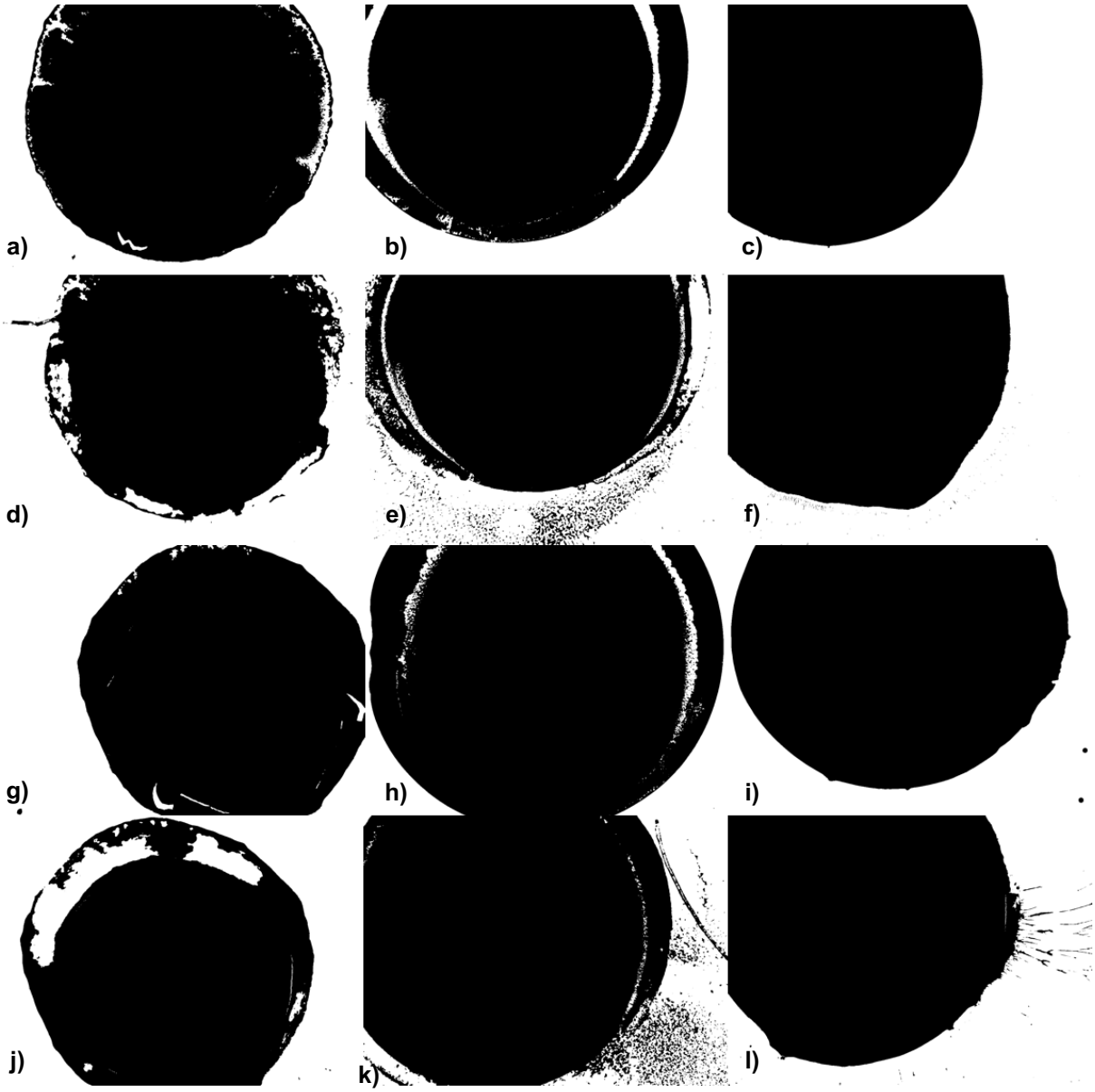

Figure 5.22 Images from 350 nL microarray with 35 nL sucrose mask of either 0.6 (a-f) or 1.0 (g-l) mol% MBA wrt AAm (20 wt% AAm, 2 wt% SIC, 7.5 wt% APS, 5 wt% TEMED). (a-c, g-i) Unwashed (d-f, j-l) washed.

Smaller sucrose mask sizes were investigated to constrain the material in a smaller area and reduce the white areas of no composite. It was expected that this would also reduce leaching through resulting in a denser network structure. 17.5 nL sucrose masks were used to synthesise 40 more 0.6 mol% and 1.0 mol% MBA wrt AAm 350 nL gels. Some of these gels were able to be imaged in their entirety and were then assessed in terms of their uniformity (Table 5.8). The uniformity was similar to the other printed gels, although the circularity calculated differed substantially after

washing for 0.6 mol% MBA gels. As not all gels were within the field of view for full imaging it was difficult to assess this thoroughly, however if the 1.0 mol% MBA gels retain integrity while the 0.6 mol% MBA gels are damaged it may aid transduction.

Table 5.8 Measured circularity, aspect ratio and roundness from 350 nL microarray of either 0.6 or 1.0 mol% MBA wrt AAm (17.5 nL sucrose mask, 20 wt% AAm, 2 wt% SIC, 7.5 wt% APS, 5 wt% TEMED). Analysis conducted in ImageJ.

MBA (mol% wrt AAm)	Washed	Circularity	Standard Deviation	Aspect Ratio	Standard Deviation	Roundness	Standard Deviation
0.6	Unwashed	0.82	0.17	1.22	0.73	0.93	0.19
0.6	Washed	0.60	0.14	1.10	0.03	0.91	0.07
1.0	Unwashed	0.85	0.85	1.04	1.04	0.96	0.02
1.0	Washed	0.85	0.06	1.04	0.03	0.96	0.02

The gel images using the 17.5 nL mask showed a far more homogeneous material, with significantly fewer instances of white space within the gel and to a far lesser extent even when it was apparent (Figure 5.23). There were still occasional indications of leaching, but less frequently and to a lesser extent than seen using the 35 nL mask. There were some instances of gel shrinking, whereby the gel was smaller after washing. This was thought to be due to material polymerised and adsorbed to the area outside of the sucrose mask swelling away from the glass and then rearranging to be close to the centre of each mask area. The gels which covered a larger area than the mask should permit were likely formed due to the flow from droplet addition causing polymerisation outside of the mask. Full optimisation of mask size, preferably using photolithography for improved precision, wafer distance and gel composition could further improve the reproducibility of this method and uniformity of size and shape. However, it was not a priority for the aim of printing MO functionalised composites at this stage.

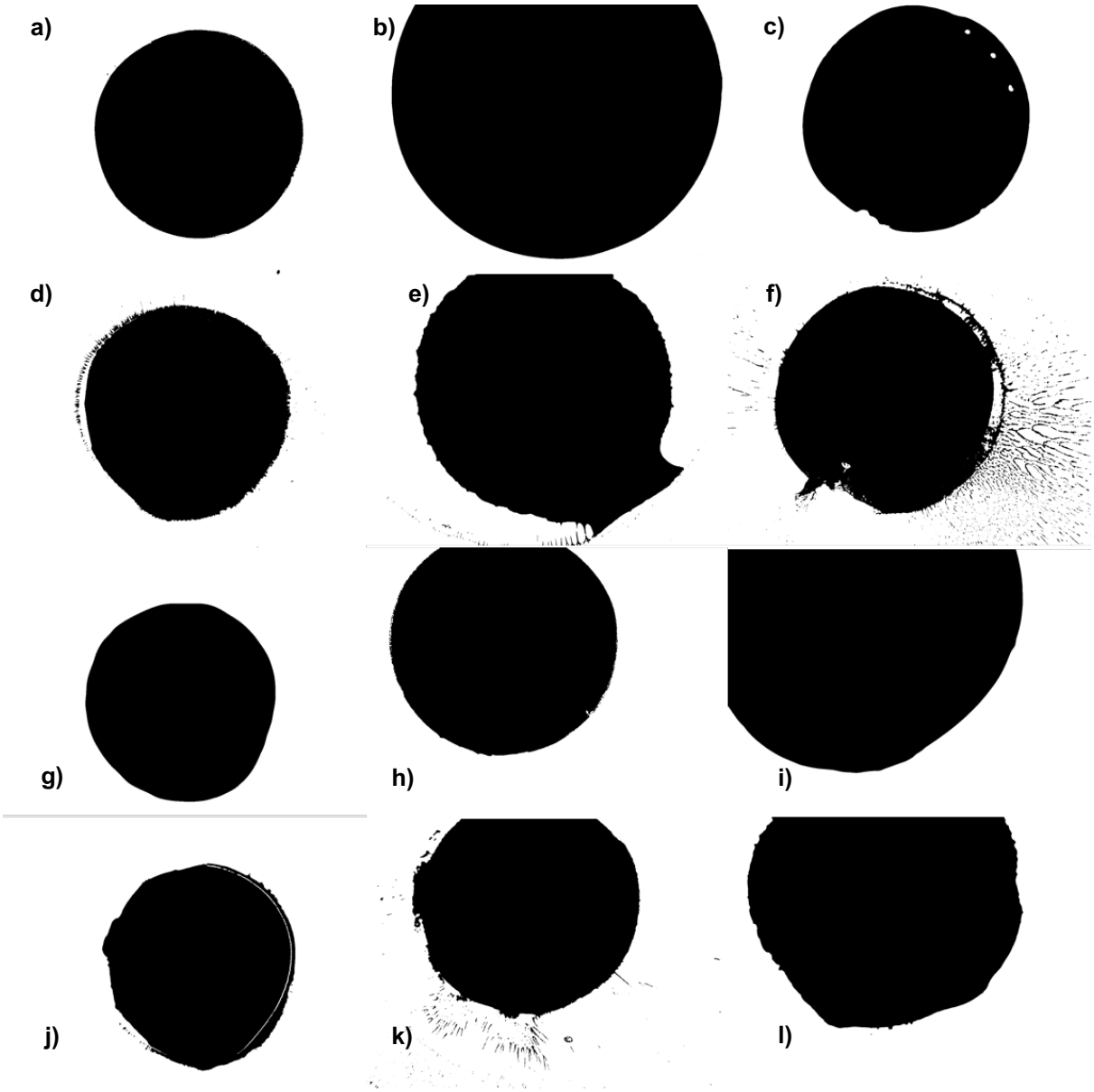

Figure 5.23 Images from 350 nL microarray with 17.5 nL sucrose mask of either 0.6 (a-f) or 1.0 (g-l) mol% MBA wrt AAm (20 wt% AAm, 2 wt% SIC, 7.5 wt% APS, 5 wt% TEMED). (a-c, g-i) Unwashed (d-f, j-l) washed.

Further printing was conducted on electrodes to assess the electrical transduction of the printed composite. As preliminary testing, only d.c. resistance was investigated to compare to the previous CNP based work. Initial results swelling in 1 mM PBS did not appear promising as once again the percolating dried composite rapidly went to MΩs (Figure 5.24) and some leaching was again visible.

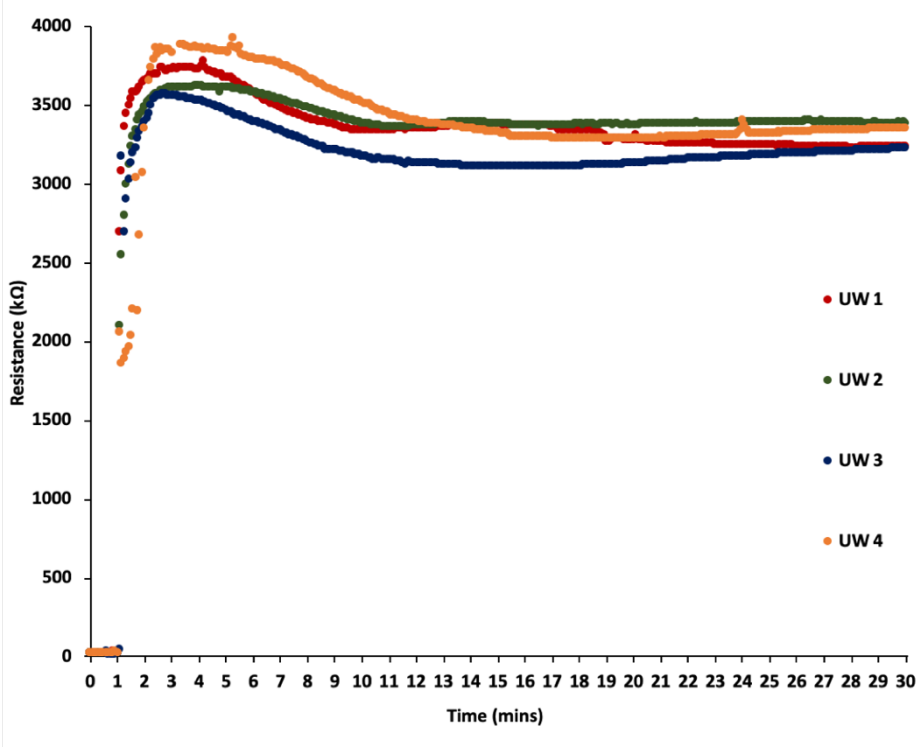

Figure 5.24 The d.c. resistance profiles of 4 unwashed gels printed on electrodes, 17.5 nL sucrose mask. Polymerisation was carried out with 7.5 wt% APS (35 nL) and 5 wt% TEMED with 20 wt% AAm, 0.6 mol% MBA wrt AAm and 2 wt% SIC (315 nL).

Upon drying and retesting the gels the resistance profile went to kΩs instead of MΩs. The starting resistance values varied from 25-100 kΩs, although this may have been due to incomplete drying. The end resistance values were similar to the previous CNP based system. As discussed in Chapter 4, it is possible that the auto-ranging of the multimeter is overshooting the required current due to the rapid change in resistance, resulting a different measured resistance for the non-ohmic material. This may be more likely than delamination causing MΩ resistances as repeated swelling would be expected to cause repeated delamination or detachment. Unlike CNP based composites, the SIC gels appeared homogeneous and less likely to detach or delaminate, facilitating reswelling.

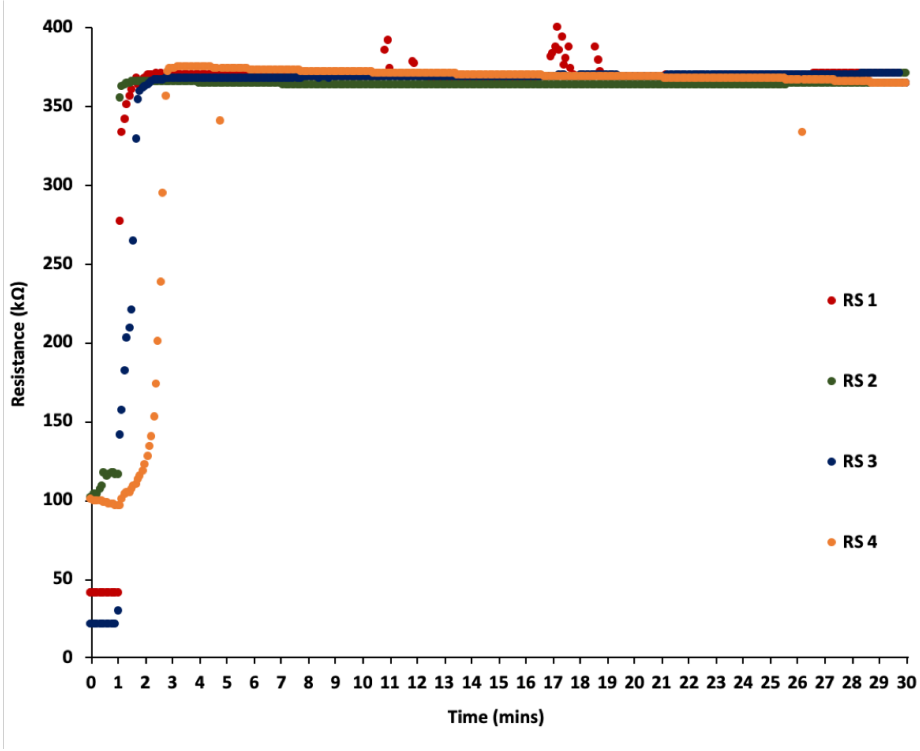

Figure 5.25 The d.c. resistance profiles of 4 washed gels printed on electrodes (First swelling shown in Figure 5.24), 17.5 nL sucrose mask. Polymerisation was carried out with 7.5 wt% APS (35 nL) and 5 wt% TEMED with 20 wt% AAm, 0.6 mol% MBA wrt AAm and 2 wt% SIC (315 nL).

Upon testing of the third swelling response, having been dried thoroughly overnight, the starting resistance values were far more variable (Figure 5.26a). One gel was at MΩs, two <100 kΩs and one failed to report any resistance. This may be due to electrode damage or delamination from the electrode whilst remaining on the wafer. Upon swelling the three working samples all gave different responses. Sample 1 exhibited the typical response from 30 to 500 kΩs, sample 2 went to MΩs, while sample 3 went from MΩs down to kΩs, potentially caused by swelling increasing electrode contact.

Comparison of the swelling responses showed that the first swelling reliably reached MΩs with minimal variation despite showing leaching, whereas the second swelling reliably went to kΩs with minimal variation (Figure 5.26b). The third swelling was far more variable and unreliable, likely due to gel damage. Omitting sample 2 which went to MΩs, however, resulted in the same resistance as the second swelling.

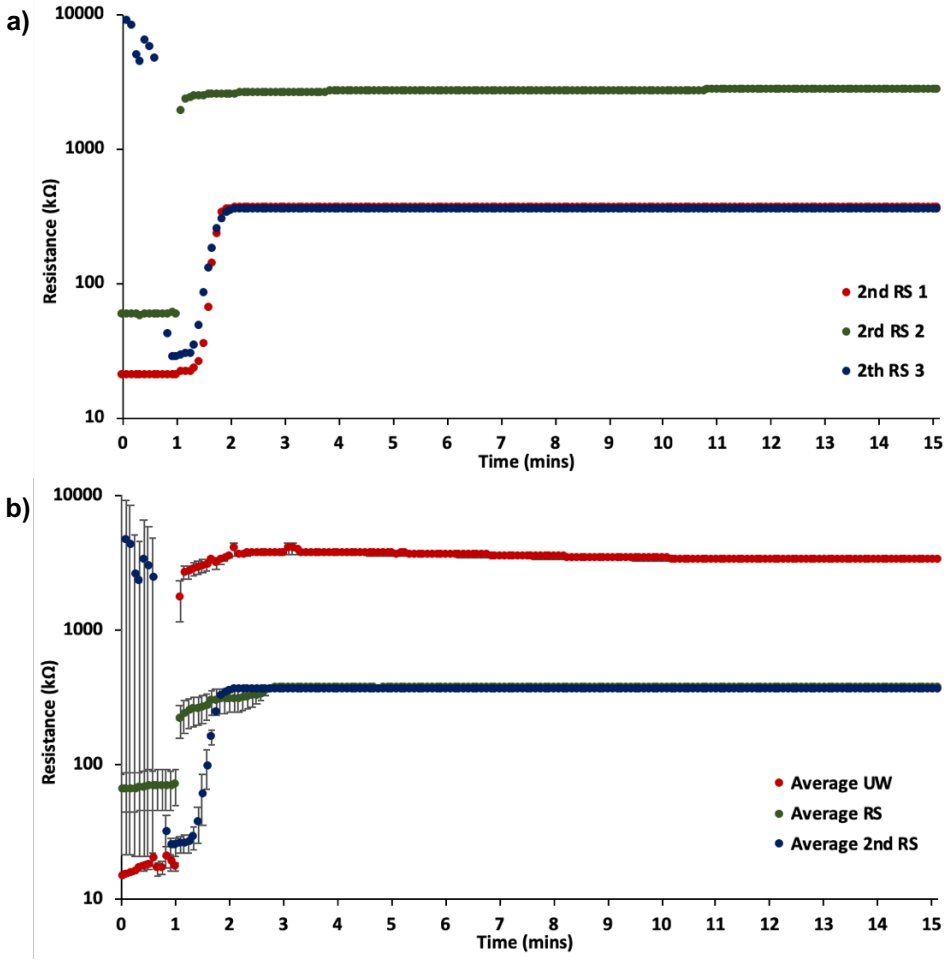

Figure 5.26 The d.c. resistance profiles of 3 twice washed gels printed on electrodes (First swelling shown in Figure 5.24, gel 4 failed), 17.5 nL sucrose mask. Polymerisation was carried out with 7.5 wt% APS (35 nL) and 5 wt% TEMED with 20 wt% AAm, 0.6 mol% MBA wrt AAm and 2 wt% SIC (315 nL). (a) 3rd Swelling d.c. resistance (b) Average unwashed, first reswelling and 2nd reswelling (Samples 1 and 3 only). Standard error of the mean calculated using equation 3.2b (n = 3).

It is clear from the repeated swelling tests with d.c. resistance that the gels have better attachment to the wafer, are less affected by leaching, or a mixture of both. Similarly, the placement precision is improved over the hand-pipetted CNP gels, despite there being some variation in terms of dried gel area. Optical assessments suggested improved homogeneity with composition optimisation reducing any white gaps in the gels, however it was not possible to assess the microstructures due to the pigmentation provided by using SIC.

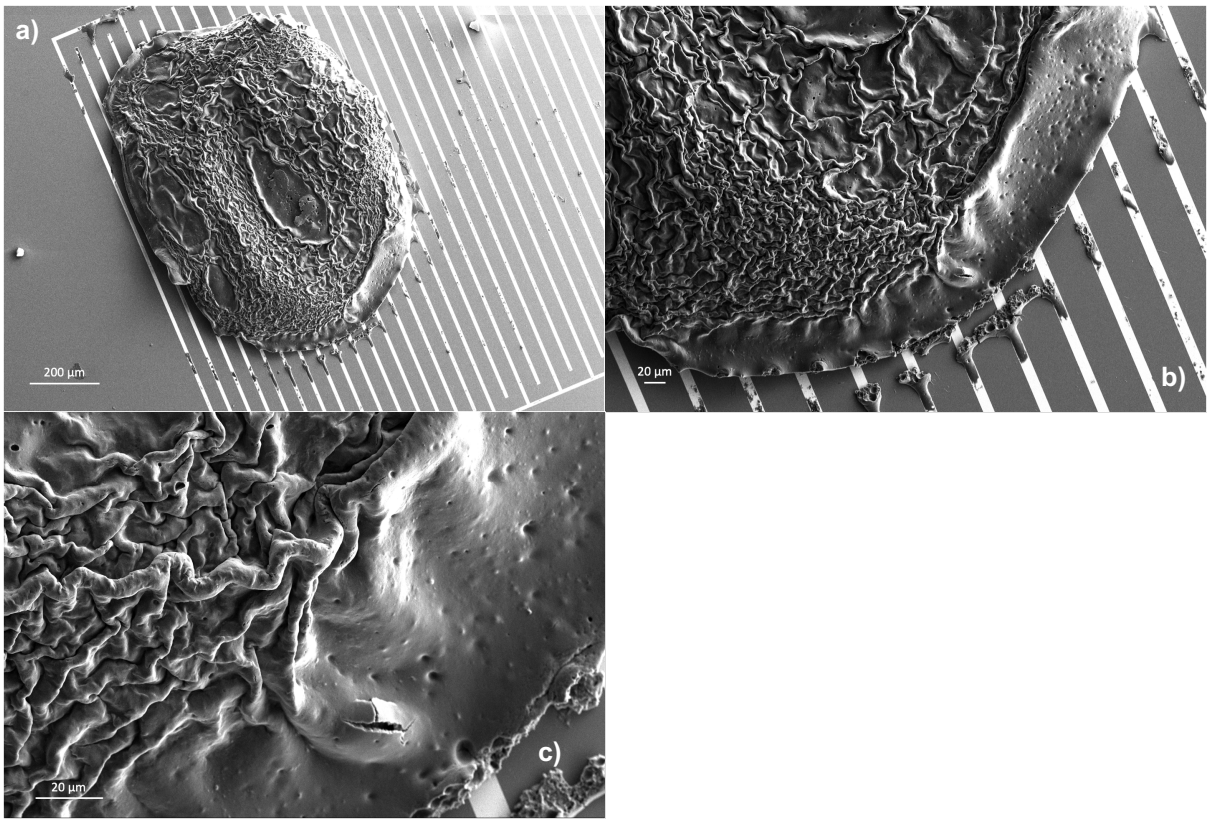

Figure 5.27 SEM images of printed gel on 17.5 nL sucrose mask. Polymerisation was carried out with 7.5 wt% APS (35 nL) and 5 wt% TEMED with 20 wt% AAm, 0.6 mol% MBA wrt AAm and 2 wt% SIC (315 nL).

SEM imaging of a printed composite revealed a number of interesting features (Figure 5.27). Firstly, the material itself appeared far more homogeneous than the CNP composites with no clusters of high conductive particle density visible on the gel surface. Secondly, some composite remains detached from the gel body and instead remains adsorbed to the platinum electrode. This is likely due to the hydrophobic modification on the wafer surface, yet the area this reaches from the gel body is substantial. Finally, there appears to be crumpling at the top of the gel. The polymerisation can be expected to be quickest at the wafer surface where the APS was dried, meaning the deposited pregel solution will be polymerised mostly densely at the wafer surface. Interestingly this is the opposite to the UV photoinitiation where initiation occurs at the top of the gel droplet. As material continues to be added and results in mixing, the later material at the surface will not only have a lower radical concentration, but also be more susceptible to oxygen inhibition. Another factor may be the gel shrinkage from being placed under vacuum, as the less dense material will

crumple. As with the CNP based composite, the area of most interest is the area closest to the electrode surface. If this is a reproducible feature it may explain reduce delamination as the stress and strain from drying and swelling at the wafer surface could be lessened by the crumpling and expansion at the top of the gel. The material still attached to the platinum may also suggest that the gel density improved adhesion not only to the wafer but to the electrode too.

5.2 Morpholino Oligonucleotide Crosslinked Polymer Composites

5.2.1 Printable Solutions

Based on the improvements achieved during optimisation and preliminary testing of the printed SIC composite, further optimisation was attempted using the MOR2 crosslinks. Due to the cost of material and the volume required for inkjet printing, the number of attempts were limited. Having dissolved 0.4 mol% wrt AAm MO crosslinks into the monomer mixture and mixed into the SIC dispersion, it appeared no different to previous pregel solutions. However, upon aspiration into the printer nozzle, it quickly became apparent that air bubbles had formed within the nozzle. Despite further degassing of the solution and clearing the printer of air bubbles it was clear that every time aspiration was attempted bubbles would form. Considering addition of MOs increased solution viscosity, it is likely that this increased viscosity was causing air to enter the printer during solution aspiration, as well as altering the extensional viscosity during droplet formation.[286,393,399,400] Any potential interaction between SIC and MOs could not be investigated due to lack of sufficient amounts of material.

Although there are numerous methods to reduce viscosity, such as increased temperature or alternative solvents or nozzles, time was too limited to investigate these.[285–287,291,401] In particular pneumatically driven inkjet printing could be used to print viscous solutions.[288] Attempts to print the MO solution separately were unsuccessful due to the viscosity and further dilution would have required optimisation. Instead the concentration of MO crosslinks was halved, such that either 0.2 mol% MO

wrt 20 wt% AAm or 0.4 mol% MO wrt 10 wt% AAm was used. In either case there were still issues during aspiration of air bubbles forming resulting in substantial wasted material. Even on occasions when printing was possible the droplets were poor and the volume varied widely from gel to gel. As the volume also affects the initiator concentration these gels will vary in both macro and microstructures.[381]

The 0.2 mol% MO wrt 20 wt% AAm gels printed were visibly misshapen (Figure 5.28). As well as the inconsistent shape and volume, there were visible dents in the gels where there was less material. Furthermore, a visible residue of material radiated around the gels. Previously this had only been seen on wafers after swelling had washed out loose material. The bubbles in solution prevented consistent droplet volume, meaning that splashing or spraying likely occurred to spread the material so far from the gel centre.

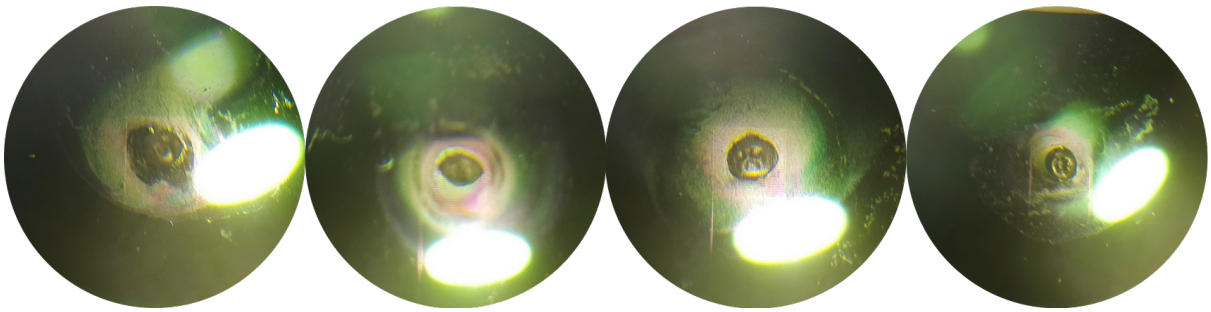

Figure 5.28 Images of printed MO gels on 17.5 nL sucrose mask. Polymerisation was carried out with 7.5 wt% APS (35 nL) and 5 wt% TEMED with 20 wt% AAm, 0.6 mol% MBA wrt AAm, 2 wt% SIC and 0.2 mol% MOR2 (315 nL).

Despite the poor gel structure, SEM images indicated a relatively homogeneous material (Figure 5.29). Unlike the previous printed gel SEM there were no large crumpled areas. As well as the clear halo of material around the gel, the edges appear less defined than the previous gel. The gel surface appears rougher than the hand-pipetted MOR2 gels, seemingly with bumpy areas and a relatively consistently mottled surface which may indicate the SIC dispersion remains consistently spread despite the inaccurate printing process.

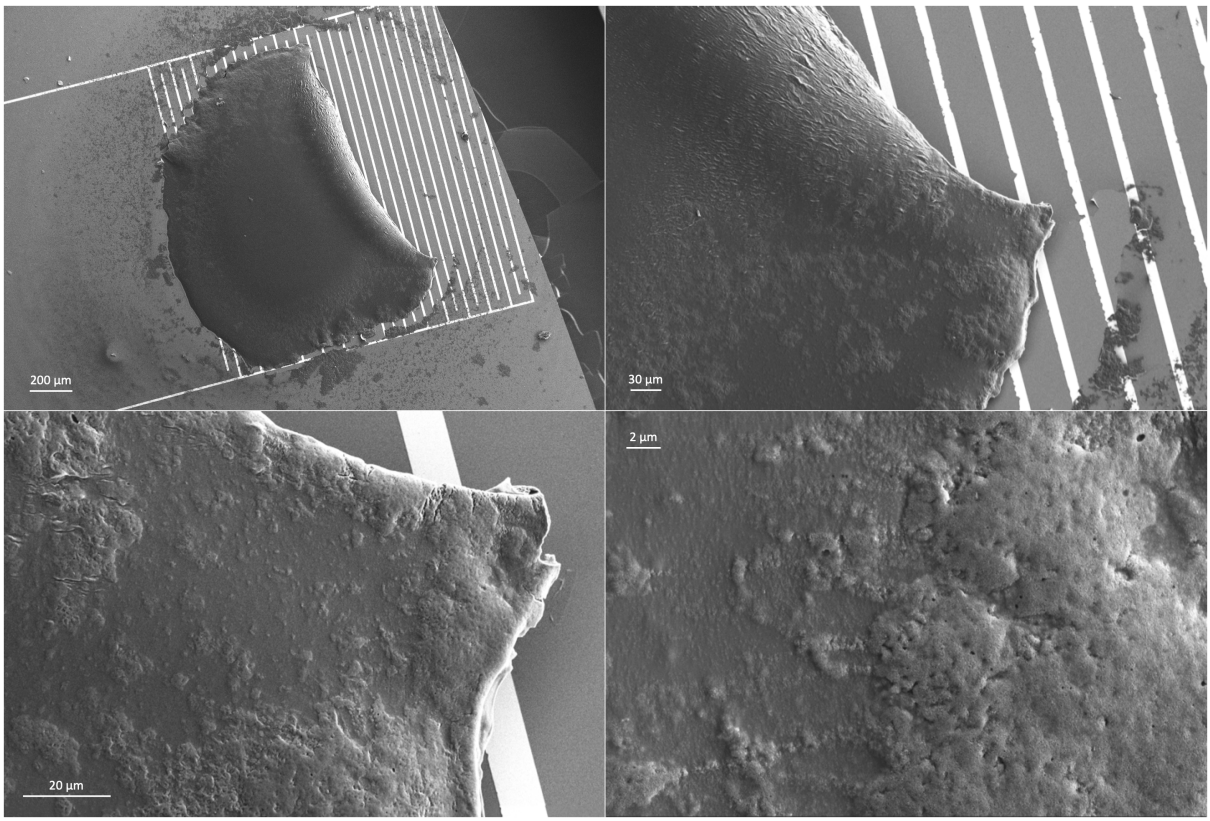

Figure 5.29 SEM images of a printed MO gel on 17.5 nL sucrose mask. Polymerisation was carried out with 7.5 wt% APS (35 nL) and 5 wt% TEMED with 20 wt% AAm, 0.6 mol% MBA wrt AAm, 2 wt% SIC and 0.2 mol% MOR2 (315 nL).

Due to time limitations the synthesis was not optimised for 10 wt% AAm gels. As such the initiator concentration was likely higher than optimal and the mask size may also be too large for reproducible results. In spite of this, the inaccuracies of deposition due to sample viscosity and air bubbles would remain the biggest source of variation. Figure 5.30 shows examples of the 10 wt% AAm gels. As with the 20 wt% AAm gels there are malformities and loose material around the gels.

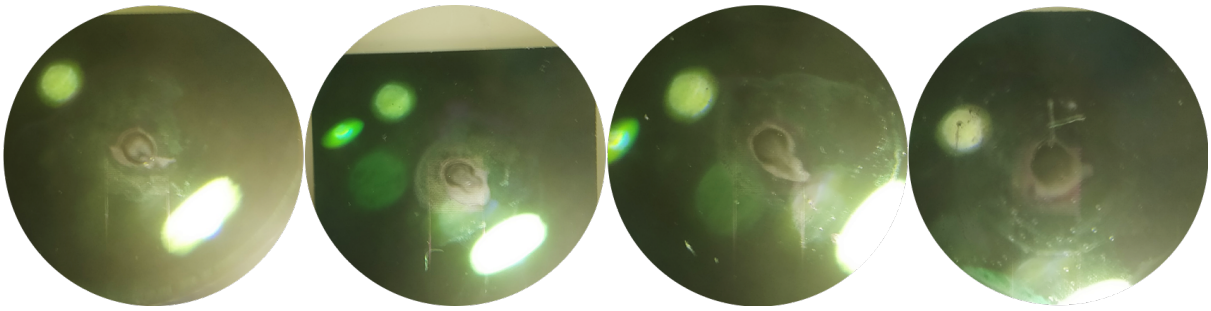

Figure 5.30 Images of printed MO gels on 17.5 sucrose mask. Polymerisation was carried out with 7.5 wt% APS (35 nL) and 5 wt% TEMED with 10 wt% AAm, 0.6 mol% MBA wrt AAm, 2 wt% SIC and 0.4 mol% MOR2 (315 nL).

Washing of the 10 wt% AAm gels showed how incomplete the polymerisation was, as substantial areas of gel were washed away (Figure 5.31). With appropriate optimisation 10 wt% AAm gels should be entirely printable, although 20 wt% AAm gels were preferred to reduce particle leaching.

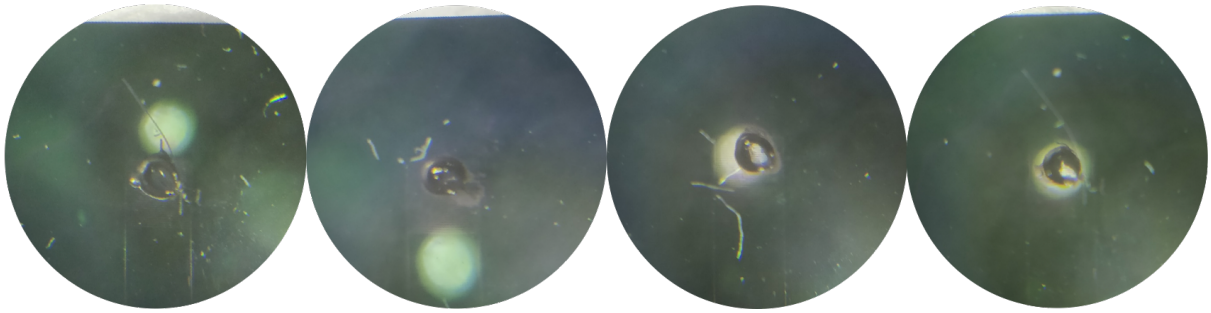

Figure 5.31 Images of swollen printed MO gels on 17.5 sucrose mask. Polymerisation was carried out with 7.5 wt% APS (35 nL) and 5 wt% TEMED with 10 wt% AAm, 0.6 mol% MBA wrt AAm, 2 wt% SIC and 0.4 mol% MOR2 (315 nL). Substantial amounts of material washed away resulting in holes within the centre of the gels.

SEM imaging of a 10 wt% AAm gel showed similar structures to the 20 wt% gel with the mottled surfaces, more sizeable pores, and bumpy areas of increased density (Figure 5.32).

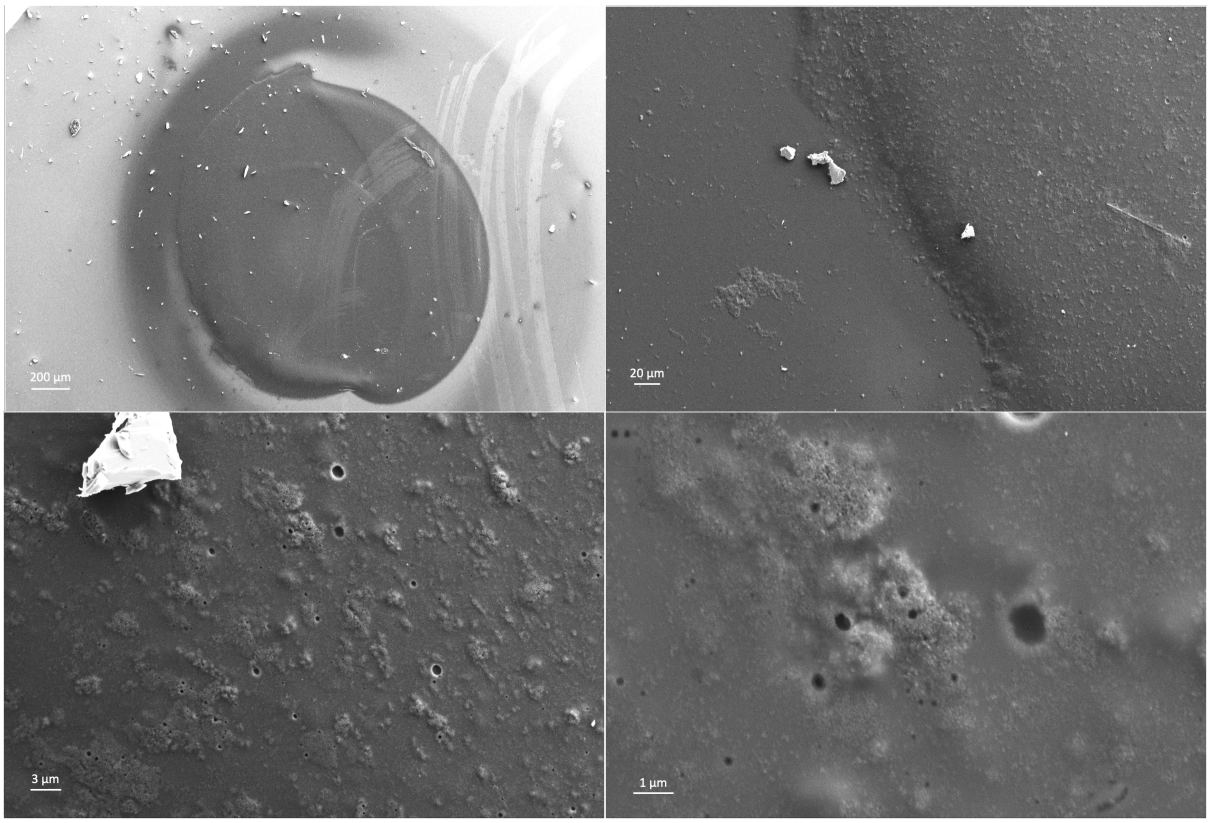

Figure 5.32 SEM images of a printed MO gel on 17.5 nL sucrose mask. Polymerisation was carried out with 7.5 wt% APS (35 nL) and 5 wt% TEMED with 10 wt% AAm, 0.6 mol% MBA wrt AAm, 2 wt% SIC and 0.4 mol% MOR2 (315 nL). Note, due to fracturing of the electrode wafer there are white silicon shards on the surface.

5.2.2 Optical Analysis

Despite the inaccurate dispensing of material, attempts were made to get some swelling information from the synthesised gels. Gels with large defects were discarded and the best gels were tested for optical transduction. The 10 wt% AAm gels were about half the size of the 175 nL 20 wt% gels tested during the scale up optimisation (Figure 5.33). It was clear that these were too small to assess accurately with the optical transduction set up, even more so as any gel deviations could have a much larger influence on measured volume.

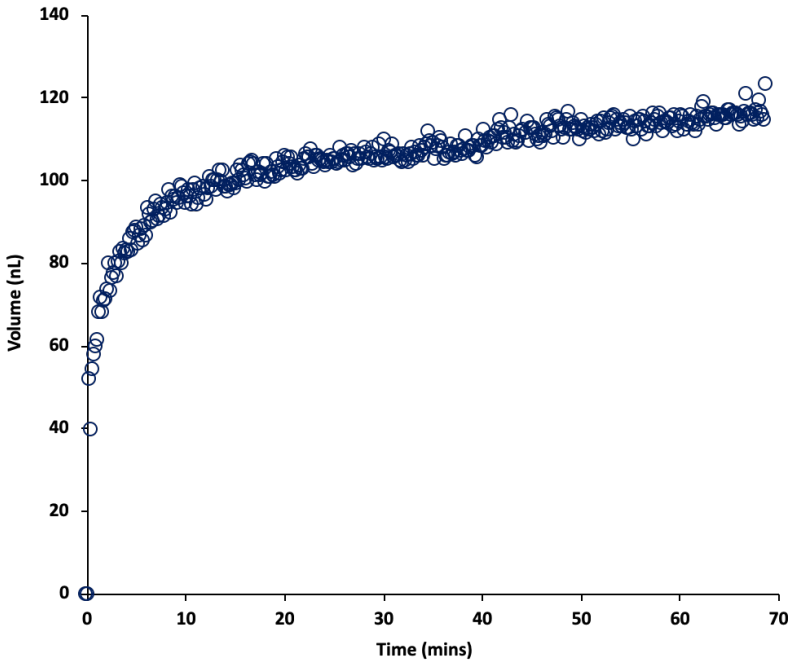

Figure 5.33 Swelling kinetics of a printed MO gels on 17.5 nL sucrose mask. Polymerisation was carried out with 7.5 wt% APS (35 nL) and 5 wt% TEMED with 10 wt% AAm, 0.6 mol% MBA wrt AAm, 2 wt% SIC and 0.4 mol% MOR2 (315 nL).

As expected from the deposited volume inaccuracies, the 20 wt% AAm gels offered no differential swelling in analyte solutions (Figure 5.34). Given the smaller gel volume it would be expected that gels would be at least as sensitive as the hand pipetted MOR2 gels. However the increased AAm concentration increased the gel density, albeit the total MOR2 crosslinks remained equal due to the reduced MO crosslink concentration. Despite the unexpected relatively small standard error of the mean for each set of samples and the increased swelling in DNA solutions compared to buffer, the largest swelling response was seen in 100 nM random solution. It can be assumed that the errors incorporated during synthesis meant the deposited volumes were more influential than the swelling solution and that errors were relatively small through the chance of random solution assignment.

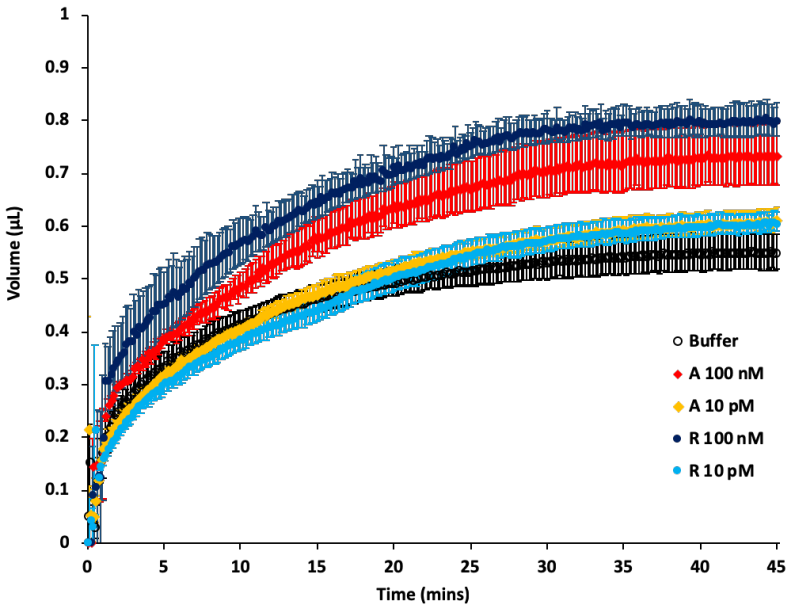

Figure 5.34 Comparison of swelling kinetics of printed MO gels on 17.5 sucrose mask. Polymerisation was carried out with 7.5 wt% APS (35 nL) and 5 wt% TEMED with 20 wt% AAm, 0.6 mol% MBA wrt AAm, 2 wt% SIC and 0.2 mol% MOR2 (315 nL). Swelling conducted in 1 mM PBS buffer (hollow black circles, bottom series at 45 mins) with 10 pM or 100 nM of analyte (red and yellow diamonds) or random sequence (solid blue circles). Standard error of the mean calculated using equation 3.2b (n = 3).

In an attempt to overcome the inaccurate gel volumes, the rate of swelling was considered as swelling should occur faster if MO crosslinks are broken (Figure 5.35). However, the rate of swelling is still dependent on the gel volume and shape. As such, the swelling rate offered no improvements for the signal transduction.

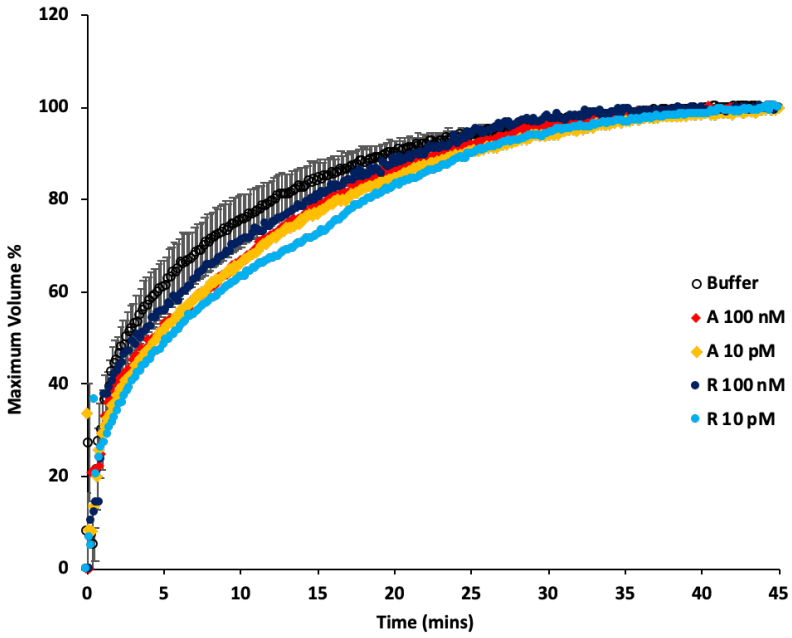

Figure 5.35 Comparison of swelling kinetics of printed MO gels on 17.5 sucrose mask. Polymerisation was carried out with 7.5 wt% APS (35 nL) and 5 wt% TEMED with 20 wt% AAm, 0.6 mol% MBA wrt AAm, 2 wt% SIC and 0.2 mol% MOR2 (315 nL). Swelling conducted in 1 mM PBS buffer (hollow blue circles) with 10 pM or 100 nM of analyte (red and yellow diamonds) or random sequence (solid blue circles). Error bars show standard error of the mean. The maximum average swollen volume within 60 minutes of swelling was used to calculate the swelling %. Standard error of the mean calculated using equation 3.2b (n = 3).

To illustrate the issues with swelling rate use, the swelling of each of the samples swollen in buffer were compared to the average (Figure 5.36). In this case it is clear that the gel swelling plateau point varies substantially. For example sample 4 plateaus within 10 minutes, while sample 2 doesn't plateau until 40 minutes. It is dependent on shape as well as size as sample 3 is the smallest gel yet plateaus later than sample 4.

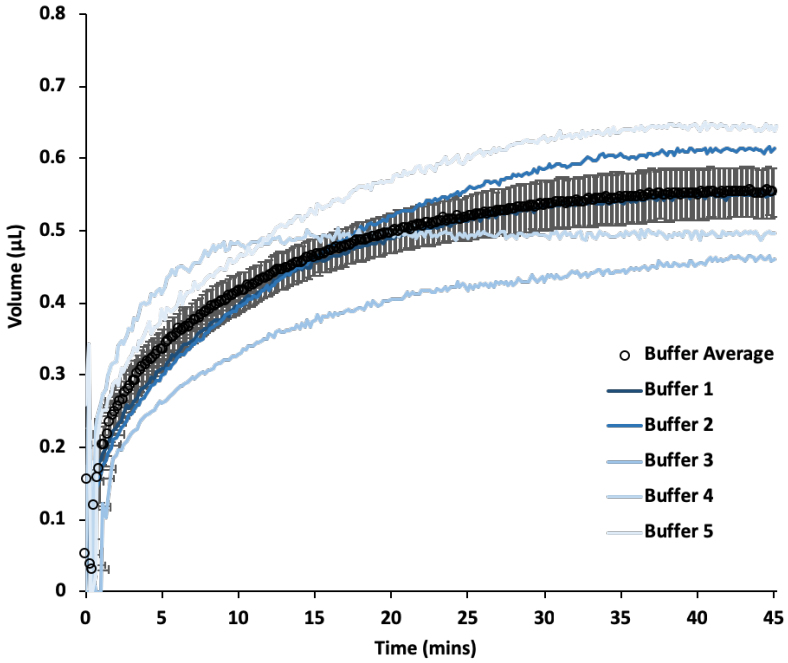

Figure 5.36 Comparison of swelling kinetics of printed MO gels on 17.5 sucrose mask. Polymerisation was carried out with 7.5 wt% APS (35 nL) and 5 wt% TEMED with 20 wt% AAm, 0.6 mol% MBA wrt AAm, 2 wt% SIC and 0.2 mol% MOR2 (315 nL). Swelling conducted in 1 mM PBS buffer. Standard error of the mean calculated using equation 3.2b (n = 3).

In a final attempt to achieve some optical validation of selective swelling for these printed gels, the gels were swollen in buffer before swelling in analyte or random (Figure 5.37). In this way the swollen volume in buffer can be used in place of the deposited volume to calculate the Δ% and more accurately assess gel swelling as the deposited volume is somewhat factored in. To remove the influence of swelling rate gels were swollen for 24 hours. Although the 10 wt% gels (Sol. B) were too small to accurately assess, the 20 wt% gels (Sol. A) did appear to swell more in analyte than random sequence solutions. This remains an inaccurate method of transduction as the initial and final images were taken with slightly different positions and camera focus and the gels themselves were not perfectly circular droplets. As well as this the long equilibration and swelling times make it wholly impractical for a point-of-care device, yet it can serve to show that MO crosslinks appear to remain responsive during inkjet printing.

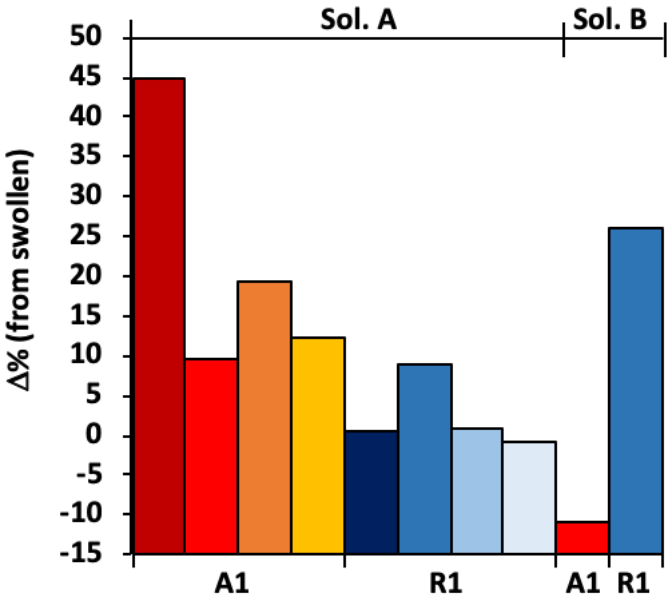

Figure 5.37 Comparison of swollen volume of printed MO gels on 17.5 sucrose mask. Polymerisation was carried out with 7.5 wt% APS (35 nL) and 5 wt% TEMED with 20 wt% AAm, 0.2 mol% MOR2 (Sol. A) or 10 wt% AAm, 0.4 mol% MOR2 (Sol. B) 0.6 mol% MBA wrt AAm, 2 wt% SIC and (315 nL). Gels were preswollen in 1 mM PBS buffer overnight and transferred into 100 nM of analyte (A1, red-yellow) or random sequence (R1, blue) for 60 minutes. Preswollen volumes were used to calculate Δ% using equation 3.2a.

5.2.3 Electrical Analysis

Much like the optical transduction, electrical results will be affected by both gel structure and placement. It is therefore not unexpected that even the dried percolating resistance would differ from gels printed without MO crosslinks. In each case the dried gels were at MΩs before washing and resistance would lower, albeit still at MΩs, once immersed in buffer (Figure 5.38). After this washing step, the 10 wt% AAm gels had a mixture of dried resistance at MΩs or below 100 kΩs, yet all swelled to similar MΩ levels. 20 wt% AAm gels offered little improvement, other than all washed gels being <100 kΩs when dried.

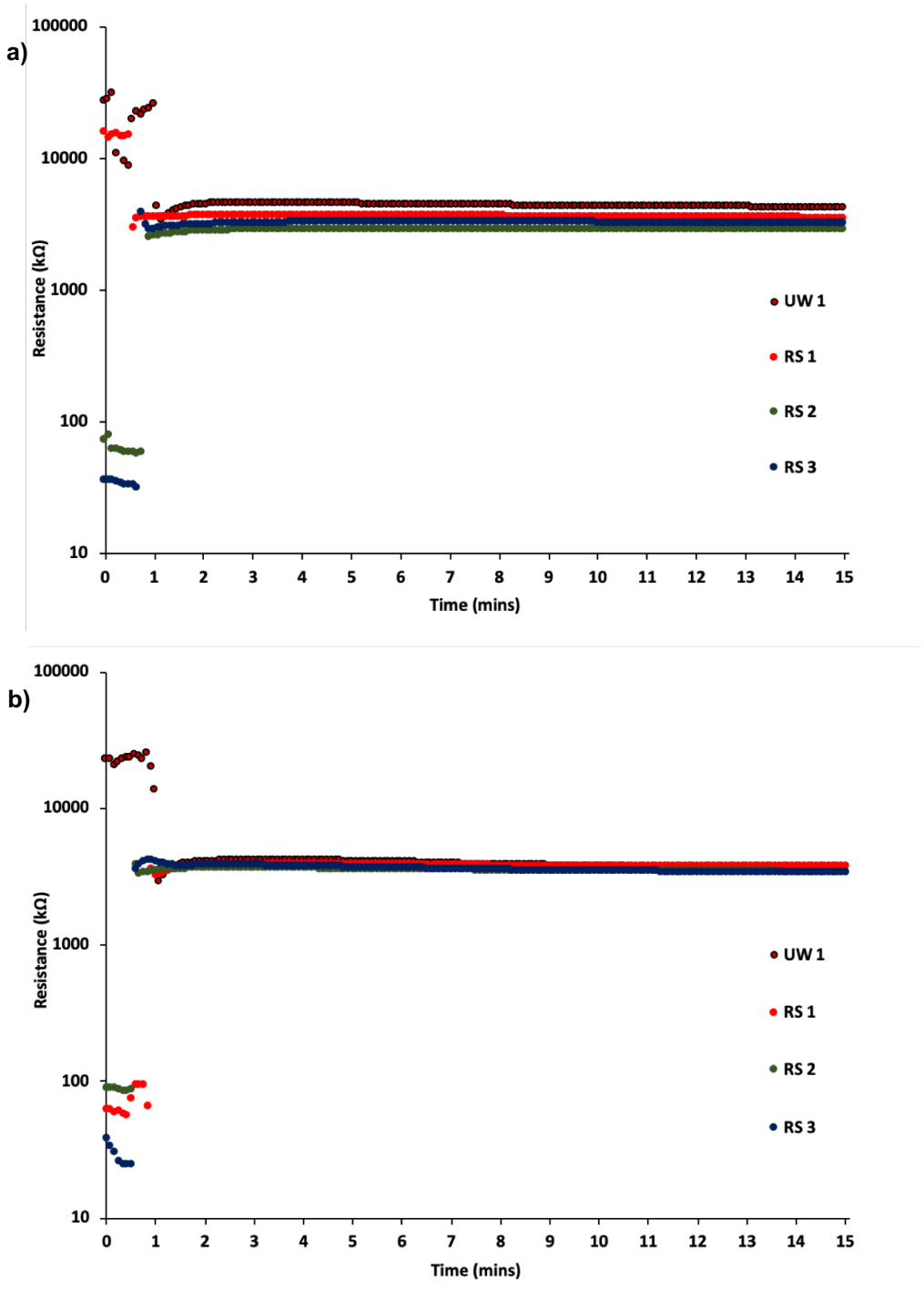

Figure 5.38 The d.c. resistance profiles of 1 unwashed gel and 3 washed gels printed on electrodes, 17.5 sucrose mask. Polymerisation was carried out with 7.5 wt% APS (35 nL) and 5 wt% TEMED with (a) 10 wt% AAm, 0.6 mol% MBA wrt AAm, 2 wt% SIC and 0.4 mol% MOR2 or (b) 20 wt% AAm, 0.6 mol% MBA wrt AAm, 2 wt% SIC and 0.2 mol% MOR2 (315 nL).

Given the inconsistencies during synthesis, the variation in not only electrode contact but also gel microstructures due to varying APS concentrations, it is little wonder that

resistance measurements for printed MOR2 crosslinked gels were worse than the gels without MO crosslinks.

5.3 Conclusions and Ongoing Challenges

A water stable SIC electrostatic dispersion was used due to the lack of stability of CNP in aqueous solution. Both PBS and NaCl caused aggregation of SIC particles, according to DLS measurements. Consequently, HPLC grade water was used in further experiments. Attempts to optimise SIC composite synthesis by hand was impossible with UV photoinitiation as the improved dispersion prevented UV penetration into the pregel droplet. Using redox initiation with APS and TEMED was problematic, first due to oxygen inhibition and the due to the lack of mixing resulting in localised polymerisation.

An inkjet printed method was developed and optimised including a hydrophobic mask to constrain droplet placement and spreading.[393] The polymerisation method was simplified from adding components individually to drying the APS before printing on the pregel mixture containing monomers, dispersion and TEMED. Multiple microarrays were used to optimise the concentration of each component and due to the nature of the small droplets decisions were made predominantly on gel macrostructure homogeneity and shape. Larger gels were printed onto the electrodes used previously for hand-pipetted gels using a wafer holder for precision. Gel and mask size were optimised and preliminary optical and electrical results were promising. With SEM imaging indication a more homogeneous gel than the CNP hand-pipetted material, gels were more robust and able to undergo multiple swelling and drying cycles without delamination, resulting in relatively consistent resistance profiles.

Incorporation of MO crosslinks into the pregel solution resulted in a viscosity which could not be properly aspirated or printed. Halving the MO concentration enabled both aspiration and printing yet caused great inaccuracies in gel shape and volume due to air bubbles in the aspirated aliquot. Attempts to assess optically were inaccurate due to the various shapes and volumes. Using preswollen gels transferred into analyte or

random sequence solutions achieved an elevated swelling response to the analyte sequence, which indicated MO crosslinks were intact through printing. Electrical transduction was similarly impossible due to gel variation. SEM imaging showed mottled and bumpy surfaces seemingly from the SIC particle density.

Further optimisation was impossible due to lack of material and time. Potential solutions to the MO viscosity issues would be to use an elevated temperature, alternative solvents (as MO hybridisation should endure solvent mixtures better than DNA) or a wider printer nozzle and slower aspiration rate. Similarly, alternative printable conductive fillers or drop-on-demand printer heads could be investigated.[283,284,373,388,393,402–405] Other simple improvements would be using photolithography to prepare more precise hydrophobic masks to improve gel placement and shape, the use of more appropriately designed electrodes or electrode substrates for smaller volumes.[406] Once printable, different gel layers, patterns and coatings could also be investigated which could improve gel reswellability or filter solutions.[290,407–409]

Chapter 6 Summary and Conclusions

6.1.1 Summary

Current miRNA detection methods are complex, costly and time-consuming. As such, the great potential of miRNA as non-invasive biomarkers of a huge range of diseases has yet to be realised. Oligonucleotide crosslinks have been shown to be specific and sensitive bioreceptors for miRNA and their incorporation into hydrogels resulted in a selective and specific controlled swelling response.

Optical transduction of DNA crosslinked hydrogel swelling showed various crosslink designs capable of detecting miRNA or sRNA sequences, as well as an aptamer crosslink for adenosine, which exemplified the adaptability of this material. The challenges of using DNA, namely the charged backbone and viscosity, was reduced through intelligent crosslink design, using minimal blocking strand lengths of multiple strand crosslink junctions. However, issues of gel detachment and thermal dehybridisation of the DNA crosslinks remained problematic and limited the solvents and synthetic methods available.

A novel MO crosslinked hydrogel material was developed to improve thermal stability, salt dependency and the anionic charge associated with DNA crosslinks. Selective and specific swelling was observed as with DNA gels in the presence of an analyte DNA sequence with mismatch discrimination, to a 100-fold improved sensitivity of 100 pM. This was further enhanced through halving the hydrogel volume and removing salt from both synthesis and testing to maximise swelling, resulting in a limit of detection of 10 pM. The improved thermal stability coupled with the diminished salt sensitivity suggest significant promise for MOCHs as a more stable and controllable alternative to DNA-based responsive hydrogel systems and facilitate alternative synthesis methods previously unavailable to DNA-crosslinked materials.

The sensitivity and sensor design remain insufficient for practicable point-of-care testing. Detection of miRNA has yet to be demonstrated, although MO-RNA hybridisation is expected to be stronger than MO-DNA and as such may be expected

to be more sensitive. Reduced hydrogel volumes would also further improve sensitivity, yet a more accurate optical transduction method would be required. Poor multiplex capabilities for optical transduction would limit the usefulness of miRNA detection, as the most accurate diagnoses are obtained by assessing a number of miRNA sequences in miRNA fingerprinting.

Electrical transduction using an oligonucleotide crosslinked polymer composite would provide rapid results with multiplex capabilities. However, the composite material developed by Dr Ferrier exhibited numerous reproducibility issues, in particular when using longer DNA crosslinks. Each composition tested, when delamination had not occurred, exhibited resistance values unrelated to the swollen volume. It was identified that the flow of conductive particles through the hydrogel matrix, rather than hydrogel volume, was mechanism of resistance change. Furthermore, poor UV initiation efficiency, owing to the density of carbon nanopowder required for conductivity, was highlighted as a flawed choice for material synthesis as more homogenous pregel solutions with carbon would polymerise less efficiently.

The use of MO crosslinked hydrogel composites for electrical transduction indicated that a more homogenous dispersion of CNP removed the percolation of the material, as shown by SEM. DNA crosslinked hydrogel composites showed areas of dense hydrogel and CNP, resulting in areas of conductivity. Pregel solutions containing a water stable SIC electrostatic dispersion could not be UV initiated. Alternative initiation strategies were impractical when hand pipetting.

Inkjet printing of the composite material was achieved and optimised using the water stable SIC electrostatic dispersion and initiation using APS and TEMED. Gels appeared homogenous and robust enough to undergo multiple swelling cycles. The electrical transduction was far more consistent using inkjet printed gels and washes could be conducted to remove loose conductive particles. Only MOs could be used for inkjet printing with the dispersion as DNA hybridisation necessitates salt which caused particle aggregation. However, the viscosity of the MO solutions resulted in bubbles during aspiration and any printed MO crosslinked hydrogel composite volumes were therefore inconsistent.

6.1.2 Conclusions and Remaining Challenges

The research presented in this thesis improved a number of facets of oligonucleotide crosslinked hydrogels and composites. Firstly, the benefits of DNA crosslinks as bioreceptors were clearly accentuated by using MO crosslinks and MO crosslinks can be used. These MO crosslinks, much like other DNA analogues like PNA or LNA could be readily utilised in established technologies using DNA as a bioreceptor. Much like LNA, MOs would improve sensitivity. Furthermore, MOs could be used in low salt conditions if using a solid-phase method, or no salt conditions if using solution-phase techniques or hydrogels.

Optical transduction of hydrogel swelling could be improved most easily by using MO crosslinks in the sensor design developed by Stokke *et al.* However, the lack of multiplex capabilities means this technology is not viable for POC testing. The pNIPAm microgel etalons developed by Serpe *et al.* could be multiplexed, yet the microgel synthesis conditions (thermal initiation of APS above the lower critical solution temperature of pNIPAm)[410] would cause thermal dehybridisation of DNA or MO crosslinks. Synthesis of pNIPAm microgels at 40 °C using APS and TEMED was achieved and optimised for copolymerisation with MO crosslinks, as the temperature is below the T_m of the MO crosslink.[411] However, addition of the MO crosslinks caused aggregation at even the lowest concentrations. Further exploration and understanding of this may enable synthesis of MO crosslinked pNIPAm microgels that could be incorporated into etalons for miRNA detection.

The composite UV initiation issues were overcome through inket printing using APS and TEMED for initiation. Printing of the MO crosslinks, either with the monomer solutions or as a separate solution, should be achievable using an alternative nozzle or solvents. Accurate dispensing would then allow accurate investigation into swelling and electrical properties of the printed MO crosslinked composites and further optimisation if required. Initial SEM images suggested an improved composite homogeneity, although cryo-fractured samples would need to be imaged to inform of the internal structures within the composite. Alternative conductive components could be investigated, in particular any printable materials should be readily adaptable. Rather than unattached conductive components, alternatives such as

copolymerisation with poly(ionic liquid)s, or a conductive polymer formed within the hydrogel matrix, should reduce any leaching and may increase the reproducibility of results.

Alternative electrode designs could prove to be more appropriate for investigating the electrical properties of this material and could reduce the delamination issues. A sandwich stacked electrode, wherein the composite is between an anode on bottom and a cathode layer on top (or *vice versa*) would prevent detachment and minimise the area through which leaching could occur.[412] Solution could be flowed in from the edges and pressure controls could be implemented to control hydrogel swelling directions. Similarly, a well electrode, in which a 3D layers of insulator and electrode are constructed and a hole drilled for material to fill, would again allow for composite investigation without drastic delamination or detachment.[413] Furthermore, the well hole ensures that material will be placed and remain in the appropriate location during synthesis. Adapting the hardware to minimise the voltage applied may also help to reduce delamination and ensure that the measured resistance is within an appropriate range, while uncharged MO crosslinks may enable alternative electrical interrogation methods such as impedance monitoring.

6.1.3 Concluding Remarks

This thesis has established the benefits of MO crosslinks in a world's first MO crosslinked hydrogel using optical transduction to show improved sensitivity, thermal stability and no salt sensitivity. Optical transduction remains insufficiently sensitive for real world applications. Steps to address the challenges of the oligonucleotide crosslinked composite sensor design developed previously by Dr Ferrier were made, namely development of an inkjet printable composite material. Further improvements are required to accurately print MO crosslinks and more appropriate electrode designs necessary. Inkjet printed MO crosslinked composites have the potential to be rapid, specific and sensitive miRNA sensors and electrical transduction would facilitate rapid miRNA fingerprinting for disease diagnosis. This avenue of research could prove to

be revolutionary for healthcare if improvements achieve the electrical transduction with appropriate sensitivity for POC diagnostics.

References

(1) Hasanzadeh, M.; Shadjou, N. Electrochemical Nanobiosensing in Whole Blood: Recent Advances. *Trends Anal. Chem.* **2016**, *80*, 167–176.

(2) Tanaka, M.; Oikawa, K.; Takanashi, M.; Kudo, M.; Ohyashiki, J.; Ohyashiki, K.; Kuroda, M. Down-Regulation of MiR-92 in Human Plasma Is a Novel Marker for Acute Leukemia Patients. *PLoS One* **2009**, *4* (5), 1–5.

(3) Hamidi-Asl, E.; Palchetti, I.; Hasheminejad, E.; Mascini, M. A Review on the Electrochemical Biosensors for Determination of MicroRNAs. *Talanta* **2013**, *115*, 74–83.

(4) Lee, R. C.; Feinbaum, R. L.; Ambros, V. The C . Elegans Heterochronic Gene Lin-4 Encodes Small RNAs with Antisense Complementarity to Lin-14. *Cell* **1993**, *75* (5), 843–854.

(5) Wightman, B.; Ha, I.; Ruvkun, G. Posttranscriptional Regulation of the Heterochronic Gene Lin-14 by W-4 Mediates Temporal Pattern Formation in C. Elegans. *Cell* **1993**, *75* (5), 855–862.

(6) Ruvkun, G. Glimpses of a Tiny RNA World. *Science (80-.).* **2001**, *294* (5543), 797–799.

(7) Kozomara, A.; Birgaoanu, M.; Griffiths-Jones, S. MiRBase: From MicroRNA Sequences to Function. *Nucleic Acids Res.* **2019**, *47*, 155–162.

(8) Friedman, R. C.; Farh, K. K. H.; Burge, C. B.; Bartel, D. P. Most Mammalian MRNAs Are Conserved Targets of MicroRNAs. *Genome Res.* **2009**, *19* (1), 92–105.

(9) Garzon, R.; Calin, G. A.; Croce, C. M. MicroRNAs in Cancer. *Annu. Rev. Med.* **2009**, *60*, 167–179.

(10) David P. Bartel. Genomics, Biogenesis, Mechanism, and Function. *Cell* **2004**, *116* (2), 281–297.

(11) Maqbool, R.; Hussain, M. U. MicroRNAs and Human Diseases: Diagnostic and Therapeutic Potential. *Cell Tissue Res.* **2014**, *358* (1), 1–15.

(12) He, L.; Hannon, G. J. MicroRNAs: Small RNAs with a Big Role in Gene Regulation. *Nat. Rev. Genet.* **2004**, *5* (7), 522–531.

(13) Mathieu, J.; Ruohola-baker, H. Regulation of Stem Cell Populations by MicroRNAs. In *Transcriptional and Translational Regulation of Stem Cells*; 2013; pp 329–351.

(14) Carleton, M.; Cleary, M. A.; Linsley, P. S. MicroRNAs and Cell Cycle Regulation. *Cell Cycle* **2007**, *6* (17), 2127–2132.

(15) Zen, K.; Zhang, C.-Y. Circulating MicroRNAs: A Novel Class of Biomarkers to Diagnose and Monitor Human Cancers. *Med. Res. Rev.* **2012**, *32* (2), 326–348.

(16) Winter, J.; Jung, S.; Keller, S.; Gregory, R. I.; Diederichs, S. Many Roads to Maturity: MicroRNA Biogenesis Pathways and Their Regulation. *Nat. Cell Biol.* **2009**, *11* (3), 228–234.

(17) Lee, Y.; Jeon, K.; Lee, J. T.; Kim, S.; Kim, V. N. MicroRNA Maturation: Stepwise Processing and Subcellular Localization. *EMBO J.* **2002**, *21* (17), 4663–4670.

(18) Lee, Y.; Ahn, C.; Han, J.; Choi, H.; Kim, J.; Yim, J.; Lee, J.; Provost, P.; Radmark, O.; Sunyoung, K.; et al. The Nuclear RNase III Drosha Initiates MicroRNA Processing. *Nature* **2003**, *425* (6956), 415–419.

(19) Zeng, Y.; Cullen, B. R. Structural Requirements for Pre-MicroRNA Binding and Nuclear Export by Exportin 5. *Nucleic Acids Res.* **2004**, *32* (16), 4776–4785.

(20) Bernstein, E.; Caudy, A. A.; Hammond, S. M.; Hannon, G. J. Role for a Bidentate Ribonuclease in the Initiation Step of RNA Interference. *Nature* **2001**, *409* (6818), 363–366.

(21) Caudy, A. A.; Hammond, S. M.; Rauhut, R.; Lendeckel, W.; Lim, E. P.; Weinstein, E. G.; Bartel, D. P.; Ambros, V.; Feinbaum, R. L.; Ambros, V.; et al. A MicroRNA in a Multiple-Turnover RNAi Enzyme Complex. **2002**, *297*, 2056–2061.

(22) Lim, L. P.; Lau, N. C.; Garrett-Engele, P.; Grimson, A.; Schelter, J. M.; Castle, J.; Bartel, D. P.; Linsley, P. S.; Johnson, J. M. Microarray Analysis Shows That Some MicroRNAs Downregulate Large Numbers of Target MRNAs. *Nature* **2005**, *433*, 769–773.

(23) Calin, G. A.; Dumitru, C. D.; Shimizu, M.; Bichi, R.; Zupo, S.; Noch, E.; Aldler, H.; Rattan, S.; Keating, M.; Rai, K.; et al. Frequent Deletions and Down-Regulation of Micro- RNA Genes MiR15 and MiR16 at 13q14 in Chronic Lymphocytic Leukemia. *PNAS* **2002**, *99* (24), 15524–15529.

(24) Cimmino, A.; Calin, G. A.; Fabbri, M.; Iorio, M. V.; Ferracin, M.; Shimizu, M.; Wojcik, S. E.; Aqeilan, R. I.; Zupo, S.; Dono, M.; et al. MiR-15 and MiR-16 Induce Apoptosis by Targeting BCL2. *Proc. Natl. Acad. Sci.* **2005**, *102* (39), 13944–13949.

(25) Calin, G. A.; Ferracin, M.; Cimmino, A.; Di Leva, G.; Shimizu, M.; Wojcik, S. E.; Iorio, M. V.; Visone, R.; Sever, N. I.; Fabbri, M.; et al. A MicroRNA Signature Associated with Prognosis and Progression in Chronic Lymphocytic Leukemia. *N. Engl. J. Med.* **2005**, *353* (17), 1793–1801.

(26) Pekarsky, Y.; Croce, C. M. Role of MiR-15/16 in CLL. *Cell Death Differ.* **2015**, *22* (1), 6–11.

(27) Jiang, Q.; Wang, Y.; Hao, Y.; Juan, L.; Teng, M.; Zhang, X.; Li, M.; Wang, G.; Liu, Y. MiR2Disease: A Manually Curated Database for MicroRNA Deregulation in Human Disease. *Nucleic Acids Res.* **2009**,

37, 98–104.
(28) Kosaka, N.; Iguchi, H.; Ochiya, T. Circulating MicroRNA in Body Fluid: A New Potential Biomarker for Cancer Diagnosis and Prognosis. *Cancer Sci.* **2010**, *101* (10), 2087–2092.
(29) Wang, J.; Chen, J.; Sen, S. MicroRNA as Biomarkers and Diagnostics. *J. Cell. Physiol.* **2016**, *231* (1), 25–30.
(30) Detassis, S.; Grasso, M.; Del Vescovo, V.; Denti, M. A. MicroRNAs Make the Call in Cancer Personalized Medicine. *Front. Cell Dev. Biol.* **2017**, *5*, 1–20.
(31) Schulte, C.; Zeller, T. MicroRNA-Based Diagnostics and Therapy in Cardiovascular Disease-Summing up the Facts. *Cardiovasc. Diagn. Ther.* **2015**, *5* (1), 17–36.
(32) Correia, C. N.; Nalpas, N. C.; McLoughlin, K. E.; Browne, J. A.; Gordon, S. V.; MacHugh, D. E.; Shaughnessy, R. G. Circulating MicroRNAs as Potential Biomarkers of Infectious Disease. *Front. Immunol.* **2017**, *8* (118), 1–17.
(33) Louten, J.; Beach, M.; Palermino, K.; Weeks, M.; Holenstein, G. MicroRNAs Expressed during Viral Infection: Biomarker Potential and Therapeutic Considerations. *Biomark. Insights* **2015**, *10*, 25–52.
(34) Manzano-Roman, R.; Siles-Lucas, M. MicroRNAs in Parasitic Diseases: Potential for Diagnosis and Targeting. *Mol. Biochem. Parasitol.* **2012**, *186* (2), 81–86.
(35) Li, Y.; Kowdley, K. V. MicroRNAs in Common Human Diseases. *Genomics. Proteomics Bioinformatics* **2012**, *10* (5), 246–253.
(36) Mushtaq, G.; Greig, N. H.; Shaik, M. M.; Tamargo, I. A.; Kamal, M. A. MiRNAs as Circulating Biomarkers for Alzheimer's Disease and Parkinson's Disease. *Med Chem* **2016**, *12* (3), 217–225.
(37) Wu, H. Z. Y.; Ong, K. L.; Seeher, K.; Armstrong, N. J.; Thalamuthu, A.; Brodaty, H.; Sachdev, P.; Mather, K. Circulating MicroRNAs as Biomarkers of Alzheimer's Disease: A Systematic Review. *J. Alzheimer's Dis.* **2015**, *49* (3), 755–766.
(38) Salvatore, M.; Magrelli, A.; Taruscio, D. The Role of MicroRNAs in the Biology of Rare Diseases. *Int. J. Mol. Sci.* **2011**, *12* (10), 6733–6742.
(39) Atif, H.; Hicks, S. D. A Review of MicroRNA Biomarkers in Traumatic Brain Injury. *J. Exp. Neurosci.* **2019**, *13*, 1–12.
(40) Hanson, E.; Lubenow, H.; Ballantyne, J. Identification of Forensically Relevant Body Fluids Using a Panel of Differentially Expressed MicroRNAs. *Anal. Biochem.* **2009**, *387*, 303–314.
(41) Lux, C.; Schyma, C.; Madea, B.; Courts, C. Identification of Gunshots to the Head by Detection of RNA in Backspatter Primarily Expressed in Brain Tissue. *Forensic Sci. Int.* **2014**, *237*, 62–69.
(42) Wang, L.; Han, Y.; Zhou, S.; Wang, G.; Guan, X. Nanopore Biosensor for Label-Free and Real-Time Detection of Anthrax Lethal Factor. *ACS Appl. Mater. Interfaces* **2014**, *6* (10), 7334–7339.
(43) Paniel, N.; Baudart, J.; Hayat, A.; Barthelmebs, L. Aptasensor and Genosensor Methods for Detection of Microbes in Real World Samples. *Methods* **2013**, *64* (3), 229–240.
(44) Nakamura, K.; Sawada, K.; Yoshimura, A.; Kinose, Y.; Nakatsuka, E.; Kimura, T. Clinical Relevance of Circulating Cell-Free MicroRNAs in Ovarian Cancer. *Mol. Cancer* **2016**, *15* (1), 1–10.
(45) Fesler, A.; Jiang, J.; Zhai, H.; Ju, J. Circulating MicroRNA Testing for the Early Diagnosis and Follow-up of Colorectal Cancer Patients. *Mol. Diagnosis Ther.* **2014**, *18* (3), 303–308.
(46) Nalejska, E.; Mączyńska, E.; Lewandowska, M. A. Prognostic and Predictive Biomarkers: Tools in Personalized Oncology. *Mol. Diagnosis Ther.* **2014**, *18* (3), 273–284.
(47) MacDonagh, L.; Gray, S. G.; Finn, S. P.; Cuffe, S.; O'Byrne, K. J.; Barr, M. P. The Emerging Role of MicroRNAs in Resistance to Lung Cancer Treatments. *Cancer Treat. Rev.* **2015**, *41* (2), 160–169.
(48) Li, H.; Yang, B. B. MicroRNA in Drug Resistance. *Oncoscience* **2014**, *1* (1), 3–4.
(49) Li, H.; Yang, B. B. MicroRNA in Drug Resistance . *Oncoscience* **2014**, *1* (1), 3–4.
(50) Jung, E. J.; Santarpia, L.; Kim, J.; Esteva, F. J.; Moretti, E.; Buzdar, A. U.; Di Leo, A.; Le, X. F.; Bast, R. C. J.; Park, S. T.; et al. Plasma MiR-210 Levels Correlate with Sensitivity to Trastuzumab and Tumor Presence in Breast Cancer Patients. *Cancer* **2012**, *118* (10), 2603–2614.
(51) Kosaka, N.; Iguchi, H.; Ochiya, T. Circulating MicroRNA in Body Fluid: A New Potential Biomarker for Cancer Diagnosis and Prognosis. *Cancer Sci.* **2010**, *101* (10), 2087–2092.
(52) Rosenfeld, N.; Aharonov, R.; Meiri, E.; Rosenwald, S.; Spector, Y.; Zepeniuk, M.; Benjamin, H.; Shabes, N.; Tabak, S.; Levy, A.; et al. MicroRNAs Accurately Identify Cancer Tissue Origin. *Nat. Biotechnol.* **2008**, *26* (4), 462–469.
(53) Rane, J. K.; Scaravilli, M.; Ylipaa, A.; Pellacani, D.; Mann, V. M.; Simms, M. S.; Nykter, M.; Collins, A. T.; Visakorpi, T.; Maitland, N. J. MicroRNA Expression Profile of Primary Prostate Cancer Stem Cells as a Source of Biomarkers and Therapeutic Targets. *Eur. Urol.* **2015**, *67* (1), 7–10.
(54) Zeng, H.; Fang, C.; Nam, S.; Cai, Q.; Long, X. The Clinicopathological Significance of MicroRNA-155 in Breast Cancer: A Meta-Analysis. *Biomed Res. Int.* **2014**, *2014*, 1–7.
(55) Yu, S. L.; Chen, H. Y.; Chang, G. C.; Chen, C. Y.; Chen, H. W.; Singh, S.; Cheng, C. L.; Yu, C. J.; Lee, Y. C.; Chen, H. S.; et al. MicroRNA Signature Predicts Survival and Relapse in Lung Cancer.

Cancer Cell **2008**, *13* (1), 48–57.
(56) Pignot, G.; Cizeron-Clairac, G.; Vacher, S.; Susini, A.; Tozlu, S.; Vieillefond, A.; Zerbib, M.; Lidereau, R.; Debre, B.; Amsellem-Ouazana, D.; et al. MicroRNA Expression Profile in a Large Series of Bladder Tumors: Identification of a 3-MiRNA Signature Associated with Aggressiveness of Muscle-Invasive Bladder Cancer. *Int. J. Cancer* **2013**, *132* (11), 2479–2491.
(57) Reid, G.; Kirschner, M. B.; van Zandwijk, N. Circulating MicroRNAs: Association with Disease and Potential Use as Biomarkers. *Crit. Rev. Oncol. Hematol.* **2011**, *80* (2), 193–208.
(58) Ramaswamy, S.; Tamayo, P.; Rifkin, R.; Mukherjee, S.; Angelo, M.; Ladd, C.; Reich, M.; Latulippe, E.; Mesirov, J. P.; Gerald, W.; et al. Multiclass Cancer Diagnosis Using Tumor Gene Expression Signatures. *PNAS* **2001**, *98* (26), 15149–15154.
(59) Lu, J.; Getz, G.; Miska, E. A.; Alvarez-Saavedra, E.; Lamb, J.; Peck, D.; Sweet-Cordero, A.; Ebert, B. L.; Mak, R. H.; Ferrando, A. A.; et al. MicroRNA Expression Profiles Classify Human Cancers. *Nature* **2005**, *435* (7043), 834–838.
(60) Stenman, U. H.; Leinonen, J.; Zhang, W. M.; Finne, P. Prostate-Specific Antigen. *Cancer Biol.* **1999**, *9*, 83–93.
(61) Rawlings-Goss, R. A.; Campbell, M. C.; Tishkoff, S. A. Global Population-Specific Variation in MiRNA Associated with Cancer Risk and Clinical Biomarkers. *BMC Med. Genomics* **2014**, *7* (1), 1–14.
(62) Planell-Saguer, M. de; Rodicio, M. C. Analytical Aspects of MicroRNA in Diagnostics: A Review. *Anal. Chim. Acta* **2011**, *699* (2), 134–152.
(63) Harris, L.; Fritsche, H.; Mennel, R.; Norton, L.; Ravdin, P.; Taube, S.; Somerfield, M. R.; Hayes, D. F.; Bast, R. C. American Society of Clinical Oncology 2007 Update of Recommendations for the Use OfTumor Markers in Breast Cancer. *J. Clin. Oncol.* **2007**, *25* (33), 5287–5312.
(64) Ramaswamy, S.; Tamayo, P.; Rifkin, R.; Mukherjee, S.; Yeang, C. H.; Angelo, M.; Ladd, C.; Reich, M.; Latulippe, E.; Mesirov, J. P.; et al. Multiclass Cancer Diagnosis Using Tumor Gene Expression Signatures. *Proc. Natl. Acad. Sci. U. S. A.* **2001**, *98* (26), 15149–15154.
(65) Carrascosa, L. G.; Huertas, C. S.; Lechuga, L. M. Prospects of Optical Biosensors for Emerging Label-Free RNA Analysis. *TrAC - Trends Anal. Chem.* **2016**, *80*, 177–189.
(66) Aras, O.; Shet, A.; Bach, R. R.; Hysjulien, J. L.; Slungaard, A.; Hebbel, R. P.; Escolar, G.; Jilma, B.; Key, N. S. Induction of Microparticle- and Cell-Associated Intravascular Tissue Factor in Human Endotoxemia. *Blood* **2004**, *103* (12), 4545–4553.
(67) Lorentzen, E.; Conti, E. Structural Basis of 3′ Bnd RNA Becognition and Bxoribonucleolytic Bleavage by an Bxosome RNase PH Bore. *Mol. Cell* **2005**, *20* (3), 473–481.
(68) Pritchard, C. C.; Cheng, H. H.; Tewari, M. MicroRNA Profiling: Approaches and Considerations. *Nat. Rev. Genet.* **2015**, *13* (5), 358–369.
(69) Lawrie, C. H.; Gal, S.; Dunlop, H. M.; Pushkaran, B.; Liggins, A. P.; Pulford, K.; Banham, A. H.; Pezzella, F.; Boultwood, J.; Wainscoat, J. S.; et al. Detection of Elevated Levels of Tumour-Associated MicroRNAs in Serum of Patients with Diffuse Large B-Cell Lymphoma. *Br. J. Haematol.* **2008**, *141* (5), 672–675.
(70) Chen, Q.; Si, Q.; Xiao, S.; Xie, Q.; Lin, J.; Wang, C.; Chen, L.; Chen, Q.; Wang, L. Prognostic Significance of Serum MiR-17-5p in Lung Cancer. *Med. Oncol.* **2013**, *30* (1), 5–10.
(71) Qi, J.; Wang, J.; Katayama, H.; Sen, S.; Liu, S. Circulating MicroRNAs (CmiRNAs) as Novel Potential Biomarkers for Hepatocellular Carcinoma. *Neoplasma* **2013**, *60* (2), 135–142.
(72) Tiberio, P.; Callari, M.; Angeloni, V.; Daidone, M. G.; Appierto, V. Challenges in Using Circulating MiRNAs as Cancer Biomarkers. *Biomed Res. Int.* **2015**, *2015*, 1–11.
(73) Zubakov, D.; Boersma, A. W. M.; Choi, Y.; Van Kuijk, P. F.; Wiemer, E. A. C.; Kayser, M. MicroRNA Markers for Forensic Body Fluid Identification Obtained from Microarray Screening and Quantitative RT-PCR Confirmation. *Int. J. Legal Med.* **2010**, *124* (3), 217–226.
(74) Cancer Research UK, https://www.cancerresearchuk.org/health-professional/cancer-statistics/statistics-by-cancer-type/leukaemia#heading-One, Accessed March 2019.
(75) Smittenaar, C. R.; Petersen, K. A.; Stewart, K.; Moitt, N. Cancer Incidence and Mortality Projections in the UK until 2035. *Br. J. Cancer* **2016**, *115* (9), 1147–1155.
(76) Siegel, R. L.; Miller, K. D.; Jemal, A. Cancer Statistics, 2016. *CA. Cancer J. Clin.* **2016**, *66* (7), 7–30.
(77) Shephard, E. A.; Hamilton, W.; Neal, R. D.; Rose, P. W.; Walter, F. M. Symptoms of Adult Chronic and Acute Leukaemia before Diagnosis: Large Primary Care Case-Control Studies Using Electronic Records. *Br. J. Gen. Pract.* **2016**, *66* (644), e182–e188.
(78) Hallek, M.; Cheson, B. D.; Catovsky, D.; Caligaris-Cappio, F.; Dighiero, G.; Döhner, H.; Hillmen, P.; Keating, M. J.; Montserrat, E.; Rai, K. R.; et al. Guidelines for the Diagnosis and Treatment of Chronic Lymphocytic Leukemia: A Report from the International Workshop on Chronic Lymphocytic Leukemia Updating the National Cancer Institute-Working Group 1996 Guidelines. *Blood* **2008**, *111* (12), 5446–5456.

(79) Pfeifer, H.; Wassmann, B.; Hofmann, W. K.; Komor, M.; Scheuring, U.; Brück, P.; Binckebanck, A.; Schleyer, E.; Gökbuget, N.; Wolff, T.; et al. Risk and Prognosis of Central Nervous System Leukemia in Patients with Philadelphia Chromosome-Positive Acute Leukemias Treated with Imatinib Mesylate. *Clin. Cancer Res.* **2003**, *9* (13), 4674–4681.
(80) Mi, S.; Lu, J.; Sun, M.; Li, Z.; Zhang, H.; Neilly, M. B.; Wang, Y.; Qian, Z.; Jin, J.; Zhang, Y.; et al. MicroRNA Expression Signatures Accurately Discriminate Acute Lymphoblastic Leukemia from Acute Myeloid Leukemia. *Proc. Natl. Acad. Sci.* **2007**, *104* (50), 19971–19976.
(81) Ferrier, D. Nucleic Acid Detection Using Oligonucleotide Cross-Linked Polymer Composites, 2017.
(82) Johnson, B. N.; Mutharasan, R. Biosensor-Based MicroRNA Detection: Techniques, Design, Performance, and Challenges. *Analyst* **2014**, *139* (7), 1576–1589.
(83) Liu, A.; Wang, K.; Weng, S.; Lei, Y.; Lin, L.; Chen, W.; Lin, X.; Chen, Y. Development of Electrochemical DNA Biosensors. *TrAC - Trends Anal. Chem.* **2012**, *37*, 101–111.
(84) Sassolas, A.; Leca-Bouvier, B. D.; Blum, L. J. DNA Biosensors and Microarrays. *Chem. Rev.* **2008**, *108* (1), 109–139.
(85) Kim, Y. S.; Raston, N. H. A.; Gu, M. B. Aptamer-Based Nanobiosensors. *Biosens. Bioelectron.* **2016**, *76*, 2–19.
(86) Bhalla, N.; Jolly, P.; Formisano, N.; Estrela, P. Introduction to Biosensors. *Essays Biochem.* **2016**, *60*, 1–8.
(87) National Institute for Health and Care Excellence, https://www.nice.org.uk/guidance/DG14, Accessed March 2019.
(88) Curtis, L.; Burns, A. *Unit Costs of Health & Social Care 2016*; 2016.
(89) Bayer HealthCare. *Commissioning Effective Anticoagulation Services for the Future A Resource Pack for Commissioners*; 2013.
(90) Benes, V.; Castoldi, M. Expression Profiling of MicroRNA Using Real-Time Quantitative PCR, How to Use It and What Is Available. *Methods* **2010**, *50* (4), 244–249.
(91) Hunt, E. A.; Goulding, A. M.; Deo, S. K. Direct Detection and Quantification of MicroRNAs. *Anal. Biochem.* **2009**, *387* (1), 1–12.
(92) Zhang, X.; Lu, X.; Lopez-Berestein, G.; Sood, A. K.; Calin, G. In Situ Hybridization-Based Detection of MicroRNAs in Human Diseases. *microRNA Diagnostics Ther.* **2013**, *1* (1), 12–23.
(93) Ragan, C.; Zuker, M.; Ragan, M. A. Quantitative Prediction of MiRNA-MRNA Interaction Based on Equilibrium Concentrations. *PLoS Comput. Biol.* **2011**, *7* (2), 1–11.
(94) Liang, Y.; Ridzon, D.; Wong, L.; Chen, C. Characterization of MicroRNA Expression Profiles in Normal Human Tissues. *BMC Genomics* **2007**, *8*, 1–20.
(95) Campuzano, S.; Pedrero, M.; Pingarrón, J. M. Electrochemical Genosensors for the Detection of Cancer-Related MiRNAs. *Anal. Bioanal. Chem.* **2014**, *406* (1), 27–33.
(96) Miotto, E.; Saccenti, E.; Lupini, L.; Callegari, E.; Negrini, M.; Ferracin, M. Quantification of Circulating MiRNAs by Droplet Digital PCR: Comparison of EvaGreen- and TaqMan-Based Chemistries. *Cancer Epidemiol. Biomarkers Prev.* **2014**, *23* (12), 2638–2642.
(97) Weber, J. A.; Baxter, D. H.; Zhang, S.; Huang, D. Y.; Huang, K. H.; Lee, M. J.; Galas, D. J.; Wang, K. The MicroRNA Spectrum in 12 Body Fluids. *Clin. Chem.* **2010**, *56* (11), 1733–1741.
(98) Tsujiura, M.; Ichikawa, D.; Komatsu, S.; Shiozaki, A.; Takeshita, H.; Kosuga, T.; Konishi, H.; Morimura, R.; Deguchi, K.; Fujiwara, H.; et al. Circulating MicroRNAs in Plasma of Patients with Gastric Cancers. *Br. J. Cancer* **2010**, *102* (7), 1174–1179.
(99) Koscianska, E.; Starega-Roslan, J.; Sznajder, L. J.; Olejniczak, M.; Galka-Marciniak, P.; Krzyzosiak, W. J. Northern Blotting Analysis of MicroRNAs, Their Precursors and RNA Interference Triggers. *BMC Mol. Biol.* **2011**, *12* (1), 14–21.
(100) Várallyay, É.; Burgyán, J.; Havelda, Z. MicroRNA Detection by Northern Blotting Using Locked Nucleic Acid Probes. *Nat. Protoc.* **2008**, *3* (2), 190–196.
(101) Schwarzkopf, M.; Pierce, N. A. Multiplexed MiRNA Northern Blots via Hybridization Chain Reaction. *Nucleic Acids Res.* **2016**, *44* (15), e129-136.
(102) Pall, G. S.; Codony-Servat, C.; Byrne, J.; Ritchie, L.; Hamilton, A. Carbodiimide-Mediated Cross-Linking of RNA to Nylon Membranes Improves the Detection of SiRNA, MiRNA and PiRNA by Northern Blot. *Nucleic Acids Res.* **2007**, *35* (8), e60-69.
(103) Válóczi, A.; Hornyik, C.; Varga, N.; Burgyán, J.; Kauppinen, S.; Havelda, Z. Sensitive and Specific Detection of MicroRNAs by Northern Blot Analysis Using LNA-Modified Oligonucleotide Probes. *Nucleic Acids Res.* **2004**, *32* (22), e175-182.
(104) Li, W.; Ruan, K. MicroRNA Detection by Microarray. *Anal. Bioanal. Chem.* **2009**, *394* (4), 1117–1124.
(105) Nelson, P. T.; Baldwin, D. A.; Scearce, L. M.; Oberholtzer, J. C.; Tobias, J. W.; Mourelatos, Z. Microarray-Based, High-Throughput Gene Expression Profiling of MicroRNAs. *Nat. Methods* **2004**, *1* (2), 155–161.

(106) Castoldi, M.; Schmidt, S.; Benes, V.; Noerholm, M.; Kulozik, A. E.; Hentze, M. W.; Muckenthaler, M. U. A Sensitive Array for MicroRNA Expression Profiling (MiChip) Based on Locked Nucleic Acids (LNA). *RNA* **2006**, *12* (5), 913–920.
(107) Kong, W.; Zhao, J. J.; Lili, H. E.; Cheng, J. Q. Strategies for Profiling MicroRNA Expression. *J. Cell. Physiol.* **2009**, *218* (1), 22–25.
(108) Reza, A. M. T.; Cho, S.; Choi, Y.; Hong, K.; Kim, J.-H. Data Descriptor : Microarray Profiling of MiRNA and MRNA Expression in Rag 2 Knockout and Wild-Type Mouse Spleens. *Sci. Data* **2018**, *5*, 1–9.
(109) Conzone, S. D.; Pantano, C. G. Glass Slides to DNA Microarrays. *Mater. Today* **2004**, *7* (3), 20–26.
(110) Liu, C. -g.; Calin, G. A.; Volinia, S.; Croce, C. M. MicroRNA Expression Profiling Using Microarrays. *Nat. Protoc.* **2008**, *3* (4), 563–578.
(111) Jian, Y.; Wang, H.; Lan, F.; Liang, L.; Ren, N.; Liu, H.; Ge, S.; Yu, J. Electrochemiluminescence Based Detection of MicroRNA by Applying an Amplification Strategy and Hg(II)-Triggered Disassembly of a Metal Organic Frameworks Functionalized with Ruthenium(II)Tris(Bipyridine). *Microchim. Acta* **2018**, *185* (2), 1–8.
(112) Xie, H.; Zhang, C.; Gao, Z. Amperometric Detection of Nucleic Acid at Femtomolar Levels with a Nucleic Acid/Electrochemical Activator Bilayer on Gold Electrode. *Anal. Chem.* **2004**, *76* (6), 1611–1617.
(113) Gao, Z.; Yang, Z. Detection of MicroRNAs Using Electrocatalytic Nanoparticle Tags. *Anal. Chem.* **2006**, *78* (5), 1470–1477.
(114) Zhou, Y.; Wang, M.; Meng, X.; Yin, H.; Ai, S. Amplified Electrochemical MicroRNA Biosensor Using a Hemin-G-Quadruplex Complex as the Sensing Element. *RSC Adv.* **2012**, *2* (18), 7140–7145.
(115) Labib, M.; Ghobadloo, S. M.; Khan, N.; Kolpashchikov, D. M.; Berezovski, M. V. Four-Way Junction Formation Promoting Ultrasensitive Electrochemical Detection of MicroRNA. *Anal. Chem.* **2013**, *85* (20), 9422–9427.
(116) Driskell, J. D.; Tripp, R. A. Label-Free SERS Detection of MicroRNA Based on Affinity for an Unmodified Silver Nanorod Array Substrate. *Chem. Commun.* **2010**, *46* (19), 3298–3300.
(117) Wang, H. N.; Crawford, B. M.; Fales, A. M.; Bowie, M. L.; Seewaldt, V. L.; Vo-Dinh, T. Multiplexed Detection of MicroRNA Biomarkers Using SERS-Based Inverse Molecular Sentinel (IMS) Nanoprobes. *J. Phys. Chem. C* **2016**, *120* (37), 21047–21055.
(118) Driskell, J. D.; Seto, A. G.; Jones, L. P.; Jokela, S.; Dluhy, R. A.; Zhao, Y. P.; Tripp, R. A. Rapid MicroRNA (MiRNA) Detection and Classification via Surface-Enhanced Raman Spectroscopy (SERS). *Biosens. Bioelectron.* **2008**, *24* (4), 917–922.
(119) Fang, S.; Lee, H. J.; Wark, A. W.; Corn, R. M. Attomole Microarray Detection of MicroRNAs by Nanoparticle- Amplified SPR Imaging Measurements of Surface Polyadenylation Reactions. *J Am Chem Soc.* **2006**, *128* (43), 14044–14046.
(120) Ho, H. P.; Loo, F. C.; Wu, S. Y.; Gu, D.; Yong, K.-T.; Kong, S. K. MicroRNA Biosensing with Two-Dimensional Surface Plasmon Resonance Imaging. In *Biosensors and Biodetection: Methods and Protocols Volume 1: Optical-Based Detectors*; 2017; Vol. 1, pp 117–127.
(121) Xue, T.; Liang, W.; Li, Y.; Sun, Y.; Xiang, Y.; Zhang, Y.; Dai, Z.; Duo, Y.; Wu, L.; Qi, K.; et al. Ultrasensitive Detection of MiRNA with an Antimonene-Based Surface Plasmon Resonance Sensor. *Nat. Commun.* **2019**, *10* (28), 1–9.
(122) Bak, M.; Silahtaroglu, A.; Møller, M.; Christensen, M.; Rath, M. F.; Skryabin, B.; Tommerup, N.; Kauppinen, S. MicroRNA Expression in the Adult Mouse Central Nervous System. *RNA* **2008**, *14* (3), 432–444.
(123) Moltzahn, F.; Olshen, A.; Baeher, L.; Peek, A.; Fong, L.; Stöppler, H.; Simko, J.; Hilton, J. F.; Carrol, P.; Blelloch, R. Microfluidic Based Multiplex QRT-PCR Identifies Diagnostic and Prognostic MicroRNA Signatures in Sera of Prostate Cancer Patients. *Cancer Res.* **2011**, *4* (164), 550–560.
(124) Chen, C.; Ridzon, D. A.; Broomer, A. J.; Zhou, Z.; Lee, D. H.; Nguyen, J. T.; Barbisin, M.; Xu, N. L.; Mahuvakar, V. R.; Andersen, M. R.; et al. Real-Time Quantification of MicroRNAs by Stem-Loop RT-PCR. *Nucleic Acids Res.* **2005**, *33* (20), e179-188.
(125) Raymond, C. K.; Roberts, B. S.; Garrett-engele, P.; Lim, L. E. E. P.; Johnson, J. M. Simple, Quantitative Primer-Extension PCR Assay for Direct Monitoring of MicroRNAs and Short-Interfering RNAs. *RNA* **2005**, *11*, 1737–1744.
(126) Lu, Z.; Duan, D.; Cao, R.; Zhang, L.; Zheng, K.; Li, J. A Reverse Transcription-Free Real-Time PCR Assay for Rapid MiRNAs Quantification Based on Effects of Base Stacking. *Chem. Commun.* **2011**, *47* (26), 7452–7454.
(127) Zhao, G.; Jiang, T.; Liu, Y.; Huai, G.; Lan, C.; Li, G.; Jia, G.; Wang, K.; Yang, M. Droplet Digital PCR-Based Circulating MicroRNA Detection Serve as a Promising Diagnostic Method for Gastric Cancer. *BMC Cancer* **2018**, *18* (1), 1–10.
(128) Almassian, D. R.; Cockrell, L. M.; Nelson, W. M. Portable Nucleic Acid Thermocyclers. *Chem. Soc.*

Rev. **2013**, *42* (22), 8769–8798.
(129) Ahrberg, C. D.; Ilic, B. R.; Manz, A.; Neužil, P. Handheld Real-Time PCR Device. *Lab Chip* **2016**, *16* (3), 586–592.
(130) Priye, A.; Ugaz, V. M. Smartphone-Enabled Detection Strategies for Portable PCR–Based Diagnostics. In *Biosensors and Biodetection: Methods and Protocols Volume 1: Optical-Based Detectors*; 2017; pp 251–266.
(131) Mendoza-Gallegos, R. A.; Rios, A.; Garcia-Cordero, J. L. An Affordable and Portable Thermocycler for Real-Time PCR Made of 3D-Printed Parts and Off-the-Shelf Electronics. *Anal. Chem.* **2018**, *90* (9), 5563–5568.
(132) Neely, L. A.; Patel, S.; Garver, J.; Gallo, M.; Hackett, M.; McLaughlin, S.; Nadel, M.; Harris, J.; Gullans, S.; Rooke, J. A Single-Molecule Method for the Quantitation of MicroRNA Gene Expression. *Nat. Methods* **2006**, *3* (1), 41–46.
(133) Urbanek, M. O.; Nawrocka, A. U.; Krzyzosiak, W. J. Small RNA Detection by in Situ Hybridization Methods. *Int. J. Mol. Sci.* **2015**, *16* (6), 13259–13286.
(134) Song, R.; Ro, S.; Yan, W. In Situ Hybridization Detection of MicroRNAs. In *RNA Therapeutics, Methods in Molecular Biology*; 2010; pp 285–292.
(135) Lu, C.; Meyers, B. C.; Green, P. J. Construction of Small RNA CDNA Libraries for Deep Sequencing. *Methods* **2007**, *43* (2), 110–117.
(136) Hafner, M.; Landgraf, P.; Ludwig, J.; Rice, A.; Ojo, T.; Lin, C.; Tuschl, T. Identification of MicroRNAs and Other Small Regulatory RNAs Using CDNA Library Sequencing. *Methods* **2008**, *44* (1), 3–12.
(137) Leshkowitz, D.; Horn-Saban, S.; Parmet, Y.; Feldmesser, E. Differences in MicroRNA Detection Levels Are Technology and Sequence Dependent. *RNA* **2013**, *19* (4), 527–538.
(138) Ferrier, D. C.; Shaver, M. P.; Hands, P. J. W. Micro- and Nano-Structure Based Oligonucleotide Sensors. *Biosens. Bioelectron.* **2015**, *68*, 798–810.
(139) Arlett, J. L.; Myers, E. B.; Roukes, M. L. Comparative Advantages of Mechanical Biosensors. *Nat. Nanotechnol.* **2011**, *6* (4), 203–215.
(140) Mo, Z.; Wang, H.; Liang, Y.; Liu, F.; Xue, Y. Highly Reproducible Hybridization Assay of Zeptomole DNA Based on Adsorption of Nanoparticle-Bioconjugate. *Analyst* **2005**, *130* (12), 1589–1594.
(141) Xu, Q.; Chang, K.; Lu, W.; Chen, W.; Ding, Y.; Jia, S.; Zhang, K.; Li, F.; Shi, J.; Cao, L.; et al. Detection of Single-Nucleotide Polymorphisms with Novel Leaky Surface Acoustic Wave Biosensors, DNA Ligation and Enzymatic Signal Amplification. *Biosens. Bioelectron.* **2012**, *33* (1), 274–278.
(142) Johnson, B. N.; Mutharasan, R. Sample Preparation-Free, Real-Time Detection of MicroRNA in Human Serum Using Piezoelectric Cantilever Biosensors at Attomole Level. *Anal. Chem.* **2012**, *84* (23), 10426–10436.
(143) Chen, C. P.; Ganguly, A.; Lu, C. Y.; Chen, T. Y.; Kuo, C. C.; Chen, R. S.; Tu, W. H.; Fischer, W. B.; Chen, K. H.; Chen, L. C. Ultrasensitive in Situ Label-Free DNA Detection Using a GaN Nanowire-Based Extended-Gate Field-Effect-Transistor Sensor. *Anal. Chem.* **2011**, *83* (6), 1938–1943.
(144) Wanunu, M.; Dadosh, T.; Ray, V.; Jin, J.; McReynolds, L.; Drndić, M. Rapid Electronic Detection of Probe-Specific MicroRNAs Using Thin Nanopore Sensors. *Nat. Nanotechnol.* **2010**, *5* (11), 807–814.
(145) Fogel, R.; Limson, J.; Seshia, A. A. Acoustic Biosensors. *Essays Biochem.* **2016**, *60* (1), 101–110.
(146) Le Guillou-Buffello, D.; Hélary, G.; Gindre, M.; Pavon-Djavid, G.; Laugier, P.; Migonney, V. Monitoring Cell Adhesion Processes on Bioactive Polymers with the Quartz Crystal Resonator Technique. *Biomaterials* **2005**, *26* (19), 4197–4205.
(147) Zheng, F.; Wang, P.; Du, Q.; Chen, Y.; Liu, N. Simultaneous and Ultrasensitive Detection of Foodborne Bacteria by Gold Nanoparticles-Amplified Microcantilever Array Biosensor. *Front. Chem.* **2019**, *7* (April), 1–12.
(148) Rijal, K.; Mutharasan, R. PEMC-Based Method of Measuring DNA Hybridization at Femtomolar Concentration Directly in Human Serum and in the Presence of Copious Noncomplementary Strands. *Anal. Chem.* **2007**, *79* (19), 7392–7400.
(149) Gao, Z.; Agarwal, A.; Trigg, A.; Singh, N. Silicon Nanowire Arrays for Label-Free Detection of DNA. *Anal. Chem.* **2007**, *79* (9), 3291–3297.
(150) Zhang, G. J.; Chua, J. H.; Chee, R. E.; Agarwal, A.; Wong, S. M.; Buddharaju, K. D.; Balasubramanian, N. Highly Sensitive Measurements of PNA-DNA Hybridization Using Oxide-Etched Silicon Nanowire Biosensors. *Biosens. Bioelectron.* **2008**, *23* (11), 1701–1707.
(151) Wanunu, M. Nanopores: A Journey towards DNA Sequencing. *Phys. Life Rev.* **2012**, *9* (2), 125–158.
(152) Islam, M. R.; Serpe, M. J. Polymer-Based Devices for the Label-Free Detection of DNA in Solution: Low DNA Concentrations Yield Large Signals. *Anal. Bioanal. Chem.* **2014**, *406* (19), 4777–4783.
(153) Watson, J.; Crick, F. Molecular Structure of Nucleic Acids. *Nature* **1953**, *171* (4356), 737–738.
(154) Rapoport, S. Rosalind Franklin: Unsung Hero of the DNA Revolution. *Hist. Teacher* **2002**, *36* (1), 116–127.

(155) Hoogsteen, K. The Crystal and Molecular Structure of a Hydrogen-Bonded Complex Between 1-Methylthymine and 9-Methyladenine. *Acta Crystallogr.* **1963**, *16* (9), 907–916.
(156) CRICK, F. H. Codon-Anticodon Pairing: The Wobble Hypothesis. *J. Mol. Biol.* **1966**, *19*, 548–555.
(157) D. E. Huizenga; J. W. Szostak. A DNA Aptamer That Binds Adenosine and ATP. *Biochemistry* **1995**, *34*, 656–665.
(158) Lin, C. H.; Patel, D. J. Structural Basis of DNA Folding and Recognition in an AMP-DNA Aptamer Complex: Distinct Architectures but Common Recognition Motifs for DNA and RNA Aptamers Complexed to AMP. *Chem. Biol.* **1997**, *4* (11), 817–832.
(159) Liu, J.; Cao, Z.; Lu, Y. *Functional Nucleic Acid Sensors*; 2009; Vol. 109.
(160) Sassanfar, M.; Szostak, J. An RNA Motif That Binds ATP. *Nature* **1993**, *364*, 550–553.
(161) Liu, J.; Mazumdar, D.; Lu, Y. A Simple and Sensitive "Dipstick" Test in Serum Based on Lateral Flow Separation of Aptamer-Linked Nanostructures. *Angew. Chemie - Int. Ed.* **2006**, *45* (47), 7955–7959.
(162) Yin, B.-C.; Ye, B.-C.; Wang, H.; Zhu, Z.; Tan, W. Colorimetric Logic Gates Based on Aptamer-Crosslinked Hydrogels. *Chem. Commun.* **2012**, *48* (9), 1248–1250.
(163) Zhu, Z.; Wu, C.; Liu, H.; Zou, Y.; Zhang, X.; Kang, H.; Yang, C. J.; Tan, W. An Aptamer Cross-Linked Hydrogel as a Colorimetric Platform for Visual Detection. *Angew. Chemie* **2010**, *122*, 1070–1074.
(164) Rahimi, F.; Bitan, G. Selection of Aptamers for Amyloid β-Protein, the Causative Agent of Alzheimer's Disease. *J. Vis. Exp.* **2010**, *39*, 1–7.
(165) Tsukakoshi, K.; Abe, K.; Sode, K.; Ikebukuro, K. Selection of DNA Aptamers That Recognize α-Synuclein Oligomers Using a Competitive Screening Method. *Anal. Chem.* **2012**, *84* (13), 5542–5547.
(166) Helwa, Y.; Dave, N.; Froidevaux, R.; Samadi, A.; Liu, J. Aptamer-Functionalized Hydrogel Microparticles for Fast Visual Detection of Mercury(II) and Adenosine. *ACS Appl. Mater. Interfaces* **2012**, *4* (4), 2228–2233.
(167) Nutiu, R.; Li, Y. Structure-Switching Signaling Aptamers: Transducing Molecular Recognition into Fluorescence Signaling. *Chem. - A Eur. J.* **2004**, *10* (8), 1868–1876.
(168) Kibbe, W. A. OligoCalc: An Online Oligonucleotide Properties Calculator. *Nucleic Acids Res.* **2007**, *35*, 43–46.
(169) Bishop, J.; Wilson, C.; Chagovetz, A. M.; Blair, S. Competitive Displacement of DNA during Surface Hybridization. *Biophys. J.* **2007**, *92* (1), 10–12.
(170) Alivisatos, A. P.; Johnsson, K. P.; Peng, X.; Wilson, T. E.; Loweth, C. J.; Bruchez Jr, M. P.; Schultz, P. G. Organization of "nanocrystal Molecules" Using DNA. *Nature* **1996**, *382*, 609–611.
(171) Marras, S. A. E.; Tyagi, S.; Kramer, F. R. Real-Time Assays with Molecular Beacons and Other Fluorescent Nucleic Acid Hybridization Probes. *Clin. Chim. Acta* **2006**, *363* (1–2), 48–60.
(172) Gawel, K.; Barriet, D.; Sletmoen, M.; Stokke, B. T. Responsive Hydrogels for Label-Free Signal Transduction within Biosensors. *Sensors* **2010**, *10*, 4381–4409.
(173) Xiong, X.; Wu, C.; Zhou, C.; Zhu, G.; Chen, Z.; Tan, W. Responsive DNA-Based Hydrogels and Their Applications. *Macromol. Rapid Commun.* **2013**, *34* (16), 1271–1283.
(174) Peng, L.; Wu, C. S.; You, M.; Han, D.; Chen, Y.; Fu, T.; Ye, M.; Tan, W. Engineering and Applications of DNA-Grafted Polymer Materials. *Chem. Sci.* **2013**, *4* (5), 1928–1938.
(175) Murakami, Y.; Maeda, M. DNA-Responsive Hydrogels That Can Shrink or Swell. *Biomacromolecules* **2005**, *6* (6), 2927–2929.
(176) Gao, M.; Gawel, K.; Stokke, B. T. Toehold of DsDNA Exchange Affects the Hydrogel Swelling Kinetics of a Polymer–DsDNA Hybrid Hydrogel. *Soft Matter* **2011**, *7* (5), 1741.
(177) Lin, D. C.; Yurke, B.; Langrana, N. A. Mechanical Properties of a Reversible, DNA-Crosslinked Polyacrylamide Hydrogel. *J. Biomech. Eng.* **2004**, *126* (1), 104–110.
(178) Liu, J.; Lu, Y. Fast Colorimetric Sensing of Adenosine and Cocaine Based on a General Sensor Design Involving Aptamers and Nanoparticles. *Angew. Chemie - Int. Ed.* **2005**, *45* (1), 90–94.
(179) Labib, M.; Ghobadloo, S. M.; Khan, N.; Kolpashchikov, D. M.; Berezovski, M. V. Four-Way Junction Formation Promoting Ultrasensitive Electrochemical Detection of MicroRNA. *Anal. Chem.* **2013**, *85* (20), 9422–9427.
(180) Qi, H.; Ghodousi, M.; Du, Y.; Grun, C.; Bae, H.; Yin, P.; Khademhosseini, A. DNA Directed Self-Assembly of Shape-Controlled Hydrogels. *Nat. Commun.* **2013**, *4*, 2275–2294.
(181) Xia, N.; Liu, K.; Zhou, Y.; Li, Y.; Yi, X. Sensitive Detection of MicroRNAs Based on the Conversion of Colorimetric Assay into Electrochemical Analysis with Duplex-Specific Nuclease-Assisted Signal Amplification. *Int. J. Nanomedicine* **2017**, *12*, 5013–5022.
(182) Ren, Y.; Deng, H.; Shen, W.; Gao, Z. A Highly Sensitive and Selective Electrochemical Biosensor for Direct Detection of MicroRNAs in Serum. *Anal. Chem.* **2013**, *85* (9), 4784–4789.
(183) Dave, N.; Liu, J. Fast Molecular Beacon Hybridization in Organic Solvents with Improved Target Specificit. *J. Phys. Chem. B* **2010**, *114* (47), 15694–15699.
(184) Owczarzy, R.; You, Y.; Moreira, B. G.; Manthey, J. A.; Huang, L.; Behlke, M. A.; Walder, J. A. Effects

of Sodium Ions on DNA Duplex Oligomers: Improved Predictions of Melting Temperatures. *Biochemistry* **2004**, *43* (12), 3537–3554.
(185) Herskovits, T. T. Nonaqueous Solutions of DNA: Factors Determining the Stability of the Helical Configuration in Solution. *Arch. Biochem. Biophys.* **1962**, *97* (3), 474–484.
(186) Sorokin, V. A.; Gladchenko, G. O.; Valeev, V. A.; SySa, I. V; Petrova, L. G.; Blagoi, Y. P. Effect of Salt and Organic Solvents on DNA Thermal Stability and Structure. *J. Mol. Struct.* **1997**, *408/409*, 237–240.
(187) Hammouda, B.; Worcester, D. The Denaturation Transition of DNA in Mixed Solvents. *Biophys. J.* **2006**, *91* (6), 2237–2242.
(188) Shah, P.; Cho, S. K.; Thulstrup, P. W.; Bhang, Y. J.; Ahn, J. C.; Choi, S. W.; Rørvig-Lund, A.; Yang, S. W. Effect of Salts, Solvents and Buffer on MiRNA Detection Using DNA Silver Nanocluster (DNA/AgNCs) Probes. *Nanotechnology* **2014**, *25* (4), 1–7.
(189) Hershey, A. D.; Goldberg, E.; Burgi, E.; Ingraham, L. Local Denaturation of DNA by Shearing Forces and by Heat. *J. Mol. Biol.* **1963**, *6* (3), 230–243.
(190) Herskovits, T. T.; Singer, S. J.; Geiduscheck, E. P. Nonaqueous Solutions of DNA. Denaturation in Methanol and Ethanol. *Arch. Biochem. Biophys.* **1961**, *94* (18), 99–114.
(191) Kay, E. Double-Stranded DNA in Methanol-Ethanol-Buffer Solvent System. **1976**, *15* (24), 5241–5246.
(192) Nakano, S.; Sugimoto, N. The Structural Stability and Catalytic Activity of DNA and RNA Oligonucleotides in the Presence of Organic Solvents. *Biophys. Rev.* **2016**, *8* (1), 11–23.
(193) Geiduschek, E. P.; Herskovits, T. T. Nonaqueous Solutions of DNA. Reversible and Irreversible Denaturation in Methanol. *Arch. Biochem. Biophys.* **1961**, *95*, 114–129.
(194) Summerton, J. E. Morpholinos and PNAs Compared. *Lett. Pept. Sci.* **2003**, *10* (3–4), 215–236.
(195) Obernosterer, G.; Martinez, J.; Alenius, M. Locked Nucleic Acid-Based in Situ Detection of MicroRNAs in Mouse Tissue Sections. *Nat. Protoc.* **2007**, *2* (6), 1508–1514.
(196) Karkare, S.; Bhatnagar, D. Promising Nucleic Acid Analogs and Mimics: Characteristic Features and Applications of PNA, LNA, and Morpholino. *Appl. Microbiol. Biotechnol.* **2006**, *71* (5), 575–586.
(197) Natsume, T.; Ishikawa, Y.; Dedachi, K.; Tsukamoto, T.; Kurita, N. Hybridization Energies of Double Strands Composed of DNA, RNA, PNA and LNA. *Chem Phys Lett.* **2008**, *148* (4), 825–832.
(198) Petersen, M.; Wengel, J. LNA: A Versatile Tool for Therapeutics and Genomics. *Trends Biotechnol.* **2003**, *21* (2), 74–81.
(199) Summerton, J. Morpholino, SiRNA, and S-DNA Compared: Impact of Structure and Mechanism of Action on Off-Target Effects and Sequence Specificity. *Curr. Top. Med. Chem.* **2007**, *7* (7), 651–660.
(200) Summerton, J.; Weller, D. Morpholino Antisense Oligomers: Design, Preparation, and Properties. *Antisense Nucleic Acid Drug Dev.* **1997**, *7*, 187–195.
(201) Janson, C. G.; During, M. J. *Peptide Nucleic Acids, Morpholinos and Related Antisense Biomolecules*; 2006.
(202) HUDZIAK, R. M.; BAROFSKY, E.; BAROFSKY, D. F.; WELLER, D. L.; HUANG, S.-B.; WELLER, D. D. Resistance of Morpholino Phosphorodiamidate Oligomers to Enzymatic Degradation. *Antisense Nucleic Acid Drug Dev.* **1996**, *6* (4), 267–272.
(203) Zu, Y.; Ting, A. L.; Yi, G.; Gao, Z. Sequence-Selective Recognition of Nucleic Acids under Extremely Low Salt Conditions Using Nanoparticle Probes. *Anal. Chem.* **2011**, *83* (11), 4090–4094.
(204) Ouyang, X.; Shestopalov, I. A.; Sinha, S.; Zheng, G.; Pitt, C. L. W.; Li, W. H.; Olson, A. J.; Chen, J. K. Versatile Synthesis and Rational Design of Caged Morpholinos. *J. Am. Chem. Soc.* **2009**, *131* (37), 13255–13269.
(205) Lagendijk, A. K.; Moulton, J. D.; Bakkers, J. Revealing Details: Whole Mount MicroRNA in Situ Hybridization Protocol for Zebrafish Embryos and Adult Tissues. *Biol. Open* **2012**, *1* (6), 566–569.
(206) Deiters, A.; Garner, R. A.; Lusic, H.; Govan, J. M.; Dush, M.; Nascone-Yoder, N. M.; Yoder, J. A. Photocaged Morpholino Oligomers for the Light-Regulation of Gene Function in Zebrafish and Xenopus Embryos. *J. Am. Chem. SOC* **2010**, *132* (44), 15644–15650.
(207) Jarreau, C. M. Caged Morpholino Oligonucleotide for Control of Gene Expression in Zebrafish. *LSU Master's Theses* **2010**, *3969*.
(208) Abu-Daya, A.; Steer, W. M.; Trollope, A. F.; Friedeberg, C. E.; Patient, R. K.; Thorne, A. W.; Guille, M. J. Zygotic Nucleosome Assembly Protein–like 1 Has a Specific, Non–Cell Autonomous Role in Hematopoiesis. *Blood* **2005**, *106* (2), 514–520.
(209) GILES, R. V.; SPILLER, D. G.; CLARK, R. E.; TIDD, D. M. Antisense Morpholino Oligonucleotide Analog Induces Missplicing of C-Myc MRNA. *Antisense Nucleic Acid Drug Dev.* **1999**, *9* (2), 213–220.
(210) Kloosterman, W. P.; Lagendijk, A. K.; Ketting, R. F.; Moulton, J. D.; Plasterk, R. H. A. Targeted Inhibition of MiRNA Maturation with Morpholinos Reveals a Role for MiR-375 in Pancreatic Islet Development. *PLoS Biol.* **2007**, *5* (8), 1738–1749.

(211) Levicky, R.; Koniges, U.; Tercero, N. Diagnostic Applications of Morpholinos and Label-Free Electrochemical Detection of Nucleic Acids. In *Morpholino Oligomers: Methods and Protocols*; 2017; pp 181–190.
(212) Qiao, W.; Kalachikov, S.; Liu, Y.; Levicky, R. Charge-Neutral Morpholino Microarrays for Nucleic Acid Analysis. *Anal. Biochem.* **2013**, *434* (2), 207–214.
(213) Zhao, Y.; Cao, L.; Ouyang, J.; Wang, M.; Wang, K.; Xia, X. H. Reversible Plasmonic Probe Sensitive for PH in Micro/Nanospaces Based on I-Motif-Modulated Morpholino-Gold Nanoparticle Assembly. *Anal. Chem.* **2013**, *85* (2), 1053–1057.
(214) Chen, J.; Wu, J.; Hong, Y. The Morpholino Molecular Beacon for Specific RNA Visualization in Vivo. *Chem. Commun.* **2016**, *52* (15), 3191–3194.
(215) Hu, W.; Hu, Q.; Li, L.; Kong, J.; Zhang, X. Detection of Sequence-Specific DNA with a Morpholino-Functionalized Silicon Chip. *Anal. Methods* **2015**, *7* (6), 2406–2412.
(216) Bagi, A.; Soelberg, S. D.; Furlong, C. E.; Baussant, T. Implementing Morpholino-Based Nucleic Acid Sensing on a Portable Surface Plasmon Resonance Instrument for Future Application in Environmental Monitoring. *Sensors* **2018**, *18*, 1–17.
(217) Zu, Y.; Tan, M.-H.; Chowbay, B.; Lee, S. C.; Yap, H.; Lee, M. T. M.; Lu, L.-S.; Chang, C.-P.; Y, J. Y. Nanoprobe-Based Genetic Testing. *Nano Today* **2014**, *9*, 166–171.
(218) Tercero, N.; Wang, K.; Gong, P.; Levicky, R. Morpholino Monolayers: Preparation and Label-Free DNA Analysis by Surface Hybridization. *J. Am. Chem. Soc.* **2009**, *131* (13), 4953–4961.
(219) Tercero, N.; Wang, K.; Levicky, R. Capacitive Monitoring of Morpholino-DNA Surface Hybridization: Experimental and Theoretical Analysis. *Langmuir* **2010**, *26* (17), 14351–14358.
(220) He, Y.; Zhang, J.; Ruffin, S.; Ji, L.; Wang, K.; Levicky, R.; Xia, X. An Electrochemical Study of the Surface Hybridization Process of Morpholino-DNA: Thermodynamics and Kinetics. *Electroanalysis* **2016**, *28* (7), 1647–1653.
(221) Martins, D.; Levicky, R.; Song, Y. A. Enhancing the Speed of Morpholino-DNA Biosensor by Electrokinetic Concentration of DNA in a Microfluidic Chip. *Biosens. Bioelectron.* **2015**, *72*, 87–94.
(222) Wang, X.; Smirnov, S. Label-Free DNA Sensor Based on Surface Charge Modulated Ionic Conductance. *ACS Nano* **2009**, *3* (March), 1004–1010.
(223) Zhang, G. J.; Luo, Z. H. H.; Huang, M. J.; Tay, G. K. I.; Lim, E. J. A. Morpholino-Functionalized Silicon Nanowire Biosensor for Sequence-Specific Label-Free Detection of DNA. *Biosens. Bioelectron.* **2010**, *25* (11), 2447–2453.
(224) Burki, U.; Keane, J.; Blain, A.; O'Donovan, L.; Gait, M. J.; Laval, S. H.; Straub, V. Development and Application of an Ultrasensitive Hybridization-Based ELISA Method for the Determination of Peptide-Conjugated Phosphorodiamidate Morpholino Oligonucleotides. *Nucleic Acid Ther.* **2015**, *25* (5), 275–284.
(225) Cao, L.; Zhao, Y.; Ji, L. N.; Zhang, J.; Wang, K.; Xia, X. H. The Enhanced Enzymolysis Resistance of Surface-Immobilized DNA Caused by Hybridizing with Morpholino. *Electroanalysis* **2013**, *25* (4), 1074–1079.
(226) Shaver, M. P.; Hands, P. J. W.; Ferrier, D. Biosensor WO 2017/006122 A1, 2017.
(227) Ferrier, D. C.; Shaver, M. P.; Hands, P. J. W. Conductive Composites for Oligonucleotide Detection. *Sens. Bio-Sensing Res.* **2018**, *17*, 1–6.
(228) Mateescu, A.; Wang, Y.; Dostalek, J.; Jonas, U. Thin Hydrogel Films for Optical Biosensor Applications. *Membranes (Basel)*. **2012**, *2* (4), 40–69.
(229) Mahkam, M.; Doostie, L. The Relation Between Swelling Properties and Cross-Linking of Hydrogels Designed for Colon- Specific Drug Delivery. *Drug Deliv.* **2005**, *12*, 343–347.
(230) Denisin, A. K.; Pruitt, B. L. Tuning the Range of Polyacrylamide Gel Stiffness for Mechanobiology Applications. *ACS Appl. Mater. Interfaces* **2016**, *8* (34), 21893–21902.
(231) Vanchugova, L. V.; Valuev, L. I.; Valuev, I. L.; Talyzenkov, Y. A. Control of the Structure of Polyacrylamide Hydrogel. *Polym. Sci. Ser. B* **2013**, *55* (1–2), 77–80.
(232) Holback, H.; Yeo, Y.; Park, K. *Hydrogel Swelling Behavior and Its Biomedical Applications*; Woodhead Publishing Limited, 2011.
(233) Stockmayer, W. H. Theory of Molecular Size Distribution and Gel Formation in Branched Polymers: II. General Cross Linking. *J. Chem. Phys.* **1944**, *12* (4), 125–131.
(234) Flory, J. Molecular Size Distribution in Three Dimensional Polymers. I. Gelation. *J. Am. Chem. Soc.* **1941**, *63*, 3083–3090.
(235) Brinker, C. J.; Scherer, G. W. Gelation. In *Sol-Gel Science*; 1990; pp 302–355.
(236) Li, J.; Mooney, D. J. Designing Hydrogels for Controlled Drug Delivery. *Nat. Rev. Mater.* **2016**, *1*, 1–17.
(237) Varaprasad, K.; Raghavendra, G. M.; Jayaramudu, T.; Yallapu, M. M.; Sadiku, R. A Mini Review on Hydrogels Classification and Recent Developments in Miscellaneous Applications. *Mater. Sci. Eng. C*

2017, *79*, 958–971.
(238) Tanaka, T.; Fillmore, D. J. Kinetics of Swelling of Gels. *J. Chem. Phys.* **1979**, *70* (3), 1214–1218.
(239) Cohen, Y.; Ramon, O.; Kopelman, I. J.; Mizrahi, S. Characterization of Inhomogeneous Polyacrylamide Hydrogels. *J. Polym. Sci. Part B Polym. Phys.* **1992**, *30* (9), 1055–1067.
(240) Gun'ko, V.; Savina, I.; Mikhalovsky, S. Properties of Water Bound in Hydrogels. *Gels* **2017**, *3* (4), 1–30.
(241) Amsden, B. Solute Diffusion within Hydrogels. Mechanisms and Models. *Macromolecules* **1998**, *31*, 8382–8395.
(242) Banerjee, I.; Mishra, D.; Das, T. al; Maiti, T. K. Wound PH-Responsive Sustained Release of Therapeutics from a Poly (NIPAAm-Co-AAc) Hydrogel. *J. Biomater. Sci.* **2012**, No. December, 37–41.
(243) Ahiabu, A.; Serpe, M. J. Rapidly Responding PH- and Temperature-Responsive Poly(N-Isopropylacrylamide)-Based Microgels and Assemblies. *ACS Omega* **2017**, *2* (5), 1769–1777.
(244) Taylor, M.; Tomlins, P.; Sahota, T. Thermoresponsive Gels. *Gels* **2017**, *3* (1), 1–31.
(245) Zhao, B.; Moore, J. S. Fast PH- and Ionic Strength-Responsive Hydrogels in Microchannels. *Langmuir* **2001**, *17* (16), 4758–4763.
(246) Ter Schiphorst, J.; Coleman, S.; Stumpel, J. E.; Azouz, A. Ben; Diamond, D.; Schenning, A. P. H. J. Molecular Design of Light-Responsive Hydrogels, for in Situ Generation of Fast and Reversible Valves for Microfluidic Applications. *Chem. Mater.* **2015**, *27* (17), 5925–5931.
(247) Li, H. Kinetics of Smart Hydrogels Responding to Electric Field: A Transient Deformation Analysis. *Int. J. Solids Struct.* **2009**, *46* (6), 1326–1333.
(248) Namdeo, M.; Bajpai, S. K.; Kakkar, S. Preparation of a Magnetic-Field-Sensitive Hydrogel and Preliminary Study of Its Drug Release Behavior. *J. Biomater. Sci. Polym. Ed.* **2009**, *20* (12), 1747–1761.
(249) Ahn, S. K.; Kasi, R. M.; Kim, S. C.; Sharma, N.; Zhou, Y. Stimuli-Responsive Polymer Gels. *Soft Matter* **2008**, *4*, 1151–1157.
(250) Ahmed, E. M. Hydrogel: Preparation, Characterization, and Applications: A Review. *J. Adv. Res.* **2015**, *6* (2), 105–121.
(251) Liu, J. Oligonucleotide-Functionalized Hydrogels as Stimuli Responsive Materials and Biosensors. *Soft Matter* **2011**, *7*, 6757–6767.
(252) Islam, M. R.; Serpe, M. J. Penetration of Polyelectrolytes into Charged Poly(N-isopropylacrylamide) Microgel Layers Confined between Two Surfaces. *Macromolecules* **2013**, *46*, 1599–1606.
(253) Islam, M. R.; Serpe, M. J. A Novel Label-Free Colorimetric Assay for DNA Concentration in Solution. *Anal. Chim. Acta* **2014**, *843*, 83–88.
(254) Nagahara, S.; Matsuda, T. Hydrogel Formation via Hybridization of Oligonucleotides Derivatized in Water-Soluble Vinyl Polymers. *Polym. Gels Networks* **1996**, *4* (2), 111–127.
(255) Lin, D.; Yurke, B.; Langrana, N. Mechanical Properties of a Reversible, DNA-Crosslinked Polyacrylamide Hydrogel. *J. Biomech. Eng.* **2004**, *126* (1), 104–110.
(256) Yang, H. H.; Liu, H. P.; Kang, H. Z.; Tan, W. H. Engineering Target-Responsive Hydrogels Based on Aptamer-Target Interactions. *J. Am. Chem. Soc.* **2008**, *130* (20), 6320–6321.
(257) Liedl, T.; Dietz, H.; Yurke, B.; Simmel, F. Controlled Trapping and Release of Quantum Dots in a DNA-Switchable Hydrogel. *Small* **2007**, *3* (10), 1688–1693.
(258) Yang, H.; Liu, H.; Kang, H.; Tan, W. Engineering Target-Responsive Hydrogels Based on Aptamer-Target Interactions. *J. Am. Ceram. Soc* **2008**, *130* (20), 6320–6321.
(259) Tierney, S.; Stokke, B. T. Development of an Oligonucleotide Functionalized Hydrogel Integrated on a High Resolution Interferometric Readout Platform as a Label-Free Macromolecule Sensing Device. *Biomacromolecules* **2009**, *10* (6), 1619–1626.
(260) Gao, M.; Gawel, K.; Stokke, B. Swelling Dynamics of a DNA-Polymer Hybrid Hydrogel Prepared Using Polyethylene Glycol as a Porogen. *Gels* **2015**, *1*, 219–234.
(261) Gawe, K.; Stokke, B. T. Logic Swelling Response of DNA–Polymer Hybrid Hydrogel. *Soft Matter* **2011**, *7*, 4615–4618.
(262) Richter, A.; Bund, A.; Keller, M.; Arndt, K. F. Characterization of a Microgravimetric Sensor Based on PH Sensitive Hydrogels. *Sensors Actuators, B Chem.* **2004**, *99* (2–3), 579–585.
(263) Hu, L.; Serpe, M. J. Color-Tunable Etalons Assembled from Poly (N-Isopropylacrylamide) Based Microgels. *Polymers (Basel).* **2012**, *4* (1), 134–149.
(264) Sorrell, C. D.; Carter, M. C. D.; Serpe, M. J. Color Tunable Poly (N-Isopropylacrylamide)-Co-Acrylic Acid Microgel–Au Hybrid Assemblies. *Adv. Funct. Mater.* **2011**, *21* (3), 425–433.
(265) Tierney, S.; Hjelme, D. R.; Stokke, B. T. Determination of Swelling of Responsive Gels with Nanometer Resolution. Fiber-Optic Based Platform for Hydrogels as Signal Transducers. *Anal. Chem.* **2008**, *80* (13), 5086–5093.

(266) Kim, J.; Singh, N.; Lyon, L. A. Label-Free Biosensing with Hydrogel Microlenses. *Angew. Chemie - Int. Ed.* **2006**, *45* (9), 1446–1449.
(267) Kim, J.; Nayak, S.; Lyon, L. A. Bioresponsive Hydrogel Microlenses. *J. Am. Chem. Soc.* **2005**, *127* (26), 9588–9592.
(268) Asher, S. A.; Holtz, J. H. Polymerized Colloidal Crystal Hydrogel Films as Intelligent Chemical Sensing Materials. *Nature* **1997**, *389* (6653), 829–832.
(269) Toma, M.; Jonas, U.; Mateescu, A.; Knoll, W.; Dostalek, J. Active Control of SPR by Thermoresponsive Hydrogels for Biosensor Applications. *J. Phys. Chem. C* **2013**, *117*, 11705–11712.
(270) Khan, S.; Ranjha, N. M. Effect of Degree of Cross-Linking on Swelling and on Drug Release of Low Viscous Chitosan/Poly(Vinyl Alcohol) Hydrogels. *Polym. Bull.* **2014**, *71* (8), 2133–2158.
(271) Guenther, M.; Gerlach, G.; Wallmersperger, T. Piezoresistive Biochemical Sensors Based on Hydrogels. *Microsyst. Technol.* **2010**, *16* (5), 703–715.
(272) Bashir, R.; Hilt, J. Z.; Elibol, O.; Gupta, A.; Peppas, N. A. Micromechanical Cantilever as an Ultrasensitive PH Microsensor. *Appl. Phys. Lett.* **2002**, *81* (16), 3091–3093.
(273) Karim, A. A.; Young, D. J.; Tan, M. J.; Loh, X. J.; Thoniyot, P. Nanoparticle-Hydrogel Composites: Concept, Design, and Applications of These Promising, Multi-Functional Materials. *Adv. Sci.* **2015**, *2* (1–2), 1400010.
(274) Zhang, W.; Feng, P.; Chen, J.; Sun, Z.; Zhao, B. Electrically Conductive Hydrogels for Flexible Energy Storage Systems. *Prog. Polym. Sci.* **2019**, *88*, 220–240.
(275) Kim, Y. S.; Ha, S. C.; Yang, Y.; Kim, Y. J.; Cho, S. M.; Yang, H.; Kim, Y. T. Portable Electronic Nose System Based on the Carbon Black-Polymer Composite Sensor Array. *Sensors Actuators, B Chem.* **2005**, *108* (1-2 SPEC. ISS.), 285–291.
(276) Ryan, M. a; Shevade, a V; Zhou, H.; Homer, M. L. Polymer–Carbon Black Composite Sensors in an Electronic Nose for Air-Quality Monitoring. *MRS Bull.* **2004**, *29* (10), 714–719.
(277) Lonergan, M. C.; Severin, E. J.; Doleman, B. J.; Beaber, S. A.; Grubbs, R. H.; Lewis, N. S. Array-Based Vapor Sensing Using Chemically Sensitive, Polymer Composite Resistors. *Chem. Mater.* **1996**, *8* (9), 2298–2312.
(278) Zhang, D.; Liu, Q. Biosensors and Bioelectronics on Smartphone for Portable Biochemical Detection. *Biosens. Bioelectron.* **2016**, *75*, 273–284.
(279) Katunin, A. Analysis of Critical Percolation Clusters of Mixtures of Conducting and Dielectric Polymers. *J. Appl. Math. Comput. Mech.* **2016**, *15* (1), 59–69.
(280) Ruschau, G. R.; Yoshikawa, S.; Newnham, R. E. Resistivities of Conductive Composites. *J. Appl. Phys.* **1992**, *72* (3), 953–959.
(281) van der Kooij, H. M.; van de Kerkhof, G. T.; Sprakel, J. A Mechanistic View of Drying Suspension Droplets. *Soft Matter* **2016**, *12* (11), 2858–2867.
(282) McLachlan, D. S. An Equation for the Conductivity of Binary Mixtures with Anisotropic Grain Structures. *J. Phys. C Solid State Phys.* **1987**, *20* (7), 865–877.
(283) Calvert, P. Inkjet Printing for Materials and Devices. *Chem. Mater.* **2001**, *13* (10), 3299–3305.
(284) Scoutaris, N.; Ross, S.; Douroumis, D. Current Trends on Medical and Pharmaceutical Applications of Inkjet Printing Technology. *Pharm. Res.* **2016**, *33* (8), 1799–1816.
(285) Kwon, K. S.; Kim, H. S.; Choi, M. Measurement of Inkjet First-Drop Behavior Using a High-Speed Camera. *Rev. Sci. Instrum.* **2016**, *87* (3), 1–10.
(286) Christanti, Y.; Walker, L. M. Effect of Fluid Relaxation Time of Dilute Polymer Solutions on Jet Breakup Due to a Forced Disturbance. *J. Rheol. (N. Y. N. Y).* **2002**, *46* (3), 733–748.
(287) Dong, H.; Carr, W. W.; Morris, J. F. An Experimental Study of Drop-on-Demand Drop Formation. *Phys. Fluids* **2006**, *18* (7), 1–17.
(288) Choi, I. H.; Kim, J. A Pneumatically Driven Inkjet Printing System for Highly Viscous Microdroplet Formation. *Micro Nano Syst. Lett.* **2016**, *4* (1), 1–7.
(289) Liberski, A.; Zhang, R.; Bradley, M. Inkjet Fabrication of Polymer Microarrays and Grids - Solving the Evaporation Problem. *Chem. Commun.* **2009**, No. 3, 334–336.
(290) Liberski, A. R.; Zhang, R.; Bradley, M. In Situ Nanoliter-Scale Polymer Fabrication for Flexible Cell Patterning. *J. Lab. Autom.* **2009**, *14* (5), 285–293.
(291) Pedrosa, J. M. L.; Bradley, M. A High-Throughput and Design of Experiment Mediated Optimization of Pigment-Based Ink Formulations. *Pigment Resin Technol.* **2008**, *37* (3), 131–139.
(292) Hansen, A.; Zhang, R.; Bradley, M. Fabrication of Arrays of Polymer Gradients Using Inkjet Printing. *Macromol. Rapid Commun.* **2012**, *33* (13), 1114–1118.
(293) Chiweshe, S. M.; Steketee, P. C.; Jayaraman, S.; Paxton, E.; Neophytou, K.; Erasmus, H.; Labuschagne, M.; Cooper, A.; MacLeod, A.; Grey, F. E.; et al. Parasite Specific 7SL-Derived Small RNA Is an Effective Target for Diagnosis of Active Trypanosomiasis Infection. *PLoS Negl. Trop. Dis.* **2019**, *13* (2).

(294) Liu, Q.; Deiters, A. Photochemical Control of Gene Function in Zebrafish Embryoswith Light-Activated Morpholinos. In *Concepts and Case Studies in Chemical Biology*; Waldmann, H., Janning, P., Eds.; Wiley-VCH Verlag GmbH & Co. KGaA, 2014; pp 337–350.
(295) Keithley. Data Sheet: 2000 - 7 1/2-Digit Multimeter. **2010**, 1–3.
(296) Seeman, N. C. DNA in a Material World. *Nature* **2003**, *421* (January), 427–430.
(297) Rehman, F. N.; Audeh, M.; Abrams, E. S.; Hammond, P. W.; Kenney, M.; Boles, T. C. Immobilization of Acrylamide-Modified Oligonucleotides by Co-Polymerization. *Nucleic Acids Res.* **1999**, *27* (2), 649–655.
(298) Baumann, C. G.; Smith, S. B.; Bloomfield, V. A.; Bustamante, C. Ionic Effects on the Elasticity of Single DNA Molecules. *Proc. Natl. Acad. Sci. USA* **1997**, *94*, 6185–6190.
(299) Bustamante, C.; Bryant, Z.; Smith, S. B. Ten Years of Single Molecule DNA Mechanics. *Nature* **2003**, *421*, 423–427.
(300) Chi, Q.; Wang, G.; Jiang, J. The Persistence Length and Length per Base of Single-Stranded DNA Obtained from Fluorescence Correlation Spectroscopy Measurements Using Mean Field Theory. *Phys. A Stat. Mech. its Appl.* **2013**, *392* (5), 1072–1079.
(301) Ellington, A. D.; Szostak, J. W. In Vitro Selection of RNA Molecules That Bind Specific Ligands. *Nature* **1990**, *346* (August), 818–822.
(302) Tuerk, C.; Gold, L. Systematic Evolution of Ligands by Exponential Enrichment: RNA Ligands to Bacteriophage T4 DNA Polymerase. *Science (80-.).* **1990**, *249* (4968), 505–510.
(303) Stoltenburg, R.; Reinemann, C.; Strehlitz, B. SELEX—A (r)Evolutionary Method to Generate High-Affinity Nucleic Acid Ligands. *Biomol. Eng.* **2007**, *24* (4), 381–403.
(304) Berezovski, M. V.; Lechmann, M.; Musheev, M. U.; Mak, T. W.; Krylov, S. N. Aptamer-Facilitated Biomarker Discovery (AptaBiD). *J. Am. Chem. Soc.* **2008**, *130* (28), 9137–9143.
(305) Nielsen, L. J.; Olsen, L. F.; Ozalp, V. C. Aptamers Embedded in Polyacrylamide Nanoparticles: A Tool for in Vivo Metabolite Sensing. *ACS Nano* **2010**, *4* (8), 4361–4370.
(306) Lu, C.-H.; Qi, X.-J.; Li, J.; Yang, H.-H. Aptamer-Based Hydrogels and Their Applications. In *Aptamers Selected by Cell-SELEX for Theranostics*; 2015; pp 163–195.
(307) Rupcich, N.; Nutiu, R.; Li, Y.; Brennan, J. D. Entrapment of Fluorescent Signaling DNA Aptamers in Sol-Gel-Derived Silica. *Anal. Chem.* **2005**, *77* (14), 4300–4307.
(308) Wang, R.; Li, Y. Hydrogel Based QCM Aptasensor for Detection of Avian Influenzavirus. *Biosens. Bioelectron.* **2013**, *42*, 148–155.
(309) Minunni, M.; Tombelli, S.; Gullotto, a.; Luzi, E.; Mascini, M. Development of Biosensors with Aptamers as Bio-Recognition Element: The Case of HIV-1 Tat Protein. *Biosens. Bioelectron.* **2004**, *20* (6), 1149–1156.
(310) Kennedy, P. G. E. Clinical Features, Diagnosis, and Treatment of Human African Trypanosomiasis (Sleeping Sickness). *Lancet Neurol.* **2013**, *12* (2), 186–194.
(311) Mableson, H. E.; Okello, A.; Picozzi, K.; Welburn, S. C. Neglected Zoonotic Diseases-The Long and Winding Road to Advocacy. *PLoS Negl. Trop. Dis.* **2014**, *8* (6), 1–5.
(312) Van Camp, W.; Gao, H.; Prez, F. E. Du; Matyjaszewski, K. Effect of Crosslinker Multiplicity on the Gel Point in ATRP. *J. Polym. Sci. Part A Polym. Chem.* **2010**, *48* (9), 2016–2023.
(313) Howell, W. M.; Jobs, M.; Brookes, A. J. IFRET: An Improved Fluorescence System for DNA-Melting Analysis. *Genome Res.* **2002**, *12* (9), 1401–1407.
(314) Gao, Y.; Wolf, L. K.; Georgiadis, R. M. Secondary Structure Effects on DNA Hybridization Kinetics: A Solution versus Surface Comparison. *Nucleic Acids Res.* **2006**, *34* (11), 3370–3377.
(315) Khasnis, A. A.; Nettleman, M. D. Global Warming and Infectious Disease. *Arch. Med. Res.* **2005**, *36*, 689–696.
(316) Brinker, C. J.; Scherer, G. W. Theory of Deformation and Flow in Gels. In *Sol-Gel Science*; 1990; pp 406–451.
(317) Brinker, C. J.; Scherer, G. W. Aging of Gels. In *Sol-Gel Science*; 1990; pp 356–405.
(318) Brinker, C. J.; Scherer, G. W. Drying. In *Sol-Gel Science*; 1990; pp 452–513.
(319) Lubelli, B.; van Hees, R. P. J.; Groot, C. J. W. P. The Effect of Environmental Conditions on Sodium Chloride Damage: A Step in the Development of an Effective Weathering Test. *Stud. Conserv.* **2006**, *51* (1), 41–56.
(320) Shibayama, M.; Tanaka, T. Volume Phase Transition and Related Phenomena of Polymer Gels. *Responsive Gels Vol. ransitions I Adv. Polym. Sci.* **1979**, *109* (1993), 1–62.
(321) Tsortos, A.; Papadakis, G.; Gizeli, E. The Intrinsic Viscosity of Linear DNA. *Biopolymers* **2011**, *95* (12), 824–832.
(322) Li, Y.; Burke, D. T.; Kopelman, R.; Burns, M. A. Asynchronous Magnetic Bead Rotation (AMBR) Microviscometer for Label-Free DNA Analysis. *Biosensors* **2014**, *4* (1), 76–89.
(323) Odian, G. *Principles of Polymerization Fourth Edition*; 2004.

(324) De Sterck, B.; Vaneerdeweg, R.; Du Prez, F.; Waroquier, M.; Van Speybroeck, V. Solvent Effects on Free Radical Polymerization Reactions: The Influence of Water on the Propagation Rate of Acrylamide and Methacrylamide. *Macromolecules* **2010**, *43* (2), 827–836.
(325) Valdebenito, A.; Encinas, M. V. Effect of Solvent on the Free Radical Polymerization of N,N-Dimethylacrylamide. *Polym. Int.* **2010**, *59* (9), 1246–1251.
(326) Piperazine Di-Acrylamide (PDA). In *Bio-Rad Tech Note*; 2000.
(327) Photoinitiators for UV Curing - Key Products Selection Guide. In *Ciba Specialty Chemicals Inc.*; 2003; pp 1–8.
(328) Photoinitiators for UV Curing - Formulator's Guide for Coatings. *Ciba Spec. Chem. Inc.* **2003**.
(329) AlShaafi, M. M. Factors Affecting Polymerization of Resin-Based Composites: A Literature Review. *Saudi Dent. J.* **2017**, *29* (2), 48–58.
(330) Alvarez, J.; Encinas, M. V.; Lissi, E. A. Solvent Effects on the Rate of Polymerization of 2-Hydroxyethyl Methacrylate Photoinitiated with Aliphatic Azo Compounds. *Macromol. Chem. Phys.* **1999**, *200* (10), 2411–2415.
(331) Yoshida, E. Effect of Azoinitiators on Nitroxide-Mediated Photo-Living Radical Polymerization of Methyl Methacrylate. *Colloid Polym. Sci.* **2010**, *288* (3), 341–345.
(332) Fujita, K.; Ikemi, T.; Nishiyama, N. Effects of Particle Size of Silica Filler on Polymerization Conversion in a Light-Curing Resin Composite. *Dent. Mater.* **2011**, *27* (11), 1079–1085.
(333) Kabiri, K.; Omidian, H.; Hashemi, S. A.; Zohuriaan-Mehr, M. J. Synthesis of Fast-Swelling Superabsorbent Hydrogels: Effect of Crosslinker Type and Concentration on Porosity and Absorption Rate. *Eur. Polym. J.* **2003**, *39* (7), 1341–1348.
(334) Flory, P. J.; Rehner, J. Statistical Mechanics of Cross-Linked Polymer Networks II. Swelling. *J. Chem. Phys.* **1943**, *11*, 521–526.
(335) Baselga, J.; Hernández-Fuentes, I.; Piérola, I. F.; Llorente, M. A. Elastic Properties of Highly Cross-Linked Polyacrylamide Gels. *Macromolecules* **1987**, *20* (12), 3060–3065.
(336) Quijano, E.; Bahal, R.; Ricciardi, A.; Saltzman, W. M.; Glazer, P. M. Therapeutic Peptide Nucleic Acids: Principles, Limitations, and Opportunities. *Yale J. Biol. Med.* **2017**, *90* (4), 583–598.
(337) Lee, E. J.; Lim, H. K.; Cho, Y. S.; Hah, S. S. Peptide Nucleic Acids Are an Additional Class of Aptamers. *RSC Adv.* **2013**, *3* (17), 5828–5831.
(338) Chu, T.-W.; Feng, J.; Yang, J.; Kopeček, J. Hybrid Polymeric Hydrogels via Peptide Nucleic Acid (PNA)/DNA Complexation. *J. Control. Release* **2015**, *220*, 608–616.
(339) Qiao, W.; Chiang, H.-C.; Xie, H.; Levicky, R. Surface vs Solution Hybridization: Effects of Salt, Temperature and Probe Type. *Chem. Commun. (Camb).* **2015**, *51* (97), 17245–17248.
(340) Liu, Y.; Irving, D.; Qiao, W.; Ge, D.; Levicky, R. Kinetic Mechanisms in Morpholino - DNA Surface Hybridization. *J. Am. Chem. Soc.* **2011**, *133* (30), 11588–11596.
(341) Yan, C.; Kramer, P. L.; Yuan, R.; Fayer, M. D. Water Dynamics in Polyacrylamide Hydrogels. *J. Am. Chem. Soc.* **2018**, *140* (30), 9466–9477.
(342) Li, Y.; Tanaka, T. Kinetics of Swelling and Shrinking of Gels. *J. Chem. Phys.* **1990**, *92* (2), 1365–1371.
(343) Schott, H. Kinetics of Swelling of Polymers and Their Gels. *J. Pharm. Sci.* **1992**, *81* (5), 467–470.
(344) Biala, K.; Sedova, A.; Flechsig, G.-U. Sequence and Temperature Influence on Kinetics of DNA Strand Displacement at Gold Electrode Surfaces. *ACS Appl. Mater. Interfaces* **2015**, *7* (36), 19948–19959.
(345) Hawkins, T. DNA Purification and Isolation Using Magnetic Particles. U.S. Patent 5,705,628, 1998.
(346) Rogers, W. B.; Crocker, J. C. Direct Measurements of DNA-Mediated Colloidal Interactions and Their Quantitative Modeling. *Proc. Natl. Acad. Sci.* **2011**, *108* (38), 15687–15692.
(347) Biancaniello, P. L.; Kim, A. J.; Crocker, J. C. Long-Time Stretched Exponential Kinetics in Single DNA Duplex Dissociation. *Biophys. J.* **2008**, *94* (3), 891–896.
(348) MedCalc. *Digimizer*.
(349) Tan, C. P.; Craighead, H. G. Surface Engineering and Patterning Using Parylene for Biological Applications. *Materials (Basel).* **2010**, *3* (3), 1803–1832.
(350) Ma, H.; Wallbank, R. W. R.; Chaji, R.; Li, J.; Suzuki, Y.; Jiggins, C.; Nathan, A. An Impedance-Based Integrated Biosensor for Suspended DNA Characterization. *Sci. Rep.* **2013**, *3*, 1–7.
(351) Lawrence, M.; Jiang, Y. Porosity, Pore Size Distribution, Micro-Structure. In *Bio-aggregates Based Building Materials*; 2017; Vol. 23, pp 39–71.
(352) An, H.; Liu, Q.; Ji, Q.; Jin, B. DNA Binding and Aggregation by Carbon Nanoparticles. *Biochem. Biophys. Res. Commun.* **2010**, *393* (4), 571–576.
(353) Pramanik, D.; Maiti, P. K. DNA-Assisted Dispersion of Carbon Nanotubes and Comparison with Other Dispersing Agents. *ACS Appl. Mater. Interfaces* **2017**, *9* (40), 35287–35296.
(354) Guo, C.; Liu, Q.; Ji, Q.; An, H.; Zhang, Z.; Wang, Y. Carbon Nanopowder Binds with DNA and May

Induce DNA Aggregation. In *2010 4th International Conference on Bioinformatics and Biomedical Engineering, iCBBE 2010*; 2010; pp 3–5.
(355) Mu, Q.; Jiang, G.; Chen, L.; Zhou, H.; Fourches, D.; Tropsha, A.; Yan, B. Chemical Basis of Interactions Between Engineered Nanoparticles and Biological Systems. *Chem. Rev.* **2014**, *114* (15), 7740–7781.
(356) Egerton, R. F.; Li, P.; Malac, M. Radiation Damage in the TEM and SEM. *Micron* **2004**, *35* (6), 399–409.
(357) Ivanov, V. V; Decker, C. Kinetic Study of Photoinitiated Frontal Polymerization. *Polym. Int.* **2001**, *50* (1), 113–118.
(358) Islam, M. F.; Rojas, E.; Bergey, D. M.; Johnson, A. T.; Yodh, A. G. High Weight Fraction Surfactant Solubilization of Single-Wall Carbon Nanotubes in Water. *Nano Lett.* **2003**, *3* (2), 269–273.
(359) Kim, J. W.; Lillehei, P. T.; Park, C. Assembly of Modified Ferritin Proteins on Carbon Nanotubes and Its Electrocatalytic Activity for Oxygen Reduction. *J. Mater. Chem.* **2012**, *22* (17), 8408–8412.
(360) Bansal, L.; Sanyal, A.; Kabi, P.; Pathak, B.; Basu, S. Engineering Interfacial Processes at Mini-Micro-Nano Scales Using Sessile Droplet Architecture. *Langmuir* **2018**, *34* (29), 8423–8442.
(361) Mclachlan, D. S. Analytical Functions for the Dc and Ac Conductivity of Conductor-Insulator Composites. *J. Electroceramics* **2000**, *5* (2), 93–110.
(362) Moosavi, A.; Sarkomaa, P. The Effective Conductivity of Three-Phase Composite Materials with Circular Cylindrical Inclusions. *J. Phys. D. Appl. Phys.* **2003**, *36*, 1644–1650.
(363) Wu, F.; Whites, K. W. Computation of Static Effective Permittivity for a Multiphase Lattice of Cylinders. *Electromagnetics* **2002**, *21* (2), 97–114.
(364) Shekel, G.; Barad, C.; Hayun, H.; Sadia, Y.; Gelbstein, Y. Applying the General Effective Media (GEM) Approach for Analyzing the Thermal Conductivity of ZrO2-8YSZ Composites. *Phys. Chem. Chem. Phys.* **2018**, *20*, 16666–16672.
(365) Ma, P. C.; Kim, J. K.; Tang, B. Z. Effects of Silane Functionalization on the Properties of Carbon Nanotube/Epoxy Nanocomposites. *Compos. Sci. Technol.* **2007**, *67* (14), 2965–2972.
(366) Li, J.; Ma, P. C.; Chow, W. S.; To, C. K.; Tang, B. Z.; Kim, J. K. Correlations between Percolation Threshold, Dispersion State, and Aspect Ratio of Carbon Nanotubes. *Adv. Funct. Mater.* **2007**, *17* (16), 3207–3215.
(367) Sadeghi, S.; Arjmand, M.; Otero Navas, I.; Zehtab Yazdi, A.; Sundararaj, U. Effect of Nanofiller Geometry on Network Formation in Polymeric Nanocomposites: Comparison of Rheological and Electrical Properties of Multiwalled Carbon Nanotube and Graphene Nanoribbon. *Macromolecules* **2017**, *50* (10), 3954–3967.
(368) Li, C.; Thostenson, E. T.; Chou, T. W. Dominant Role of Tunneling Resistance in the Electrical Conductivity of Carbon Nanotube-Based Composites. *Appl. Phys. Lett.* **2007**, *91* (22), 1–4.
(369) Martinez-Martinez, D. Nanocomposite. In *Encyclopedia of Tribology*; Wang, Q. J., Chung, Y.-W., Eds.; Springer US, 2013; pp 2359–2465.
(370) Li, Z.; Chang, S. C.; Williams, R. S. Self-Assembly of Alkanethiol Molecules onto Platinum and Platinum Oxide Surfaces. *Langmuir* **2003**, *19* (17), 6744–6749.
(371) Love, J. C.; Estroff, L. A.; Kriebel, J. K.; Nuzzo, R. G.; Whitesides, G. M. Self-Assembled Monolayers of Thiolates on Metals as a Form of Nanotechnology. *Chem. Rev.* **2005**, *105*, 1103–1169.
(372) Ikemura, K.; Kojima, K.; Endo, T.; Kadoma, Y. Effect of Novel Dithiooctanoate Monomers, in Comparison with Various Sulfur-Containing Adhesive Monomers, on Adhesion to Precious Metals and Alloys. *Dent. Mater. J.* **2011**, *30* (1), 72–78.
(373) Lattuada, M.; Hatton, T. A. Functionalization of Monodisperse Magnetic Nanoparticles. *Langmuir* **2007**, *23* (4), 2158–2168.
(374) Vaisman, L.; Wagner, H. D.; Marom, G. The Role of Surfactants in Dispersion of Carbon Nanotubes. *Adv. Colloid Interface Sci.* **2006**, *128–130* (2006), 37–46.
(375) Kim, M. J.; Lee, J.; Jung, D.; Shim, S. E. Electrospun Poly(Vinyl Alcohol) Nanofibers Incorporating PEGylated Multi-Wall Carbon Nanotube. *Synth. Met.* **2010**, *160* (13–14), 1410–1414.
(376) Chen, T.; Hou, K.; Ren, Q.; Chen, G.; Wei, P.; Zhu, M. Nanoparticle–Polymer Synergies in Nanocomposite Hydrogels: From Design to Application. *Macromol. Rapid Commun.* **2018**, *39* (21), 1800337.
(377) Li, Z.; Tang, M.; Dai, J.; Wang, T.; Bai, R. Effect of Multiwalled Carbon Nanotube-Grafted Polymer Brushes on the Mechanical and Swelling Properties of Polyacrylamide Composite Hydrogels. *Polymer (Guildf).* **2016**, *85*, 67–76.
(378) Wessling, B. Dispersion Hypothesis and Non Equillibrium Thermodynamics: Key Elements of Material Science of Conductive Polymers. *Synth. Met.* **1991**, *45*, 119–149.
(379) Gemeinhart, R. A.; Park, H.; Park, K. Pore Structure of Superporous Hydrogels. *Polym. Adv. Technol.* **2000**, *11* (8–12), 617–625.

(380) Dinh, N. T.; Kanoun, O. Temperature-Compensated Force/Pressure Sensor Based on Multi-Walled Carbon Nanotube Epoxy Composites. *Sensors* **2015**, *15* (5), 11133–11150.
(381) Weiss, N.; van Vliet, T.; Silberberg, A. Influence of Polymerization Initiation Rate on Permeability of Aqueous Polyacrylamide Gels. *J. Polym. Sci. Polym. Phys. Ed.* **1981**, *19* (10), 1505–1512.
(382) Mampallil, D.; Eral, H. B. A Review on Suppression and Utilization of the Coffee-Ring Effect. *Adv. Colloid Interface Sci.* **2018**, *252*, 38–54.
(383) Schlecht, C. a.; Maurer, J. a. Functionalization of Glass Substrates: Mechanistic Insights into the Surface Reaction of Trialkoxysilanes. *RSC Adv.* **2011**, *1*, 1446–1448.
(384) Petrovykh, D. Y.; Kimura-Suda, H.; Opdahl, A.; Richter, L. J.; Tarlov, M. J.; Whitman, L. J. Alkanethiols on Platinum: Multicomponent Self-Assembled Monolayers. *Langmuir* **2006**, *22* (6), 2578–2587.
(385) Yildiz, G.; Catalgil-Giz, H.; Giz, A. Effect of Ultrasound on Electrochemically Initiated Acrylamide Polymerization. *J. Appl. Polym. Sci.* **2002**, *84* (1), 83–89.
(386) Guiseppi-Elie, A. Electroconductive Hydrogels: Synthesis, Characterization and Biomedical Applications. *Biomaterials* **2010**, *31* (10), 2701–2716.
(387) Kim, B. C.; Spinks, G. M.; Wallace, G. G.; John, R. Electroformation of Conducting Polymers in a Hydrogel Support Matrix. *Polymer (Guildf).* **2000**, *41* (5), 1783–1790.
(388) Kosmala, A.; Wright, R.; Zhang, Q.; Kirby, P. Synthesis of Silver Nano Particles and Fabrication of Aqueous Ag Inks for Inkjet Printing. *Mater. Chem. Phys.* **2011**, *129* (3), 1075–1080.
(389) Kholghi, S.; Chinnappan, A.; Jayathilaka, W. A. D. M.; Khatibzadeh, M.; Kowsari, E.; Ramakrishna, S. A Review on Inkjet Printing of CNT Composites for Smart Applications. *Appl. Mater. Today* **2017**, *9*, 372–386.
(390) Smith, P.; Morrin, A. Reactive Inkjet Printing. *J. Mater. Chem.* **2012**, *22*, 10965–10970.
(391) Neumann, K.; Conde-gonz, A.; Owens, M.; Venturato, A.; Zhang, Y.; Geng, J.; Bradley, M. Supporting Information: An Approach to the High-Throughput Microarrays through Thiol-Ene Chemistry Glycopolymer. *Macromolecules* **2017**, *50* (16), 6026–6031.
(392) Tekin, E.; Smith, P. J.; Schubert, U. S. Inkjet Printing as a Deposition and Patterning Tool for Polymers and Inorganic Particles. *Soft Matter* **2008**, *4*, 703–713.
(393) Cummins, G.; Desmulliez, M. P. Y. Inkjet Printing of Conductive Materials: A Review. *Circuit World* **2012**, *38* (4), 193–213.
(394) Joh, D. Y.; Hucknall, A. M.; Wei, Q.; Mason, K. A.; Lund, M. L.; Fontes, C. M.; Hill, R. T.; Blair, R.; Zimmers, Z.; Achar, R. K.; et al. Inkjet-Printed Point-of-Care Immunoassay on a Nanoscale Polymer Brush Enables Subpicomolar Detection of Analytes in Blood. *Proc. Natl. Acad. Sci.* **2017**, *114* (34), 7054–7062.
(395) Tourniaire, G.; Collins, J.; Campbell, S.; Mizomoto, H.; Ogawa, S.; Thaburet, J. F.; Bradley, M. Polymer Microarrays for Cellular Adhesion. *Chem. Commun.* **2006**, *20*, 2118–2120.
(396) Sola, L.; Damin, F.; Chiari, M. Array of Multifunctional Polymers for Localized Immobilization of Biomolecules on Microarray Substrates. *Anal. Chim. Acta* **2019**, *1047*, 188–196.
(397) Tian, D.; Song, Y.; Jiang, L. Patterning of Controllable Surface Wettability for Printing Techniques. *Chem. Soc. Rev.* **2013**, *42* (12), 5184–5209.
(398) Castrejón-Pita, J. R.; Kubiak, K. J.; Castrejón-Pita, A. A.; Wilson, M. C. T.; Hutchings, I. M. Mixing and Internal Dynamics of Droplets Impacting and Coalescing on a Solid Surface. *Phys. Rev. E - Stat. Nonlinear, Soft Matter Phys.* **2013**, *88* (2), 1–12.
(399) Stringer, J.; Althagathi, T. M.; Tse, C. C. W.; Ta, V. D.; Shephard, J. D.; Esenturk, E.; Connaughton, C.; Wasley, T. J.; Li, J.; Kay, R. W.; et al. Integration of Additive Manufacturing and Inkjet Printed Electronics: A Potential Route to Parts with Embedded Multifunctionality. *Manuf. Rev.* **2016**, *3* (12), 1–17.
(400) Gans, B. B. De; Duineveld, P. C.; Schubert, U. S. Inkjet Printing of Polymers : State of the Art and Future Developments. *Adv. Mater.* **2004**, *16* (3), 203–213.
(401) Dybowska-Sarapuk, L.; Kielbasinski, K.; Arazna, A.; Futera, K.; Skalski, A.; Janczak, D.; Sloma, M.; Jakubowska, M. Efficient Inkjet Printing of Graphene-Based Elements: Influence of Dispersing Agent on Ink Viscosity. *Nanomaterials* **2018**, *8* (8), 1–11.
(402) Denneulin, A.; Bras, J.; Carcone, F.; Neuman, C.; Blayo, A. Impact of Ink Formulation on Carbon Nanotube Network Organization within Inkjet Printed Conductive Films. *Carbon N. Y.* **2011**, *49* (8), 2603–2614.
(403) Qu, L. T.; Peng, Q.; Dai, L. M.; Spinks, G. M.; Wallace, G. G.; Baughman, R. H. Carbon Nanotube Electroactive Polymer Materials: Opportunities and Challenges. *Mater. Res. Soc. Bull.* **2008**, *33* (3), 215–224.
(404) Romanov, V.; Davidoff, S. N.; Miles, A. R.; Grainger, D. W.; Gale, B. K.; Brooks, B. D. A Critical Comparison of Protein Microarray Fabrication Technologies. *Analyst* **2014**, *139* (6), 1303–1326.

(405) Hue P. Le. Progress and Trends in Ink-Jet Printing Technology. *J. Imaging Sci. Technol.* **1998**, *42* (1), 49–62.
(406) Li, B.; Zhang, Z.; Qi, J.; Zhou, N.; Qin, S.; Choo, J.; Chen, L. Quantum Dot-Based Molecularly Imprinted Polymers on Three-Dimensional Origami Paper Micro Fl Uidic Chip for Fluorescence Detection of Phycocyanin. *ACS Sensors* **2017**, *2*, 243–250.
(407) Seok, H.; Seok, O.; Kim, J.; Conde, J.; Artzi, N. 3D Hydrogel Scaffold Doped with 2D Graphene Materials for Biosensors and Bioelectronics. *Biosens. Bioelectron.* **2017**, *89*, 187–200.
(408) Smith, P. J.; Fleet, E. J.; Zhang, Y. Inkjet Printing of Functional Polymers into Carbon Fiber Composites. In *Nanomaterials for 2D and 3D Printing*; 2017; pp 275–291.
(409) Lange, A.; Wegener, M.; Fischer, B.; Janietz, S.; Wedel, A. Solar Cells with Inkjet Printed Polymer Layers. *Energy Procedia* **2012**, *31*, 150–158.
(410) Schild, H. G. Poly(N-Isopropylacrylamide): Experiment, Theory and Application. *Prog. Polym. Sci.* **1992**, *17*, 163–249.
(411) Hu, X.; Tong, Z.; Lyon, L. A. Control of Poly(N-Isopropylacrylamide) Microgel Network Structure by Precipitation Polymerization near the Lower Critical Solution Temperature. *Langmuir* **2011**, *27* (7), 4142–4148.
(412) Liu, L.; Zhao, H.; Lei, Y. Advances on Three-dimensional Electrodes for Micro-supercapacitors: A Mini-review. *InfoMat* **2019**, *1* (1), 74–84.
(413) Chee, L. T.; Razak, M. A. A. Software for Extraction of Cell Properties from Dielectrophoretic Data Using Well Electrode. *J. Teknol. (Sciences Eng.* **2013**, *61* (2), 59–64.

Appendix A

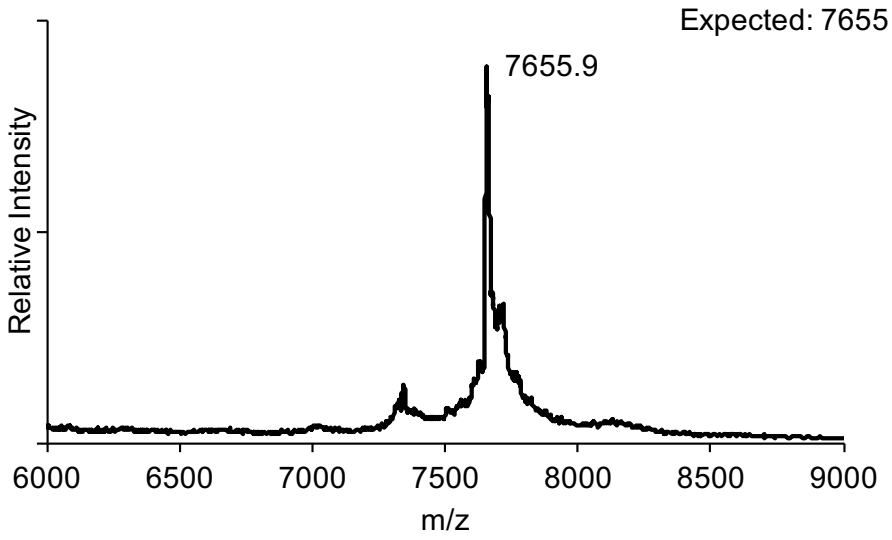

Figure A1 MALDI-ToF Spectrum of Modified 'Sensor' Morpholino Oligonucleotide

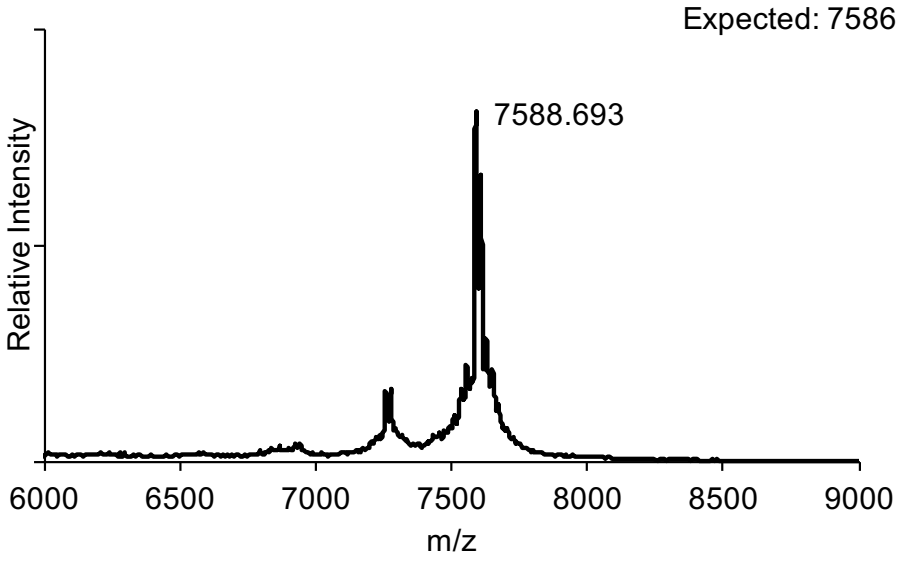

Figure A2 MALDI-ToF Spectrum of Modified 'Blocker' Morpholino Oligonucleotide

Appendix B

```
function V= gel vol 1(I,LHS,RHS,horizon,top,width,chip size)
%-----------------------------------------------------------------
%Function to calculate droplet volume from an image given a %pre-defined ' region of interest '
%-----------------------------------------------------------------
%AUTHOR: David Ferrier
%DATE: 26/11/15
%-----------------------------------------------------------------
%Inputs :
%I - image data
%LHS - left hand extent of region of interest
%RHS - right hand extent of region of interest
%width - width of chip (in pixels)
%horizon - lower extent of region of interest
%top - upper extent of region of interest
%chip size - width of chip in mm
% ---------------------------------
%Output:
%V - Droplet volume (in uL)
%-----------------------------------------------------------------
I = double(255 I ); %Invert image ( light to dark)
%-----------------------------------------------------------------
%Crop image to region of interest
J = I(top:horizon,LHS:RHS);
[row,col] = size(J);
%-----------------------------------------------------------------
%----------
%Define threshold for droplet edge detection based on image
%edges
left edge = J(: ,1);
right edge = J(: , col );
left max = max(left edge);
right max = max(right edge);
edge max = max(left max ,right max);
thresh = edge max + 10;
%----------
%Find edges of droplet for every row
lhs = zeros(row,1); %Left hand side
for ind = 1:row
    for dni = 1:col
        if J(ind,dni)>thresh
            lhs(ind,1) = dni;
            break
        end
    end
end
rhs = zeros(row,1); %Right hand side
for ind = 1:row
    for dni = col:-1:1
        if J(ind,dni)>thresh
            lhs(ind,1) = dni;
            break
        end
    end
end
%-----------------------------------------------------------------
%-----------------------------------------------------------------
%Calculate volume by assuming droplet is composed of a series
%of perfect circles stacked on top of each other
Vpix = 0;
for ind = 1:row
    if rhs(ind,1)==col || lhs(ind,1)==1;
        continue
    end
    d = rhs(ind ,1) - lhs(ind ,1); %diameter of circle a = pi*(d/2)^2; %number of pixels in layer       Vpix = Vpix + a;
end
%-----------------------------------------------------------------
%-----------------------------------------------------------------
%Convert from pixels to real scale
pixel d = chip size/width; %mm
pixel d = pixel d /1000; %m
pixel v = pixel d^3; %m3
V= Vpix*pixel v; %m3
V=V*1e9; %uL
%-----------------------------------------------------------------
%-----------------------------------------------------------------
```